# CHARGE SEPARATION AND RECOMBINATION IN DYE SENSITISED SEMICONDUCTOR SOLAR CELLS

YASUHIRO TACHIBANA

Submitted to the University of London in partial fulfilment for the degree of Doctor of Philosophy

**1999**

Molecular Dynamics Group,
Centre for Photomolecular Sciences,
Departments of Chemistry and Biochemistry,
Imperial College, London



# Abstract

The dynamics of interfacial electron transfer in dye-sensitised titanium dioxide ($TiO_2$) nanocrystalline films has been studied by means of the femtosecond to millisecond transient absorption spectroscopy.

The project required the construction of a nanosecond transient absorption spectrometer, and the development of a femtosecond optical parametric amplifier to provide a tuneable excitation source and a pump-probe system for ultrafast transient absorption measurements. The construction and operation of the laser are described in detail.

Interfacial electron transfer kinetics have been studied for the sensitiser dye *cis*-ruthenium$^{II}$(2,2'-bipyridyl-4,4'-dicarboxylate)$_2$(NCS)$_2$ ($Ru(dcbpy)_2(NCS)_2$) adsorbed onto the surface of nanocrystalline $TiO_2$ films. This system was chosen as it is attracting considerable attention for application in photoelectrochemical solar energy conversion. A method to assign the kinetics of electron transfer reactions at the dye / semiconductor interface has been established. It has been found that the electron injection is multi-exponential on femtosecond / picosecond timescales. In contrast, the charge recombination completes on microsecond-millisecond timescales.

The parameters influencing the electron injection kinetics in $Ru(dcbpy)_2(NCS)_2$ sensitised nanocrystalline $TiO_2$ films have been studied. $Ru(dcbpy)_2(NCS)_2$ is compared with other sensitiser dyes in order to address the origin of the high efficiency achieved with this dye. Different experimental conditions were employed in order to compare the injection kinetics in $Ru(dcbpy)_2(NCS)_2$ sensitised $TiO_2$ films, including excitation wavelength, solvent environment, electrolyte composition and application of external voltages.

The results of these experiments are discussed in terms of heterogeneous electron transfer theory. The relevance of these results to the function of dye sensitised semiconductor photoelectrochemical solar cells is also discussed, relating in particular to the energy conversion efficiency and the long-term stability of the cell.

# Acknowledgements

Firstly, I would like to acknowledge my co-supervisors, David R. Klug and James R. Durrant, for their great advice and exciting scientific influence for my research project.

I would also like to thank my parents, Shigesada and Yoshino Tachibana, for their understanding of my PhD study in England and for their continuous financial support and patience.

Special thanks to both Professor George Porter for his valuable encouragement and financial help, and to Professor Shozo Yanagida for his kind advice.

I am also grateful to Michael Grätzel and Jacques E. Moser for their support and many helpful discussions, and to M. K. Nazeeruddin and Pascal Comte for sample preparations.

Special thanks to Chris Barnett for his excellent technical support, to Steve Merry, Saif Haque, Ivan Montanari and Richard Willis for help in data collection, to Wolfgang Mohr and Martin Bell for their help in computer analysis, to Jenny Nelson, Ian Mercer, Stefan Abend and Udo Bach for many helpful discussions.

Finally, I would like to acknowledge Carol Olson for her great encouragement and assistance for my thesis writing in English, Richard Tompkins, Melissa Joseph and my special friend, Richard Tilcock, for teaching me useful and practical English phrases, Manfred Fettweis, Laura Barter, Chris Jeans, Maria Schilstra, Manos Topoglidis, Thierry Lutz, Shogo Tanaka, Hideyuki Yamakoshi, Norio Nagayama, Jennifer Wu, Marcel Potter, Giles Marlow, Tomoka Sakihara, Toshiyuki Okada and Linda Giorgi for their kind encouragement and entertainment during my PhD life.

*Dedicated to my parents*

# Contents


Title ..... 1

Abstract ..... 2

Acknowledgements ..... 3

Contents ..... 5

List of Figures and Tables ..... 10

Abbreviations ..... 18

**Chapter 1: Introduction ..... 20**

**1.1 Solar energy conversion and photoelectrochemical cells ..... 20**

**1.2 Dye sensitised nanocrystalline semiconductor solar cells ..... 23**

**1.3 Electron transfer at dye / semiconductor interface ..... 27**

**1.4 Motivation and aim of the PhD studies ..... 29**

**Chapter 2: Experiments ..... 32**

**2.1 Transient absorption spectroscopy ..... 32**

2.1.1 Principle ..... 32

2.1.2 Calculation of absorption difference ..... 33

2.1.3 Contribution to absorption difference spectra ..... 34

**2.2 Femtosecond transient absorption spectrometer ..... 35**

2.2.1 Femtosecond dye laser system ..... 35

2.2.1.1 Introduction ..... 35

2.2.1.2 Femtosecond pulse generation ..... 35

2.2.1.3 Pulse amplification ..... 38

2.2.1.4 Pump-probe set-up ..... 38

2.2.2 Solid-state femtosecond Ti:sapphire laser system ..... 39

2.2.2.1 Overview of chirped pulse amplifier (CPA) system ..... 39

2.2.2.2 Femtosecond pulse generation ..... 40

2.2.2.3 Pulse expansion ..... 41

2.2.2.4 Regenerative pulse amplifier ..... 41

2.2.2.5 Pulse compression ..... 42

2.2.3 Optical Parametric Amplifier (OPA) ..... 42

2.2.3.1 Introduction ..... 42
2.2.3.2 Comparison between the OPA and the bow-tie dye jet amplifier ..... 43
2.2.3.3 Principle of optical parametric amplification ..... 45
2.2.3.4 Arrangement of the OPA system ..... 50
2.2.3.5 White light continuum seed arm ..... 51
2.2.3.6 Second harmonic (405 nm) pump arm ..... 52
2.2.3.7 Optical parametric amplification ..... 53
2.2.4 Ultrafast transient absorption spectrometer in the Ti:sapphire laser system . 56
2.2.4.1 Introduction ..... 56
2.2.4.2 Pump arm ..... 56
2.2.4.3 White light continuum probe arm ..... 58
2.2.5 Data collection and analysis ..... 59
2.2.5.1 Multi-channel data collection system ..... 59
2.2.5.2 Synchronisation in the transient absorption spectroscopy ..... 60
2.2.5.3 Data analysis ..... 62
2.2.5.4 Noise and artifacts in the laser apparatus and improvement of the system ..... 63
**2.3 Other experimental apparatus ..... 66**
2.3.1 Introduction ..... 66
2.3.2 Steady state UV / vis absorption and emission spectrometer ..... 67
2.3.3 Microsecond-millisecond transient absorption spectrometer ..... 67
2.3.4 Nanosecond transient absorption and emission spectrometer ..... 69
2.3.4.1 Introduction ..... 69
2.3.4.2 Arrangement of the apparatus ..... 69
2.3.5 Monochromatic photocurrent measurement ..... 71
**2.4 Sample preparation ..... 71**
2.4.1 Preparation of nanocrystalline anatase $TiO_2$ films ..... 71
2.4.2 Preparation of dye ethanol solution ..... 74
2.4.3 Sensitisation procedure ..... 76

**Chapter 3: Fundamental concepts of electrochemistry and interfacial electron transfer ..... 79**
**3.1 Introduction ..... 79**

**3.2 Interfacial electrochemistry ..... 79**
3.2.1 Description of interfacial structure (Bockris, et al. 1993) ..... 79
3.2.2. Energy bands of the semiconductor electrode (Finklea 1988, Miller, et al. 1995, Schmickler 1996) ..... 81
3.2.3 Potential profile and band bending of the semiconductor (Finklea 1988, Gerischer 1990, Schmickler 1996) ..... 83
3.2.4 Surface states (Bockris and Khan 1993, Christensen and Hamnett 1994, Finklea 1988) ..... 85
3.2.5 Nanocrystalline $TiO_2$ films ..... 87
3.2.6 Three electrode cell configuration (Finklea 1988, Schmickler 1996) ..... 92
3.2.6.1 Configuration ..... 92
3.2.6.2 Application of the external bias (Finklea 1988) ..... 93
**3.3 Theoretical treatment of electron transfer ..... 95**
3.3.1 Introduction ..... 95
3.3.2 Homogeneous electron transfer ..... 96
3.3.2.1 Non-adiabatic electron transfer ..... 96
3.3.2.2 Adiabatic electron transfer ..... 104
3.3.3 Extension of homogeneous electron transfer theory to electron injection in dye sensitised semiconductors ..... 105
3.3.3.1 Non-adiabatic electron transfer ..... 106
3.3.3.2 Adiabatic electron transfer ..... 110

**Chapter 4: Assignment of interfacial electron transfer kinetics in $Ru(dcbpy)_2(NCS)_2$ sensitised $TiO_2$ films ..... 113**
**4.1 Introduction ..... 113**
**4.2 Previous studies of interfacial electron injection kinetics ..... 114**
**4.3 Assignment of interfacial electron transfer rates in $Ru(dcbpy)_2(NCS)_2$ sensitised $TiO_2$ films ..... 117**
4.3.1 Experimental conditions ..... 118
4.3.1.1 Samples ..... 118
4.3.1.2 Transient measurements ..... 118
4.3.2 Experimental results ..... 121
4.3.2.1. Steady state absorption and emission spectra ..... 121

4.3.2.2 Transient results: solution phase ..... 123
4.3.2.3 Transient data: Nanocrystalline films ..... 128
4.3.3 Discussion ..... 138
**4.4 Stability of $Ru(dcbpy)_2(NCS)_2$ sensitised $TiO_2$ films under optical experiments ..... 145**

**Chapter 5: Parameters influencing electron injection kinetics ..... 148**
**5.1 Introduction ..... 148**
**5.2 Experimental condition ..... 150**
5.2.1 Ti:sapphire laser transient absorption spectrometer ..... 150
5.2.2 Photoelectrochemical experiments ..... 150
**5.3 Dependence on excitation wavelengths ..... 152**
5.3.1 Introduction ..... 152
5.3.2 Results ..... 153
5.3.3 Discussion ..... 156
**5.4 Dependence on surrounding solvents ..... 156**
5.4.1 Results ..... 157
5.4.2 Discussion ..... 158
**5.5 Dependence on $TiO_2$ Fermi level ..... 159**
5.5.1 Introduction ..... 159
5.5.2 Results ..... 160
5.5.3 Discussion ..... 165
**5.6 Dependence on conduction band energetics ..... 169**
5.6.1 Introduction ..... 169
5.6.2 Results ..... 172
5.6.3 Discussion ..... 174
**5.7 Dependence on sensitiser dyes ..... 176**
5.7.1 Introduction ..... 176
5.7.2 Results ..... 178
5.7.2.1 $Ru(dcbpy)_2(NCS)_2$ ..... 178
5.7.2.2 ZnTCPP ..... 179
5.7.2.3 $H_2TCPP$ ..... 183
5.7.2.4 Comparison of the three sensitiser dyes ..... 188

5.7.2.5 Excitation power dependence ..... 190
5.7.3 Discussion ..... 192
**5.8 General discussion ..... 196**
**5.9 Relevance to solar cells ..... 199**

**Chapter 6: Electron injection kinetics in dye sensitised solar cells.... 203**
**6.1 Introduction ..... 203**
**6.2 Experiment ..... 203**
6.2.1 Fabrication of the solar cell ..... 203
6.2.2 Experimental condition of the fs transient measurement ..... 204
**6.3 Results ..... 205**
**6.4 Discussion ..... 208**

**Chapter 7: Conclusion ..... 211**

**Appendix A: Distribution analysis of electron injection kinetics ..... 214**

**Appendix B: Global analysis ..... 222**

References ..... 224

# List of Figures and Tables

## List of Figures

### *Chapter 1*

Figure 1.1. Two forms of energy generated in photoelectrochemical cells (Lewis 1996). .....20

Figure 1.2. Schematic diagrams of four types of semiconductor based photoelectrochemical cells mimicking solar water splitting (Bard and Fox 1995). .....21

Figure 1.3. Photoelectrochemical solar cell based upon ruthenium dye sensitised $TiO_2$ nanocrystalline film. .....23

Figure 1.4. Diagram illustrated for the dye sensitised semiconductor nanocrystalline solar cells. .....24

Figure 1.5. Photocurrent action spectra for the $TiO_2$ sensitised by $RuL_2(NCS)_2$, $RuL_2Cl_2$ and $RuL_2(CN)_2$ where L is a dcbpy ligand (Nazeeruddin, et al. 1993). .....25

Figure 1.6. Schematic potential diagram of ruthenium dye sensitised $TiO_2$ solar cell. ..27

Figure 1.7. Schematic representation of charge separation in ruthenium dye sensitised $TiO_2$ nanocrystalline films. .....28

### *Chapter 2*

Figure 2.1. Arrangement of the femtosecond dye laser system taken from the PhD thesis of Dr. M. Joseph (Joseph 1996). .....37

Figure 2.2. Diagram of the femtosecond Ti:sapphire laser system, modified from the figure in the PhD thesis of Dr. R. Tompkins (Tompkins 1998). .....40

Figure 2.3. Refractive index plotted as a function of direction in a birefringent crystal. .....47

Figure 2.4. Section of refractive index plots containing the optic axis in an uniaxial negative crystal. .....48

Figure 2.5. Schematic description of conservation of momentum. .....49

Figure 2.6. Phase matching curve (Reed, et al. 1995) calculated for the BBO crystal for a pump wavelength of 400 nm (Kato 1986). .....49
Figure 2.7. Schematic diagram of the OPA system. All of the BBO crystals employed in this system have a thickness of 1 cm and are mounted on the translation stage. .....50
Figure 2.8. Schematic diagram of the pump-probe apparatus for the femtosecond Ti:sapphire laser system. .....57
Figure 2.9. Diagrams presenting the synchronisation for both dye laser and Ti:sapphire laser systems. .....61
Figure 2.10. Schematic diagram of the μs-ms transient absorption spectrometer. .....68
Figure 2.11. Schematic diagram of the nanosecond transient absorption spectrometer. 70
Figure 2.12. Scanning electron micrographs of the nanocrystalline $TiO_2$ film, taken from the recent report by Nazeeruddin et al. (Nazeeruddin, et al. 1993). .....74
Figure 2.13. Structure of sensitiser dyes; (a) $Ru(dcbpy)_2(NCS)_2$, (b) ZnTCPP and (c) $H_2TCPP$. .....75

## *Chapter 3*

Figure 3.1. Potential profiles of the interface on the (a) Helmholtz, (b) diffuse layer and (c) Stern models. .....80
Figure 3.2. An example of the double layer structure in the electrode / electrolyte interface. .....80
Figure 3.3. Energy band diagram of an n-type semiconductor. Fermi level is shifted towards the conduction band due to the presence of donors. .....82
Figure 3.4. Potentials of band edges and band gaps for a series of bulk semiconductors in an aqueous electrolyte at pH = 1. .....83
Figure 3.5. Band structures of an n-type semiconductor in contact with an electrolyte. .....84
Figure 3.6. Flat band potentials as a function of the pH in the electrolyte for $SnO_2$ (•); $TiO_2$ (○); $KTaO_3$ (▲); $KTa_{0.77}Nb_{0.23}O_3$ (□); and $SrTiO_3$ (■) semiconductors. .....87
Figure 3.7. Potentials of the space charge layer in a large (bulk) and a small semiconductor particle in contact with the redox active electrolyte. .....88
Figure 3.8. Potential profile presenting the band bending in depletion and accumulation modes for small $TiO_2$ particle (average diameter: 15 nm). .....90

Figure 3.9. Dependence of the flat band potential on pH in the aqueous solution for a nanocrystalline $TiO_2$ electrode. .....91
Figure 3.10. The photograph of the three-electrode cell. .....93
Figure 3.11. Electronic potential energy diagram for discrete donor and acceptor states as square wells. .....97
Figure 3.12. One dimensional profile of many dimensional free energy surface of reactant (R) and product (P) states. .....98
Figure 3.13. Relationship between electronic potential energy curves (on the left) and the free energy curves (on the right). .....100
Figure 3.14. Profiles of free energy surfaces of reactant and product states for three different types of electron transfer reactions. .....103
Figure 3.15. Example of experimental evidence for the presence of the inverted region (Miller, et al. 1984). .....104
Figure 3.16. Potential energy diagram representing the electron injection reaction from the dye excited state (donor) into the multiple states (acceptor) in the conduction band. .....106
Figure 3.17. Free energy diagram of the non-adiabatic electron injection reaction from the dye excited state to the conduction band of the semiconductor. .....108
Figure 3.18. Comparison of the relationship between an electron transfer rate and free energy difference for the homogeneous reaction (a) and the dye sensitisation (b). ....110
Figure 3.19. Free energy diagram of adiabatic electron injection reaction in the dye sensitised semiconductor. .....111

## *Chapter 4*

Figure 4.1. (a) Steady state absorption (·····) and emission (——) spectra of $Ru(dcbpy)_2(NCS)_2$. (b) Steady state absorption spectra of $Ru(dcbpy)_2(NCS)_2$ in ethanol (·····) and the same dye adsorbed onto the surface of a nanocrystalline $TiO_2$(——) and $ZrO_2$(– –) films. .....122
Figure 4.2. Absorption difference spectra of $Ru(dcbpy)_2(NCS)_2$ in ethanol solution. .124
Figure 4.3. Absorption difference spectra (——) and kinetic spectra (·····) of the kinetic components obtained for $Ru(dcbpy)_2(NCS)_2$ in ethanol solution. .....125

Figure 4.4. Nanosecond transient absorption decay for $Ru(dcbpy)_2(NCS)_2$ in ethanol solution ($5 \times 10^{-5}$ M) monitored at 700 nm with an excitation wavelength of 510 nm. .....126

Figure 4.5. Absorption difference spectra of the formation of cation (—o—) and excited (·····) states of $Ru(dcbpy)_2(NCS)_2$ in ethanol solution. .....127

Figure 4.6. Nanosecond transient absorption decays for $Ru(dcbpy)_2(NCS)_2$ sensitised $TiO_2$ (•) and $ZrO_2$ (o) films. .....128

Figure 4.7. Nanosecond emission decay kinetics for $TiO_2$ (——) and $ZrO_2$ (·····) films coated by $Ru(dcbpy)_2(NCS)_2$. .....129

Figure 4.8. Transient absorption difference spectra obtained for $TiO_2$ (——) and $ZrO_2$ (·····) films sensitised by $Ru(dcbpy)_2(NCS)_2$ taken at a time delay of 5 ns following 510 nm excitation. .....130

Figure 4.9. Absorption difference spectra obtained for $TiO_2$ (——) and $ZrO_2$ (·····) coated by $Ru(dcbpy)_2(NCS)_2$ taken at a time delay of 5 ps after 605 nm excitation. ..131

Figure 4.10. Transient absorption spectra obtained for $Ru(dcbpy)_2(NCS)_2$ sensitised $TiO_2$ films covered in EC / PC. .....133

Figure 4.11. Transient absorption kinetics obtained for the $Ru(dcbpy)_2(NCS)_2$ coated $TiO_2$ films. .....134

Figure 4.12. (a) Spectrum of the amplitude of the 1 ps component observed with the dye coated $TiO_2$ film (——) with 605 nm excitation. (b) Amplitude spectra of the 1 (·····) and 13 (——) ps components obtained as a result of global analysis for the data of the dye coated $TiO_2$ film with an excitation wavelength of 560 nm. .....136

Figure 4.13. The kinetics of charge recombination for the $Ru(dcbpy)_2(NCS)_2$ coated $TiO_2$ film, monitored by the decay of the cation absorption band at 820 nm. .....137

Figure 4.14. Summary presenting the interfacial electron transfer and the dye excited state kinetics for $Ru(dcbpy)_2(NCS)_2$ sensitised $TiO_2$ films.....144

Figure 4.15. Comparison of the transient absorption spectra obtained for the dye in ethanol (1), the fresh dye sensitised $TiO_2$ films (2) and the sensitised films left for one day in air (3) at a time delay of 5 ps after 605 nm excitation. .....146

## *Chapter 5*

Figure 5.1. Schematic representation of potential diagram of dye sensitised $TiO_2$ nanocrystalline films. .....153

Figure 5.2. Absorption difference spectra obtained for $Ru(dcbpy)_2(NCS)_2$ sensitised $TiO_2$ films covered in EC / PC at a time delay of 60 ps after 525 (·····), 560 (——) and 600 (------) nm excitations. .....154

Figure 5.3. Transient kinetics obtained for the dye coated $TiO_2$ films with excitation wavelengths of 525 (Δ), 560 (•) and 600 (o) nm at a probe wavelength of 760 nm. ...155

Figure 5.4. Kinetic spectra obtained for the dye coated $TiO_2$ films with excitation wavelengths of 525 (·····), 560 (——) and 600 (------) nm. .....155

Figure 5.5. Electron injection kinetics for the dye coated $TiO_2$ films under different solvent environments at a probe wavelength of 760 nm. .....158

Figure 5.6. Dependence of electron injection kinetics upon the magnitude of the external voltages applied to $Ru(dcbpy)_2(NCS)_2$ sensitised $TiO_2$ electrode. .....161

Figure 5.7. Transient absorption spectra taken at 60 ps after 623 nm excitation with bias application of >-0.4 ~ -0.9 V vs Ag/AgCl to the dye sensitised $TiO_2$ electrode in electrolyte B. .....162

Figure 5.8. Transient injection kinetics for the films in electrolyte B, obtained with applied biases of –0.4 ~ -0.8 V vs Ag/AgCl at a probe wavelength of 760 nm with 623 nm excitation. .....163

Figure 5.9. Absorption difference spectra taken at a time delay of 8 ps following 525 nm excitation with bias application of 0, -0.6 and –0.8 V vs Ag/AgCl into the dye sensitised $TiO_2$ electrode in electrolyte A. .....164

Figure 5.10. Transient kinetics collected at bias application of 0 (circle), -0.4 (square), -0.6 (triangle) and -0.8 (diamond) V vs Ag/AgCl to $Ru(dcbpy)_2(NCS)_2$ sensitised $TiO_2$ electrode in electrolyte A at a probe wavelength of 760 nm following 525 nm excitation. The results of the kinetic fitting are shown as solid lines. .....165

Figure 5.11. Absorbance of electrons collected in the $TiO_2$ electrode in the anhydrous acetonitrile electrolyte (0.1 M TBAP contained) in the presence (square) and the absence (circle) of 0.1 M $LiClO_4$. .....170

Figure 5.12. Schematic representation of potential energy diagram of dye sensitised $TiO_2$ nanocrystalline films covered in electrolyte B and C. $k_{ei}$ and $k_{cr}$ refer to electron injection and charge recombination, respectively. .....171

Figure 5.13. Transient absorption spectra obtained (a) at 150 fs (————) and 60 ps (·····) in the presence of 0.1 M $Li^+$ (electrolyte B) and (b) at 150 fs (————) and 600 ps (·····) in the absence of $Li^+$ (electrolyte C). .....173

Figure 5.14. Electron injection kinetics for $Ru(dcbpy)_2(NCS)_2$ sensitised $TiO_2$ films collected in the presence (circle) and the absence (triangle) of $Li^+$ in electrolyte (electrolytes B and C respectively) at a probe wavelength of 760 nm following 623 nm excitation. Results of the kinetic fitting are shown as solid lines. .....174

Figure 5.15. Schematic representation of potential energy diagram of dye sensitised $TiO_2$ nanocrystalline films. .....178

Figure 5.16. Steady state absorption (·····) and emission(——) spectra of ZnTCPP in ethanol. An excitation wavelength for the emission was 560 nm. .....179

Figure 5.17. Picosecond absorption difference spectra obtained for ZnTCPP in ethanol (·····) and sensitised $TiO_2$ films (——) at time delays of 6 and 60 ps, respectively, with an excitation wavelength of 560 nm. .....180

Figure 5.18. Transient absorption spectra obtained for ZnTCPP coated $TiO_2$ films taken at time delays of 0.1 (·····), 3 (————) and 30 (--------) ps following 560 nm excitation. .....182

Figure 5.19. Transient absorption kinetics obtained for ZnTCPP in ethanol (o) and sensitised $TiO_2$ film (•) at a probe wavelength of 665 nm after 560 nm excitation. ...182

Figure 5.20. Amplitude spectra of the 1.1 (·····) and 8.5 (——) ps components obtained for ZnTCPP coated $TiO_2$ film by global analysis. .....183

Figure 5.21. Steady state absorption (·····) and emission (——) spectra of $H_2TCPP$ in ethanol. The emission was observed at an excitation wavelength of 589 nm. .....184

Figure 5.22. Absorption difference spectra obtained for $H_2TCPP$ in ethanol (·····) and the sensitised $TiO_2$ films (——), observed at time delays of 60 and 600 ps, respectively with an excitation wavelength of 645 nm. .....185

Figure 5.23. Transient absorption spectra observed for $H_2TCPP$ sensitised $TiO_2$ films at time delays of 0.1 (·····), 6 (————), 600 (--------) ps after 645 nm excitation. .186

Figure 5.24. Transient kinetics obtained for $H_2TCPP$ in ethanol (o) and its coated $TiO_2$ film (•) at a probe wavelength of 720 nm following 645 nm excitation. .....187

Figure 5.25. Kinetic spectra of the 0.75 (——) and 9.5 (·····) ps components obtained as a result of global analysis for $H_2TCPP$ sensitised $TiO_2$ films. .....187
Figure 5.26. Comparison of electron injection yield for $TiO_2$ films sensitised by $Ru(dcbpy)_2(NCS)_2$ (filled circle), ZnTCPP (open circle) and $H_2TCPP$ (open square). .....189
Figure 5.27. Kinetic spectra obtained for $TiO_2$ films sensitised by $Ru(dcbpy)_2(NCS)_2$ (a), ZnTCPP (b) and $H_2TCPP$ (c) with high (——) or low (·····) excitation power. ...191
Figure 5.28. Kinetic spectrum of the 340 ps component obtained for $H_2TCPP$ sensitised $TiO_2$ films with the higher excitation power at an excitation wavelength of 645 nm. .192
Figure 5.29. Examples of the geometrical structures presenting the linkage of $Ru(dcbpy)_2(NCS)_2$ onto $TiO_2$ surface (Shklover, et al. 1998). .....194

## *Chapter 6*

Figure 6.1. Steady state absorption spectra of the dye sensitised $TiO_2$ solar cell (.....) and the dye free cell (_ _ _ _ _ _). .....205
Figure 6.2 Current-voltage characteristics of a sandwich type solar cell employing N719 sensitised $TiO_2$ film. .....206
Figure 6.3. Transient absorption spectra obtained for the solar cell employing the $TiO_2$ film sensitised by N719 at time delays of 150 fs (·····) and 600 ps (————) following an excitation at 630 nm under the open circuit condition. .....208

## *Appendix A*

Figure A1. Time / amplitude (A) relations for distribution analysis. .....214
Figure A2. Kinetic decay obtained by arithmetic manipulation of the transient data observed for $Ru(dcbpy)_2(NCS)_2$ sensitised $TiO_2$ film covered in EC / PC at a probe wavelength of 760 nm with an excitation wavelength of 560 nm as shown in figure 4.11c. .....215
Figure A3. Transient decays of equations A1a (-------), A1b (————) and A1c (·····) created with arbitrary time constants and amplitudes. .....217
Figure A4. Results of distribution analysis for the transient kinetics of equations A1a (-----), A1b (————) and A1c (·····). .....217

Figure A5. Transient decay (filled circle) obtained by addition of equation A1a and Gaussian noise generated by equation A2 with σ = 35. .....219
Figure A6. Results of distribution analysis for the decays generated by combinations of equations A1a (-------), A1b (————) and A1c (·····), and Gaussian noise with σ = 4 (a), 6 (b) and 35 (c). .....220

***Appendix B***

Figure B1. Multi-channel transient absorption data obtained for $Ru(dcbpy)_2(NCS)_2$ sensitised $TiO_2$ films covered in EC / PC. .....223

## List of Tables

***Chapter 4***

Table 4.1. Previous transient kinetic studies of electron injection in dye sensitised $TiO_2$. .....114

***Chapter 5***

Table 5.1. Lifetimes and amplitudes[b] of normalised electron injection yield[a].....189

# Abbreviations

| | |
|---|---|
| Ag/AgCl | Silver / Silver chloride |
| ASE | Amplified stimulated emission |
| BBO | Barium-Borate |
| CCD | Charged Coupled Device |
| CPA | Chirped pulse amplifier |
| CPM | Colliding pulse mode-locking |
| CVL | Copper Vapour Laser |
| ΔOD | Differences in optical density |
| EC / PC | Ethylene carbonate / propylene carbonate |
| FI | Faraday Isolator |
| Fs | Femtosecond |
| F-$SnO_2$ | Fluorine doped tin oxide |
| FWHM | Full width at half maximum |
| GVD | Group Velocity Dispersion |
| $H_2TCPP$ | Free base tetracarboxyphenyl porphyrin |
| IHP | Inner Helmholtz plane |
| IPCE | Incident photon-to-current conversion efficiency |
| LMCT | Ligand to metal charge transfer |
| MLCT | Metal-to-ligand charge transfer |
| μs | Microsecond |
| ms | Millisecond |
| $MVCl_2$ | Methyl viologen dichloride hydrate |
| N719 | Tetrabutyl ammonium salt of $Ru(dcbpy)_2(NCS)_2$ |
| Nd:YLF | Neodymium-doped yttrium lithium fluoride |
| ns | Nanosecond |
| OHP | Outer Helmholtz plane |
| OPA | Optical parametric amplifier |
| ps | Picosecond |
| $Ru(bpy)_3^{2+}$ | Ruthenium (II) trisbipyridyl |
| $Ru(dcbpy)_2(NCS)_2$ | *cis*-ruthenium$^{II}$(2,2'-bipyridyl-4,4'-dicarboxylate)$_2$(NCS)$_2$ |
| SCE | Saturated calomel electrode |

| | |
|---|---|
| SHG | Second harmonic generation |
| SPM | Self-phase modulation |
| TBAP | Tetrabutyl ammonium perchlorate |
| TBAT | Tetrabutyl ammonium triflate |
| $TiO_2$ | Titanium dioxide |
| UV | Ultra violet |
| ZnTCPP | Zinc tetracarboxyphenyl porphyrin |
| $ZrO_2$ | Zirconium dioxide |

# Chapter 1: Introduction

## 1.1 Solar energy conversion and photoelectrochemical cells

Photoelectrochemistry has offered a wide variety of applications for solar energy conversion. Practical applications of photoelectrochemical cells have greatly progressed since the energy crisis began to be considered in the 1970s (Lewis 1996). In the photoelectrochemical cells, solar light energy is converted into electrical and / or chemical energy. Figure 1.1 illustrates examples of the generation of electrical and chemical energy from such cells (Lewis 1996). These two forms of energy can be stored for subsequent utilisation; for example, an electrical form of energy can be stored as charges on the plates of a capacitor, and a chemical form as in a rechargeable battery or hydrogen obtained by the electrolysis of water.

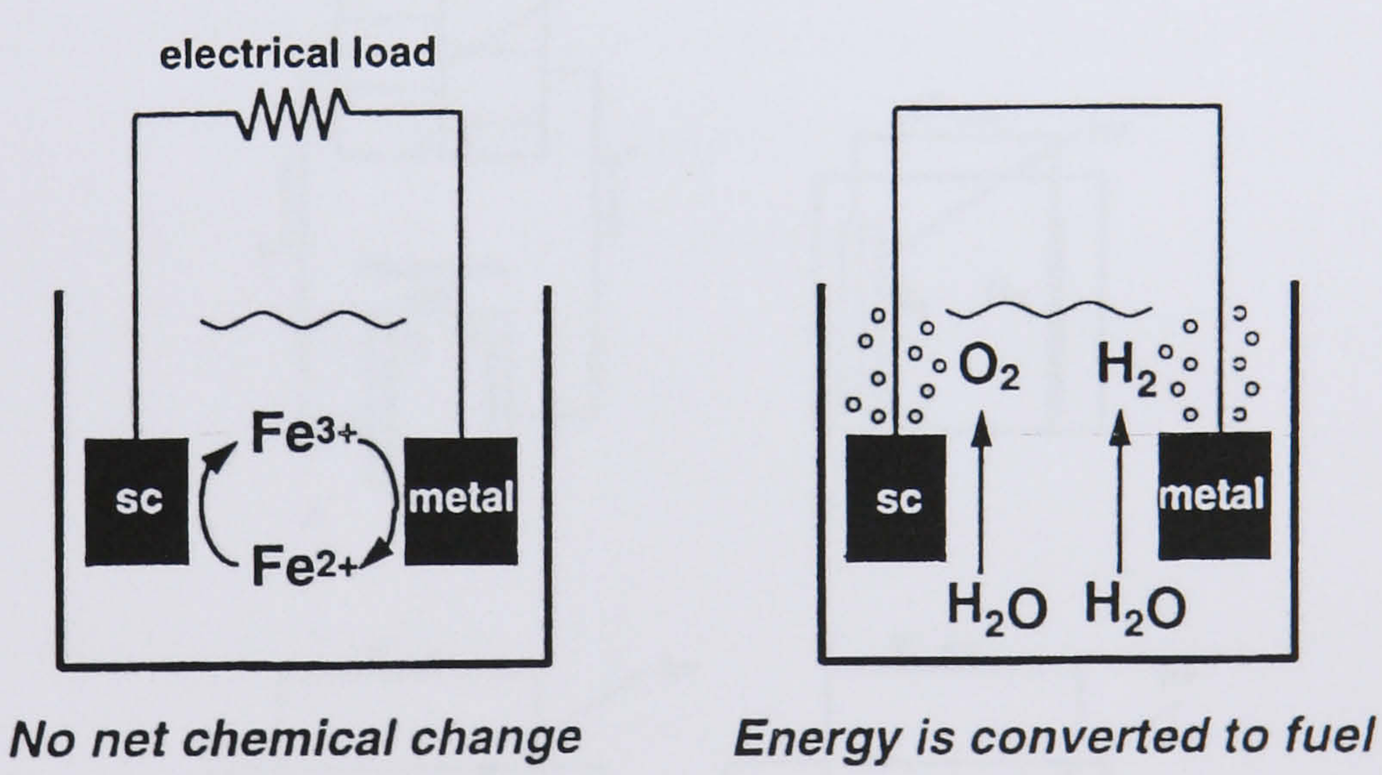



Figure 1.1. Two forms of energy generated in photoelectrochemical cells (Lewis 1996). In both cases, the semiconductor electrode absorbs the light and produces electrons flowing through the circuit. In contrast, the difference between these cells results from the type of chemical reactions occurring in the electrolyte. In the cell in the left-hand side, no net chemical change occurs and light is converted into electrical energy. In the cell in the right-hand side, both current and chemical fuels are produced, for example, with water splitting into hydrogen and oxygen as illustrated.

The photoelectrochemical processes are often described as artificial photosynthesis, i.e. photoinduced reactions mimic photosynthetic process in plants (Bard, et al. 1995, Hagfeldt, et al. 1995). For example, the charge separation process in the semiconductor corresponds to primary charge separation in the reaction centres in photosynthesis. Thus, the photoelectrochemical cells may be fabricated to mimic, for example, carbon dioxide fixation and water splitting.

Mimicking the water splitting process in photosynthesis has been intensively studied (Bard and Fox 1995, Fujishima, et al. 1972), i.e. the light driven conversion of liquid water to gaseous hydrogen and oxygen as shown in equation 1.1.

$$H_2O\,(l) \rightarrow H_2\,(g, 1\,atm) + \frac{1}{2}O_2\,(g, 1\,atm) \qquad \text{Equation 1.1}$$

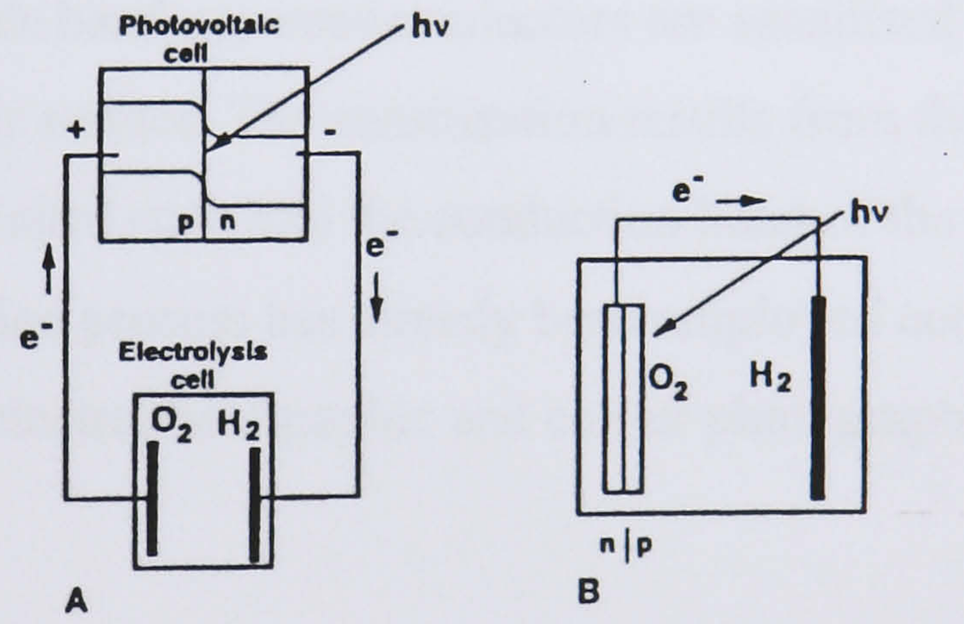



Figure 1.2. Schematic diagrams of four types of semiconductor based photoelectrochemical cells mimicking solar water splitting (Bard and Fox 1995); solid state photovoltaic cell driving a water electrolyser (A), semiconductor p / n junction in the electrolyte (B), semiconductor / liquid junction cell (C) and dye sensitised semiconductor cell (D).

Hydrogen could serve directly as a fuel, for example, for transportation or for the production of electricity in fuel cells without producing pollutants or green house gases upon combustion. Figure 1.2 shows four different types of cells for water splitting reactions (Bard and Fox 1995). On the one hand, solid state photovoltaic solar cells are employed to generate electricity which is subsequently used for water splitting reactions (figure 1.2 a and b). On the other hand, direct water splitting is achieved at the semiconductor / electrolyte interface (figure 1.2 c and d).

As another application, the photoinduced charge separation process in semiconductors is attractive for the generation of electricity. The semiconductor / liquid junction photovoltaic cells have been developed using semiconductor electrodes by several groups (Bard 1980, Fujishima and Honda 1972, Gerischer 1990, Nozik 1980). There has also been interest in the development of dye sensitised semiconductor solar cells which have offered efficient use of the solar spectrum (Bard and Fox 1995, Hagfeldt and Grätzel 1995) as wide band gap semiconductors are sensitised to visible light by the adsorption of dye to their surface. The sensitisation results from the injection of an electron from the dye excited state into the conduction band of the semiconductor. This concept of the sensitisation process has already been employed commercially in, for example, most modern electrophotographic and colour photographic processes (Tani 1990, Tani, et al. 1990).

For the dye sensitised semiconductor solar cells, flat single crystal metal oxide electrodes were initially used to investigate the photocurrent generated in the semiconductor by injection of an electron from photoexcited dye (Anderson, et al. 1979, Fujihira, et al. 1977). The maximum photon-to-current conversion efficiency obtained was very low despite intensive studies carried out (Kavan, et al. 1989, Spitler 1986, Spitler, et al. 1977) due to low optical density achievable with monolayer dye coverage. However it was reported in 1991 that the solar cells based upon dye sensitised nanocrystalline titanium dioxide ($TiO_2$) thin films (O' Regan, et al. 1991) (figure 1.3) could achieve a solar to electric energy conversion efficiency of >10 % (Nazeeruddin, et al. 1993). Such cells have subsequently attracted considerable commercial interest due to their potential for production costs significantly lower than conventional solid state photovoltaic devices.

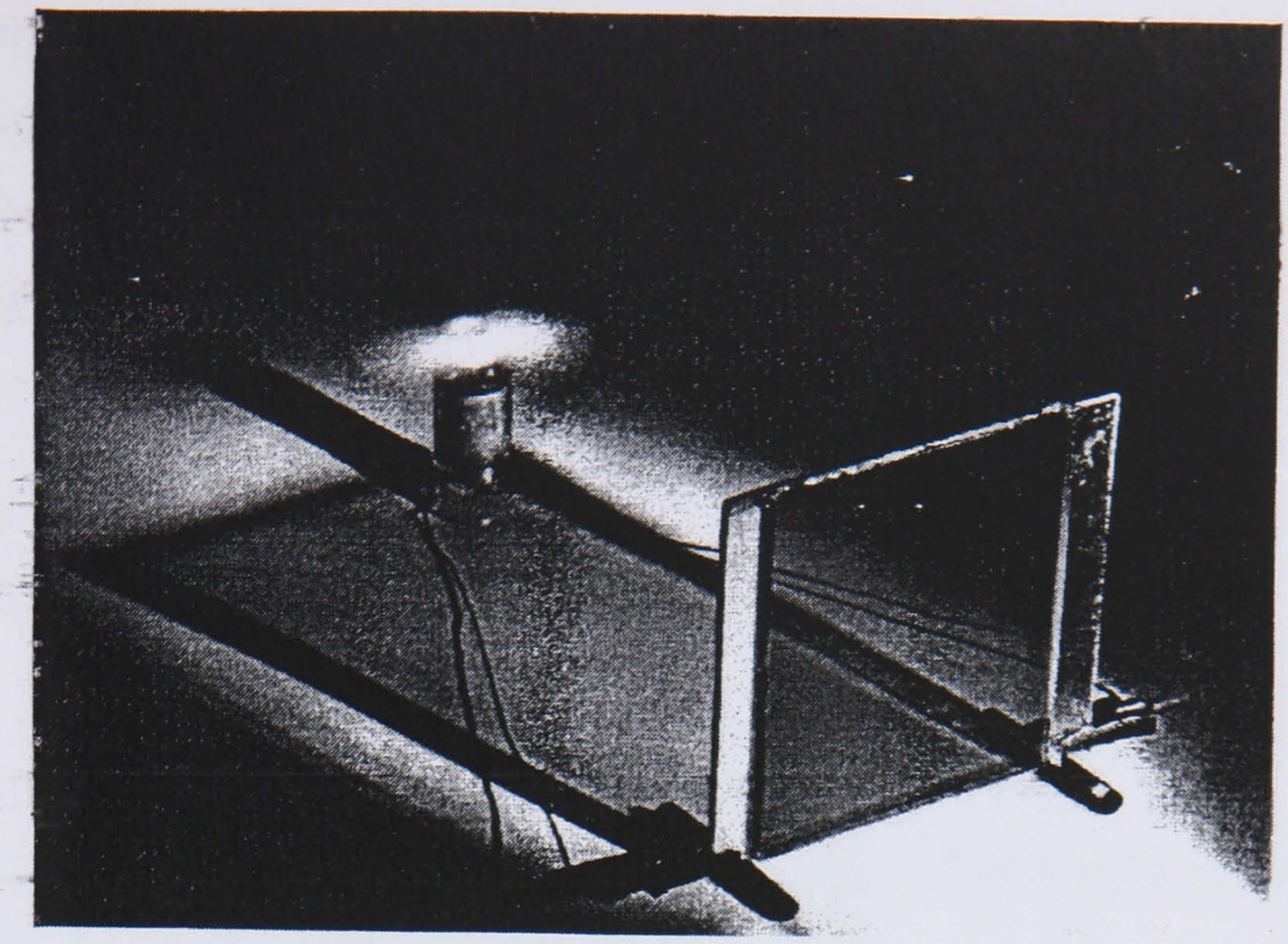


Figure 1.3. Photoelectrochemical solar cell based upon ruthenium dye sensitised $TiO_2$ nanocrystalline film. The picture was provided by Professor Michael Grätzel in EPFL, Lausanne.

## 1.2 Dye sensitised nanocrystalline semiconductor solar cells

Figure 1.4 illustrates a diagram of the photoelectrochemical solar cells based upon the dye sensitised $TiO_2$ films. Crucial to the development of such devices has been the use of nanocrystalline semiconductor films; the high surface area of these films yields high dye optical density for only monolayer dye coverage, resulting in efficient light absorption. For example, it was estimated that the surface area of anatase $TiO_2$ nanocrystalline films (thickness: 8 μm and average particle diameter: 15 nm) is increased by a factor of ~$10^3$ compared to flat single crystal $TiO_2$ electrode (surface roughness factor of ~1000) (O' Regan and Grätzel 1991). Therefore, the dye sensitised films are capable of absorbing incident light with high efficiency (Nazeeruddin, et al. 1993).

The cell consists of dye sensitised $TiO_2$ nanocrystalline film which is deposited on transparent fluorine doped tin oxide conducting glass (F-$SnO_2$ glass) as a working electrode, a platinum coated F-$SnO_2$ glass plate as a counter electrode and a redox active electrolyte ($I_3^-$ / $I^-$). The most efficient sensitiser dye reported to date is *cis*-ruthenium$^{II}$(2,2'-bipyridyl-4,4'-dicarboxylate)$_2$(NCS)$_2$ (Ru(dcbpy)$_2$(NCS)$_2$), exhibiting a

solar to electric energy conversion efficiency of >10 % (Nazeeruddin, et al. 1993). The carboxylates of $Ru(dcbpy)_2(NCS)_2$ support linkage of the dye onto $TiO_2$ surface, resulting in enhanced electronic coupling between the dye molecule and the semiconductor (see chapters 2 and 3 for the details).

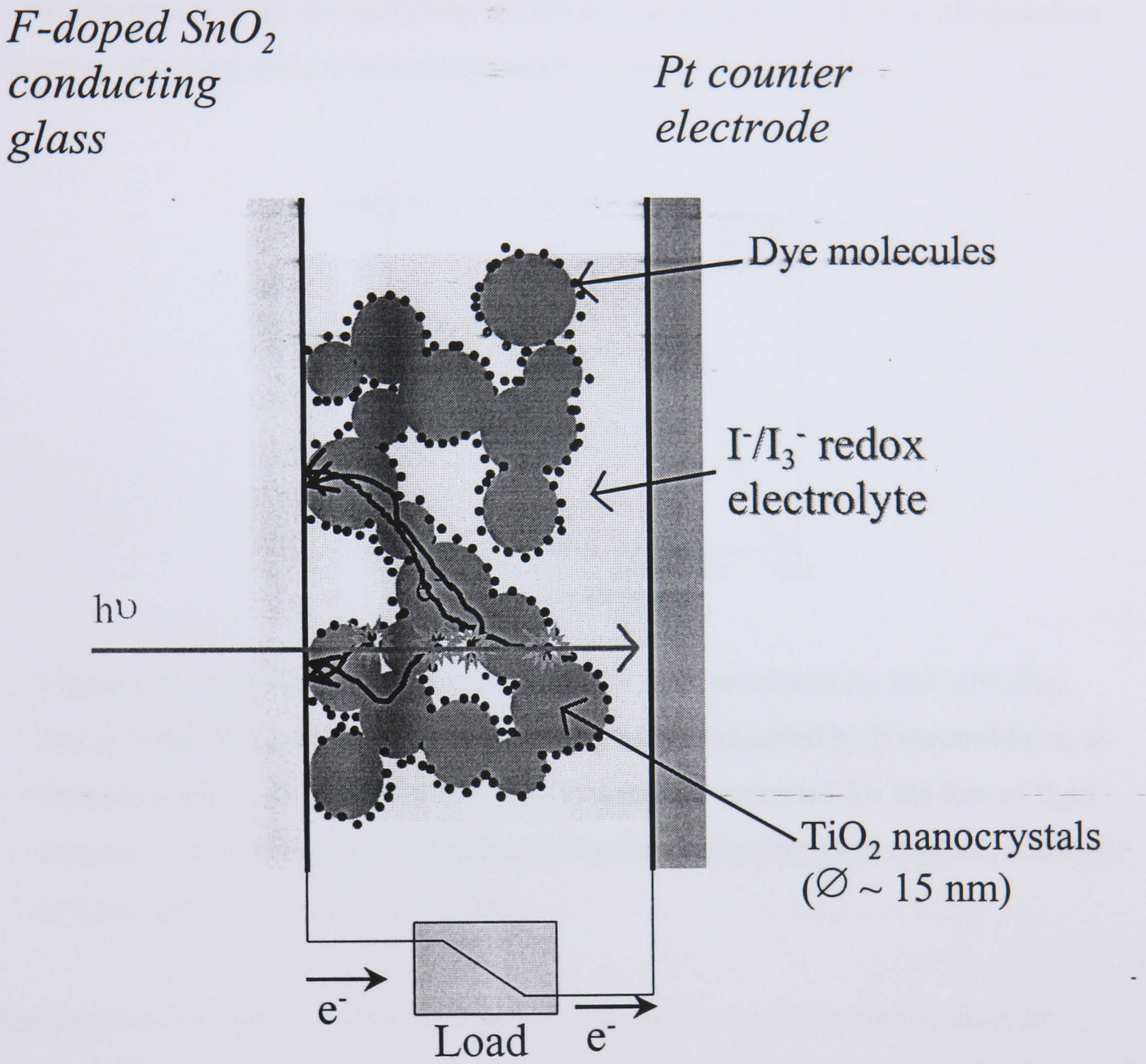



Figure 1.4. Diagram illustrated for the dye sensitised semiconductor nanocrystalline solar cells. The cell consists of the dye sensitised $TiO_2$ film, the platinum counter electrode and the redox active electrolyte. Absorption of incident light by adsorbed dye molecules is enhanced by high surface area of the film resulting from small semiconductor particle size (average diameter: 15 nm).

Solar cell performance is often characterised by the incident photon-to-current conversion efficiency (IPCE), indicating the quantum efficiency for the conversion of

incident photons to electric current (see chapter 6 for the details). The wavelength response of the cell is compared by plotting values of the IPCE as a function of incident light wavelength (action spectrum). Figure 1.5 represents IPCE action spectra for ruthenium dye sensitised $TiO_2$ films (Nazeeruddin, et al. 1993). It is apparent that $Ru(dcbpy)_2(NCS)_2$ exhibits efficient conversion over 350~700 nm. When the IPCE values are corrected for the inevitable reflection and absorption losses, a cell quantum efficiency of nearly unity is achieved around its absorption maximum.

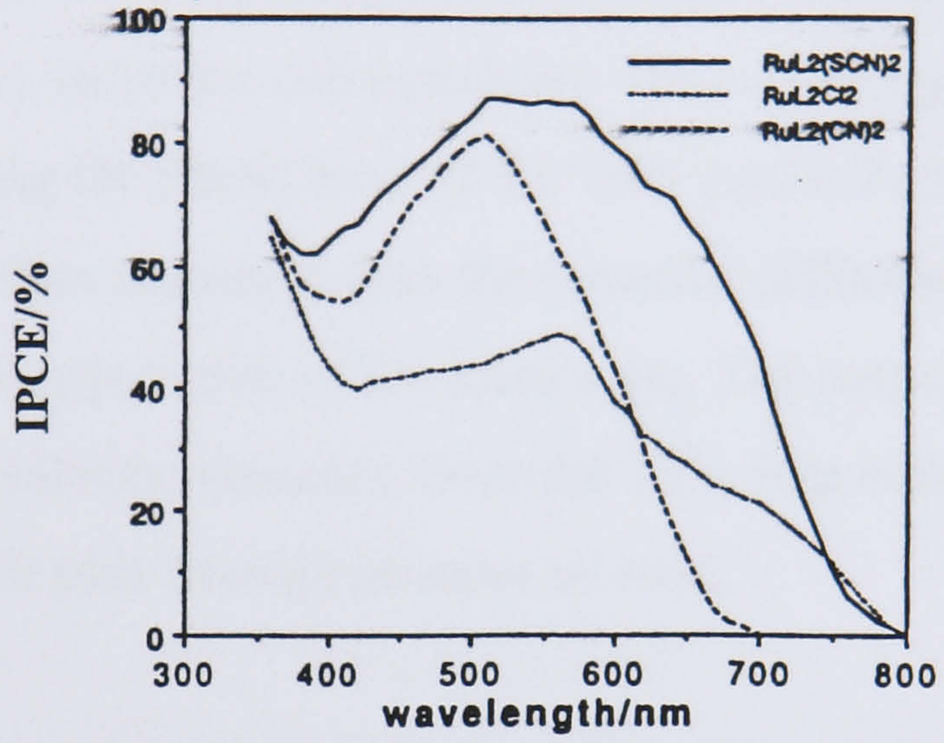



Figure 1.5. Photocurrent action spectra for the $TiO_2$ sensitised by $RuL_2(NCS)_2$, $RuL_2Cl_2$ and $RuL_2(CN)_2$ where L is a dcbpy ligand, reported by Nazeeruddin et al. (Nazeeruddin, et al. 1993). The IPCE values are not corrected for the loss of light intensity due to absorption and reflection by the conducting glass support, and due to light scatter by the $TiO_2$ particles.

The photovoltaic function of these solar cells is described in the potential diagram shown in figure 1.6 (Hagfeldt and Grätzel 1995). The oxidation potentials of the ground and excited states of $Ru(dcbpy)_2(NCS)_2$, estimated from the electrochemical and steady state absorption / fluorescence data in solution phase, are reported to be +0.8~0.85 and –0.8~-0.75 V vs saturated calomel electrode (SCE), respectively (Hagfeldt and Grätzel 1995, Nazeeruddin, et al. 1993). That of the $I_3^-$ / $I^-$ redox couple in the electrolyte was estimated to be +0.2 V vs SCE (Hagfeldt and Grätzel 1995). In figure 1.6, the cell operation is initiated by visible light excitation of the dye (1), which is followed by charge separation at the dye / semiconductor interface as a result of electron injection from the dye excited state to $TiO_2$ (2). The light absorption therefore acts as an electron pump for the conversion of light to electrical energy. The charge separation is further

supported by transport of the injected electron to the back F-$SnO_2$ conducting glass across the $TiO_2$ film (3), while the oxidised dye is immediately re-reduced by $I_3^-$ / $I^-$ redox couples (5), preventing charge recombination between the injected electron and the dye cation. The oxidised redox species in the electrolyte is further reduced at the counter electrode (4). This cell operation indicates that the charge separation is supported only by the majority carriers (electrons) in the semiconductor, whereas the conventional semiconductor / liquid junction cell is performed with minority carrier diffusion, imposing severe conditions on material quality (Bard 1980, Gerischer 1990, Nozik 1980). Moreover, all compounds are completely recycled, resulting in no net chemical change occurs under the cell operation. The cell voltage is attained by the injected electrons raising the Fermi level of the $TiO_2$ (quasi-Fermi level) under light illumination, and therefore corresponds to the potential difference between this quasi-Fermi level and the redox potential of the electrolyte. The output current is determined by the number of the collected electrons from the $TiO_2$ film collected by the back conducting glass, which pass through an external load.

The vectorial electron transport process in the cell requires fast charge separation and slow charge recombination mechanisms. Following optical excitation of the dye, injection of an electron from the dye excited state into the semiconductor conduction band must be much faster than decay of the excited state to the ground state. The charge recombination reaction between injected electrons and the concomitant dye cation must be avoided by rapid re-reduction of the dye cation by the redox couple in the liquid electrolyte. Moreover, the electron transport across the $TiO_2$ films should be faster than the charge recombination between the injected electron and the electrolyte, implying also that the reduction of the oxidised electrolyte at the counter electrode should be sufficiently fast.

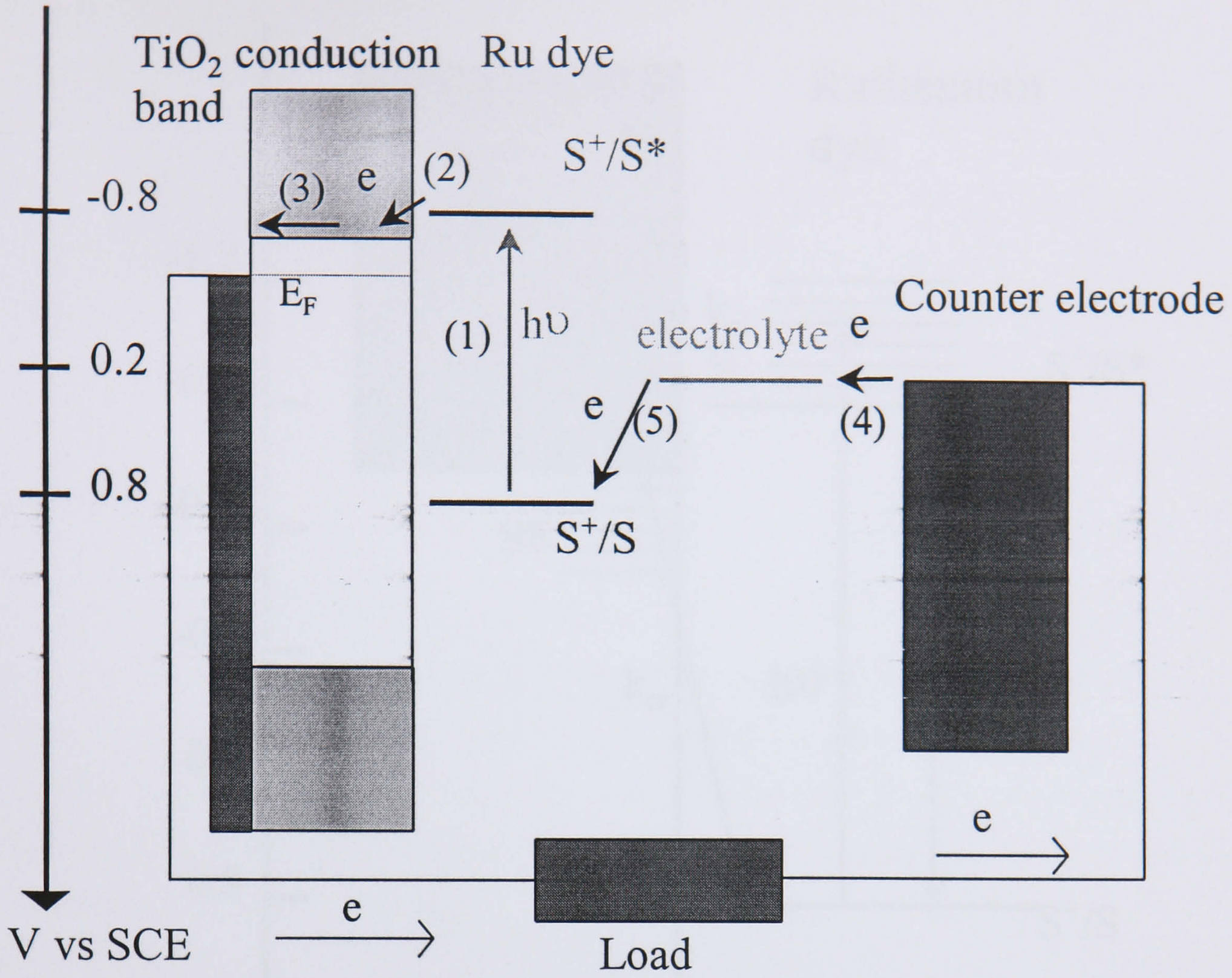



Figure 1.6. Schematic potential diagram of ruthenium dye sensitised $TiO_2$ solar cell. The redox potential of each reactive state is presented against the reference potential level (SCE). Each reaction is indicated with an arrow and numbered.

## 1.3 Electron transfer at dye / semiconductor interface

The primary charge separation, which occurs at the dye / semiconductor interface, is the vital process for the function of the cell, and the kinetics of the interfacial electron transfer reactions are potentially critical factors controlling device efficiency. The reactions occurring at the dye / $TiO_2$ interface are summarised in figure 1.7. The dye photophysical processes include not only excited state decay to ground, influencing the sensitisation efficiency, but also excited state thermal relaxation as an output potential loss. Interpretation of photophysical properties of ruthenium bipyridine complexes is currently a subject of intensive studies (Carroll, et al. 1987, Damrauer, et al. 1997, De Armond, et al. 1989, Kalyanasundaram 1982).

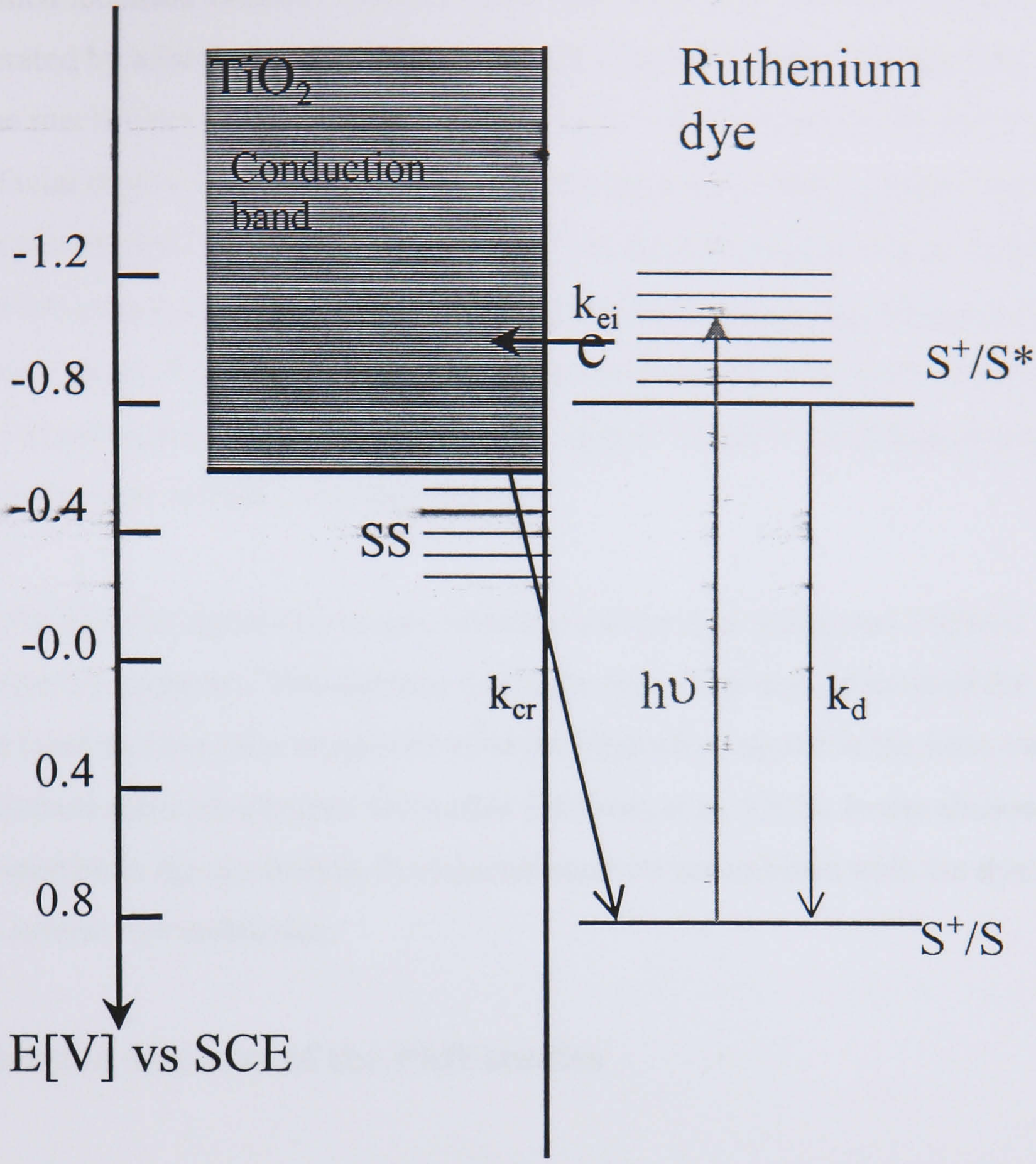



Figure 1.7. Schematic representation of charge separation in ruthenium dye sensitised $TiO_2$ nanocrystalline films. Optical excitation of $Ru(dcbpy)_2(NCS)_2$ ($S^o \rightarrow S^*$) initiates ultrafast electron injection ($k_{ei}$) into the $TiO_2$. Electron acceptor states of the semiconductor include both surface states (SS) and delocalised conduction band states. Charge recombination ($k_{cr}$) between the injected electron ($e_{cb}^-$) and oxidised dye molecule ($S^+$) occurs relatively slowly. In the functioning photovoltaic cell, the addition of appropriate electrodes and electrolyte complete the electrical circuit, and result in forward electron transport with a near unity quantum yield. $k_d$ indicates radiative and radiationless decay of $S^*$ to $S^o$. The redox potential of each state is presented with respect to SCE.

The electron injection involves the coupling of the localised molecular excited state of the dye to highly delocalised electronic levels of the semiconductor conduction band, to

poorly defined localised surface / defect (intra-band) state, or to any other state (e.g. states generated by adsorbed molecules), providing a highly complex situation to describe the mechanism of this reaction. Few theoretical studies have been reported for these interfacial electron transfer processes, suggesting that electron injection should proceed on picosecond / femtosecond timescales (the details are presented in chapter 3). However, such interfacial electron transfer relations remain poorly characterised relative to those in homogeneous solution or gas phase electron transfer. Moreover, despite increasing technological importance of dye sensitisation, detailed experimental studies of these kinetics have to date been very limited.

Following the electron injection process, relaxation of the dye cation and injected electron formed is expected. The electron relaxes to the lowest energy level of the conduction band and has been suggested to be subsequently trapped in the intra-band (surface / defect) states on ultrafast timescales (Skinner, et al. 1995). In the absence of any redox species in the electrolyte, the injected electron recombines with the dye cation in order to reform dye molecules.

## 1.4 Motivation and aim of the PhD studies

Extensive studies have been carried out to improve the efficiency of the sensitisation process. For example, porphyrins (Boschloo, et al. 1996, Kalyanasundaram, et al. 1987, Kay, et al. 1993), phthalocyanines (Nazeeruddin, et al. 1998, Shen, et al. 1995), squarine dyes (Kamat, et al. 1993) and xanthene dyes (Sayama, et al. 1998) have been investigated as a candidate of an alternative sensitiser dye, and in order to use different wavelengths of the solar light spectrum. Despite these studies, nanocrystalline $TiO_2$ films sensitised by $Ru(dcbpy)_2(NCS)_2$ remain to be the most successful semiconductor film and sensitiser dye reported for such devices (Nazeeruddin, et al. 1993), even though this ruthenium dye exhibits relatively poor spectral overlap with solar irradiation. The mechanism of interfacial electron transfer kinetics in dye sensitised $TiO_2$ films remains poorly understood. This is motivating detailed studies of the mechanism of the cell operation, and the parameters controlling its efficiency. Such studies are essential not only for developing basic understanding of the electron transport process, but also for the development of dye sensitised photovoltaic devices.

Recently, femtosecond laser technology has greatly developed, allowing the production of stable short pulses without major maintenance. Such laser systems have facilitated ultrafast transient spectroscopic studies of photoinduced energy and electron transfer processes. The advantage of this spectroscopic technique is its capability in monitoring photophysical and photochemical reactions directly on femtosecond timescales, and it therefore allows direct measurements of ultrafast interfacial electron injection rates. Also, the high dye optical densities achieved by monolayer adsorption to the nanocrystalline film greatly facilitates spectroscopic studies of the dye / semiconductor interface.

The overall aim of the kinetic studies at the dye / semiconductor interface using the femtosecond laser system in my project is to determine the parameters controlling interfacial electron transfer processes. In consequence of interpretation of the mechanism of such processes, the kinetics studies are extended at other interfaces in order to determine the parameters controlling whole kinetic processes in the solar cells. The parameters determined should subsequently be used to the improve the solar cell performance, and even more efficient devices could be designed.

This thesis describes the following points in dye sensitised titanium dioxide ($TiO_2$) films by means of the sub-picosecond to millisecond transient spectroscopies.

1) **Assignment of electron transfer kinetics at $Ru(dcbpy)_2(NCS)_2$ / semiconductor interface.**
   $Ru(dcbpy)_2(NCS)_2$ has been particularly chosen as a sensitiser dye in order to investigate why the sensitisation based upon this dye is efficient.

2) **Investigation of the key parameters controlling the electron injection kinetics.**
   $Ru(dcbpy)_2(NCS)_2$ is compared with other sensitiser dyes in order to address the origin of the high efficiency achieved with this dye.
   Different experimental conditions were employed in order to compare the injection kinetics in $Ru(dcbpy)_2(NCS)_2$ sensitised $TiO_2$ films, considering excitation wavelengths, solvent environment, electrolyte composition and application of external voltages.

3) **Interpretation of the parameters with electron transfer theory.**

Heterogeneous electron transfer theory is applied to correlate with the experimental data.

4) **Correlation of the parameters with the solar cell performance.**

The project required the construction of a nanosecond transient absorption spectrometer, and the development of a femtosecond optical parametric amplifier to provide a tuneable excitation source and a pump-probe system for ultrafast transient absorption measurements. The construction and operation of the laser apparatuses and the experimental sample preparations are described in detail in chapter 2. Chapter 3 presents basics of electrochemistry to assist the experimental background, and homogeneous and heterogeneous electron transfer theories to discuss with the experimental results in chapters 4 and 5. The relevance of these results to the function of dye sensitised semiconductor solar cells is also discussed in these chapters, relating in particular to the energy conversion efficiency. Finally preliminary results of the electron injection kinetics in the solar cells are presented in chapter 6.

# Chapter 2: Experiments

Dynamics at the dye / semiconductor interface have been studied employing steady state and femtosecond-to-millisecond transient spectroscopies. The project required construction of an optical parametric amplifier and a nanosecond transient absorption spectrometer and design of a femtosecond transient absorption spectrometer. The first part of this chapter describes these technical developments.

## 2.1 Transient absorption spectroscopy

### 2.1.1 Principle

The development of transient absorption spectroscopy driven by the improvement of high power pulsed laser systems has allowed observation of physical and chemical reactions up to femtosecond timescale since the technique of the flash photolysis was introduced by Professor Porter in the 1950's (Porter 1950). The principle of the femtosecond / picosecond transient absorption spectroscopy is that a sample is irradiated with a short, intense laser pulse known as a "pump" pulse, and then resultant changes in the optical density of the sample are monitored at a certain time delay by another short weak laser pulse known as a "probe" pulse. This type of transient absorption spectroscopy is therefore termed "pump-probe". In methods which use a continuous probe beam, time resolution is limited by the response time of detection electronics in the pump-probe flash photolysis system. In contrast, in pulsed pump-probe spectroscopy, the time resolution is only limited by the laser pulse duration. Reaction rates are determined by comparing transient absorption decays obtained from plotting the amplitude of transmitted light against the delay time and by comparing transient spectra obtained from plotting the amplitude against probe wavelengths. Detailed data analysis is performed by simultaneous global analysis (see data analysis section).

### 2.1.2 Calculation of absorption difference

Physical and chemical reactions are monitored by measuring the intensity of transmitted probe light passing through a sample after excitation, and presented as differences in optical density (absorption difference or ΔOD). This ΔOD is simply a difference in optical density before and after the optical excitation of the sample in transient absorption spectroscopy. The optical density (OD) of the sample is defined by the Lambert-Beer Law in equation 2.1;

$$OD(\lambda) = \log_{10}\left(\frac{I_i(\lambda)}{I_o(\lambda)}\right) = \varepsilon(\lambda)cl \qquad \text{Equation 2.1}$$

where $I_i$ is the incident light intensity, $I_o$ is the transmitted light intensity, $\lambda$ is the probe wavelength, $\varepsilon$ is the extinction coefficient of the absorbing species at a probe wavelength, c is the concentration of the sample and l is the optical path length of the sample. Using equation 2.1, ΔOD is given as;

$$\Delta OD(\lambda, t) = OD_{pump}(\lambda, t) - OD_{unpump}(\lambda) = \log_{10}\left(\frac{I_i}{I_{o,\,pump}(\lambda, t)}\right) - \log_{10}\left(\frac{I_i}{I_{o,\,unpump}(\lambda)}\right)$$

Equation 2.2

Equation 2.2 is simplified to equation 2.3.

$$\Delta OD(\lambda, t) = \log_{10}\left(\frac{I_{o,\,unpump}(\lambda)}{I_{o,\,pump}(\lambda, t)}\right) \qquad \text{Equation 2.3}$$

where $OD_{pump}(t)$ and $I_{o,pump}(t)$ are the optical density and transmitted light intensity respectively at a delay time, t, after excitation. $OD_{unpump}$ and $I_{o,unpump}$ are the optical density and transmitted light intensity without excitation of the sample.

### 2.1.3 Contribution to absorption difference spectra

After optical excitation, the absorption difference at each particular wavelength exhibits either a positive or negative amplitude. Three major contributions to absorption difference can be observed; one is positive and two are negative.

***Positive amplitude***

1) Absorption of new molecular species

   The excitation of molecules will result in formation of new molecular species. For example, the new absorption band of the excited state appears upon the excitation of molecules. The degree of the absorption depends on the extinction coefficient of the new species. If the species has absorption bands at wavelengths different from those of the initial molecule, the new bands contribute positive amplitude at those particular wavelengths (c.f. chapter 4).

***Negative amplitude***

1) Ground state bleach

   The excitation of the sample will result in loss of ground state absorption bands of excited molecules.

2) Stimulated emission

   After the excitation of molecules, a probe pulse may stimulate radiative decay from the electronically excited to ground state, if the radiative coupling of the excited state with the ground remains. This transition enhances intensity of the probe pulse (increase of a negative amplitude) and is therefore termed "stimulated emission". Relaxation of the singlet excited state is observed as a stimulated emission decay, which is dependent upon molecules, e.g. nanosecond timescales for regular porphyrins (see chapter 5) or even femtosecond timescale for a particular ruthenium dye (see chapter 4).

It is often the case that an absorption change at a particular monitoring wavelength results from more than one contribution of the above, rendering assignment of the reaction difficult. It is then necessary to choose a range of monitoring wavelengths in order that the amplitude contributions can be unambiguously determined.

## 2.2 Femtosecond transient absorption spectrometer

### 2.2.1 Femtosecond dye laser system

#### 2.2.1.1 Introduction

The transient absorption spectrometer employing the femtosecond colliding pulse mode-locking (CPM) dye laser was developed mainly in order to study the mechanism of energy and electron transfer reactions in photosystem II in plants (Durrant, et al. 1992, Durrant, et al. 1992, Hastings, et al. 1992, Klug, et al. 1995, Merry, et al. 1996). In my PhD project, the first observation of electron injection reaction in dye sensitised $TiO_2$ films was carried out with this femtosecond dye laser system (Tachibana, et al. 1996) (see chapter 4).

This laser system was originally designed by Dr. David Klug and co-workers, and then improved by a number of post-doctoral researchers and PhD students of the Molecular Dynamics Group. The overall diagram of the latest arrangement is shown in figure 2.1. The system comprises a CPM dye laser, pulse amplifiers and a pump-probe apparatus. The apparatus has been described in detail in previous PhD theses (Durrant 1992, Joseph 1996). Only the main points of the laser operation are therefore summarised in this section.

#### 2.2.1.2 Femtosecond pulse generation

The CPM dye laser was used to generate femtosecond pulses with a typical stable pulse width of 200~300 fs. Two dye jets are placed in the ring-shaped laser cavity. A gain jet (Rhodamine 6G in ethylene glycol) is excited by a cw argon ion laser (Coherent Innova 310) and its emission travels in both directions along the ring cavity. When emission from two opposite directions is co-incident in a saturable absorber jet (DODCI in ethylene glycol), passively mode locked short pulses are generated. The pulse width is very sensitive to the concentration of the saturable absorber dye solution and to the pump power controlling the emission intensity. The Group Velocity Dispersion (GVD)

of the pulse arising from optical elements in the cavity is compensated by two pairs of silica prisms. The fine tuning of these variables can produce the shortest pulse of 60 fs (Hong, et al. 1993).

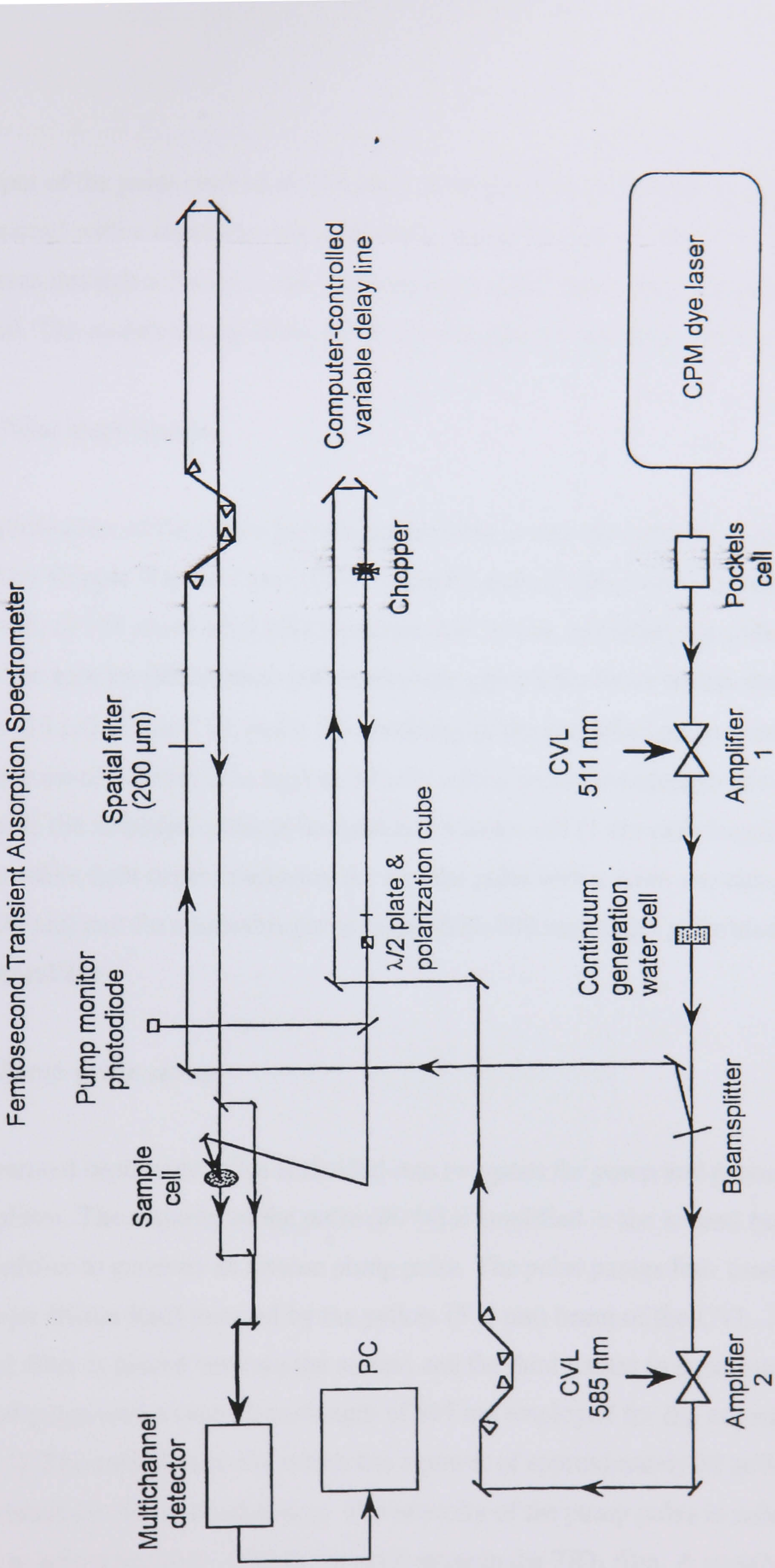



Figure 2.1. Arrangement of the femtosecond dye laser system taken from the PhD thesis of Dr. M. Joseph (Joseph 1996).

The output of the pulse centred at 620 nm is obtained through the output coupler (10 % transmission) with a repetition rate of 88 MHz and pulse energy of 200 pJ. The pulse then passes through a Pockel's cell, blocking a pre-pulse before the main pulse is amplified. The switch timing of the cell is synchronised to the trigger of the amplifier.

#### 2.2.1.3 Pulse amplification

The amplification of the output pulse is achieved by a bow-tie multi-pass amplifier pumped by Copper Vapour Laser (CVL, Oxford Lasers CU40) with a centre wavelength of 511 nm at a 6.5 kHz repetition rate. In this amplifier, the pulse passes through the gain jet (Rhodamine 640 in ethylene glycol) six times within the pulse duration (10 μs) of one CVL pulse. The intensity of the amplified pulse train with a repetition rate of 6.5 kHz is as high as 30 mW with a centre wavelength of 640 nm. Afterwards the amplified pulse is focused into a water cell (1 cm path length) to generate white light super-continuum for a probe pulse with a wide wavelength window (450~900 nm) and for a tuneable pump pulse (600~700 nm range) generated by a second amplifier.

#### 2.2.1.4 Pump-probe set-up

The generated continuum pulse is divided into two parts for pump and probe arms by a beam-splitter. The majority of the pulse (80 %) is amplified in the second bow-tie multi-pass amplifier to generate an intense pump pulse. The pulse passes four times through the gain jet (Kiton Red) pumped by the yellow (578 nm) beam of the CVL. A band pass (596 nm) filter is placed between the second and the third passes to generate an amplified pulse with a centre wavelength of 605 nm employed for the experiment (see chapter 4). The amplified pulse, which has a power of approximately 10 mW, is recompressed by two pairs of prisms. The intensity of the pump pulse is subsequently reduced to adjust the number of dye excited states in the $TiO_2$ film. A variable translation stage is controlled by the personal computer such that it changes the time delay between pump and probe pulses arriving at the sample cell. A mechanical chopper is placed after the translation stage in order to use a lock-in amplifier (see chapter 3).

The polarisation of the pump pulse is set to the magic angle (ca. 54.7°) against the probe pulse with a λ/2 wave plate.

The rest (20 %) of the continuum is used for the probe arm. The pulse is spatially filtered with a 200 μm diameter pinhole to improve beam shape. The pulse is split in half; the one side reaches the sample cell (sample), whereas the other passes through the same arrangement of optical elements without the sample cell (reference). The sample probe pulse is focused and overlapped with the pump pulse non-colinearly in the sample cell. The overlap is maximised with the signal size of the dye standard sample (the kinetics of the sample is known) in the multi-channel detection system. The probe spot size is smaller than that of the pump to avoid over-excitation of the sample. The recollimated sample and reference pulses are aligned into the multi-channel detector. Data collection in this detector is described in section 2.2.5.1.

### 2.2.2 Solid-state femtosecond Ti:sapphire laser system

In 1997, it was decided to transfer ultrafast studies of the dye sensitised $TiO_2$ films from the CPM dye laser system to the Ti:sapphire laser system. Conduction of the ultrafast experiments has required construction of an optical parametric amplifier and design of the femtosecond transient absorption spectrometer. The design and construction of these apparatuses are described in detail below.

#### 2.2.2.1 Overview of chirped pulse amplifier (CPA) system

Solid-state femtosecond Ti:sapphire laser systems have been intensively developed (Huang, et al. 1992, Sibbett, et al. 1994) since the Kerr-lens mode-locked Ti:sapphire oscillator was discovered by Spence et al (Spence, et al. 1991). In the Molecular Dynamics Group a femtosecond Ti:sapphire chirped pulse amplifier (CPA) laser system has been designed and developed by Drs. David Klug, Ian Mercer, Manfred Fettweis and Richard Tompkins (Tompkins 1998). The new system has a number of great advantages compared to the dye laser system. For example, the system is capable of producing a pulse duration of ~35 fs with an average power of about 350 mW. The high stability of the system has enabled the stable operation of a wide wavelength tuneable

optical parametric amplifier (OPA) and the transient absorption spectroscopy as described in later sections. This high stability also ensures that the system is reliable on a day-to-day basis. The warm up time (half an hour) of the new system is significantly shorter compared to the dye laser system, allowing the whole experimental time to be shorter.

The fundamental principles of the Ti:sapphire laser system have been well documented in the PhD thesis of Dr. Richard Tompkins (Tompkins 1998). In this section, only main points are summarised; a femtosecond Ti:sapphire oscillator; a pulse expander; a "MERLIN" Nd:YLF pumped regenerative amplifier and a pulse compressor. Diagram of the laser system is presented in Figure 2.2. Room temperature is maintained at 20±0.5 °C because change in temperature of more than ±1 °C causes misalignment of the whole system.

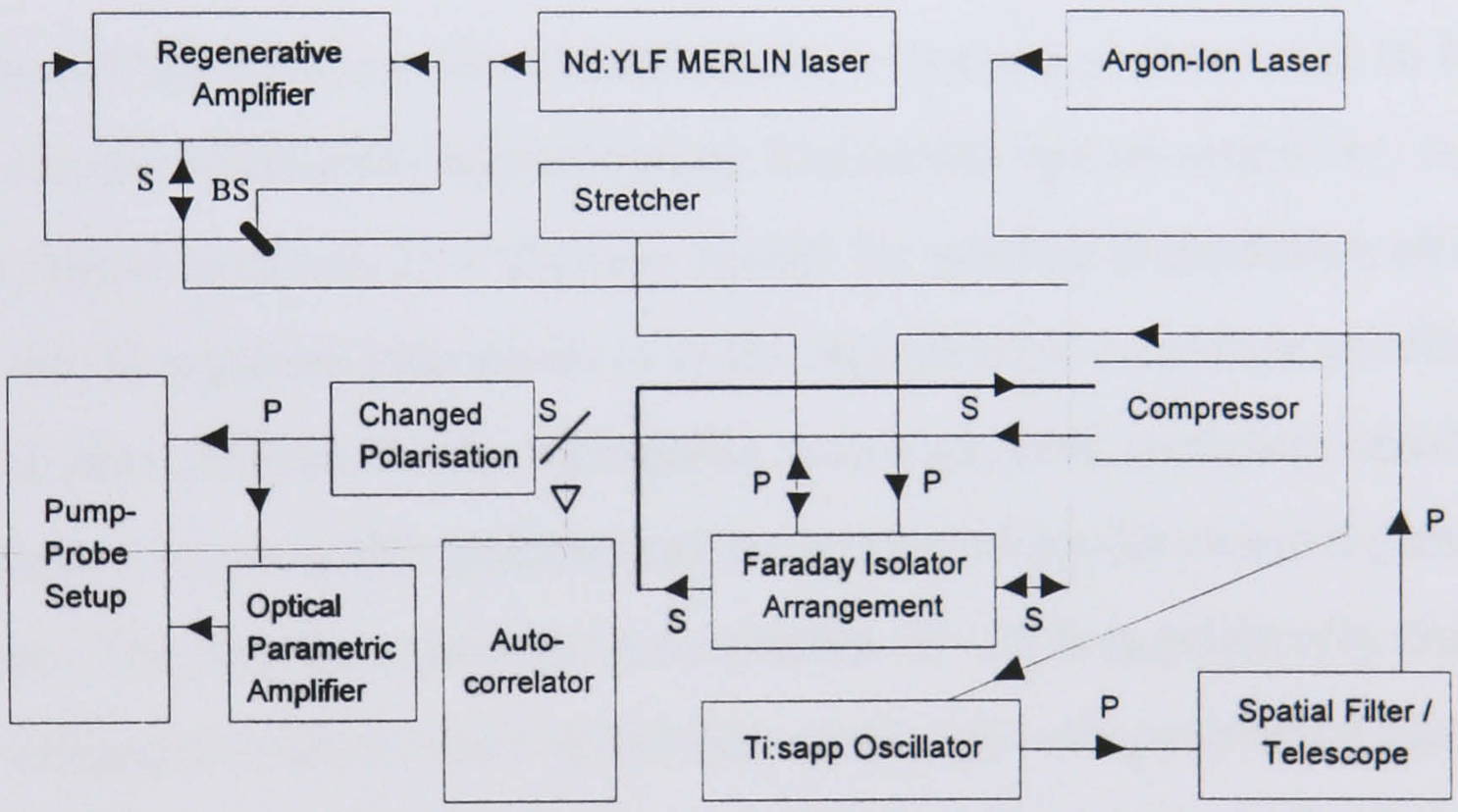



Figure 2.2. Diagram of the femtosecond Ti:sapphire laser system, modified from the figure in the PhD thesis of Dr. R. Tompkins (Tompkins 1998).

### 2.2.2.2 Femtosecond pulse generation

A home-built Ti:sapphire oscillator is employed to generate femtosecond pulses with a pulse duration of ~25 fs. The Ti:sapphire gain crystal (path length: 2 mm) is placed in "Z" shaped cavity configuration and is pumped by an Argon ion laser (Spectra Physics 2060-10S). A pair of fused silica prisms is used to compensate the GVD, controlling the output pulse length. Mode-locking can be initiated via translation of one of the cavity optics i.e. one of the prisms. The output pulse with a centre wavelength of 795 nm at a

repetition rate of 98 MHz is extracted via an output coupler. The output pulse energy of the oscillator is approximately 2 nJ.

The output pulse is cleaned by spatial filtering with a 140 μm diameter pinhole, and thereby improving the beam profile and collimation. The pulse is then sent into a pulse expander via Faraday Isolator (FI) arrangement. The purpose of using the FI set-up is to prevent amplified stimulated emission (ASE) in a regenerative amplifier from being sent back along the input path into the oscillator. In the FI arrangement, the polarisation of the pulse passing through from one direction is rotated by 90°, whereas the pulse from the opposite direction preserves the same polarisation; the feedback of the ASE into the oscillator can therefore be minimised.

2.2.2.3 Pulse expansion

Amplification of the femtosecond pulse is likely to cause a problem due to its highly intense peak power during the amplification. Unlike the dye jet amplifier, in which the dye solution experiences no fatal damage except for gradual degradation of dye molecules, the Ti:sapphire gain medium in the regenerative amplifier possibly induces self-focusing phenomenon for the laser pulse with high peak intensity, resulting in optical damage. However this problem can be prevented by the chirped pulse amplification. The oscillator pulse with a duration of ~25 fs is positively chirped (higher frequencies delayed relative to the lower frequencies) to ~50 ps (stretch factor: 2000), and then amplified, with the result that an amplified peak pulse remains below optical damage threshold in the gain medium.

2.2.2.4 Regenerative pulse amplifier

The regenerative amplifier is the closed cavity amplifier in which input seed and amplified output beams are spatially overlapped. This amplification arrangement is achieved by polarisation dependent input and output pulses collected by a Pockel's Cell and a thin film polariser. The polarisation of the vertically polarised (to the optics table) input pulse is altered into horizontal by the electro-optic switch of the Pockel's Cell, resulting in introduction of the input laser pulse in the amplifier cavity. The pulse is

then amplified in the gain medium travelling within the cavity repeatedly. After the amplified pulse reaches gain saturation, its polarisation is again switched to vertical in order to obtain the output pulse.

A pump source of the regenerative amplifier is a frequency doubled Nd:YLF laser (MERLIN; Spectra-Physics Lasers) centred at 527 nm with a repetition rate of approximately 1 kHz. An output power of the MERLIN is about 9 W with a pulse duration of 250 ns. After the pulse is seeded, optimum overlap between the seed and the pump beam in the gain medium and the optimum alignment of the seed beam into the amplifier cavity result in a minimum of seventeen round trips to reach gain saturation (build-up time: 170 ns). An amplified output power is approximately 900 mW at a repetition rate of 1 kHz.

2.2.2.5 Pulse compression

A pulse compressor consists of a grating and mirrors in order to obtain a femtosecond pulse from the amplified 50 ps pulse. The output power after the compression of the amplified pulse is 350±20 mW (~40 % of the amplifier output power) with a pulse duration of 36 fs. A fraction of the pulse is used to monitor pulse duration by an auto-correlator and the performance of the system was checked during optical experiments. The average pulse fluctuation of the output intensity is 1.5~3 %. An output beam diameter is approximately 6.5 mm (FWHM) to keep power density low and prevent self-focusing in air due to high peak intensity of the short pulse. Hereafter, the output pulse from the compressor with a wavelength centred at 810 nm is termed "fundamental" laser pulse for applications to an optical parametric amplifier (OPA) and to a pump-probe apparatus.

### 2.2.3 Optical Parametric Amplifier (OPA)

2.2.3.1 Introduction

The highly intense and stable Ti:sapphire femtosecond laser enables investigation of photophysical and photochemical reaction dynamics by pump-probe transient absorption spectroscopy. However the laser pulse centred at 810 nm generally limits

excitation and monitoring wavelengths. My PhD project therefore involved construction of the system to generate a femtosecond pulse at a desired wavelength. The Optical Parametric Amplifier (OPA) was chosen as a wavelength tuning apparatus for the femtosecond pulse.

Femtosecond optical parametric amplification is first reported by Joosen et al. in 1991 (Joosen, et al. 1991). Since then, a number of studies have been reported for the OPA, but with relatively high-energy fundamental pulses (Danielius, et al. 1993, Greenfield, et al. 1995). Recently parametric gain has been improved with low pump energy (Matousek, et al. 1996) and a pulse duration from the OPA has been shortened (Cerullo, et al. 1997, Reed, et al. 1995, Sosnowski, et al. 1996). The shortest pulse generated has to date been reported by Shirakawa et al. with a pulse duration of less than 5 fs (Shirakawa, et al. 1998).

2.2.3.2 Comparison between the OPA and the bow-tie dye jet amplifier

As an excitation tuning source for the pump-probe apparatus, the OPA was constructed in the femtosecond Ti:sapphire laser system. Choice of the OPA certainly has a number of advantages compared to the dye jet based amplifier used in the femtosecond dye laser system.

**<Advantages>**

1) Wide range tunability of laser pulse wavelength.
   A tuning wavelength range in the Ti:sapphire laser system is over 450~750 nm while the tuning range is from 600 nm to 700 nm in the dye laser system.

2) Easy tunability.
   Practical methods to tune a wavelength are to change an angle of a second harmonic crystal and to alter temporal overlap between a second harmonic pulse and a continuum pulse (see section 2.2.3.5 for the details). However in the dye laser system, every time, the tuning is achieved by changing laser dye solution and its concentration.

3) No influence from amplified stimulated emission (ASE).

In the dye laser system the ASE is often a main artifact enhanced by many passes of the laser pulse in the gain medium. The magnitude of the ASE is dependent upon a tuning wavelength and the laser dye solution used. The process to remove the ASE (the use of a saturable absorber) also decreases the intensity of main tuned laser pulses, resulting in a low gain factor in the amplifier. For the details of the ASE in the dye laser system, see the PhD thesis of Dr. James Durrant (Durrant 1992). In contrast, the ASE in the OPA is negligible.

4) Compact configuration.

   The whole system requires only small space for the generation of the second harmonic light and the white light continuum, and for mixing of these two light sources for parametric amplification. The gain of the amplification is sufficient enough with single pass. In contrast, many passes in the gain laser medium are required to obtain sufficient amplification in the dye laser system, indicating that large space is necessary for the amplifier.

5) Long lifetime.

   The second harmonic crystal is a solid state medium and usually has high damage threshold (for example >1 GW/cm$^2$ for Barium-Borate (BBO) crystal under visible laser pulses (Nikogosian 1997), however the value depends upon the type of the laser), which requires practically no maintenance and replacement. However in the dye laser system dye molecules degrade under laser light exposure, requiring the continuous adjustment of the dye concentration.

**<Disadvantages>**

1) Higher cost.

   The cost of a second harmonic crystal is dependent upon the quality of the crystal, however even a low quality crystal is expensive. In contrast, only laser dye needs to be added and changed to maintain the power generated from the second amplifier in the dye laser system.

### 2.2.3.3 Principle of optical parametric amplification

***Conservation of energy and momentum***

The mechanism of the OPA is explained previously by a number of groups (Davis 1996, Guenther 1990), and only the basic concept is therefore summarised in this section. Its fundamental principle is to convert light energy from a pump wave to the signal and idler waves, which is based upon the conservation of energy and of momentum. Each wave is coupled to the other two through polarisation waves in, for example, a non-linear crystal. In general the interaction of three waves is called the parametric interaction.

Equation 2.4 represents the conservation of energy involved in a non-linear process.

$$\omega_3 = \omega_1 + \omega_2 \qquad \text{Equation 2.4}$$

where $\omega_3$ is a pump, and $\omega_1$ and $\omega_2$ are a signal and an idler, or vice versa. The term parametric amplification indicates the transfer of energy with a frequency of $\omega_3$ into those with frequencies of $\omega_1$ and $\omega_2$. Under the condition that the idler wave is coupled to the pump wave, growth of the signal wave is observed, resulting in amplification of the signal wave. In contrast, if energy conversion occurs from the right to the left in equation 2.4, the process is regarded as sum frequency (up-conversion). The concept of the sum frequency is often used to detect ultrafast fluorescence in the reaction. If $\omega_1 = \omega_2$, the process is called second harmonic generation (SHG).

In medium, one wave generally propagates slower than other waves. The velocity of the wave is determined by the refractive index of the material at its particular frequency. A phase (wave number) difference between the waves (pump, signal and idler) resulting from their velocity difference can be expressed by equation 2.5.

$$\Delta k = k_3 - (k_1 + k_2) \qquad \text{Equation 2.5}$$

where $k_i$ is a wave number of the wave $\omega_i$.

$$k_i = \frac{\omega_i n_i}{c}$$ Equation 2.6

where $n_i$ is the refractive index of the wave i and c is the velocity of light. The phase difference $\Delta k$ therefore indicates the momentum change in the scattering event. If the scattering event is elastic, then $\Delta k = 0$, and the momentum is conserved (figure 2.5), whereas the momentum is not conserved if the scattering event is inelastic. For the parametric amplification the conservation of the momentum is required in order to obtain a maximum output energy, and therefore it is of great importance to keep $\Delta k \approx 0$. In nonlinear optics, the process of reducing the phase difference $\Delta k$ is called phase matching. Such a phase matching for the OPA system is achieved using an anisotropic (birefringent) crystal (Guenther 1990).

***Phase matching in a birefringent crystal***

In a birefringent crystal, a refractive index of a light wave is dependent upon both the wavelength and the polarisation of the wave propagating within the crystal. The magnitude of the refractive index plotted as a function of direction in the crystal is illustrated in figure 2.3 (uniaxial negative crystal). The crystal in the figure has a main axis called the principal optic axis which is through the centre of these plots. The definition of the principal optic axis is that when a wave propagates in the crystal parallel to the optic axis, the refractive index of the wave is independent of its polarisation direction. If there is only one optic axis in the crystal, it is called an uniaxial crystal.

In the uniaxial crystal, only two types of waves can propagate; one is called the ordinary wave and the other is called the extraordinary wave. The ordinary wave indicates that the wave-plane is polarised perpendicular to the plane formed by the optic axis and the direction of propagation while the extraordinary wave has the wave-plane polarised parallel to this plane. If the refractive index for the ordinary wave, $n_o$, is larger than that for the extraordinary wave, $n_e$, the crystal is called positive; if $n_e < n_o$, it is called negative as shown in figure 2.3. The refractive index of the extraordinary wave depends

upon its angle of propagation relative to the optic axis, whereas that for the ordinary wave is unchanged. The refractive index $n_e(\theta)$ of an extraordinary wave whose wave vector k has a direction at angle $\theta$ to the optic axis can be calculated geometrically with reference to figure 2.4. The value of $n_e(\theta)$ is the length OP shown in the figure, indicating that the refractive index of an extraordinary wave can be determined as a function of the direction of the wave vector k, i.e. the refractive index can be altered by adjusting the angle between the wave vector direction and the optic axis of the crystal.

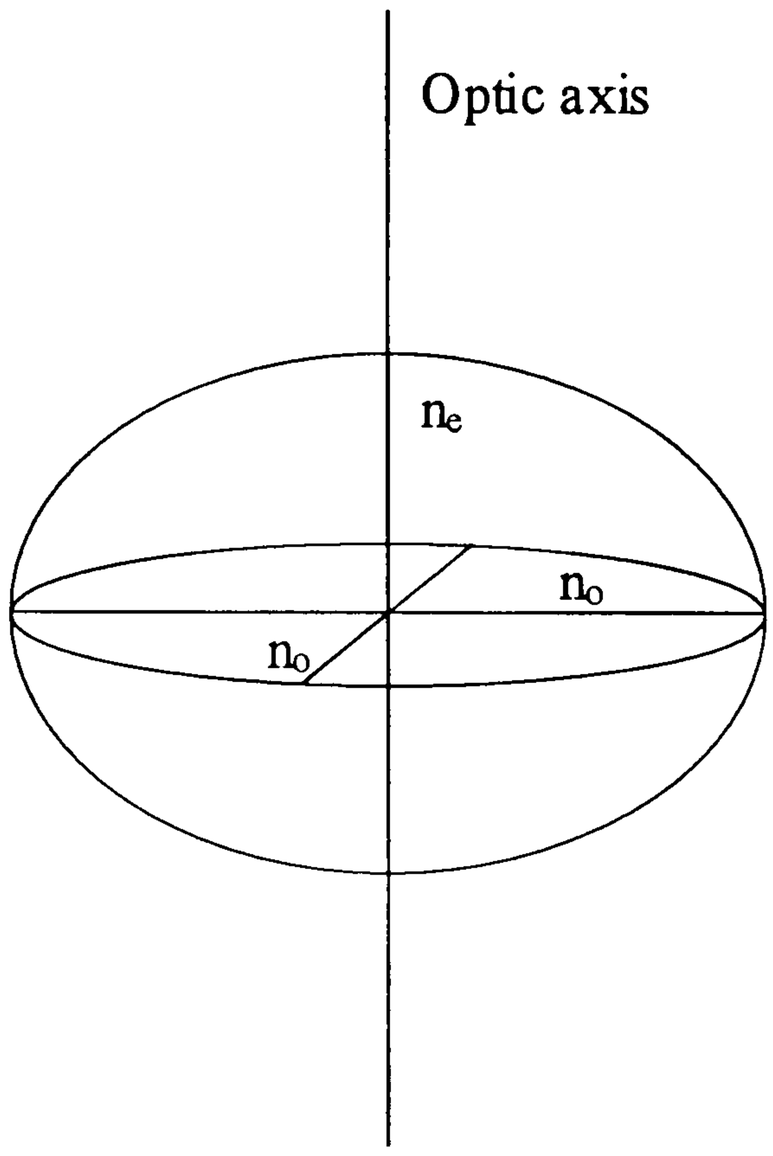



Figure 2.3. Refractive index plotted as a function of direction in a birefringent crystal. An uniaxial negative ($n_e < n_o$) crystal (see text for the details) is used as an example.

For the construction of the OPA, Type I Barium-Borate (BBO) crystal has been chosen as a birefringent crystal for both of the SHG and parametric amplification. As the BBO crystal is a negative uniaxial crystal ($n_e < n_o$) (Nikogosian 1997), the above description of the negative uniaxial crystal can be applied for the SHG and the OPA.

For the SHG, the relation that $\omega_3 = 2\omega_1$ and $\omega_1 = \omega_2$ is required in order to achieve the conservation of energy. The phase matching condition ($\Delta k = 0$) for the optimum SHG can be derived as equation 2.7 from equations 2.5 and 2.6.

$$n_e(\theta) = n_o$$ Equation 2.7

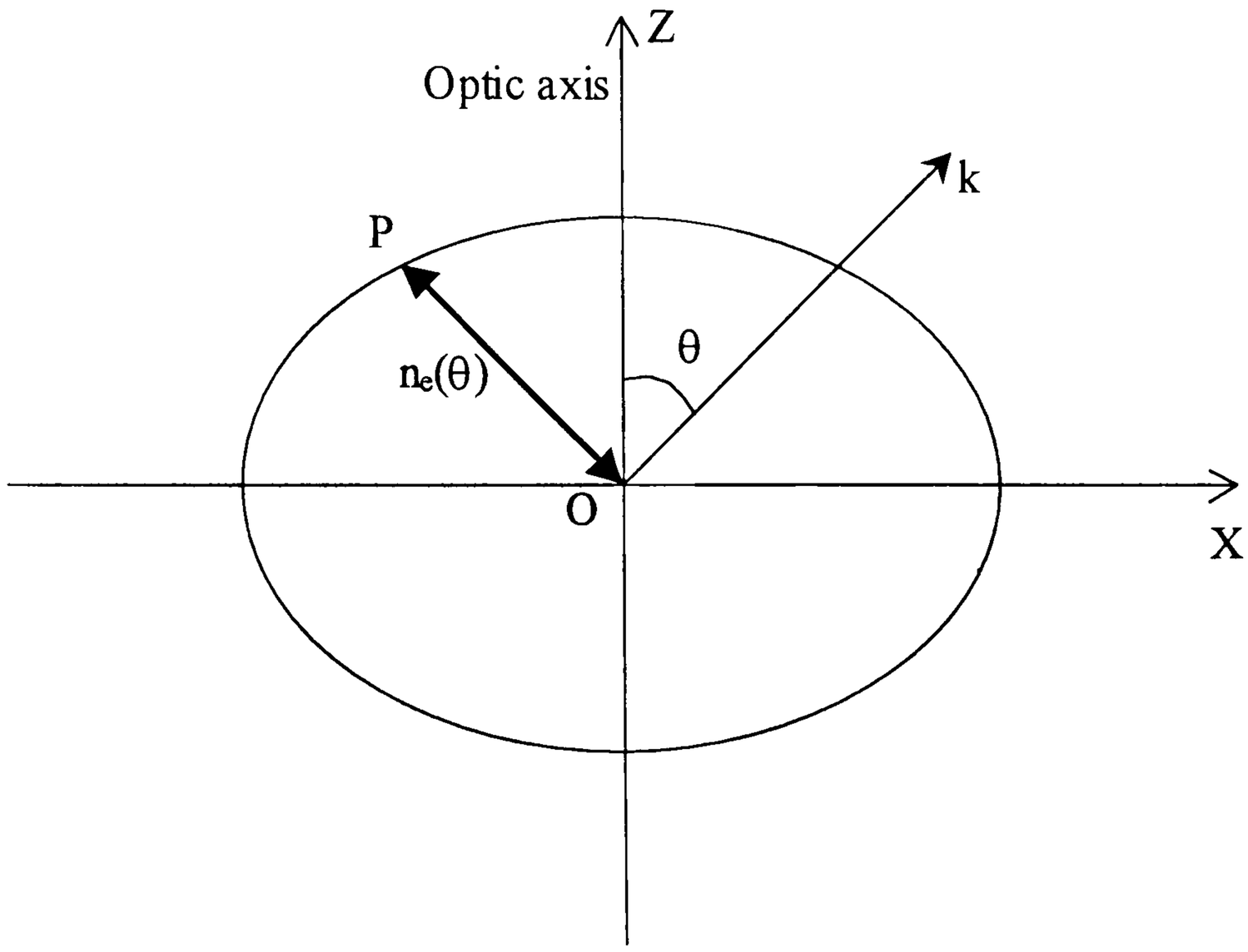



Figure 2.4. Section of refractive index plots containing the optic axis in an uniaxial negative crystal. In this figure, wave vector k has a direction at angle θ to the optic axis.

where θ is the phase matching angle which is the same as the angle between the direction of the wave vector of the incident fundamental wave and the optic axis as discussed above. The refractive index $n_e$ of the second harmonic wave is tuned to be equivalent to the refractive index $n_o$ of the fundamental wave. The calculated phase matching angle is 28.8° in order to generate a second harmonic beam of 405 nm from a fundamental beam of 810 nm (Kato 1986, Nikogosian 1997).

The optical parametric phase matching is achieved by a non-collinear technique in which the conservation of momentum is satisfied in figure 2.5. From equations 2.5 and 2.6, the phase matching condition is expressed by equation 2.8.

$$n_3(\theta)\omega_3 = n_1\omega_1 + n_2\omega_2$$ Equation 2.8

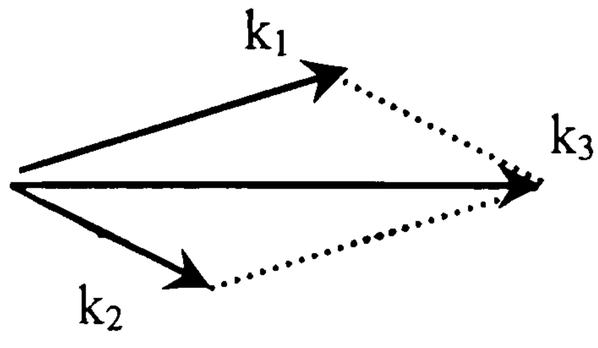



Figure 2.5. Schematic description of conservation of momentum.

As indicated above, the Type I BBO crystal exhibits the case of $n_e < n_o$, and therefore in the phase matching condition for the OPA, the signal and the idler waves should be ordinary; the pump be extraordinary. Figure 2.6 represents the calculated phase matching curve for the BBO crystal for a pump wavelength of 400 nm (Davis 1996, Kato 1986, Reed, et al. 1995). This curve indicates that the phase matching angle should be 29.2 ° to obtain a signal (or an idler) wavelength of 800 nm, or be about 27 ° to obtain a signal of 600 nm and a idler of 1200 nm. It also implies that the OPA is theoretically tunable approximately from 480 nm to 2.4 μm (absorption edge of the BBO crystal).

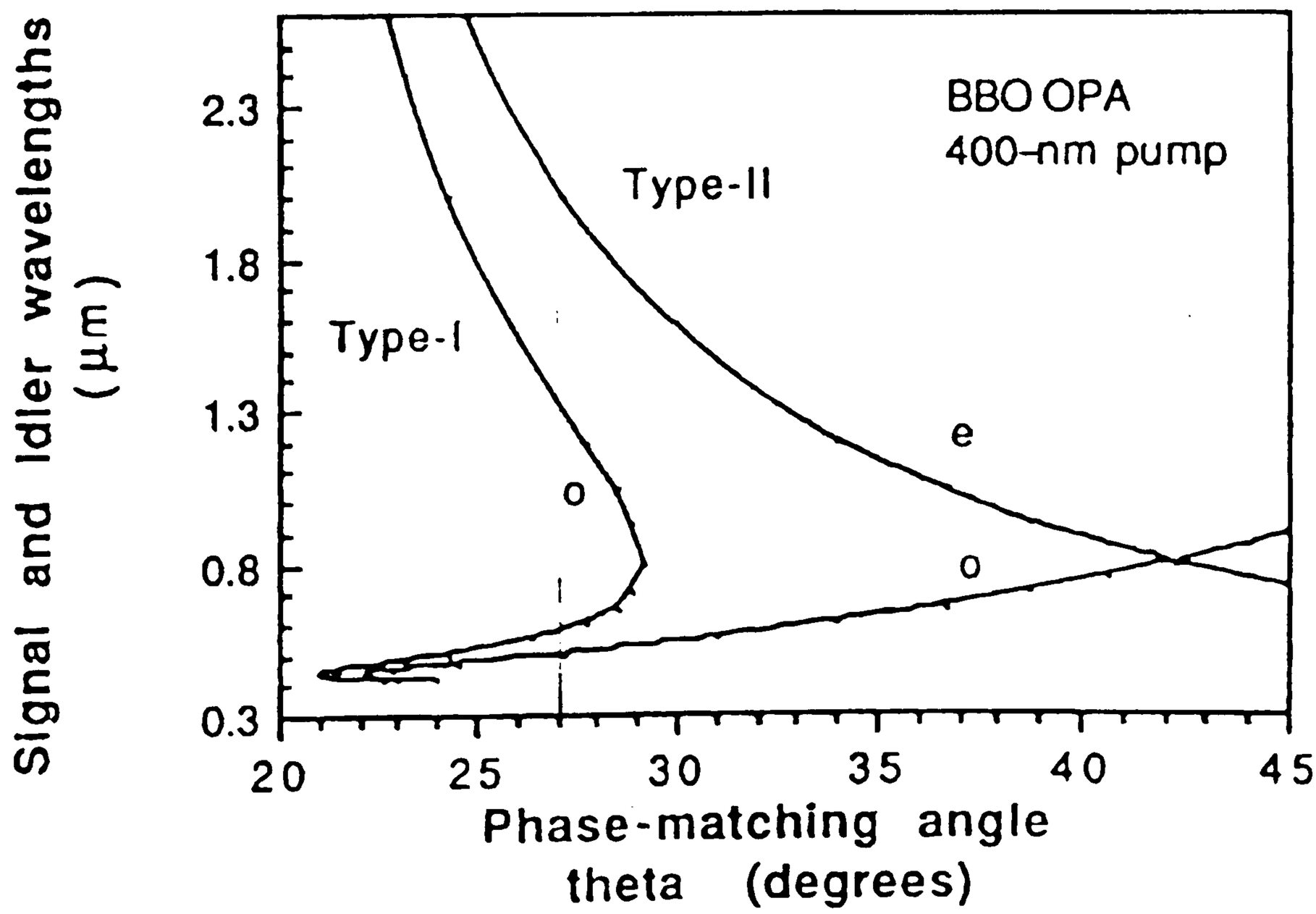



Figure 2.6. Phase matching curve (Reed, et al. 1995) calculated for the BBO crystal for a pump wavelength of 400 nm (Kato 1986).

### 2.2.3.4 Arrangement of the OPA system

The configuration of the OPA system was obtained after modification and further arrangement of the system reported by Reed et al (Reed, et al. 1995). The system basically consists of white light continuum and second harmonic generation and the OPA generation by mixing these two beams in a non-linear crystal. The white light continuum, which is equivalent to $\omega_1$ or $\omega_2$ in equation 2.4 is used as a seed source for the amplification. The pump source is the generated second harmonic pulses ($\omega_3$) resulting from the frequency doubling of the fundamental pulses. An amplified wavelength range in the white light continuum is chosen by the phase matching angle in the BBO crystal as shown in figure 2.6. In practice, the phase matching is achieved by tilting the crystal against the continuum, resulting in the perturbation of the second harmonic phase matching condition (see above). The simultaneously generated idler pulses are currently not used for further application and are blocked after this amplifier.

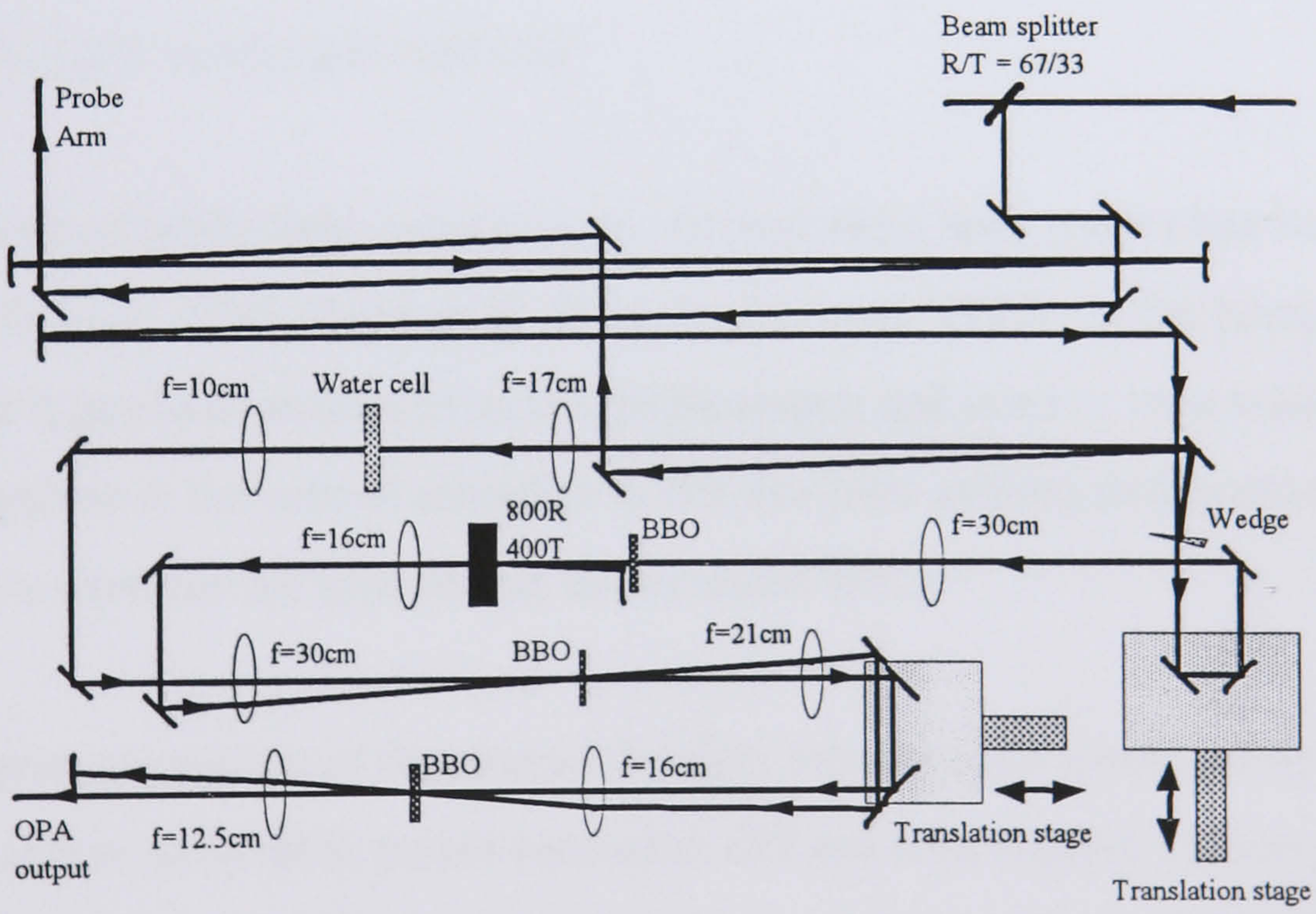



Figure 2.7. Schematic diagram of the OPA system. All of the BBO crystals employed in this system have a thickness of 1 cm and are mounted on the translation stage.

The schematic diagram of the OPA apparatus is shown in figure 2.7. The polarisation of the output femtosecond pulses from the compressor is altered from vertical (to the optic table) to horizontal. These horizontally polarised pulses centred at 810 nm with an

energy of approximately 230 μJ are used as fundamental laser pulses for the OPA and the transient absorption spectroscopy. A variable neutral density filter (Edmund Scientific) is placed after this beam splitter to maintain the same input power (approximately 140 μJ) since the output power from the Ti:sapphire laser system varies by up to 10 %. Correcting for this power variation is essential because the quality (divergence, stability and power) of white light continuum and the power of the second harmonic light are sensitive to the input power to the OPA.

These 140 μJ fundamental pulses are further split into three parts by a wedged glass (separation angle: 30 min) plate (AG Electro-Optics Ltd.). The back reflection, i.e. ~4 % of the fundamental pulses are used for probe pulses in the transient absorption spectroscopy and the front reflection of another ~4 % are used to generate a white light continuum as seed pulses (signal pulses) for the OPA. The rest of fundamental pulses are frequency-doubled, centred at 405 nm, to pump the OPA (pump pulses).

2.2.3.5 White light continuum seed arm

The generation of white light continuum by intense short laser pulses has been well studied (Fork, et al. 1983, Reed, et al. 1995, Smith, et al. 1977). In the pump-probe experiments it has been employed as the probe source and used to tune wavelengths of ultra-short pulses in the second amplifier in the dye laser system as described above. In the OPA, it is used for the seed source as discussed below.

The continuum generation of femtosecond pulses was first demonstrated by Fork et al., which was achieved by 80 fs pulses centred at 627 nm with a pulse intensity of $10^{13}$-$10^{14}$ W/cm$^2$ using an ethylene glycol jet (thickness: 0.5 mm) (Fork, et al. 1983). The mechanism of the ultrafast continuum generation has been the subject of study, however has been suggested to be self-phase modulation (SPM) as a result of self-focusing of the intense laser pulses (Reed, et al. 1995, Smith, et al. 1977).

In the present OPA system the continuum is produced in the 2 mm water cell using a fraction (4 %) of the fundamental pulses (~40 fs) with a pulse energy of approximately 5 μJ (see figure 2.7). Input power into the water cell is controlled by the opening of the

iris placed just before the focusing lens. Stability of the generated continuum is dependent upon the shot-to-shot fluctuation (<3 %) of the fundamental laser. The spectrum extends across the visible and the near infrared. It should be noted that the intense fundamental beam (810 nm) was not removed from the continuum pulses before the generation of the OPA since the beam quality of the OPA pulses was not affected with or without the removal of the fundamental beam, suggesting that thermal effects in the crystal by the high intense beam are negligible.

2.2.3.6 Second harmonic (405 nm) pump arm

The majority of the input beam to the OPA system is converted to second harmonic pulses to pump the OPA. The pump (405 nm) pulses are simply obtained by the frequency doubling of the fundamental laser (810 nm) pulses using a Type-I BBO crystal. Its phase matching condition is described in section 2.2.3.3.

The BBO crystal, 1 mm thick, is placed on the translation stage before the focusing position of the fundamental beam, where pulse energy density is so high that the crystal can be burnt very easily. The second harmonic conversion efficiency is increased by varying the stage position (equivalent to the movement of the crystal position) toward the focusing position of the fundamental beam and by optimising an angle of the crystal against the fundamental beam for the phase matching. The maximum conversion efficiency achieved is 16.5 % (without burning the crystal), however an efficiency of about 10 % is generally maintained for good beam shape, resulting in the good beam quality of the OPA pulses. It should be noted that a short focal length (e.g. 10cm) lens cannot be used to focus the fundamental beam in the BBO crystal at this laser power (see figure 2.7) since the SPM is introduced even in air, which originates probably from a smaller spot size achieved by the shorter focal length lens. The minimum focal length required is about 30 cm. As the BBO crystal was moved towards the beam focusing position, the instability of the pulse was observed through the appearance of scattering and the wobbly shape of the second harmonic beam. The generated second harmonic beam is filtered by the high frequency pass mirror to pump the OPA with only 405 nm light, that is, the fundamental pulses are reflected away by this mirror and blocked.

### 2.2.3.7 Optical parametric amplification

The parametric amplification is operated with two stages, for both of which a Type I BBO crystal is used for mixing seed and pump pulses. The BBO crystal was placed on the gimbal mount which enables the angle of the crystal to be changed without moving the centre position of the beam at the crystal. Tuning a desired visible wavelength is performed by rotating the BBO crystal angle about the horizontal axis for the phase matching and by varying the translation stage of the second harmonic arm in order to compensate for the temporal walk-off between the continuum and the second harmonic beams, resulting from the GVD of the continuum pulses caused in the water cell and the lenses.

As for the first stage, both the seed and the pump beams are focused with the same lens. The silver mirror placed before this focusing lens in the pump side is adjusted to optimise spatial overlap non-colinearly with a crossing angle of approximately 2° between two pulses at the BBO crystal in order to generate the OPA. It should be noted that at the overlap position, the beam size of the seed should be smaller than that of the pump beam. The focusing position of the seed beam is controlled by the lens which is mounted on the translation stage after the continuum generation (see figure 2.7). Also, note that this crossing angle (in a range of <1 ~ 2°) is found not to alter the OPA beam shape and power, i.e. the spatial walk-off between the pump and the signal pulses within the crystal is negligible.

***Procedure to obtain the OPA pulses***

The spatial overlap between the continuum and the second harmonic beams can be optimised using the CCD camera or a pinhole positioned at the overlapping position. The camera or the pinhole is then replaced with the crystal (its cut angle is assumed to be ~29°) whose surface is approximately normal to the continuum and the second harmonic beams. When the temporal phase matching between the continuum ($\omega_1$) and the second harmonic pulses ($\omega_3$) is achieved, idler pulse (wavelength near 800 nm) should appear in the direction of $\omega_2$ in figure 2.5 (this idler pulse could be seen using an infrared viewer). It should be noted that there exist several idler pulses found as the

translation stage is varied. These pulses appear when reflection of the main pulse by the optics is also temporally matched. However, the side idler pulse (generated by reflected pulses) is generally weak. In practice, six idler pulses were found by varying the translation stage within 2 cm. It is therefore important to find the overlap of the main pulses in order to obtain an intense parametric amplification.

Once the main idler is found, the crystal angle can be altered following the adjustment of the translation stage to compensate the GVD mismatch of different frequency components. The visible OPA will appear in the direction of $\omega_1$ when both spatial and temporal overlaps between the continuum and the second harmonic pulses are optimised. As the angle of the crystal is varied, the different colours of the amplified frequency components appear inside the continuum arm.

***Parametric gain of an OPA***

The high energy output can be achieved by tightly focusing the second harmonic pulse input to the BBO crystal, however this high energy density of the pump pulse distorts the OPA output beam shape. Thus, the OPA gain and the beam shape are compromised. The parametric gain (G) of an OPA can be estimated with the following equations 2.9 and 2.10, taken from the literature (Danielius, et al. 1993, Reed, et al. 1995).

$$G = \frac{1}{4}\exp(2\Gamma L) \qquad \text{Equation 2.9}$$

where

$$\Gamma^2 = \frac{8\pi^2 d_{eff}{}^2 I_{pump}}{\varepsilon_0 \lambda_s \lambda_i n_p n_s n_i c} \qquad \text{Equation 2.10}$$

and L is a crystal length, $d_{eff}$ is an effective non-linear coefficient: 2.0 pm/V for the Type-I BBO crystal (Reed, et al. 1995), $I_{pump}$ is a pump power at the BBO, $\varepsilon_0$ is the permittivity of free space, $\lambda_s$ and $\lambda_i$ are wavelengths of signal and idler beams, n is a refractive index and c is the speed of light.

The refractive indices for pump, signal and idler beams can be estimated from the literature (Kato 1986). $I_{pump}$ for the first OPA is calculated with an input pump energy of 10 μJ, a pulse duration and a diameter of the beam. The focused spot size (spot diameter: w) of the beam can be calculated from equation 2.11 (Saleh, et al. 1991).

$$w = \frac{4}{\pi}\frac{\lambda f}{D} \qquad \text{Equation 2.11}$$

where λ is a wavelength of the beam, f is a focal length of the lens and D is an incident beam diameter. Using this equation, a spot size (70±10 μm) for the pump beam (405 nm) is obtained. However, assuming a pulse duration of 50 fs, the pump intensity is expected to be $5.2 \times 10^{16}$ W/m$^2$ at the spot, which is far beyond the damage threshold. Indeed it was observed that the beam shape of the pump pulse was severely distorted when the crystal was moved towards the focusing position. For this reason, the BBO crystal is placed before the focusing position of the second harmonic pulses.

The gain obtained in the first OPA is usually in the range of 100~150, which is estimated by comparing the peak energies of the amplified and unamplified signal beams at the same wavelength. Using equations 2.9 and 2.10, this gain indicates that a beam size of the pump pulses at the position of the BBO crystal is 0.9~1 mm in diameter, assuming that there is no group velocity mismatch and no spatial walk-off between the signal and pump pulses inside the crystal, i.e. two pulses overlap while propagating through the crystal. This assumption is unlikely to be maintained since the lenses for the OPA introduce the GVD between the signal and the pump pulses. The pump beam size should therefore be reduced appropriately in order to obtain this gain value.

As for the second stage, the non-collinear spatial overlap (crossing angle: ~3 °) between the continuum and the second harmonic arms is achieved by adjusting the mirror placed just before the focusing lens in the second harmonic arm. The amplification (gain) obtained in the second stage is only a factor of 15~30. This fact implies that the pulse

duration, the pump pulse energy and the relative sizes of the continuum and the second harmonic beams may not be optimised.

The total output energy of the OPA is typically 200~300 nJ over a wavelength range of 520~680 nm, corresponding to an OPA (pump-to-signal) efficiency of 2~3 %. The output pulses are used for the excitation source in the ultrafast pump-probe experiments. A compressed pulse duration was found to be ~30 fs using the auto-correlation, measured by Mr. Stefan Abend in the Molecular Dynamics Group.

### 2.2.4 Ultrafast transient absorption spectrometer in the Ti:sapphire laser system

#### 2.2.4.1 Introduction

The pump-probe apparatus in the femtosecond Ti:sapphire laser system was constructed with the stable white light continuum probe pulses and the widely tunable femtosecond OPA pump pulses. The schematic diagram of the apparatus is presented in figure 2.8. The basic principle of the apparatus including the detection system is the same as that in the femtosecond dye laser system. However a number of points have been modified compared to the set-up in the dye laser system. For example, a stable single filament white light continuum is employed in the Ti:sapphire laser system rather than the super continuum which has been generated in the dye laser system. The single filament continuum generation is achieved with the highly stable fundamental laser pulses (shot-to-shot fluctuation of 1~3 %), resulting in better beam quality and less noise level. However such a continuum has a much lower light level than the super continuum in the dye laser system.

#### 2.2.4.2 Pump arm

The excitation (pump) arm in the pump-probe apparatus comprises a pair of prisms, a translation stage, a mechanical chopper and a pump monitor photodiode. The generated OPA pulses are used as an excitation source, producing a tunable excitation wavelength in 450~750 nm.

The output pulses from the OPA system are compressed to obtain ultrashort pump pulses at the sample using a pair of prisms (SF10) with two silver mirrors and a slit as shown in figure 2.8. The pulses are focused after the slit position in order to obtain better resolution in wavelengths at the slit. This is because a smaller beam size through the prism generally allows more precise separation of frequency components in the beam at the position of the slit. The amplified wavelength in the OPA system is selected through the slit, and the rest of the continuum, fundamental (810 nm) and second harmonic (405 nm) beams are blocked.

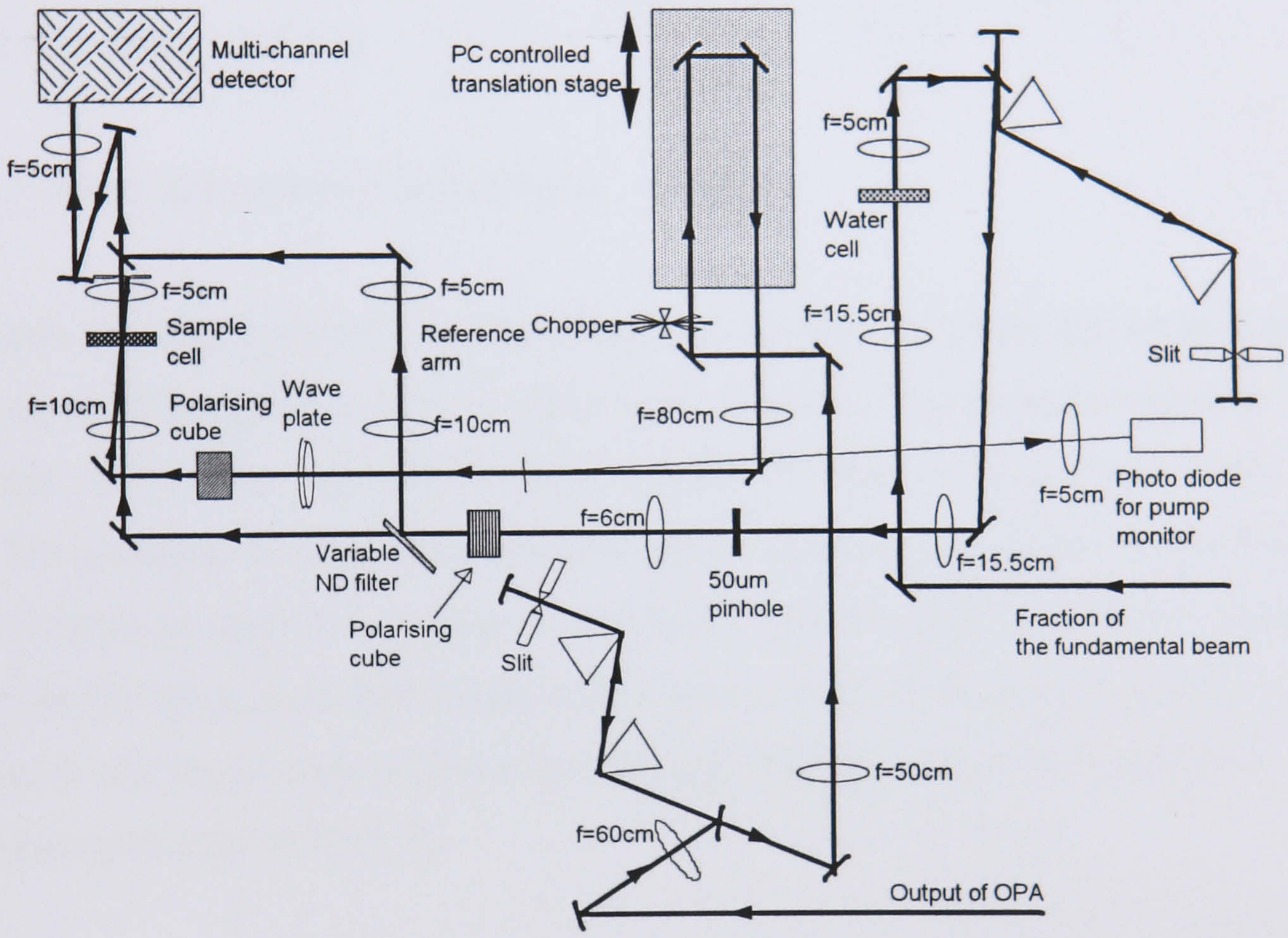



Figure 2.8. Schematic diagram of the pump-probe apparatus for the femtosecond Ti:sapphire laser system.

The output and the probe pulses are overlapped at the sample position which is placed at the focusing position of the probe pulses. The pump beam size at this position is magnified using a 80 cm diverging lens placed after the translation stage (see figure 2.8) in order to ensure that the pump beam size is larger than the probe spot size. The relative beam sizes of the pump and probe pulses are approximately 50 and 60~80 μm respectively, confirmed using the CCD camera, however they are dependent upon the wavelengths used. The maximum overlap is achieved by using the CCD camera and by monitoring a signal size for a dye standard sample with the adjustment of the mirror

before the focusing lens in the pump arm. The polarisation of the pump pulses is set to the magic angle (ca. 54.7°) with the probe pulses using a λ/2 wave plate and a polarising cube.

The pump pulse fluctuation from the OPA system is monitored by a photodiode with the personal computer, and was typically ± 10~30 %, depending mainly upon the stability of the continuum in the OPA. A fraction of the pump beam is collected and focused into the photodiode (see figure 2.8) in order to average the pump power in the computer after each scan. All transient data are normalised with the averaged pump power (see section 2.2.5.4).

2.2.4.3 White light continuum probe arm

The back reflection (4 %) of the 140 μJ fundamental laser pulses by the wedged glass plate are used as a probe source. A white light continuum is generated to monitor reactions over a wide range of wavelengths (450~1000 nm) rather than one colour (810 nm). The generated continuum consists of a single filament and is more stable than the super continuum used in the dye laser system. However the light level is low, resulting in a relatively large noise level (dark noise limited) in the multi-channel detection system. It was therefore necessary to modify the condition of multi-channel data collection (see section 2.2.5.1).

The pulses are propagated for a long distance before the continuum generation in order to compensate for the path length difference between the probe and the pump pulses resulting from the OPA (see figure 2.8). A 1-cm path length water cell is used for the continuum generation. The input power is controlled by opening of the iris placed before the focusing lens. It should be noted that a sapphire plate with a thickness of 2 mm was tested to generate the continuum, however it was found that the light level of the continuum was much lower than the water cell.

The generated continuum is then introduced into a pair of prisms (SF10) to compensate the wavelength dependent GVD caused by the continuum generation. The wavelength range is chosen by moving the second prism position in or out and by the position of a

slit. It should be noted that a wavelength range of <600 nm can not be compensated due to the severe loss of the continuum light by the prism set, and transient data are therefore collected without using the prism set. The prism set was also not used when the experiment did not require a time resolution of <250 fs.

The compensated beam is spatially filtered by the pinhole with a hole diameter of 50 μm to clean the beam shape. The beam is separated into two parts by a beam splitter; one side is for the reference beam and the other is for the sample beam. In the sample arm the beam is focused to the sample cell and afterwards recollimated. For the reference arm, the collimated beam size is also decreased by the same magnitude as the sample arm (using one set of lenses). Both the sample and the reference beams must be carefully aligned into the multi-channel detector.

### 2.2.5 Data collection and analysis

#### 2.2.5.1 Multi-channel data collection system

The multi-channel detector, i.e. the main detection system for the femtosecond transient absorption spectroscopy, was originally developed by Drs. David Klug, Thomas Rech, Chris Barnett, Chang Hong and James Durrant in the Molecular Dynamics Group (see the published paper (Rech, et al. 1994) for the brief summary). The main difference compared to a conventional monochromator is that it consists of two sets of 128 pixel silicon photodiode arrays instead of single photodiode. One array is used for the sample arm containing the actual information of reactions, and the other array for the reference arm. A set of 128 decay kinetics (the collection of ΔOD as a function of time delay) can be simultaneously observed for a range of about 95 nm with a resolution of approximately 0.74 nm per channel (silicon photodiode) over 460~900 nm.

The sample and the reference light levels are recorded by these arrays with blocking (pump off) and unblocking (pump on) excitation pulses to calculate absorption difference as shown in equation 2.12.

$$\Delta OD(\lambda,t) = \log_{10}\left(\frac{\mathrm{I}_{\text{unpump, signal}}(\lambda)}{\mathrm{I}_{\text{unpump, reference}}(\lambda)}\right) - \log_{10}\left(\frac{\mathrm{I}_{\text{pump, signal}}(\lambda,t)}{\mathrm{I}_{\text{pump, reference}}(\lambda)}\right) \qquad \text{Equation 2.12}$$

The change in probe light level due to the fluctuation of the continuum is normalised by ratioing the sample and the reference light intensities. The condition of the pump on and off is achieved by the mechanical chopper. The chopper speed is adjusted to obtain the optimum noise level in the multi-channel detector as discussed below.

The data average time in the personal computer was calculated as follows;

***Dye laser system***

The excitation frequency is reduced to 3.25 kHz by the mechanical chopper compared to a main laser frequency of 6.5 kHz, that is, every other pump pulse is blocked by the chopper blade. It therefore takes approximately 300 us per reading for one ratioing. The total reading number for one average is set to 600, and therefore one average takes about 0.18 s.

***Ti:sapphire laser system***

The optimum reading frequency is found to be 250 Hz as discussed in section 2.2.5.4, and therefore one reading time is 4 ms. The total reading number for one average in the personal computer is set to 48, corresponding to one average time of 0.19 s.

2.2.5.2 Synchronisation in the transient absorption spectroscopy

The timing between the femtosecond laser system and the pump-probe apparatus is principally controlled by the chopper in the pump arm in order to achieve optimum signal-to-noise. This timing as an external trigger source is synchronised with the fs output pulse train, the pump laser for the amplifier, the Pockel's Cell electro-optic switch and the multi-channel detector.

The diagrams of the synchronisation for both dye laser and Ti:sapphire laser systems are shown in figure 2.9. The principal organisation is the same for both laser systems,

however the timing for the pump laser and the Pockel's Cell switching are subtly different to obtain the optimum operation (for the details of synchronisation, see the PhD thesis of Drs. M. Joseph and R. Tompkins (Joseph 1996, Tompkins 1998)). Moreover, change in chopper speed can contribute a noise level of the multichannel detector as discussed in section 2.2.5.4.

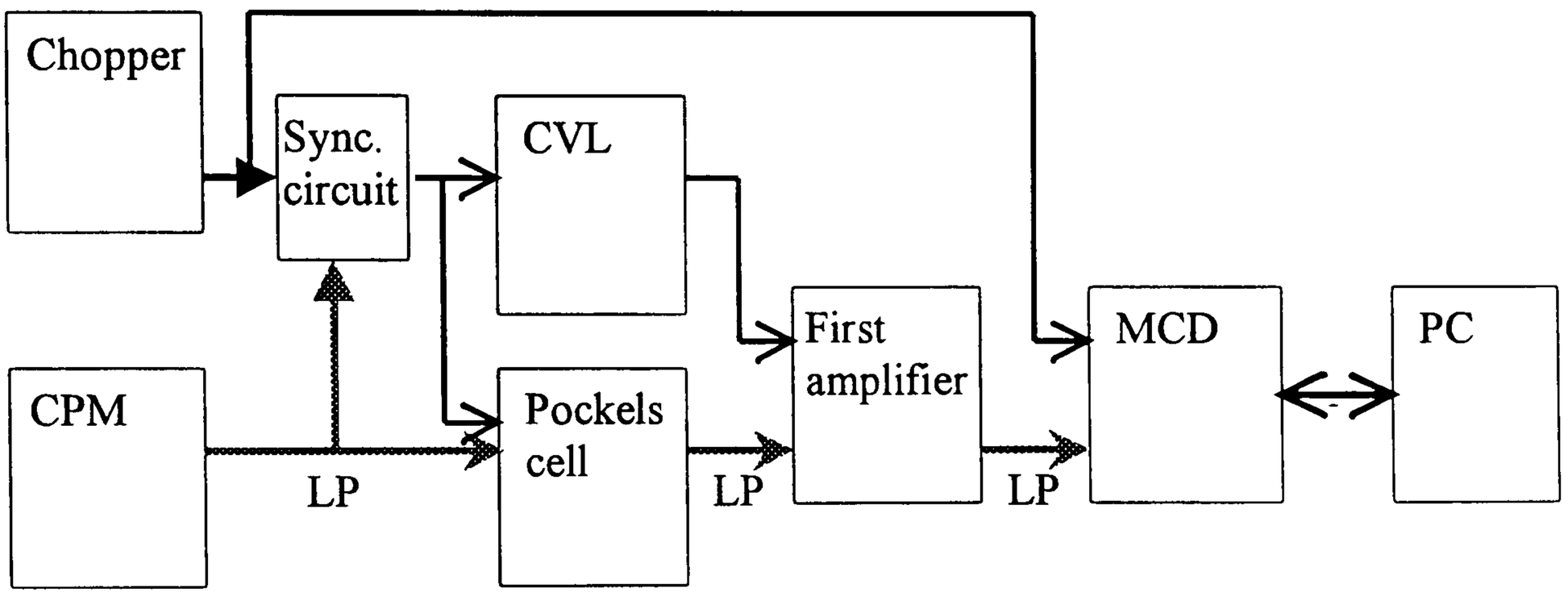



Figure 2.9. Diagrams presenting the synchronisation for both dye laser and Ti:sapphire laser systems. D denotes electronic delay and LP denotes laser pulse. Both systems are operated on the same manner.

### 2.2.5.3 Data analysis

Multi-channel transient absorption data analysis is briefly summarised in an earlier paper (Rech, et al. 1994) and thesis (Merry 1998). The data analysis presented in this thesis were mainly carried out with the computer program ("Look") which was developed by Dr. Thomas Rech and Mr. Martin Bell in the Molecular Dynamics Group. The multi-channel data consists of 128 kinetics decays (the collection of ΔODs as a function of time delay) for a range of about 95 nm. Each decay trace is adequately fitted assuming the decay as a sum of exponentials and a constant (equation 2.13).

$$\Delta OD(t) = A_{const} + A_1 \exp\left(\frac{-t}{\tau_1}\right) + A_2 \exp\left(\frac{-t}{\tau_2}\right) + A_3 \exp\left(\frac{-t}{\tau_3}\right) + \ldots\ldots \qquad \text{Equation 2.13}$$

where $A_n$ are the amplitudes (pre-exponential factors) of the kinetic components, $\tau_n$ are their corresponding lifetimes and t is the real time after the optical excitation. The set of decays is simultaneously fitted (Global analysis, see appendix B), that is, all decays are linked with a lifetime of the component. Such linked fitting is repeated routinely until a minimum deviation is achieved.

The actual time delay between the pump and the probe is determined by the dye standard (Nile Blue in methanol or ZnTCPP in ethanol) which is usually chosen due to its simple excited state structure, i.e. negligible kinetic change during the time of excitation. The pump-probe overlap (t = 0) is assumed to be a centre point of the amplitude change initiated by the excitation of the sample. The instrument response is typically 100~250 fs determined by taking 10~90 % of the rise time of the absorption signal obtained with the same dye standard. Its response time is dependent upon a probe wavelength due to the GVD of each pump and probe pulses. In addition there is signal distortion in the early time data, resulting from non-linear processes such as impulsive stimulated Raman scattering (Hong, et al. 1993) (see below). Due to such signal artifacts, analyses were conducted without the deconvolution of the instrument response, and therefore only for time delays greater than the pump / probe pulse overlap.

The data were presented as a kinetic trace, a transient absorption spectrum and a kinetic (amplitude) spectrum of the component obtained from the global analysis (see appendix B). The kinetic trace is usually presented as a function of time after an average of several decay channels. The transient spectrum is a spectrum taken at a certain time delay after the excitation. The kinetic spectrum is a plot of $A_n$ in equation 2.13 as a function of the channel wavelength.

### 2.2.5.4 Noise and artifacts in the laser apparatus and improvement of the system

It is certainly critical to reduce noises caused by the fundamental laser fluctuation and to understand artifacts caused by interaction between laser pulses and other media in order to observe the actual kinetics of photophysical and photochemical reactions. It is also of particular importance to save experimental time to average the transient data. Noise and artifacts in the femtosecond dye laser system and the improvement of such artifacts are described in detail in the PhD thesis of Dr. James Durrant (Durrant 1992). In this section, I will discuss the noise and artifacts, and describe the improvement and the optimisation of the pump-probe apparatus in the femtosecond Ti:sapphire laser system.

***Noise and artifacts upon the operation of the pump-probe experiment***

Data collection is often affected by the subtle fundamental fluctuation of the laser apparatus and the sample-laser pulse interaction. The main noises and artifacts are as follows.

1) ***White light continuum fluctuation***

   The continuum pulses in the femtosecond Ti:sapphire laser system are generated by focusing the fundamental laser pulses in a water cell. The pulse energy density at the focusing position is absolutely critical to generate the most stable continuum pulse. In practice, the input energy into the water cell is controlled by opening of an iris placed before the focusing lens (c.f. pump-probe set-up in section 2.2.3.5). The noise level is high if the fundamental input energy into the water cell is very low, while an averaged noise level is high if the input energy is too high. In addition the continuum stability is very sensitive to the fundamental pulse-to-pulse fluctuation even though the effect of the fluctuation is removed by ratioing the sample and

reference probe light as equation 2.12. It should be noted that the noise level in the multi-channel detector is severely deteriorated ($> \pm 4 \times 10^{-3}$) when the shot-to-shot fluctuation of the fundamental pulses exceeds 4 %.

2) ***Pump fluctuation***

The pump pulse is generated by the OPA in which a white light continuum is used to tune a wavelength desired. The fluctuation of the OPA pulse is sensitive to the continuum fluctuation, which is therefore sensitive to the fundamental pulse fluctuation; for example change in the fundamental pulse fluctuation from 2 to 3 % results in an increased noise level of the pump pulse by a factor of approximately 3.

3) ***Artifacts caused by interaction between a sample and a laser pulse***

During the overlap of the pump and probe pulses in the sample, stimulated Raman scattering is usually observed. This phenomenon was well studied by Drs. Qiang Hong (Hong, et al. 1993) and James Durrant (Durrant 1992). An oscillatory signal caused by this scatter in the transient data is induced by the interaction between the laser pulses and a glass medium. For example, this scatter is generated with cover glasses (100 μm thick) for a solution sample cell, a base glass plate or a conducting glass plate of nanocrystalline $TiO_2$ films. The oscillatory signal increases when thicker glass and white light continuum probe pulse are used (Hong, et al. 1993).

After the pump-probe overlap is achieved in the sample cell, it is of great importance to block the pump beam, otherwise it will be exposed to the photodiodes in the multi-channel detector. This is because the probe light intensity is extremely weak compared to the pump light intensity, and a small fraction of the pump light results in significant amplitude change. To block the pump light, an iris is placed after the sample cell (see the diagram of the pump-probe set-up in figure 2.8), and an adequate colour filter (a high or low frequency pass filter) is used depending upon the wavelengths monitored.

***Improvement of noise level in pump-probe set-up in Ti:sapphire laser system***

As discussed above, the noise level in the multi-channel detector can be affected by various factors; white light continuum probe pulses, pump pulses and the alignment of

sample and reference beam paths. The femtosecond Ti:sapphire laser system developed in the Molecular Dynamics Group is capable of producing a high intensity laser pulse with a pulse-to-pulse fluctuation of ~4 %. However even with such a stable laser system, the white light continuum and the OPA fluctuations resulting from the fundamental pulse fluctuation cause huge noise for the transient absorption experiment as discussed above. The improvement of the noise level in the pump-probe apparatus was achieved as below by the modification of the set-up.

*1) Data collection frequency*

In the multi-channel detector, a noise level at one wavelength is determined by the amount of photons (in the probe pulse) collected at each diode within the duration of the chopper motion. It is generally observed that the noise level is better at the wavelength near 810 nm (fundamental). This is because the number of photons of frequency components in the white light continuum decreases towards a higher frequency from 810 nm. The probe light level in the pump-probe apparatus is extremely weak compared to the super continuum used in the dye laser system. Therefore, the light collection setting at each photo diode needs to be optimised.

The amount of photons collected (the photon collection time) at each diode can simply be altered by changing the chopper frequency and modifying the electronic timing in the electronic circuit for the multi-channel detector, resulting in modification of the pump on and off timing. Therefore, the slower the chopper frequency is, the more photons can be collected at each diode within the duration of the chopper motion.

In consequence of the adjustment of the chopper speed, the optimum chopper frequency is 250 Hz. This means that the pump is blocked by the chopper every two pulses, i.e. the timing in the multi-channel detector is on, on, off, off, on, on, off... When the chopper speed is 500 Hz, the noise level increased. Below the frequency of 125 Hz, the accuracy of ratioing of the sample and the reference is likely to decrease due to the continuum fluctuations. The chopper frequency is, therefore, determined to be 250 Hz.

2) ***Effect of pre- and post- pulses***

It has been observed that pre- and post- pulses are leaked out from the regenerative amplifier in the vicinity of the main intense fundamental pulse. The time separation (approximately 11 ns) between the pulses in the pulse train generated in the oscillator is close to an electronic response time (7~8 ns) of the polarisation change in the Pockel's Cell. These comparable times result in imperfect blocking of pre- and post- pulses. These side pulses are also amplified with the main pulse in the regenerative amplifier. The travelling time of the pulse in the cavity of the regenerative amplifier is similar to the pulse separation time in the pulse train. The amplified pre- and post- pulses are therefore taken out from the amplifier with a time difference of approximately 200 ps between the pre- / post- pulses and the main pulse. The influence of these side pulses was studied with the dye standard (Nile Blue) in the pump-probe apparatus.

The pre- and post- pulses are too weak to generate a white light continuum. For the pump pulse, pre- and post- OPA pulses cannot therefore be generated. As for the probe arm, a variable slit is placed in the middle of the prism set after the generation of the white light continuum. The probe pulses are therefore not likely to have the pre- and post- pulses when probe wavelengths are not optimised around 810 nm. Indeed no signal was observed using the probe wavelengths of <780 and >840 nm. However signals at about 200 ps from the main pump-probe overlap were clearly observed when the fundamental pulse (810 nm) was used as the probe. The size of those signals is at most 15 % of the main signal change originated from the overlap of the pump and the main fundamental probe pulses. This observation suggests that the fundamental light cannot be used as the probe source if it significantly affects the kinetics study.

## 2.3 Other experimental apparatus

### 2.3.1 Introduction

Photophysical and photochemical reactions of dye molecules and dye sensitised semiconductor films were monitored by means of transient spectrometers on various

timescales. For example, a typical lifetime of a ruthenium dye excited state is of the order of nanoseconds, and therefore nanosecond (ns) transient absorption spectroscopy can be employed to monitor its lifetime. Moreover microsecond-millisecond (μs-ms) transient absorption spectroscopy was used since a charge separated state in dye sensitised $TiO_2$ films has a lifetime on the μs-ms timescales.

The spectrometers, described below, also allow the stability of the samples to be checked before and after the femtosecond transient experiment, and allows the electron injection efficiency of the dye sensitised $TiO_2$ film to be assessed immediately after the preparation of the film. These measurements are extremely important to save operation time in the femtosecond experiments.

### 2.3.2 Steady state UV / vis absorption and emission spectrometer

Steady state UV-visible absorption spectra were obtained on a Shimadzu UV1601 spectrometer. Spectral resolution is 2 nm with a sampling interval of 0.5 nm. Steady state emission spectroscopy was carried out on a Perkin Elmer LS50 luminescence spectrometer. The slit widths for an excitation lamp source and a detection source are 10 nm.

### 2.3.3 Microsecond-millisecond transient absorption spectrometer

The μs-ms transient absorption experiments were carried out with a nitrogen laser pumped dye laser, and the details for the apparatus are described in the PhD thesis of Dr. James Durrant (Durrant 1992). In this section the description of the apparatus is summarised.

The arrangement of the apparatus is illustrated in figure 2.10. The main difference from the previous set-up is that a dye laser (PL201, PTI) system pumped by a nitrogen laser (LN1000 Megaplus, PRA Laser) has been employed as an excitation source. The excitation wavelength can be tuned with this dye laser system. The probe light wavelength from a tungsten lamp was selected by an appropriate monochromator and by a colour filter to minimise the probe light incident upon the sample. The other

monochromator and a colour filter after the sample were employed to reduce emission and pump laser scatter from the sample. Transient data were collected with a photodiode and a Gould 475 digital oscilloscope.

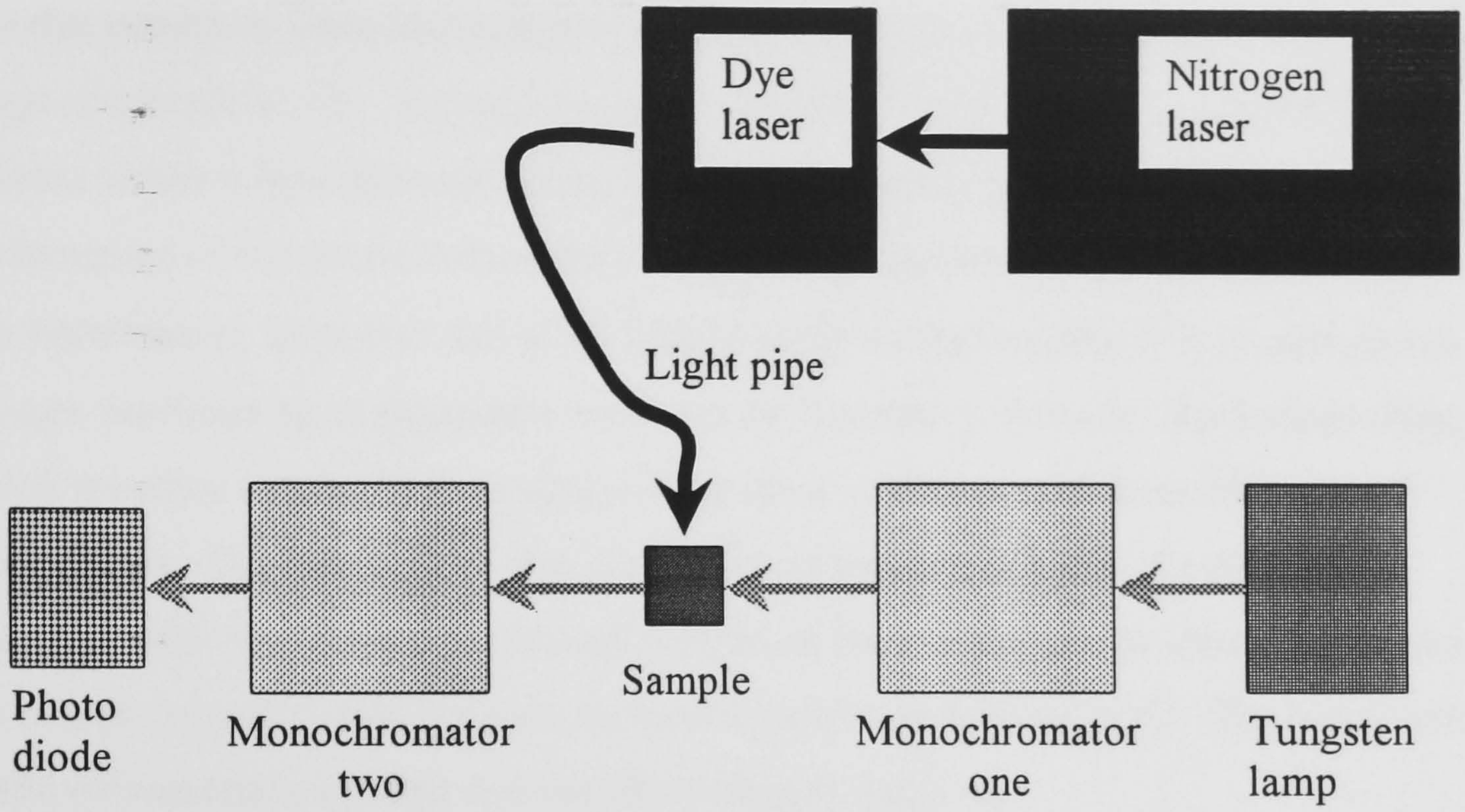



Figure 2.10. Schematic diagram of the μs-ms transient absorption spectrometer. An appropriate colour filter was placed after the sample in order to reduce emission and pump laser scatter from the sample.

The transient absorption difference is calculated by the following equation 2.14 (Durrant 1992).

$$\Delta OD(t) = \alpha \times \frac{V(t)}{V_o} \qquad \text{Equation 2.14}$$

where V(t) is the transient signal size which is proportional to transient light intensity change, Vo is the dc voltage which is proportional to the probe light level and $\alpha$ is the scale factor depending upon the amplification. In the present system $\alpha = 0.00204$.

### 2.3.4 Nanosecond transient absorption and emission spectrometer

#### 2.3.4.1 Introduction

The dye sensitised $TiO_2$ film exhibits interfacial electron transfer reactions over a wide range of timescales (fs ~ ms) as discussed in chapter 4. It is of great importance to observe electron injection and charge recombination kinetics in order to estimate the performance of the photoelectrochemical cell, and to elucidate the mechanism of the dye sensitisation. However due to the limited experimental ranges of the fs and μs-ms set-ups, reactions on ns timescales could not be observed previously. Ruthenium dyes, which are often employed as sensitiser dyes, show typical excited state lifetimes of nanoseconds. This fact implies that the dye sensitisation efficiency of a different sensitised film can easily be estimated comparing the lifetimes of the excited state and the charge separated state obtained by measurements on this timescale. The construction of the ns transient apparatus was therefore strongly required.

#### 2.3.4.2 Arrangement of the apparatus

The apparatus was developed with the considerable support of Dr. Chris Barnett in Molecular Dynamics Group. The scheme of the nanosecond transient absorption spectrometer is shown in figure 2.11. The excitation source is the nitrogen laser pumped dye laser with a repetition rate of 2 Hz, which is the same as that for the μs / ms transient absorption apparatus. The main difference between the ns and the μs / ms apparatus is the probe light source. Since the kinetics are observed on ns timescales, the apparatus requires an intense probe light, i.e. the power density of the light needs to be high in order to obtain a sufficient signal to noise ratio. For example, to obtain the same signal to noise ratio at 10 ns as that at 10 μs in the μs / ms system, the power density of the probe light in the ns flash photolysis system has to be three orders of magnitude higher than the μs / ms system. For this purpose, an intense xenon flash lamp with a pulse duration of about 15 μs was employed in order to monitor electron transfer kinetics at a wide range of probe wavelengths.

A probe light wavelength is selected by one monochromator (Jarrell Ash) after the sample. Fluorescence and excitation laser scatter by the sample are blocked by this monochromator. Unlike the μs / ms spectrometer, another monochromator is not placed before the sample (compare figures 2.10) because the light level at a selected wavelength is significantly decreased by the monochromator. Instead a colour filter (Schott) is used to select a wavelength, e.g. the light with wavelengths of <420 nm is blocked by the filter in order not to excite the $TiO_2$ semiconductor itself.

The two main problems of the operation are timing jitter of the nitrogen laser flash and saturation of the gain amplifier for the signal. The excitation laser trigger timing is synchronised to observe kinetics at the top flat (intensity maximum) part of the Xenon flash light. This synchronisation implies that the nitrogen laser jitter causes change in a probe light level during data collection since the probe light level is dependent upon the position of the pulse, resulting in increased noise level. The time jitter therefore has to be minimised; the minimum jitter time observed is approximately 150 ns. The intense Xenon probe light is capable of measuring the kinetics on ns timescales, however this strong light level easily causes the saturation of the gain amplifier in the detection system. The detection electronics need to be modified to decrease the probe light level without losing the amplification gain. Dr. Chris Barnett has been improving on these problems by introducing additional electronics.

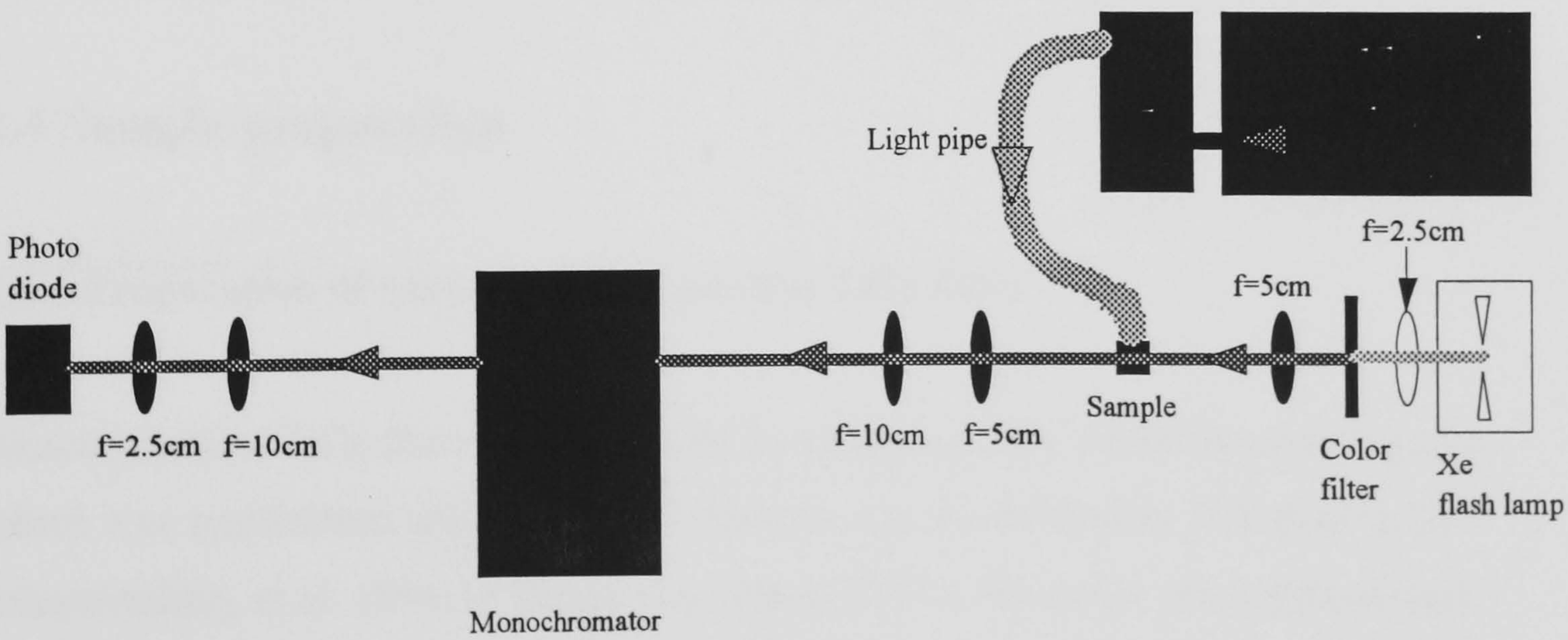



Figure 2.11. Schematic diagram of the nanosecond transient absorption spectrometer. An appropriate colour filter is used to block unnecessary frequency light incident to the sample.

Transient data were collected over the spectral range of 460~940 nm with a fast photodiode and a Gould 475 digital oscilloscope, and stored in a personal computer. Backgrounds of the data were subtracted by measuring either without the probe light or the excitation laser. The instrument response time of the apparatus was determined by monitoring the excitation laser scatter and is 4 ns FWHM. The absorption difference was calculated by equation 2.14 with $\alpha = 0.574$ in this apparatus.

The nanosecond transient emission spectroscopy was carried out with the same set-up as that of the nanosecond transient absorption apparatus, but without the probe light and the monochromator. In order to eliminate the laser scatter light, the photodiode was located at right angles with the excitation laser pulse and an appropriate colour filter was used. The emission wavelength was selected by a colour filter.

### 2.3.5 Monochromatic photocurrent measurement

The photocurrent of the solar cell employing the dye sensitised $TiO_2$ films was observed at a selected wavelength with a home-built potentiostat under the application of an external voltage. A tungsten lamp was used as a light source, and the wavelength was selected by a monochromator (Optometrics). The incident light power was calibrated by a silicon photodiode with a detection area of 1 $cm^2$ (Centronic).

## 2.4 Sample preparation

### 2.4.1 Preparation of nanocrystalline anatase $TiO_2$ films

Nanocrystalline $TiO_2$ films were prepared by spreading $TiO_2$ colloidal particle paste, which was synthesised with the sol-gel reaction, e.g. the method by O'Regan et al. (Nazeeruddin, et al. 1993, O' Regan and Grätzel 1991). The paste was prepared and gifted by Professor Michael Grätzel, EPFL, Lausanne, who allowed me to prepare nanocrystalline films here at Imperial College. The methods used to prepare nanocrystalline $TiO_2$ films have been described in detail in the literature (Hagfeldt and Grätzel 1995, Nazeeruddin, et al. 1993). In this section I will describe our method to

prepare the $TiO_2$ films, which I learned from Dr. Jacques Moser during my stay in EPFL, Lausanne in September, 1996.

***Preparation method of nanocrystalline $TiO_2$ films***

Anatase aqueous $TiO_2$ solution with a concentration of 12.2~12.5 % (average diameter: 15 nm) was prepared by Dr. Pascal Comte in EPFL, Lausanne. It was kept in the fridge until the nanocrystalline films were prepared, as the polymerisation in the $TiO_2$ gelation process is accelerated at room temperature (Livage, et al. 1988). The $TiO_2$ films were either prepared on 1 mm thick slide glasses (BDH) or 2 mm thick fluorine-doped tin dioxide ($SnO_2$) conducting glasses (Pilkington Libby Ford Owen) as follows:

1) Mix $TiO_2$ paste with carbowax (50 w% of $TiO_2$ itself excluding solvent weight) by stirring for 5 hours at room temperature. Note that this solution should not be stirred too fast otherwise there will be too many bubbles, resulting in inhomogeneous films. In addition, the length of the stirring time is also important to avoid the films cracking, e.g. an hour stirring made the films crack.

2) Clean the surface of the slide or conducting glass plate (usually 2.7 x 7.6 cm) with an appropriate solvent, e.g. methanol or ethanol. Note that there are a lot of alternative ways to clean glasses, however the above method is the easiest and quickest. Great attention should be paid to clean the conducting glass and not to scratch its surface.

3) Place this clean glass plate on a flat surface (e.g. on the large glass plate).

4) Cover both edges of the plate firmly with Scotch tape with a separation of approximately 15 mm. This film width was primarily determined by the area of the spinning cell window in the femtosecond transient absorption spectrometer. Note that a thickness of about 4 μm of the films will be obtained when one layer of the tape was placed. If n layers were placed, it will be about 4 μm multiplied by n. For all films used in my study, the thickness was confirmed to be 8.2±0.2 μm by Ms Carol Olson in Physics Department.

5) Introduce some amount (about 0.2 g) of the solution prepared in (1) on the untaped edge of the plate.

6) Slide a glass rod to spread the solution evenly over the film.

7) Remove the tapes

8) Leave the plate to dry in air in a clean area. Note that the $TiO_2$ films should become transparent when they are dry. It is critical not to fire the plate before the films become transparent (let it dry thoroughly), otherwise they will crack.

9) Heat the plates with an air heater at 450 °C for about 20 minutes. Note that great care should be taken not to exceed 500 °C. It is likely that conversion of the crystal phase of $TiO_2$ particles from anatase to rutile forms is accelerated above 500 °C (Finklea 1988).

10) Turn only the heat switch off and leave the fan on to cool down the plates gradually.

11) Cut the plate into pieces as required.

12) Keep the films in a dark and dry place.

The prepared film consists of nanometer sized $TiO_2$ particles sintered by the above described heat treatment to obtain electrical contact between the particles, resulting in a sponge-like structure. Electron micrographs of the film are presented in figure 2.12. The upper figure represents layers of the $TiO_2$ film and the substrate, whereas the lower figure exhibits a three-dimensional network of the interconnected $TiO_2$ particles, indicating the sponge-like film structure.

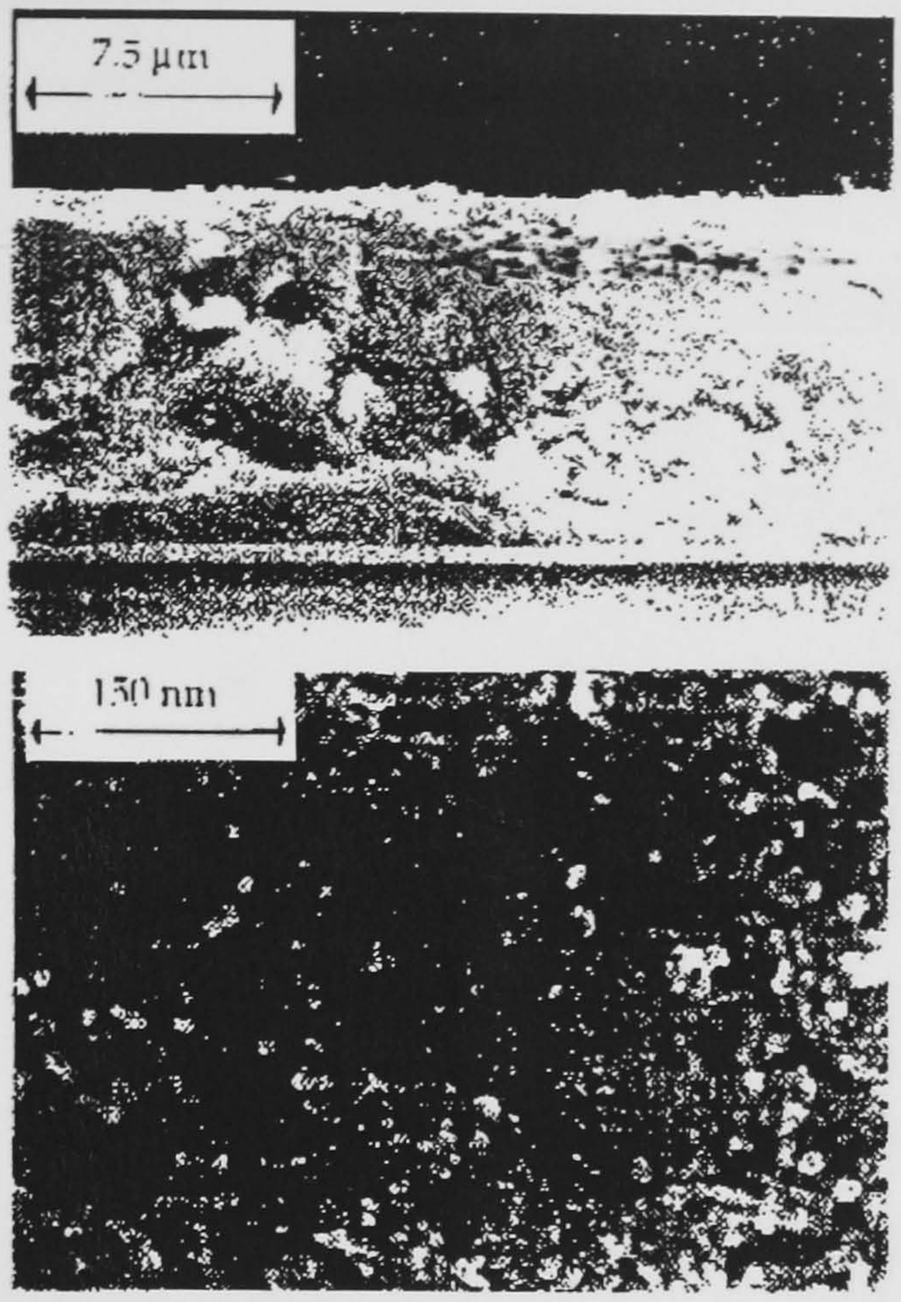



Figure 2.12. Scanning electron micrographs of the nanocrystalline $TiO_2$ film, taken from the recent report by Nazeeruddin et al. (Nazeeruddin, et al. 1993). The average particle diameter is approximately 15 nm (see the bottom picture).

### 2.4.2 Preparation of dye ethanol solution

Sensitiser dyes used for the experiment in this thesis were *cis*-Ruthenium$^{II}$(2,2'-bipyridyl-4,4'-dicarboxylate)$_2$(NCS)$_2$ (Ru(dcbpy)$_2$(NCS)$_2$), tetrabutyl ammonium salt of Ru(dcbpy)$_2$(NCS)$_2$ (N719), Zinc and free base tetracarboxyphenyl porphyrins (ZnTCPP and $H_2$TCPP, respectively). Figure 2.13 shows structures of Ru(dcbpy)$_2$(NCS)$_2$, ZnTCPP and $H_2$TCPP. Ru(dcbpy)$_2$(NCS)$_2$ and N719 were gifts from EPFL, Lausanne. ZnTCPP and $H_2$TCPP were purchased from Porphyrin Products Inc. and used without further purification. Ru(dcbpy)$_2$(NCS)$_2$ is approximately 96 % pure, estimated from the NMR and HPLC experiments in EPFL. The impurity of $H_2$TCPP was estimated to be 2~3 %. The major impurity of ZnTCPP (<5 %) appears to be $H_2$TCPP, which is the precursor of synthesised ZnTCPP, obtained by comparing steady state absorption spectra for those dyes (c.f. figures 5.16 and 5.21 in section 5) with literature data (Kalyanasundaram, et al. 1982, Pasternack, et al. 1972). For all dyes, only 2~3 % of

impure species were excited for the ultrafast measurement and its contribution to the transient absorption was confirmed to be negligible.

All of these dyes are water soluble, however ethanol was chosen to prepare the dye solution as below because the bond formation of water molecules onto the $TiO_2$ surface is competing with the dye sensitisation process, decreasing the surface coverage of dyes.

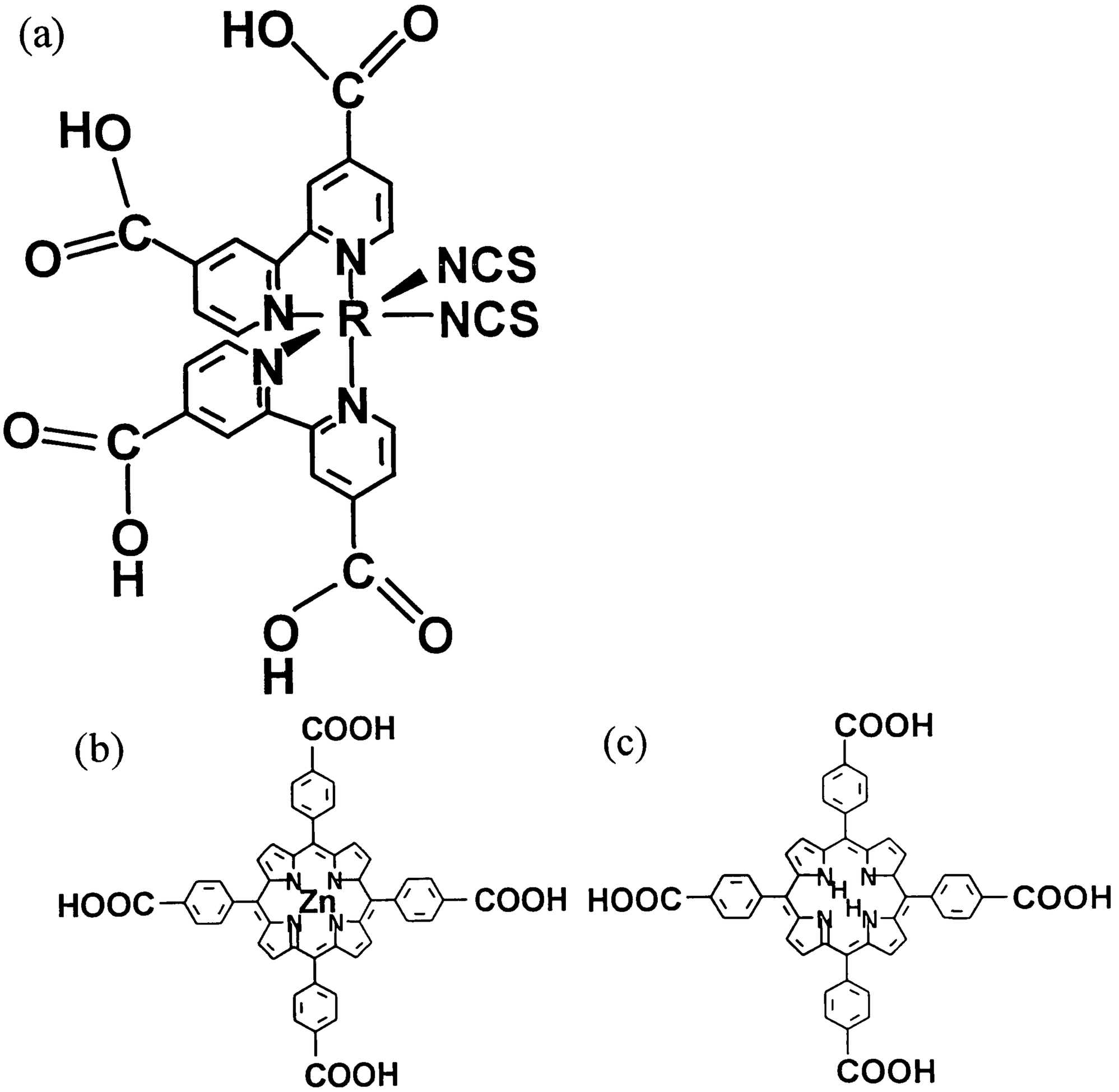



Figure 2.13. Structure of sensitiser dyes; (a) $Ru(dcbpy)_2(NCS)_2$, (b) ZnTCPP and (c) $H_2TCPP$.

• ***$Ru(dcbpy)_2(NCS)_2$ ethanol solution***

A proton concentration of $10^{-3}$ M in the dye solution was found to be the optimum concentration in order to sensitise dye molecules onto the semiconductor by the EPFL group (unpublished). First, a pH = 3 ethanol solution is prepared by adding concentrated hydrogen chloride (37 wt%) into ethanol (BDH 99.7% pure) and then $Ru(dcbpy)_2(NCS)_2$ was added to this solution in order to prepare the sensitisation solution ($1 \times 10^{-4}$ M). This solution was stored in a dark place and adequately diluted with the addition of ethanol for the sensitisation.

• ***N719 ethanol solution***

N719 was dissolved in pure ethanol ($2 \times 10^{-4}$ M) and stored in the dark. This solution was directly used to sensitise $TiO_2$ films in order to fabricate a sandwich type solar cell (see chapter 6).

• ***ZnTCPP or $H_2$TCPP ethanol solution***

Porphyrin dye was dissolved in pure ethanol ($2 \times 10^{-4}$ M) and stored in the dark. This solution was adequately diluted with the addition of ethanol for the sensitisation.

### 2.4.3 Sensitisation procedure

The sensitisation of nanocrystalline $TiO_2$ and $ZrO_2$ films by dyes was simply performed as described (Method A) in the literature (Nazeeruddin, et al. 1993). The $ZrO_2$ films were supplied from EPFL, Lausanne and have a thickness of about 8 μm. The $TiO_2$ films were prepared with the method described in the above section. The dye concentration and the sensitisation time were adjusted to yield optical densities of 0.1~0.3 at the excitation wavelength for all sensitiser dyes.

The following sensitisation procedure was employed, based upon the method described in the literature (Nazeeruddin, et al. 1993).

1) Prepare dye solution with the right concentration as described above.

2) Heat up a $TiO_2$ or $ZrO_2$ film with the air heater at 450 °C for 10 mins to remove water molecules on the surface of the films. This is because the presence of water decreases the photon to current conversion efficiency (Nazeeruddin, et al. 1993).

3) Turn only the heat switch off and leave the fan on. Note that it will cool down gradually as described above.

4) When the temperature shows 100 °C, take the film out and immediately dip it in the dye solution. Note that the film temperature is expected to be about 80 °C just before the plate is dipped. This procedure avoids the condensation of water from ambient air inside the film. Leave the glass plate in the position that the $TiO_2$ or $ZrO_2$ side faces down to the bottom of the bottle (If the semiconductor side is upward, dye molecules might precipitate onto the dye monolayer which has the ester linkage with the semiconductor).

5) Leave the plate in the dye solution bottle in dark at room temperature from 4 hours to overnight depending upon desired optical density of the sensitised film. It should be noted that there might be risk of dye aggregation if the film is left in the sensitisation bottle too long or if the absorbance of the sensitised film exceeds over 1 at 540 nm for $Ru(dcbpy)_2(NCS)_2$ (Personal communication by Dr. J. Moser).

6) After the sensitisation, take the plate out from the dye solution bottle and wash it with ethanol thoroughly.

7) Place appropriate solvent on the surface of the dye sensitised films and cover with a thin glass plate to avoid air contact. Note that it is of great importance to cover the surface of the dye sensitised films in the solvent to prevent dye degradation (see the section below). For example, the film is generally covered with ethylene carbonate / propylene carbonate (EC / PC = 1:1) solution and a thin cover glasses by capillary forces.

8) Store the films in a dark and dry place.
These covered dye sensitised films were readily used for the sub-picosecond pump-probe experiments, otherwise stored in the dark under anhydrous conditions.

Adsorption of all sensitiser dyes onto the $TiO_2$ surface was achieved via the carboxylate groups of the dye molecule. It has been suggested by infrared spectroscopic analysis for dye sensitised $TiO_2$ particles that sensitisation results from ester linkage of dye molecules onto the surface (Murakoshi, et al. 1995) or surface co-ordination of the carboxylate groups with oxo-bridging (Duffy, et al. 1997). Shklover et al. recently demonstrated that anchoring of $Ru(dcbpy)_2(NCS)_2$ on the $TiO_2$ surface by four bonds are thermodynamically the most favourable than the linkage with 1~3 bonds (Shklover, et al. 1998).

# Chapter 3: Fundamental concepts of electrochemistry and interfacial electron transfer

## 3.1 Introduction

This chapter aims to provide the background to the interpretation of experimental results. The photoelectrochemical experiments include the use of nanocrystalline semiconductor electrodes and the application of external voltages to the semiconductor electrode. The properties of the nanocrystalline semiconductor and the semiconductor / electrolyte interface, and the effect of the applied voltages are described in the first part of this chapter. The experimental results of the interfacial electron injection kinetics in the dye sensitised $TiO_2$ films are discussed with the electron transfer theory. The theory of the homogeneous reactions and their extension to heterogeneous reactions are described in the rest of the chapter.

## 3.2 Interfacial electrochemistry

### 3.2.1 Description of interfacial structure (Bockris, et al. 1993)

Electron transfer occurs at the electrode / electrolyte interface (double layer). As electroneutrality holds over the whole system; the number of excess charges on the metal side are balanced by an equal number of excess charges on the electrolyte side, the drop in potential between the metal and the electrolyte occurs dominantly at the interface. The first physical model of this interface was developed by Helmholtz, who assumed that the interface was like a parallel plate capacitor. The potential as a function of distance in this model is shown in figure 3.1a. The ions in the electrode as well as the electrolyte are imagined to be all in one plane. The thickness of this layer (Helmholtz layer) is typically 0.5~2 nm (Schmickler 1996). Gouy presented a subsequent model in 1910, in which the ions in the electrolyte are distributed over a larger region of the electrolyte (figure 3.1b). In 1924, Stern combined Helmholtz and Gouy theories and proposed a model as shown in figures 3.1c. Figure 3.2 represents an illustration of Stern model in which there are two parallel planes of ions, inner Helmholtz plane (IHP) and outer Helmholtz plane (OHP). Adsorbed anions and adsorbed organic molecules form

the IHP and solvated cations form the OHP. The cations which reach out further into the electrolyte forms the diffuse double layer or the Gouy layer.

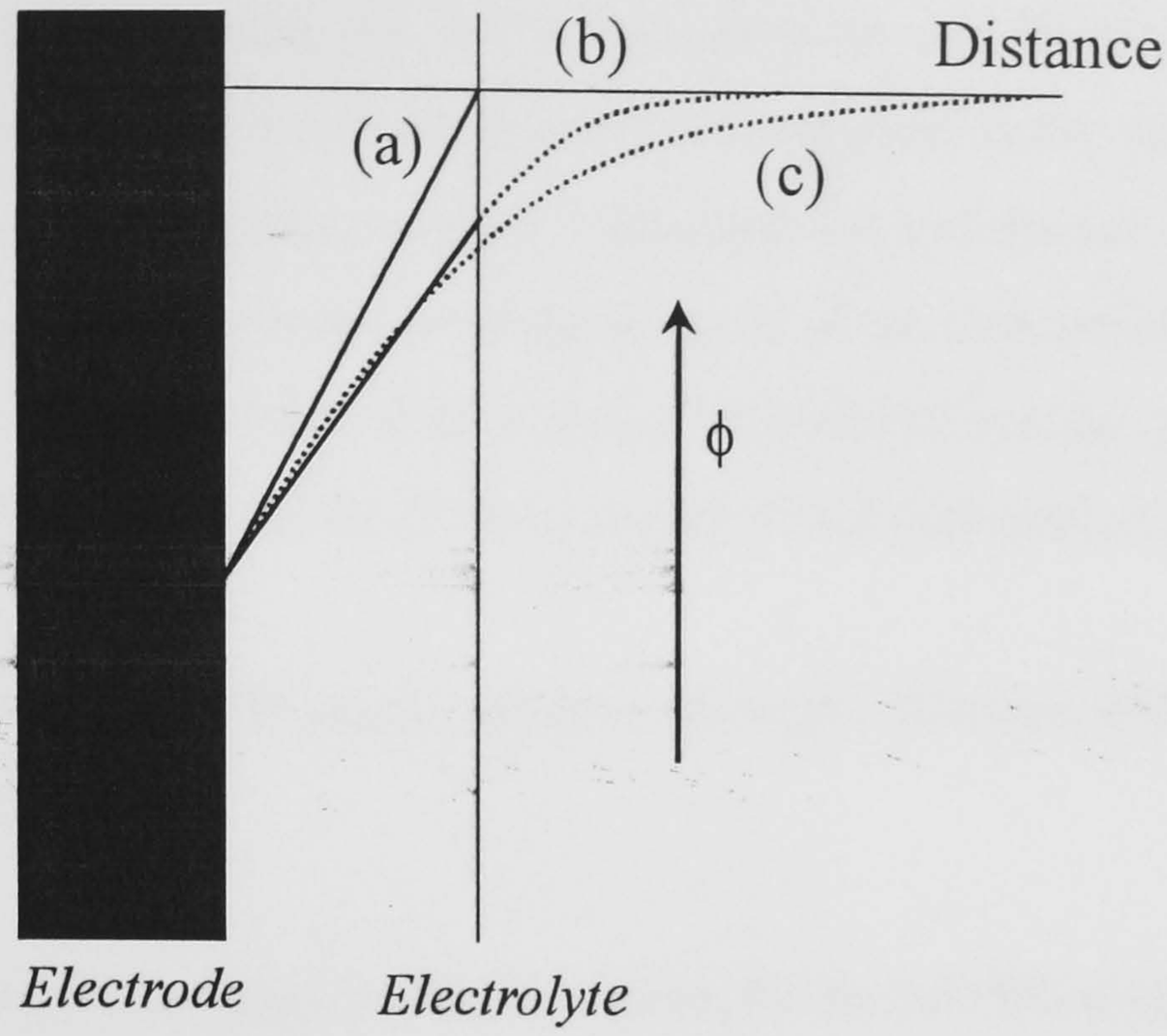



Figure 3.1. Potential profiles of the interface on the (a) Helmholtz, (b) diffuse layer and (c) Stern models.

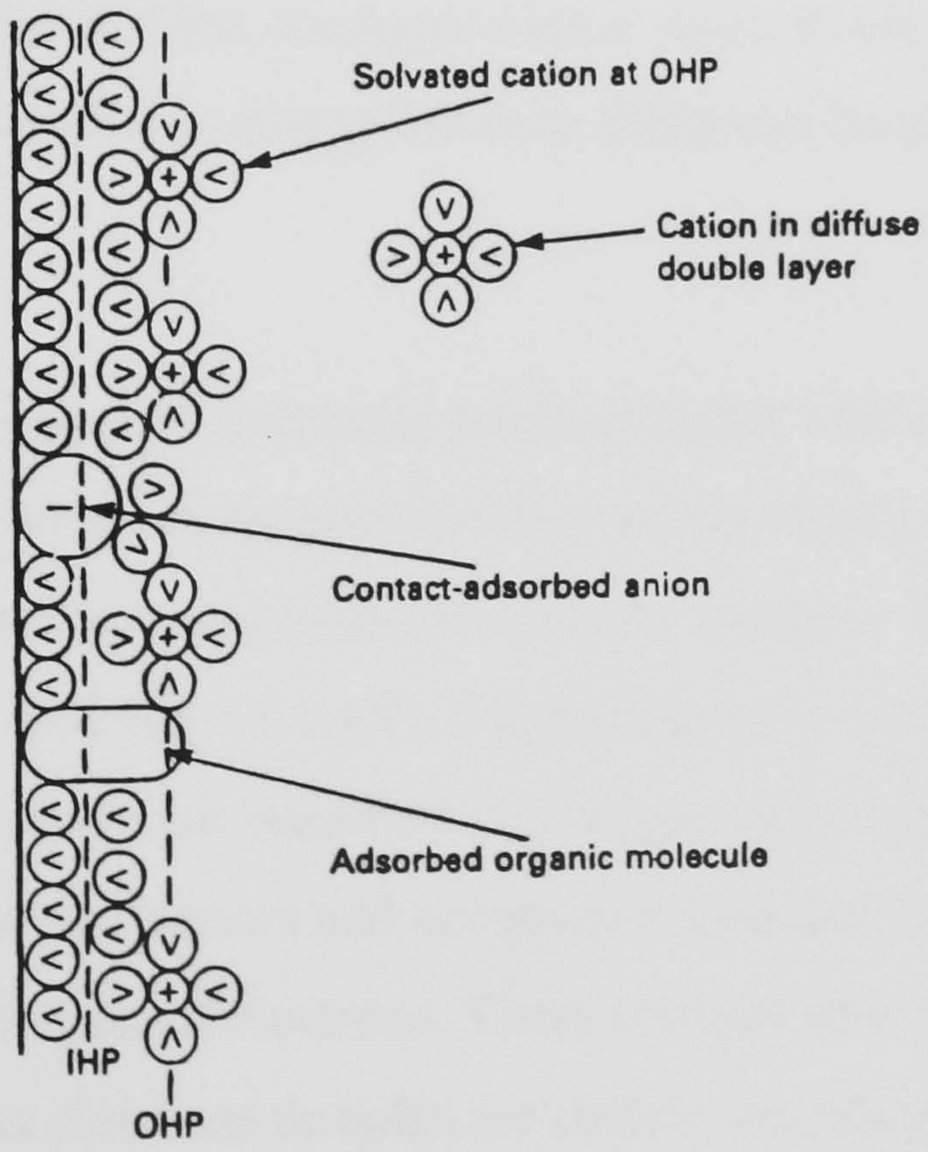



Figure 3.2. An example of the double layer structure in the electrode / electrolyte interface.

The contribution from the Helmholtz and the diffuse layers is normally dependent upon the total ionic concentration of the electrolyte. For example, Gouy (diffuse layer) model is applied only in dilute solutions. In the three electrode cell which is described in section 3.2.6, a typical electrolyte concentration employed in this study is 0.1 M. In such a high concentration, the potential drop across the interface is over an extremely short distance (~1 nm), comparable to the distance of the Helmholtz layer. The total charges are therefore cancelled almost within the Helmholtz layer, and the potential drop in the diffuse layer can therefore be neglected (Christensen, et al. 1994).

### 3.2.2. Energy bands of the semiconductor electrode (Finklea 1988, Miller, et al. 1995, Schmickler 1996)

In semiconductors, an energy level which exists for an individual atom of the lattice splits into a very large number of closely spaced energy levels. The ensemble of these energy levels is called an energy band. The energy spacing between adjacent energy levels is so small that energy bands are treated as a continuum of energy levels. The highest filled energy band and the lowest empty energy band in the semiconductor are called the valence band and the conduction band respectively, and they do not overlap (figure 3.3). The difference in energy between these two bands is called the energy gap or band gap ($E_g$).

The conductivity of a perfect (intrinsic) semiconductor with a large band gap is generally low, however it can be greatly enhanced by doping which is the introduction of impurities. The intrinsic semiconductors are for example $TiO_2$ ($E_g$ = 3.2 eV), SiC ($E_g$ = 2.6 to 3.1 eV) and ZnS ($E_g$ = 3.6 eV). Depending upon types of dopants; donors and acceptors, semiconductors are classified into n-type and p-type semiconductors, respectively. The electron donors and acceptors are neutral initially, and become charged due to loss or gain of electrons. These charged sites (dopants) are fixed in the lattice, and the excess electrons or holes are mobile, resulting in the conductivity of the semiconductor (Finklea 1988).

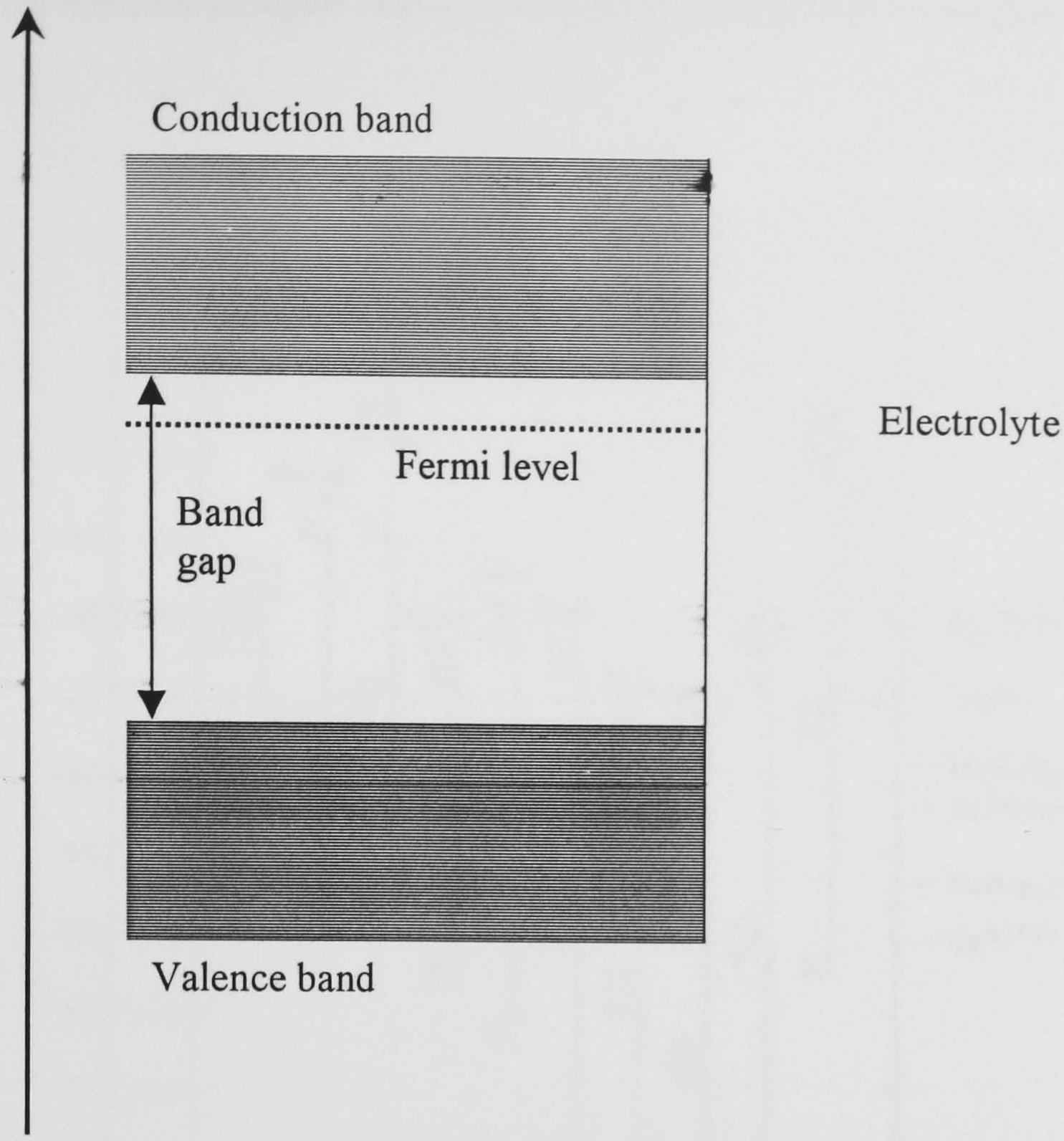



Figure 3.3. Energy band diagram of an n-type semiconductor. Fermi level is shifted towards the conduction band due to the presence of donors.

The dynamics of electrochemical and photoelectrochemical reactions in the semiconductor / electrolyte interface are largely dependent upon potential energies of the conduction and valence bands. The band gaps of different semiconductors in the bulk state are shown in figure 3.4 (Hagfeldt and Grätzel 1995). The data refer to conditions where the semiconductor is in contact with aqueous redox electrolytes of pH = 1 since the flat band potential is strongly dependent upon the pH of the electrolyte as is discussed in section 3.2.4. For interfacial electron transfer dynamics in the dye sensitised $TiO_2$ films, it is of great importance to know the potential energy level of the conduction band edge and Fermi level. The conduction band edge is interpreted as a state at the lowest potential energy level in the conduction band, and the Fermi level is interpreted as the energy level for which the occupational probability for an electron is 0.5. These potentials influence the electron transfer kinetics between the dye excited

state and the electron acceptor states in the conduction band (see electron transfer theory below).

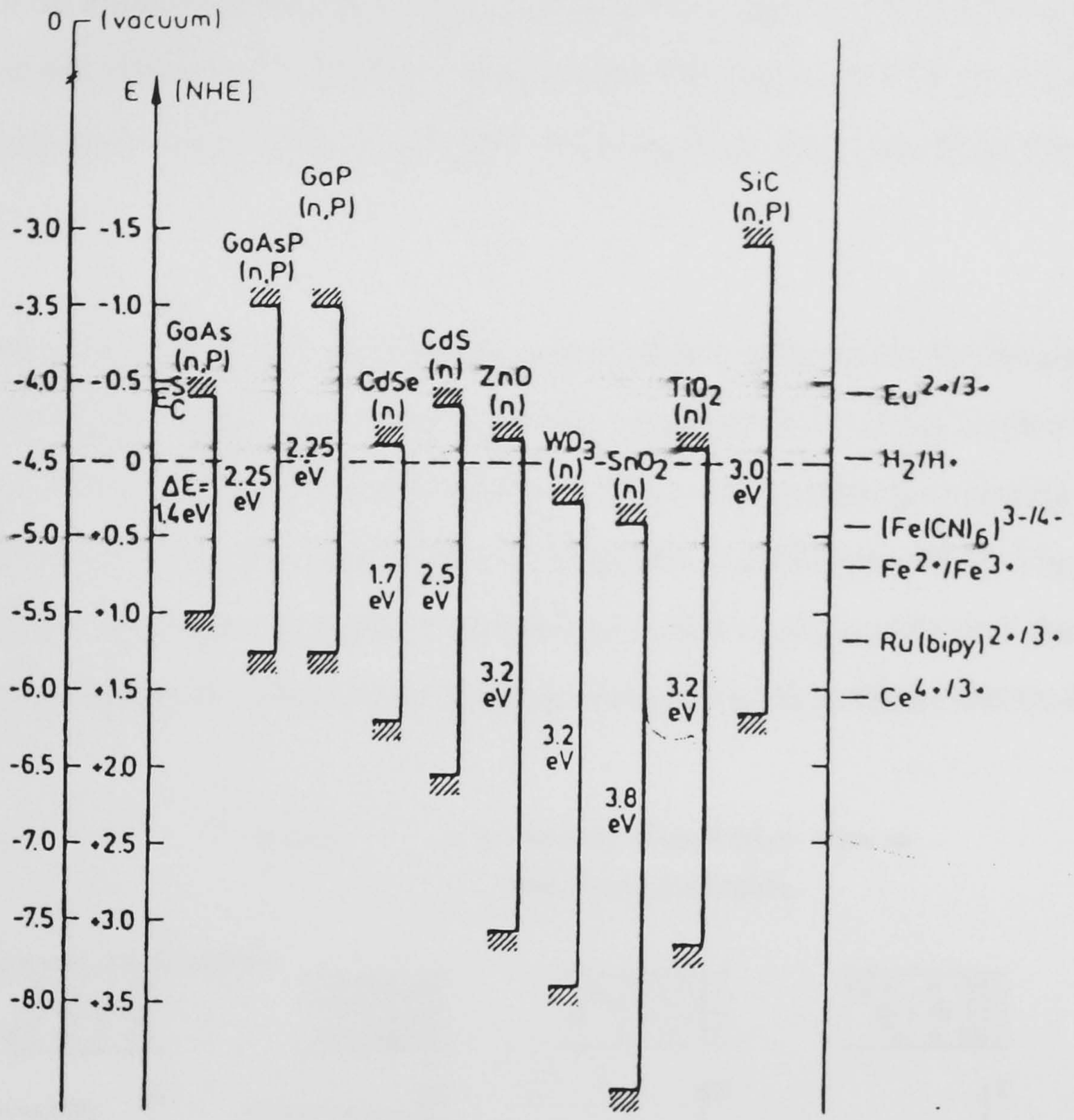



Figure 3.4. Potentials of band edges and band gaps for a series of bulk semiconductors in an aqueous electrolyte at pH = 1.

### 3.2.3 Potential profile and band bending of the semiconductor (Finklea 1988, Gerischer 1990, Schmickler 1996)

When a bulk semiconductor electrode is brought into an electrolyte solution containing redox active species, the difference in the Fermi levels of the two phases leads to electron transfer reactions between the electrode and the electrolyte. Since a semiconductor has relatively low conductivity compared with the metal, a double layer extends inside the semiconductor from its surface, i.e. the electrical potential varies from the surface to the bulk, which is called a space charge layer. As the two phases

reach equilibrium, the Fermi level finds a single energy level throughout the system as discussed above. This causes the conduction and valence bands to bend in the space charge region either positively (upwards) or negatively (downwards). Such a band bending can be modulated by application of external voltages to the electrode. It should be noted that the charge transfer takes place only in the presence of an electroactive species acting as electron donor or acceptor, assuming that there is no impurity in the electrolyte.

Here the band bending is considered for an n-type semiconductor under the application of external voltages. In the n-type semiconductor, the majority carriers are electrons and the minority carriers, holes. The band bending of this semiconductor is classified into four typical situations as shown in figure 3.5 (Hagfeldt and Grätzel 1995). The upper part of the figure represents the charge distribution at the interface whereas the lower indicates the potential as a function of distance from the surface of the electrode.

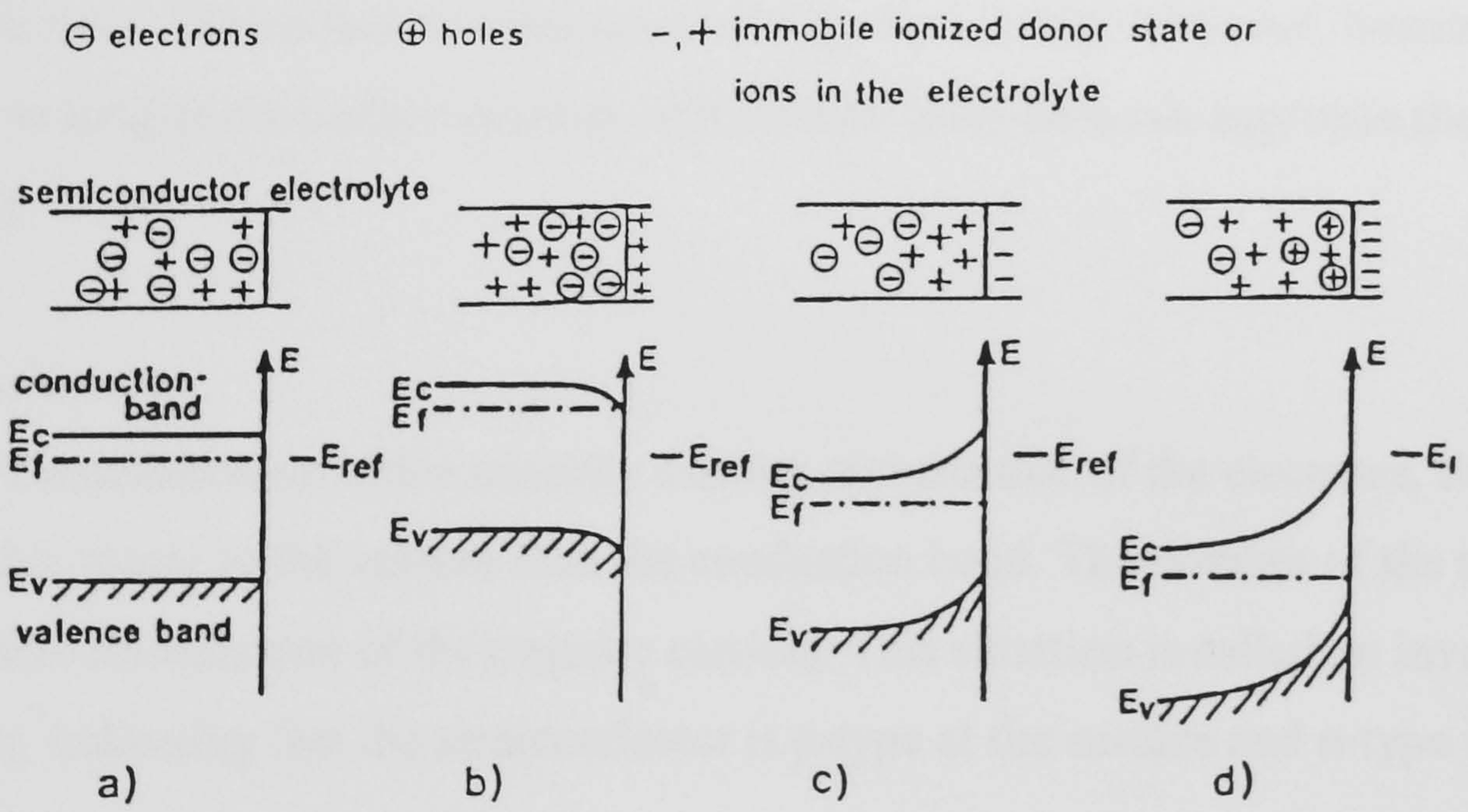



Figure 3.5. Band structures of an n-type semiconductor in contact with an electrolyte: (a) flat band, (b) accumulation, (c) depletion and (d) inversion modes. The upper part shows the distribution of charge carriers, and the lower a potential profile of the space charge layer.

(a) Flat band.

No excess of the majority carriers, that is, the positive charge of the immobile donor states is compensated by the negative charge of the mobile electrons in the

semiconductor. The bands are flat (no space charge layer). The Fermi level in this situation is called a flat band potential.

(b) Accumulation.

The conduction and valence bands bend upward from the surface of the semiconductor. The surface region has negative excess charges of the majority carriers (electrons) which accumulate near the interface and a decrease of minority carriers (holes) because electrons flow towards the electrode surface. These negative charges are compensated by positively charged ions at the interface.

(c) Depletion.

The minority carrier is increased at the interface since electrons are removed from the surface, resulting in the bending of the band downward from the interface known as the depletion mode. In this situation the positive excess charges of immobile donors are compensated by negative counter charges (ions) at the interface in the electrolyte. The surface concentration of minority carriers, however, remains very low as long as the surface position of the Fermi level does not approach the valence band.

(d) Inversion.

If the concentration of the minority carriers exceeds that of the electrons, the Fermi level is closer to the valence than the conduction band. The number of the minority carriers exceeds that of the majority carriers. This situation is called an inversion layer, indicating that the semiconductor is p-type at the surface and n-type in the bulk.

### 3.2.4 Surface states (Bockris and Khan 1993, Christensen and Hamnett 1994, Finklea 1988)

The semiconductor surface may have quantum states which differ from those of the bulk and are therefore called "surface states". They may play important roles for the surface electron transfer reactions when they are located energetically in the intra-band region. The surface states are formed from the surface termination of the crystal lattice or from the adsorption of the species onto the surface. When the semiconductor is

terminated on the surface, the surface atoms are missing at least one neighbour and the associated bond is left "dangling". The dangling bond may have a chemical reaction with the species in the electrolyte, resulting in a newly formed surface structure such as a surface oxide. The potentials of the surface states have not been well defined since heterogeneity of the surface or interaction with solvent dipoles might spread out the surface state energies.

The metal oxide semiconductors interact with $H^+$ and $OH^-$ ions as shown in equation 3.1 (Bolts, et al. 1976, Gerischer 1970). It has been reported that for many oxide semiconductors the flat-band potential varies with pH following a simple Nernstian formula as shown in equation 3.2.

$$MOH_2^+ \leftrightarrow MOH + H^+ \leftrightarrow MO^- + 2H^+ \qquad \text{Equation 3.1}$$

$$E = E^\circ + \frac{RT}{nF} \ln\left(\frac{a_R}{a_P}\right) \qquad \text{Equation 3.2}$$

where $E^\circ$ is the standard potential; "a" is an activity of species; R is the reactant and P is the product. The change in pH of the electrolyte results in change in the activities of protonated or deprotonated species. Figure 3.6 represents flat band potentials as a function of pH for different metal oxides (Bolts and Wrighton 1976). The solid straight lines indicate a slope of 0.059 V/pH. Gerischer interpreted this gradient as a result of the protonation / deprotonation equilibrium of the electrode surface as shown in equation 3.1 (Gerischer 1970). The surface gains protons in an acidic solution or loses protons in a base solution, resulting in positively or negatively charged surface. The equilibrium of these reactions depends on the pH of the solution since the amount of titanium at the surface is fixed. It should be noted that the redox potential of the proton donating and accepting electrolyte is also dependent upon the pH with the same gradient (59 mV), following the Nernst equation (equation 3.2). Therefore, the difference in the flat band potential and the redox potential ($H^-/H$) of the electrolyte is always the same.

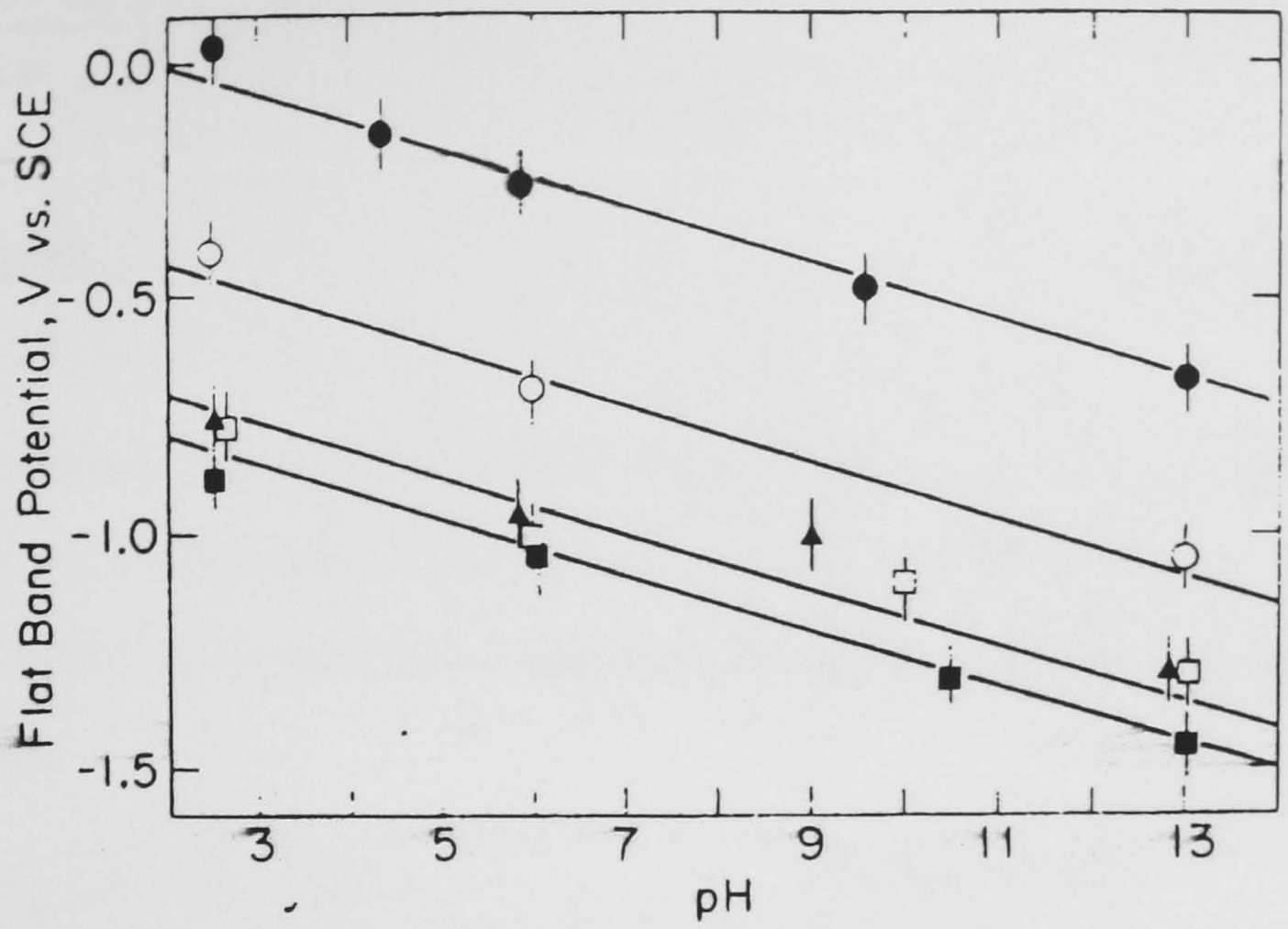



Figure 3.6. Flat band potentials as a function of the pH in the electrolyte for $SnO_2$ (●); $TiO_2$ (○); $KTaO_3$ (▲); $KTa_{0.77}Nb_{0.23}O_3$ (□); and $SrTiO_3$ (■) semiconductors.

### 3.2.5 Nanocrystalline $TiO_2$ films

Colloidal semiconductor particles have a different potential profile from bulk semiconductors because of their increased surface area and small particle size. Detailed studies have been carried out by Hagfeldt, Grätzel, Rothenberger and co-workers (Hagfeldt and Grätzel 1995, Rothenberger, et al. 1992) to describe the density of delocalised states of the conduction band and surface states in the nanocrystalline $TiO_2$ films.

**1) Potential of the band**

For a colloidal semiconductor with a small particle diameter, the band bending is different compared to that for the bulk semiconductors. The potential-distance relationship of the space charge layer in a bulk semiconductor or a small spherical semiconductor particle is shown in figure 3.7 (Hagfeldt and Grätzel 1995). The potential drop, $\Delta\phi$, between the centre ($r = 0$) and a distance r can be calculated using the following equation 3.3 (Hagfeldt and Grätzel 1995).

$$\Delta\phi = \frac{kT}{6e}\left(\frac{r - (r_0 - W)}{L_D}\right)^2\left(1 + \frac{2(r_0 - W)}{r}\right) \qquad \text{Equation 3.3}$$

$$L_D = (\varepsilon_0 \varepsilon kT/2e^2 N_D)^{0.5} \qquad \text{Equation 3.4}$$

$L_D$ is the Debye length, $N_D$ is the number of the ionised dopant molecules per cubic centimetre, $\varepsilon_0$ is the permittivity of the vacuum, $\varepsilon$ is the relative dielectric constant of the $TiO_2$, $r_0$ is the radius of the particle and W is the width of the space charge layer or the band bending.

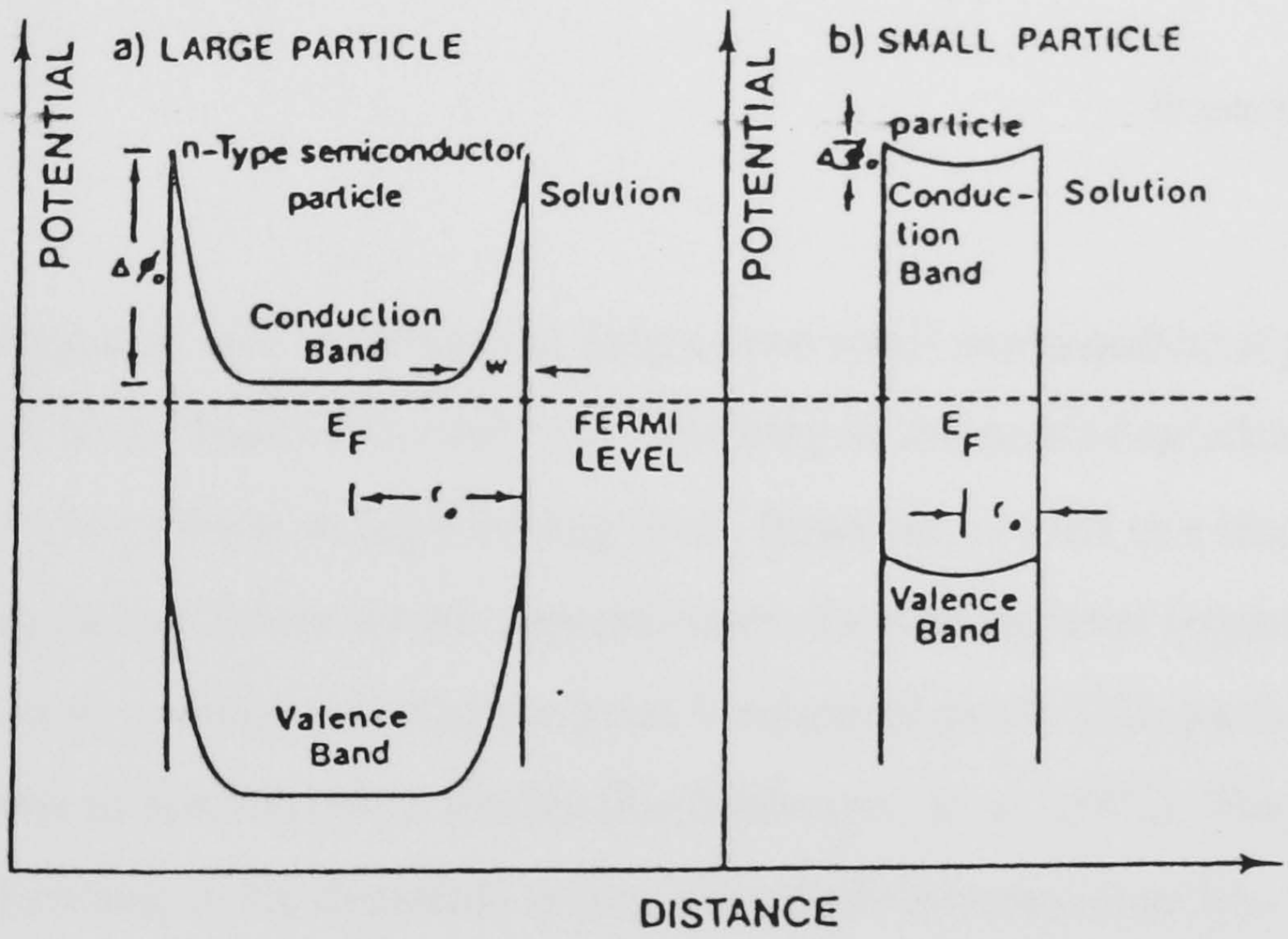



Figure 3.7. Potentials of the space charge layer in a large (bulk) and a small semiconductor particle in contact with the redox active electrolyte. The Fermi level ($E_F$) of the semiconductor is equal to the redox potential of the electrolyte. The potential drop ($\Delta\phi_0$) from the surface to the centre is considerably diminished in the case of the small particle.

For large semiconductor particles ($r_0 >> W$) or a planar semiconductor electrode, this equation can be approximated to the equation 3.5.

$$\Delta\phi_0 \approx \frac{kT}{2e}\left(\frac{W}{L_D}\right)^2$$ Equation 3.5

This equation indicates that the width of the space charge region, W, increases as a large positive external potential is applied to the semiconductor electrode as shown in figure 3.7.

For very small semiconductor particles ($r_0 << W$), the potential drop within the semiconductor is approximated into equation 3.6.

$$\Delta\phi_0 \approx \frac{kT}{6e}\left(\frac{r_0}{L_D}\right)^2$$ Equation 3.6

It is therefore apparent that the potential drop of the small semiconductor particle is small compared to the bulk semiconductor, resulting in the small depletion band bending within the particle. A high doping level, however, results in a high potential difference because the Debye length depends upon the doping level (equation 3.4). Rothenberger et al. investigated that the band bending of small $TiO_2$ particles in depletion as well as accumulation modes (Rothenberger, et al. 1992). They concluded that the band bending in the depletion mode was small whereas there was sharp band bending in the accumulation mode. Figure 3.8 shows this asymmetric profile. It should be noted that all of the above models are used on the assumption that the doping density is uniform from the centre to the surface of the $TiO_2$ particle. Goossens has demonstrated in his recent report (Goossens 1996) that semiconductor nano-particles may have non-uniform doping profiles due to highly enhanced surface area and therefore to increased density of surface defect states, resulting in larger potential drops (e.g. 0.1 V drop for 20 nm diameter particles).

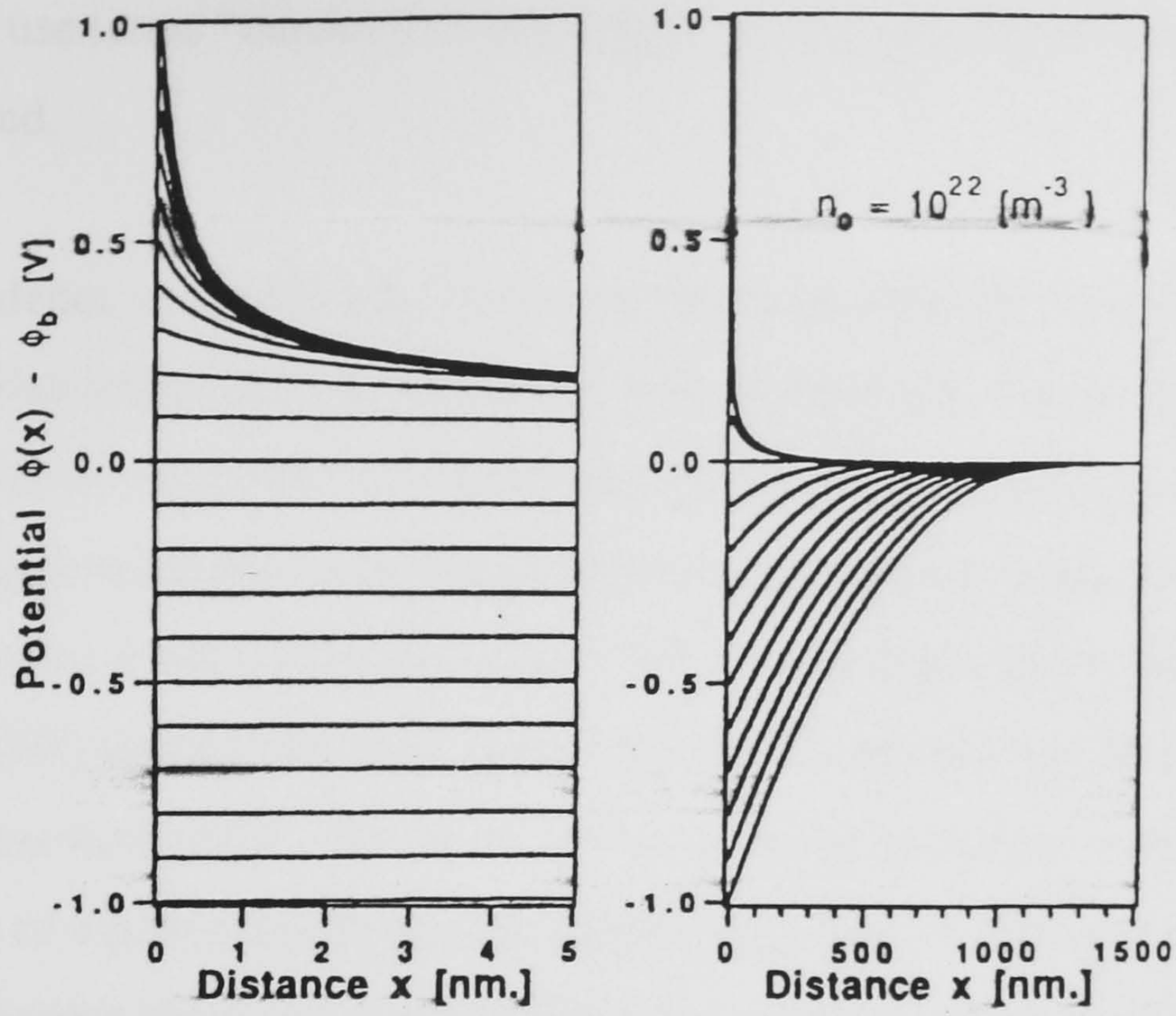



Figure 3.8. Potential profile presenting the band bending in depletion and accumulation modes for small $TiO_2$ particle (average diameter: 15 nm), taken from Rothenberger et al. (Rothenberger, et al. 1992). The difference between the local potential, $\phi(x)$, and the bulk potential, $\phi_b$ is plotted as a function of distance, x, from the semiconductor / electrolyte interface. The positive value indicates the accumulation mode while the negative value the depletion mode.

**2) Surface states**

There may exist surface, defect or trap states in the band gap of $TiO_2$. Such surface states may play more important roles in nanocrystalline $TiO_2$ colloids since the surface area is remarkably enhanced. The observation of trapped electrons in the surface states has been intensively studied by many groups (Hagfeldt and Grätzel 1995, Howe, et al. 1985, Nakato, et al. 1983). For example it has been suggested that surface states at about 1.3~1.5 eV below the conduction band edge originates probably from Ti-OH species (Sakamaki, et al. 1990). There may also be surface states just below the conduction band. Recently, Rothenberger et al. reported (Rothenberger, et al. 1992) that the conduction band has a tail of electron acceptor states towards the positive potential according to their photoelectrochemical measurement of the nanocrystalline $TiO_2$ electrodes, and the model which fits such a potential tail requires the presence of the surface states under the conduction band. These observations suggest that it is not

appropriate to use terms "conduction band edge" to describe the bottom of the conduction band.

The pH dependence of the flat band potential for nanocrystalline $TiO_2$ films also follows Nernstian behaviour (see above for bulk metal oxide semiconductors) as shown in figure 3.9. Moreover it has been found that the flat band potential is directly related to the proton generating ability of the solvent when the measurement is carried out in non-aqueous electrolytes (Redmond, et al. 1993). It has been reported (Redmond and Fitzmaurice 1993) that the flat band potential is also controlled by the potential determining ions such as $Li^+$, $Na^+$ and $Mg^{2+}$ in nonaqueous aprotic solvents, i.e. solvents in the absence of a proton adsorption-desorption equilibrium. However this dependence cannot be accounted for by the Nernst behaviour as discussed above (Lindström, et al. 1997, Redmond and Fitzmaurice 1993). The mechanism of the potential dependence upon $Li^+$ concentration has not been unambiguously established.

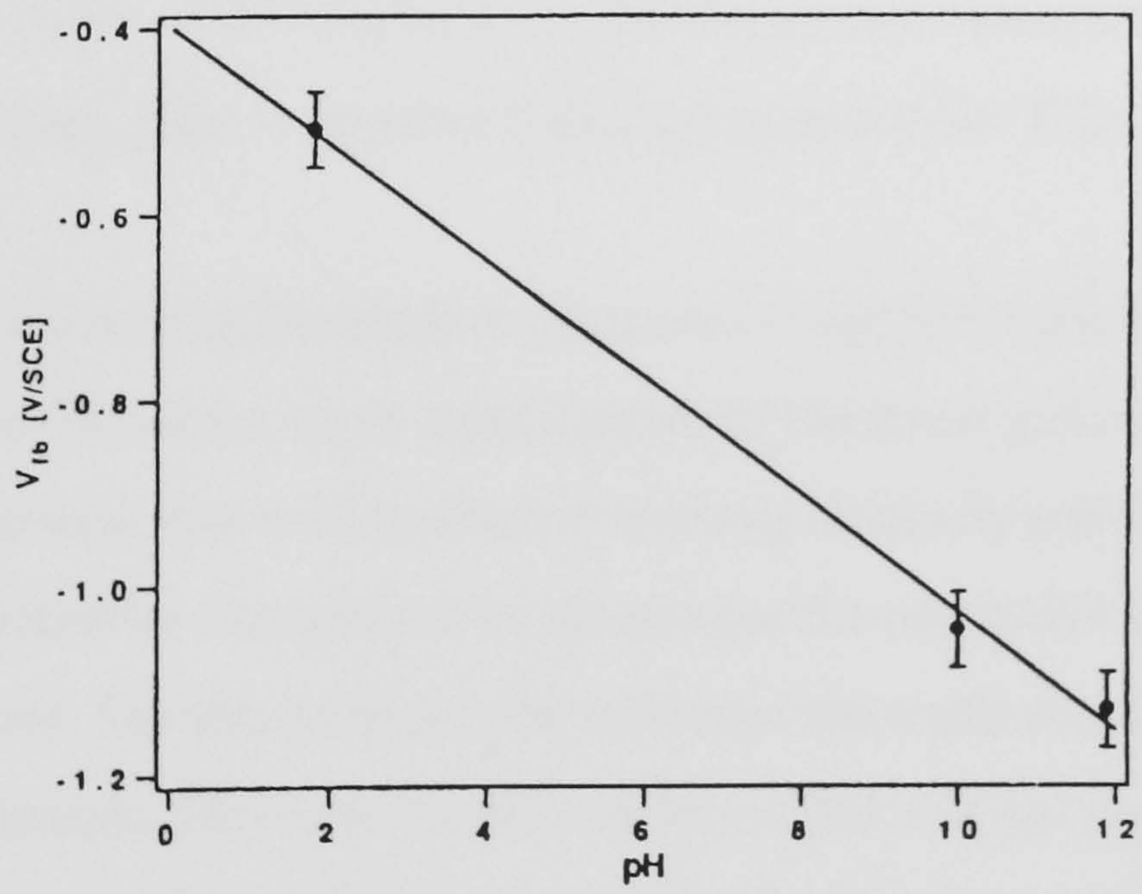



Figure 3.9. Dependence of the flat band potential on pH in the aqueous solution for a nanocrystalline $TiO_2$ electrode.

### 3.2.6 Three electrode cell configuration (Finklea 1988, Schmickler 1996)

3.2.6.1 Configuration

The investigation of the electron transfer kinetics under the application of an external voltage to the semiconductor electrode (working electrode) requires at least two electrodes to pass a current through the system. Moreover another electrode (reference electrode) and a potentiostat are needed in order to determine the potential of the working electrode, since the potential of the reference electrode must remain constant; no current should flow through it. Therefore it is common to use a three-electrode cell, consisting of the working, counter and reference electrodes. The photograph of the cell, which was used for the photoelectrochemical experiments in this thesis, is shown in figure 3.10. The cell is especially designed to carry out femtosecond transient absorption spectroscopy under the application of the external voltages into the dye sensitised nanocrystalline $TiO_2$ electrode as the electrode is transparent when the transparent conducting glass is employed as a substrate for the $TiO_2$ working electrode.

The potential of the working electrode is measured or applied with respect to that of the reference electrode. However, there exist a series of electrical potential changes (ohmic potential drops) between the semiconductor working electrode and the reference electrode. These potential changes are localised near the respective interfaces, and should be minimised. For this purpose, the reference electrode should usually be close to the working electrode. However it has been found that it is not practical to place the reference electrode near the working electrode for the femtosecond transient absorption spectroscopy. A highly concentrated supporting electrolyte (0.1 M) was therefore used to minimize the potential drop in the electrolyte. In such a high concentrated electrolyte, the potential drop due to mass (ion) transport is negligible since there is practically no concentration gradient between the working and the reference electrodes. Note that the electrolyte is a substance that dissolves in a solvent to produce a conducting solution of ions. Sometimes the solution as a whole is termed "electrolyte". In terms of the reference electrode / electrolyte interface, the potential drop between the metal of the reference electrode and the bulk of the electrolyte is negligible provided that the appropriate reference electrode is chosen and very low current flows through the

reference electrode. The potential drop should therefore be only observed at the working electrode / electrolyte interface.

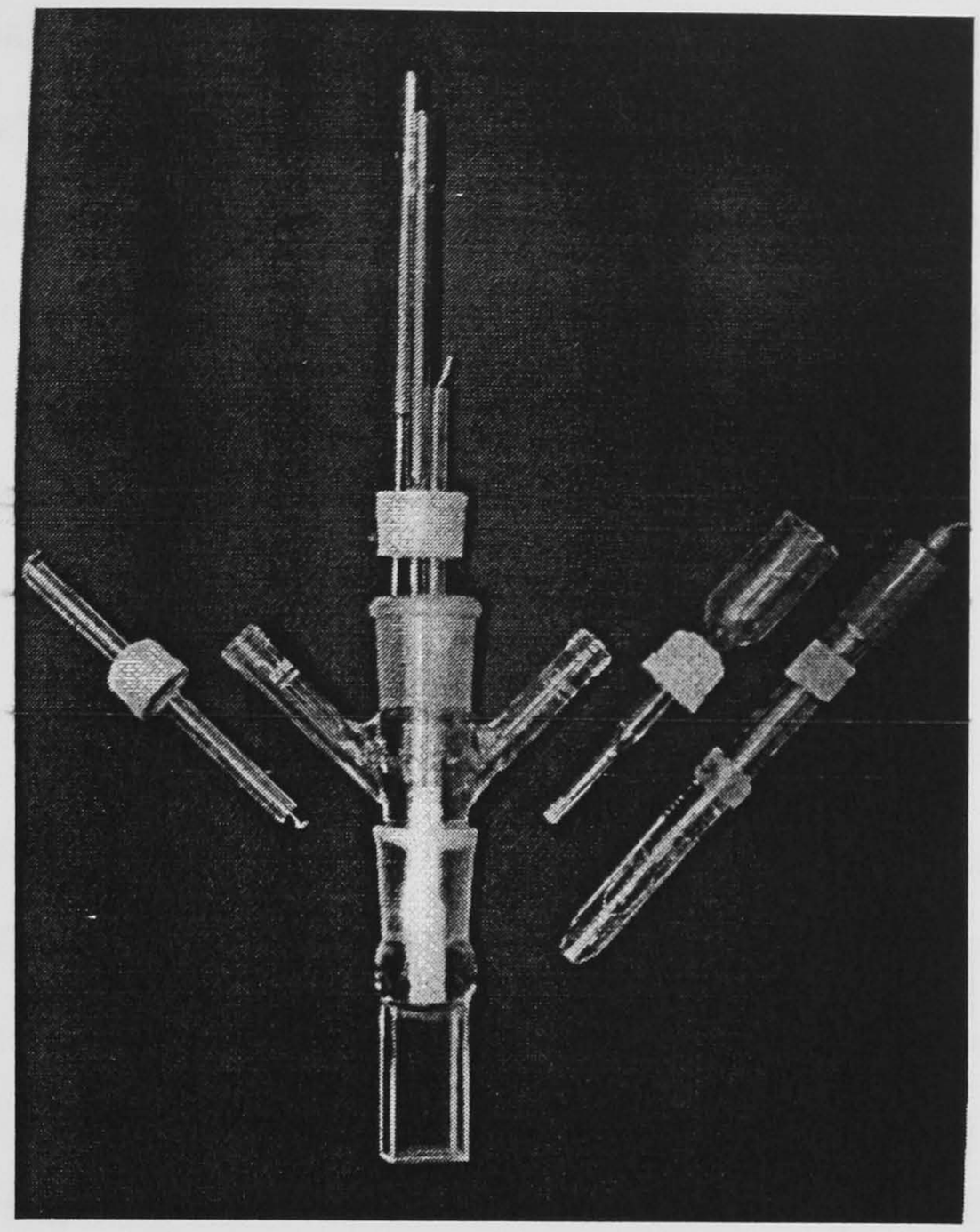


Figure 3.10. The photograph of the three-electrode cell. The bottom of the cell is especially designed for optical experiments. The middle electrode is the working electrode made of a platinum wire supported by a glass rod. The conducting glass with the dye sensitised $TiO_2$ film is held by tetrafluoro carbon material, so that connection is made between the wire and the conducting glass. The left-hand side electrode is the counter electrode made of a platinum wire. The right hand side electrode is the Ag/AgCl reference electrode connected to the main cell by a salt bridge.

3.2.6.2 Application of the external bias (Finklea 1988)

The potential of the working electrode is controlled by the potentiostat which consistently maintains its potential against the reference electrode even though chemical reactions proceed on the working electrode or in the electrolyte upon the application of the voltage. The applied potential controls the Fermi level of nanocrystalline $TiO_2$ films when the films are on the working electrode.

In the three-electrode cell in the absence of voltage application, the Fermi levels of the working electrode and of the redox active electrolyte are equal as a result of the equilibrium. This particular equilibrium (potential: $\phi_0$) can be disturbed by the application of an external electrode potential; $\phi \neq \phi_0$, which alters the Fermi level energy of the working electrode by an amount $-e\eta$, where $\eta = \phi - \phi_0$ is called the overpotential. In other words the application of an overpotential leads to a difference - $e\eta$ in the Fermi levels of the working electrode and the electrolyte. The value of the overpotential is equivalent to the applied bias against the potential of the Ag/AgCl reference electrode in the femtosecond transient absorption spectroscopy discussed in chapter 5.

It is of great importance to estimate the Fermi level of the $TiO_2$ films and the redox potential of the sensitiser dye in order to study interfacial electron transfer kinetics in dye sensitised $TiO_2$ films. The Fermi level of the $TiO_2$ films can be determined if the redox potential of the electrolyte is known or when the known external voltage is applied against the reference electrode. The oxidation redox potential of the dye ground state is generally determined by the cyclic voltammogram of a dye solution. The oxidation redox potential of the lowest excited state is estimated from the ground state potential, and the absorption and emission spectra of the dye. The relative difference in these two (sensitiser dye and $TiO_2$) potentials, which is the driving force of interfacial electron transfer, can therefore be estimated. It should be noted that the redox potential of the dye might change when it is adsorbed onto the $TiO_2$ surface (Zaban, et al. 1998, Zaban, et al. 1997). This is the subject of controversy between different groups (Yan, et al. 1997). As discussed earlier, it is likely that the potential drop of the electrode / electrolyte interface is almost complete within the Helmholtz layer, which is approximately 1 nm width with the concentrated supporting electrolyte (0.1 M). Such a potential drop, which is in part controlled by the applied bias, may influence the redox potential of the adsorbed dye since the distance between a centre of the dye molecule and the surface of $TiO_2$ is likely to be <1 nm (Shklover, et al. 1998). However the degree of influence is probably dependent upon heterogeneity of the $TiO_2$ surface and the anchoring structure of the dye.

## 3.3 Theoretical treatment of electron transfer

### 3.3.1 Introduction

Homogeneous electron transfer describes the exchange of electrons between two discrete molecular states, typically in the solution (Marcus 1965, Miller, et al. 1995). The theory of homogeneous reactions has been intensively developed by a number of groups (Devault 1980, Jortner 1980, Marcus, et al. 1985, Miller, et al. 1995, Moser, et al. 1992). In particular, the classical expression for the outer sphere electron transfer reactions in solution has been developed primarily by Dr. R. A. Marcus (Marcus and Sutin 1985), and the validity of his detailed predictions has been examined and confirmed by a number of experimental results (Closs, et al. 1988, Marcus and Sutin 1985, Moser, et al. 1992).

In contrast, heterogeneous electron transfer involves the reaction between a discrete molecular state and highly delocalised electronic states with continuous potential energy levels (Lanzafame, et al. 1994, Miller, et al. 1995). Typical examples of this class of reaction are electrode electron transfer reactions. For the electron transfer reactions at the electrode / electrolyte interface, there are additional complexities to allow for such as effect of adsorbed molecules, interaction between adsorbed molecules and the large number of available electronic states.

The electronic levels of the conduction band of semiconductors are described as highly delocalised states. Interfacial electron injection requires the coupling of these delocalised states to discrete molecular states. In order to understand some of the concepts of electron transfer at surfaces, it is useful to employ the simplified homogeneous electron transfer theory and then expand its theory to a band of delocalised electronic states connected to the molecular donor states. For the above reason, this section is divided into two parts: homogeneous electron transfer theory (section 3.3.2), and extension of the homogeneous electron transfer theory to the case for electron injection reactions in dye sensitised semiconductors (section 3.3.3).

### 3.3.2 Homogeneous electron transfer

In order to simplify the theoretical treatment, the electron transfer reactions concerned here are limited to "outer-sphere electron transfer reactions", i.e. the two reactants do not share a common atom or group. More generally, for these reactions, the interaction of the relevant electronic orbitals of the two centres is weak and so the reactions do not involve the formation or breaking of covalent bonds. An example of an outer-sphere electron transfer reaction is shown in equation 3.7.

$$[Fe^{II}(H_2O)_5X]^{2+} + [Cr^{II}(H_2O)_6]^{2+} \rightarrow [Cr^{III}(H_2O)_6]^{3+} + [Fe^{I}(H_2O)_5X]^{+}$$

Equation 3.7

Here the outer-sphere electron transfer is classified into two categories depending upon the degree of the interaction between donor and acceptor states (electronic coupling); non-adiabatic for weak electronic coupling and adiabatic for strong coupling (see the following section for the details of non-adiabatic and adiabatic limits).

#### 3.3.2.1 Non-adiabatic electron transfer

Homogeneous electron transfer reactions are considered as resonant electron tunnelling between two square well potentials of electron donor and acceptor states. This situation is illustrated in figure 3.11 (Miller, et al. 1995). An electron is initially localised in one well (donor). When the system is at resonance, the electron oscillates back and forth between donor and acceptor wells, and thus the probability of finding an electron in two wells is ½ each. As the system fluctuates by the nuclear motion, the relative energy levels of the two wells change and the electronic coupling is decreased by the energy mismatch. The probability of finding the electron increases on the lower site (acceptor well) in the system, and finally the electron becomes localised in this well.

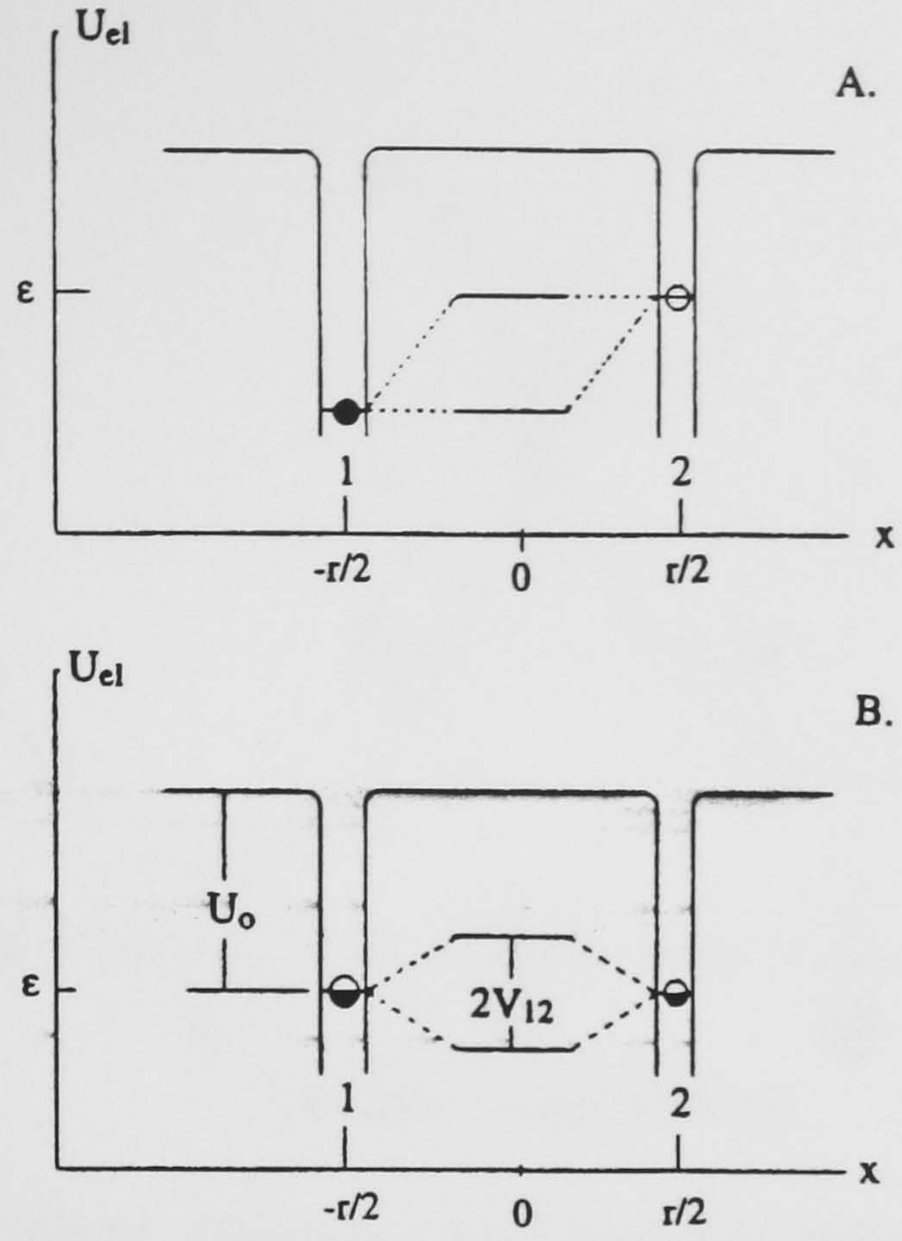



Figure 3.11. Electronic potential energy diagram for discrete donor and acceptor states as square wells. The electron is initially localised at the donor site (A). The displacement toward resonance (B) is derived from modulation of the energy levels by the coupling of two electronic levels. After completion of the electron transfer, the electron is localised on the acceptor site.

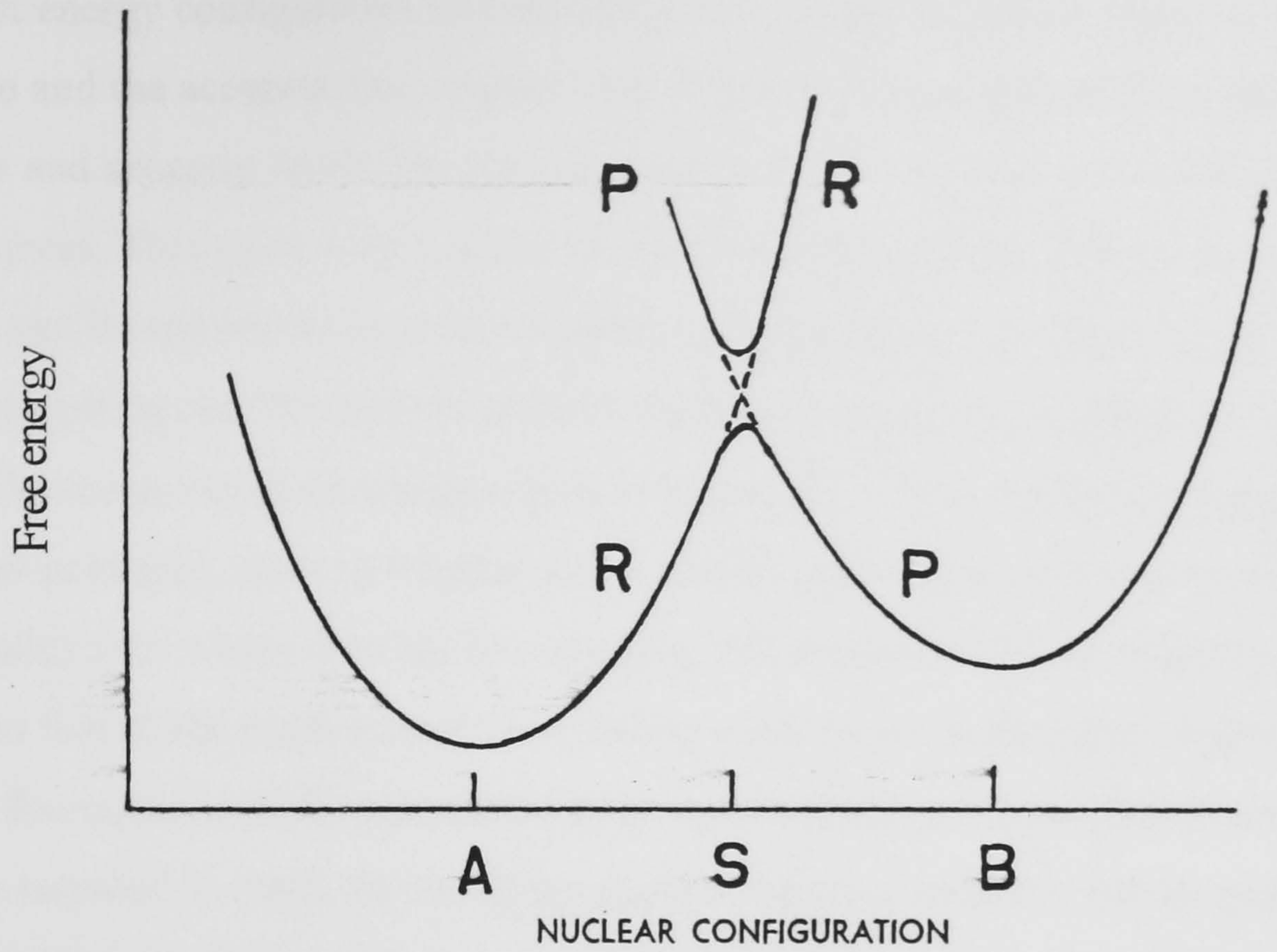



Figure 3.12. One dimensional profile of many dimensional free energy surface of reactant (R) and product (P) states. Each surface includes contribution from the surrounding medium. A and B denote nuclear coordinates for an equilibrium configuration of reactants and for products, respectively. S denotes a nuclear configuration at the intersection of the two free energy surfaces. Solid lines at the intersection region indicate splitting due to electronic interaction of donor and acceptor states.

Such an electron transfer reaction can also be described using the free energy diagram for the reactant and the product states as shown in figure 3.12 (Marcus 1964, Marcus and Sutin 1985). The diagram indicates quadratic free energy curves of two distinct electronic states; reactant (DA, labelled R) and product ($D^+A^-$, labelled P) states, where D is the electron donor and A is the electron acceptor as a function of some arbitrary parameters that define changes in nuclear configurations. The nuclear motions for these two states involve, for example, vibrational fluctuation of the reactant and orientational contributions from the surrounding medium. The free energy is therefore as a function of their multi-nuclear coordinates and defines a many dimensional free energy surface, which implies that figure 3.12 represents one dimensional profile of such a many dimensional surface. Three different points in the nuclear configurations are labelled for the reactant and the product free energy curves in figure 3.12. At the points labelled A and B, the nuclear configurations are such that the surrounding solvent molecules are in

the lowest energy configuration that stabilises the localisation of the electron on the donor site and the acceptor site, respectively. At point S, the medium fluctuations bring the donor and acceptor levels into the resonance, i.e. the crossing point of two free energy curves. This point is the traditional transition state region. The Frank-Condon principle can be applied because the electron being transferred is much lighter than the nuclei, suggesting that the electron transfer itself must be a vertical transition in figure 3.12, while conservation of energy requires the transfer to be a horizontal transition. Under this principle, electron transfer will therefore occur only at or near nuclear configurations for which the total free energy of the reactants and surrounding medium is equal to that of the products and surrounding medium (at intersection region, S). Thermal fluctuations of the coordinates from the minimum of the surface R are therefore required to reach the resonance position (nuclear motion), and its probability is calculated by the Boltzmann statistics. The probability of going from the R to the P surface depends upon the extent of coupling of the electronic orbitals of the two reactants. This electronic coupling is dependent upon the separation distance (r) of the reactants as will be discussed below.

This free energy diagram for the nuclear motion (figure 3.12) can be related to the electronic potential energy diagram (figure 3.11). The curves for three different situations are presented in figure 3.13 and the relation between two energy curves is indicated by the dashed lines. The initial nuclear equilibrium position of the reactant (at A) corresponds to the situation that the electron is occupied in the donor well in the left-hand side of figure 3.13a. After a suitable thermal fluctuation, the system reaches the resonant position (at S). This situation is equivalent to the case that electronic energy levels for the donor and the acceptor wells are equal. Further fluctuation for the system leads to an equilibrium position for the product curve (at B); the electron is occupied in the acceptor well.

In the limit of the non-adiabatic electron transfer, the electron tunnelling time is much slower than the timescale of the nuclear relaxation and the nuclear motions to reach the resonance. This is because the splitting at the intersection point (S) in figure 3.12 is relatively small, i.e. the electron transmission probability is low compared to the frequency of the passage through the intersection point along the reactant free energy curve.

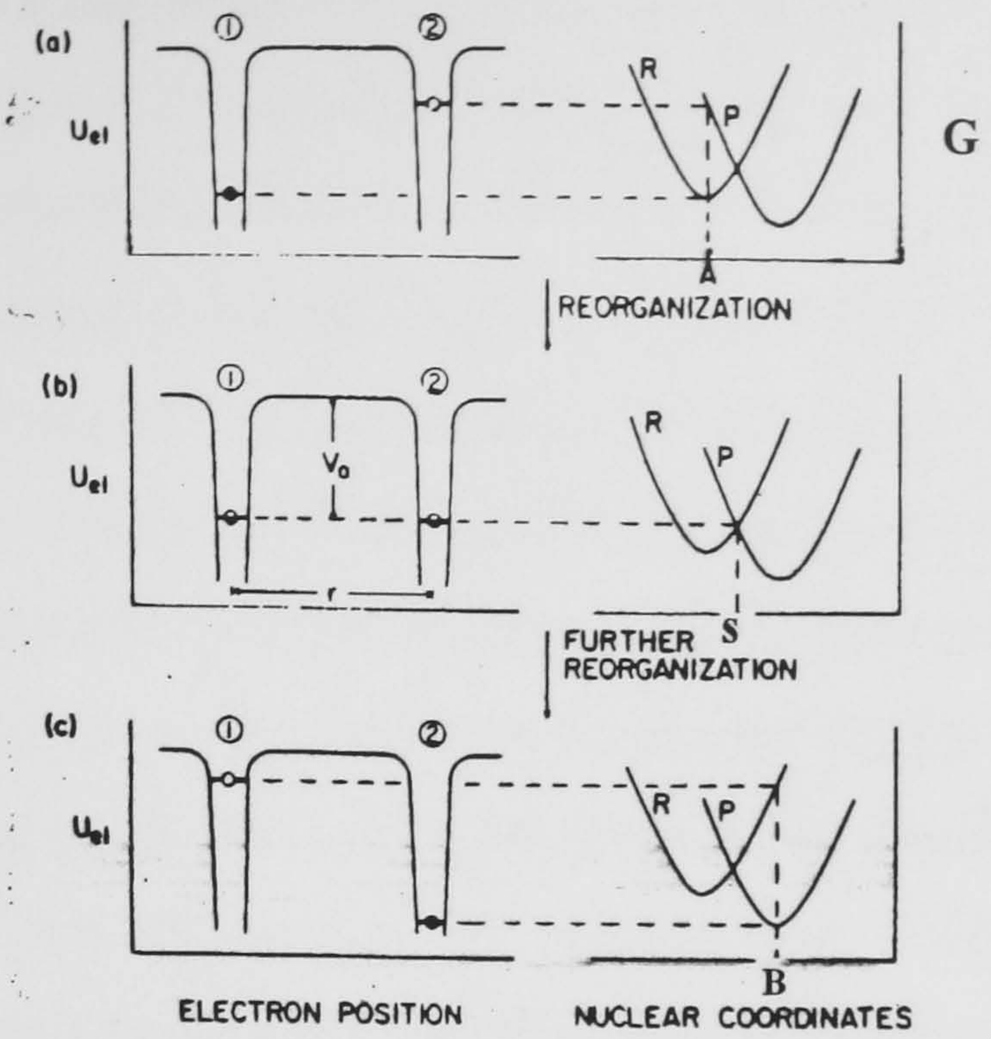



Figure 3.13. Relationship between electronic potential energy curves (on the left) and the free energy curves (on the right). The electronic energies in the two wells on the left are indicated for three nuclear configurations on the right for the donor-acceptor reaction. The levels in the wells are vertical ionisation energies. The filled and open circles denote ionisation of the reduced state and the oxidised state at their equilibrium nuclear configurations. The half-filled circles refer to ionisation of the state at the nuclear configuration corresponding to the intersection region. The level in well 1 is initially occupied in (a) and the level in well 2 in (c).

The experimental observable for electron transfer reactions is a reaction rate, and therefore the reaction is generally presented by a rate constant for quantitative analysis. The simple expression of the rate constant derived from Marcus classical treatment (Marcus 1964, Marcus and Sutin 1985) is shown in equations 3.8 and 3.9,

$$\Delta G^* = \frac{(\lambda - \Delta G^\circ)^2}{4\lambda} \qquad \text{Equation 3.8}$$

$$k = \kappa B \exp\left(\frac{-\Delta G^*}{kT}\right) \qquad \text{Equation 3.9}$$

where $k$ is Boltzmann constant. $\kappa$ is the transmission coefficient or averaged transition probability for electron transfer per passage of the system through the intersection

region (at S in figure 3.12), which describes the non-adiabacity of the reaction. If the reaction is adiabatic, $\kappa \approx 1$. B is the liquid phase collision frequency if the reaction is bimolecular, or is a vibrational frequency if mono-molecular (intramolecular). A typical value of B for many reaction systems is approximately $10^{13}$ $s^{-1}$ (Marcus 1956). $\Delta G^*$ is the activation energy and $\Delta G°$ is the standard free energy gap between the equilibrium configurations of the reactant and of the product (including the work terms needed to bring charged reactants into the reaction distance for the bimolecular reaction). $\lambda$ is termed the reorganisation energy, defined as the energy required to distort the equilibrium nuclear geometry of the reactant state into the equilibrium geometry of the product state without electron transfer. The exponent term is the Boltzmann probability of reaching the resonant region due to the thermal fluctuations. Equation 3.8 implies that the activation energy can be calculated from the standard free energy difference and the reorganisation energy.

Another expression for the rate constant was introduced by the application of Fermi's golden rule (Devault 1980, Marcus and Sutin 1985, Moser, et al. 1992) with the assumption of very weak electronic coupling of the reaction ($\kappa << 1$). Here we consider only the high temperature limit, i.e. all of the vibrational frequencies are relatively small; $h\upsilon/2kT << 1$. The expression of the rate constant assuming high temperature is shown in equation 3.10 (Devault 1980, Jortner 1980, Marcus and Sutin 1985, Moser, et al. 1992).

$$k = \left(\frac{2\pi}{\hbar}\right) V_{RP}{}^{2} \left(4\pi\lambda \mathrm{k}T\right)^{-1/2} \exp - \left[\frac{\left(\lambda + \Delta \mathrm{G}°\right)^{2}}{4\lambda \mathrm{k}T}\right] \qquad \text{Equation 3.10}$$

where $\hbar$ is Planck constant. $V_{RP}$ is the electronic coupling obtained from matrix element coupling of reactant and product electronic wavefunctions, and is equivalent to one-half the separation of the splitting at the intersection point S in figure 3.12. The non-adiabatic and adiabatic limit for electron transfer reactions is roughly estimated with the thermal energy of $k$T (Closs and Miller 1988). If $V_{RP} >> k$T, the reaction is adiabatic, whereas if $V_{RP} << k$T, it is non-adiabatic. The value of $V_{RP}{}^2$ is dominated by the spatial orientation and the separation of the donor and the acceptor, which then provides structural control of the rate constant (Jortner 1980). Ignoring the orientational effect, it

decreases exponentially with separation distance (r) between the centres of the donor and the acceptor (equation 3.11).

$$V_{RP}^{\ 2} = V_0^{\ 2}\exp[-\beta(r - r_0)] \qquad \text{Equation 3.11}$$

where $V_0^2$ is the maximum electronic coupling, $r_0$ is the distance of the closest approach or direct contact distance between the donor and the acceptor, and $\beta$ is the damping parameter of the electronic wavefunction within the barrier region separating the two states (electronic barrier). The separation distance of the reactant is therefore a critical factor to control the reaction rate.

Comparing equation 3.9 with equation 3.10, the expressions for the rate constant can be related as equation 3.12 (Devault 1980, Marcus and Sutin 1985).

$$\kappa B = \left(\frac{2\pi}{\hbar}\right) V_{RP}^{\ 2} (4\pi\lambda kT)^{-1/2} \qquad \text{Equation 3.12}$$

***Dependence of the rate (k) on standard free energy difference***

Both equations 3.9 and 3.10 indicate that the electron transfer reaction rate is dependent upon the standard free energy difference between the reactant and the product states. Three typical situations controlling the rate with the relation between $\Delta G°$ and $\lambda$ are shown in figure 3.14. When $\Delta G°$ is increased negatively with the constant $\lambda$, $\Delta G^*$ initially decreases according to equation 3.8 or 3.10; the situation of $\Delta G°$ and $\lambda$ under this condition is called the normal region (figure 3.14a). As shown in figure 3.14b, when $-\Delta G° = \lambda$, $\Delta G^*$ becomes the value of 0, i.e. the forward electron transfer reaction is barrierless and proceeds at the maximum rate. The reaction under the situation that the reactant and the product surfaces cross at the minimum of the reactant surface is termed activationless electron transfer. Further negative increase in $\Delta G°$ results in the case that $\Delta G^*$ once again begins to increase to arrange the donor states into the resonance, that is, $-\Delta G° > \lambda$ (figure 3.14c). This region is termed the inverted region as the rate for electron transfer slows down with driving force.

The simple expression for the nuclear barrier such as equations 3.8 and 3.10, and the prediction of the inverted region by Marcus have been supported by a number of experimental results (Closs and Miller 1988, Marcus and Sutin 1985, Moser, et al. 1992). Figure 3.15 represents some of the experimental evidence for the inverted region (Miller, et al. 1984).

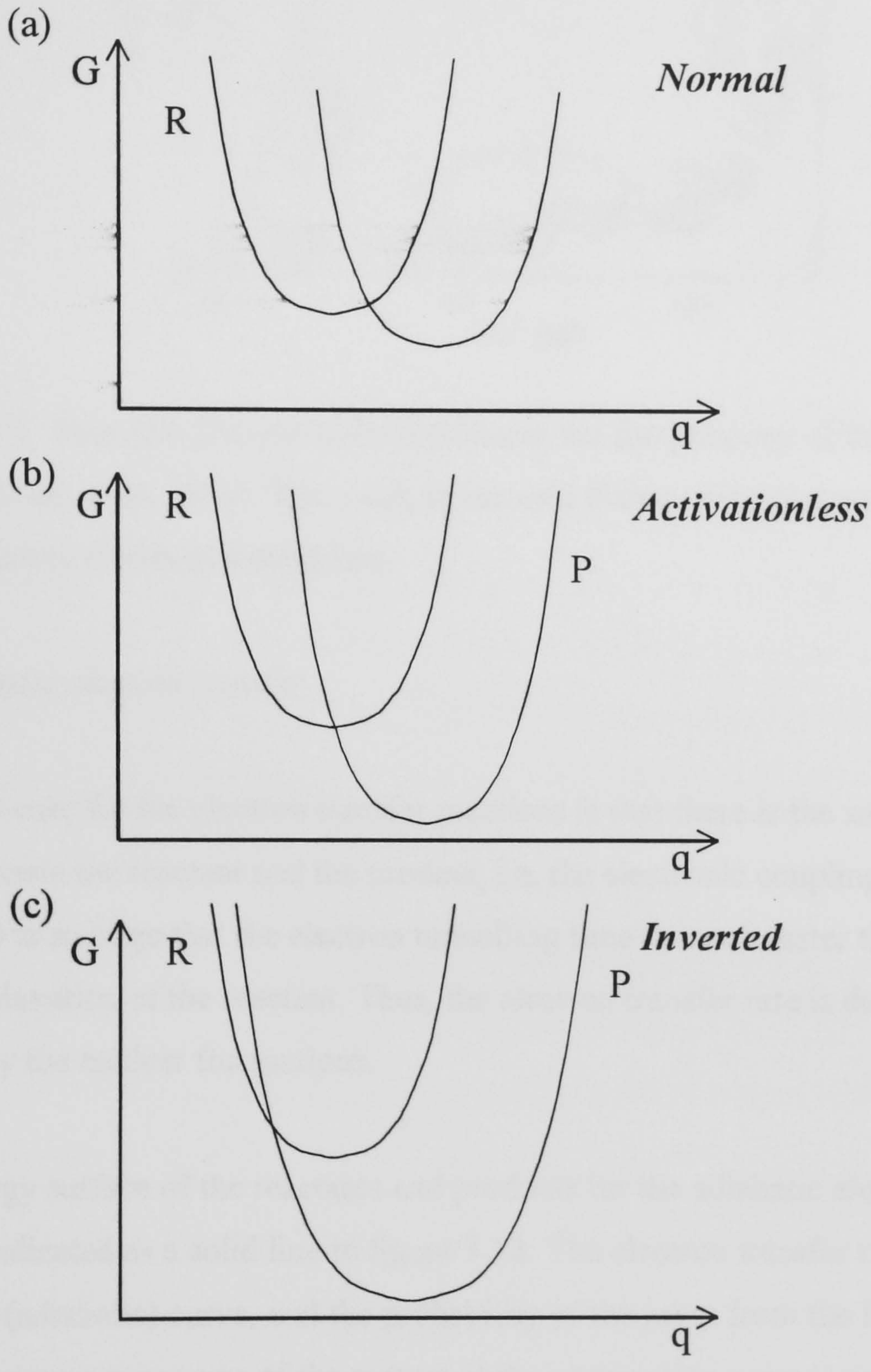



Figure 3.14. Profiles of free energy surfaces of reactant and product states for three different types of electron transfer reactions; normal region (a), activationless (b) and inverted region (c). The activationless reaction can be achieved when the free energy of the reaction ($-\Delta G^{\circ}$) matches the reorganisation energy of the reaction ($\lambda$). The reorganisation energy is assumed to be constant in this figure.

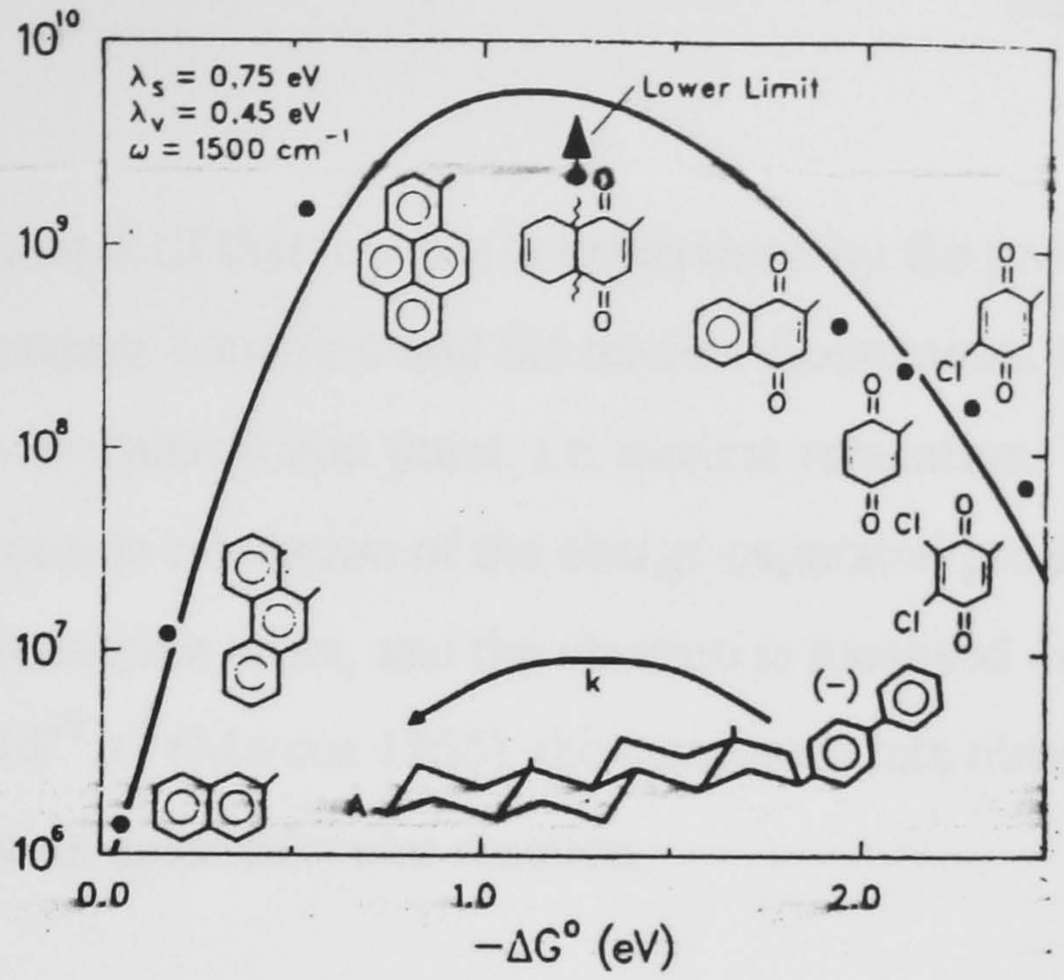



Figure 3.15. Example of experimental evidence for the presence of the inverted region (Miller, et al. 1984). The result of the data fitting using the parameters listed in the figure is shown as a solid line.

### 3.3.2.2 Adiabatic electron transfer

The adiabatic case for the electron transfer reactions is that there is the strong electronic coupling between the reactant and the product, i.e. the electronic coupling term ($V_{RP}$) in equation 3.10 is so large that the electron tunnelling time is much faster than the vibrational relaxation of the reactant. Thus, the electron transfer rate is dominantly determined by the nuclear fluctuations.

The free energy surface of the reactants and products for the adiabatic electron transfer reactions is indicated as a solid line in figure 3.12. The electron transfer reaction follows a lower solid (adiabatic) curve, and the probability of the jump from the lower solid curve to the upper per passage of the system at the intersection point is negligible (Marcus 1964).

For the expression of the rate constant, equation 3.9 can be further simplified to equation 3.13 as the transmission coefficient, $\kappa$, is close to unity for the adiabatic limit.

$$k = B \exp\left(\frac{-\Delta G^*}{kT}\right)$$ Equation 3.13

It is apparent from equation 3.13 that the rate is determined by the probability of the system attaining the resonance condition and the nuclear fluctuations that lead to a net decrease in energy from the intersection point, i.e. nuclear relaxation. The physical description of the latter case is relaxation of the charge-separated product states to equilibrium from the intersection point, and the electron is localised on the acceptor. Using the value of $B = 10^{13}$ $s^{-1}$ (Marcus 1956), the maximum rate obtained is approximately 100 fs for an intramolecular reaction.

### 3.3.3 Extension of homogeneous electron transfer theory to electron injection in dye sensitised semiconductors

Outer-sphere electron transfer reactions between an ion or molecule and an electrode have been described in a number of papers (Marcus 1965, Miller, et al. 1995, Schmickler 1996). However, application of the homogeneous theory to the electron injection kinetics in dye sensitised semiconductor has been limited to date (Lanzafame, et al. 1994, Miller, et al. 1995).

An interfacial electron injection reaction in dye sensitised semiconductors is initiated by excitation of dye molecules by photons. For selected dye molecules, the redox potential of the excited state is higher than that of the conduction band edge, resulting in rapid electron transfer from the excited dye molecule into the conduction band of the semiconductor. In contrast to the homogeneous electron transfer reactions (two level system), heterogeneous reactions in dye sensitised semiconductors involve reactions between discrete molecular excited state and continuum electronic acceptor states in the conduction band as shown in figure 3.16.

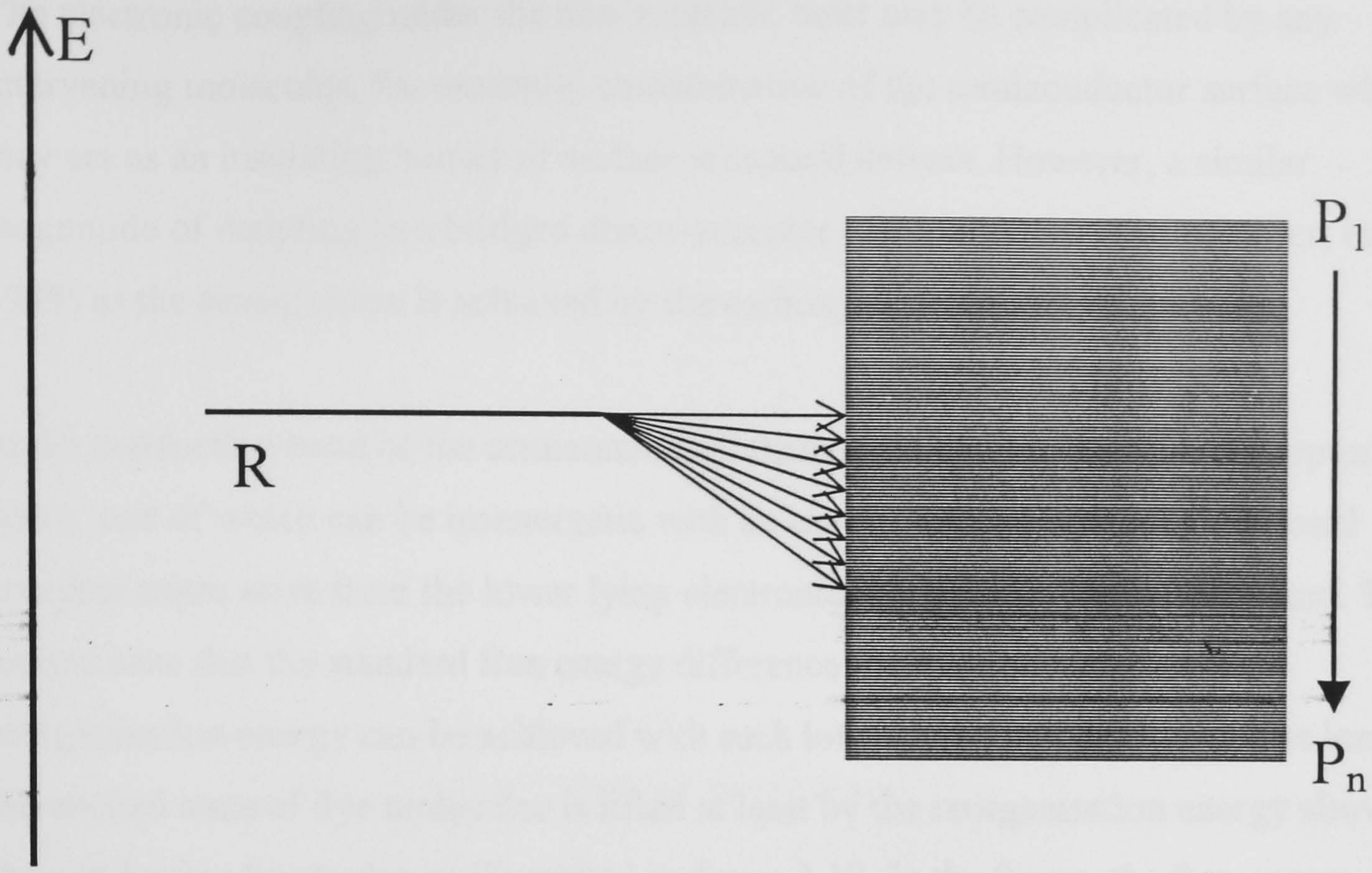



Figure 3.16. Potential energy diagram representing the electron injection reaction from the dye excited state (donor) into the multiple states (acceptor) in the conduction band. Each reactant state consists of the discrete donor state and one in the band of continuous acceptor states. Free energy difference ($\Delta G^{\circ}$) of the reaction is dependent upon the energy level of the acceptor state selected.

Here two cases of electron transfer reactions are considered; non-adiabatic and adiabatic reactions with the restriction that dye molecules are covalently linked (by carboxyl groups) to the surface of the semiconductor.

3.3.3.1 Non-adiabatic electron transfer

Following the description of the homogeneous electron transfer reaction under the non-adiabatic limit, it can be assumed for the electron injection that a reaction rate is controlled by the electronic coupling between the excited donor and the acceptor in the semiconductor and the probability of the system to reach the resonance position (nuclear motion) by means of thermal fluctuations. In addition, the electron transmission time is slower than the nuclear (vibrational) relaxation time.

The electronic coupling under the non-adiabatic limit may be complicated by any intervening molecules, for example, contamination of the semiconductor surface which may act as an insulating barrier or surface structural defects. However, a similar magnitude of coupling to a bridged donor-acceptor pair may be expected (Miller, et al. 1995) as the sensitisation is achieved by the carboxyl groups.

In the conduction band of the semiconductor, there are a series of different acceptor states, one of which can be isoenergetic with an excited donor state. The additional acceptor states arise from the lower lying electronic levels in the conduction band. The unique case that the standard free energy difference is always equivalent to the reorganisation energy can be achieved with such lower lying electronic states as long as the excited state of dye molecules is lifted at least by the reorganisation energy above the conduction band edge as illustrated in figure 3.17. In the figure, the free energy of the reactant curve is normalised to the same level for ease of comparison, although the reactant free energy may be altered when a different electron acceptor state is considered. It is assumed in this case that the reorganisation energy does not change even though any electron acceptor state in the conduction band is considered. Therefore, the reaction is always activationless, i.e. one of the acceptor states always crosses the minimum vibrational state of the reactant surface if the energy gap between the donor state and the conduction band edge ($\Delta G^\circ$) is greater than the reorganisation energy ($\lambda$).

In the high temperature limit, the activationless electron transfer reaction in the homogeneous system suggests a temperature dependence which can be deduced from the equation 3.10. This is because the system has less probability to be found at the bottom of the reactant surface with Boltzmann statistics. However, for the case of the dye sensitisation, any of the lower lying continuum electronic states in the conduction band can involve electron transfer reactions with any excited vibrational level of the reactant, resulting in a rate which is apparently independent of temperature.

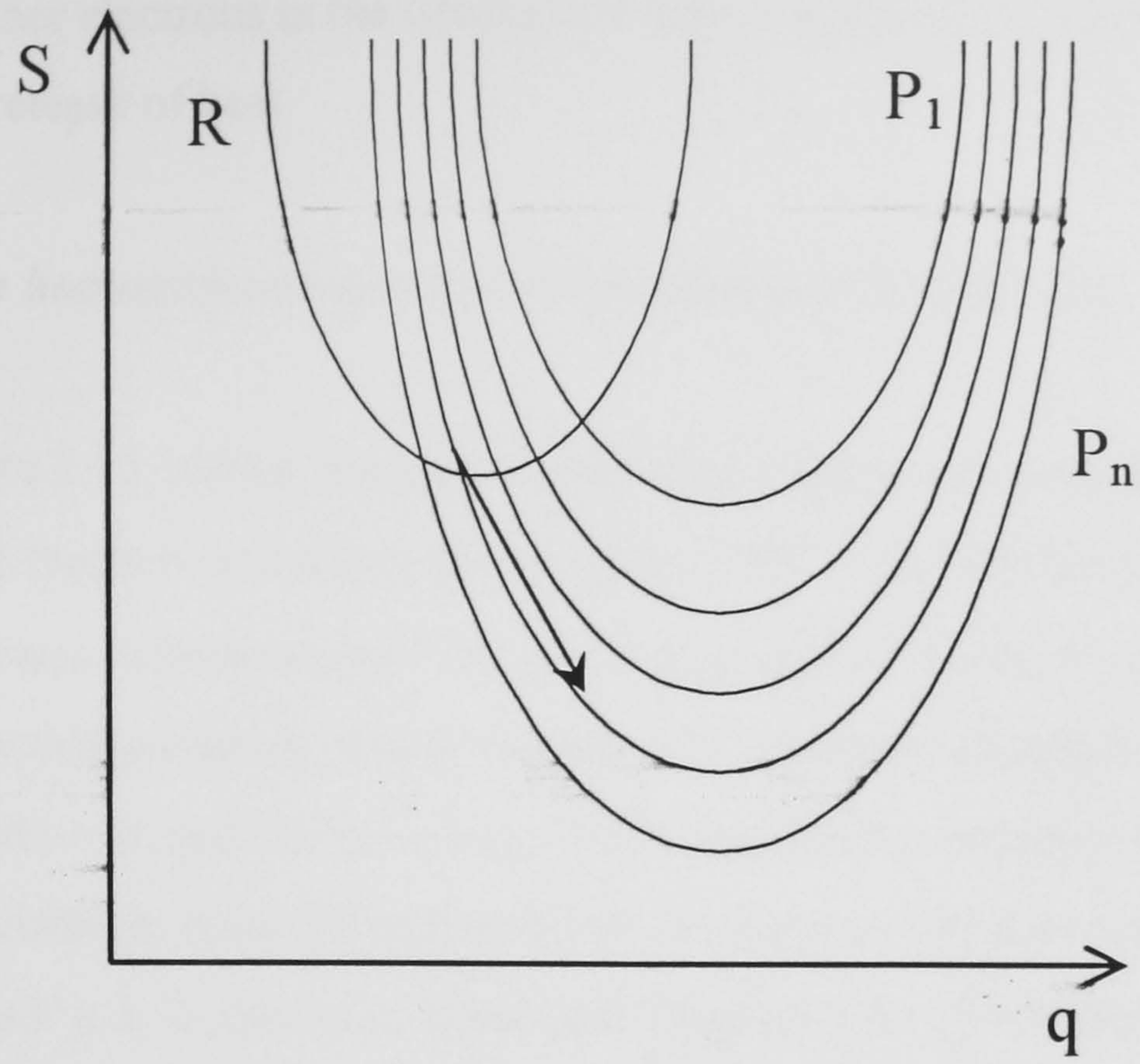



Figure 3.17. Free energy diagram of the non-adiabatic electron injection reaction from the dye excited state to the conduction band of the semiconductor. The number of reactant and product states is dependent upon the number of acceptor states involved in electron transfer reactions. In the figure, the free energy levels of the reactant surfaces are normalised at the same level, and therefore only relative energy levels of the reactant and the product states should be considered for electron transfer reactions.

The number and energy of the available electronic acceptor states will decrease when the conduction band is not wide enough or when the free energy gap is lower than the reorganisation energy. Considering that a vibrational ground state of an excited donor molecule lies at the same height or even below the conduction band edge, only the electronic states close to the bottom of the conduction band of the semiconductor can contribute significantly to the rate constant as acceptor states due to the fast exponential decrease in the occupancy of higher vibrational states.

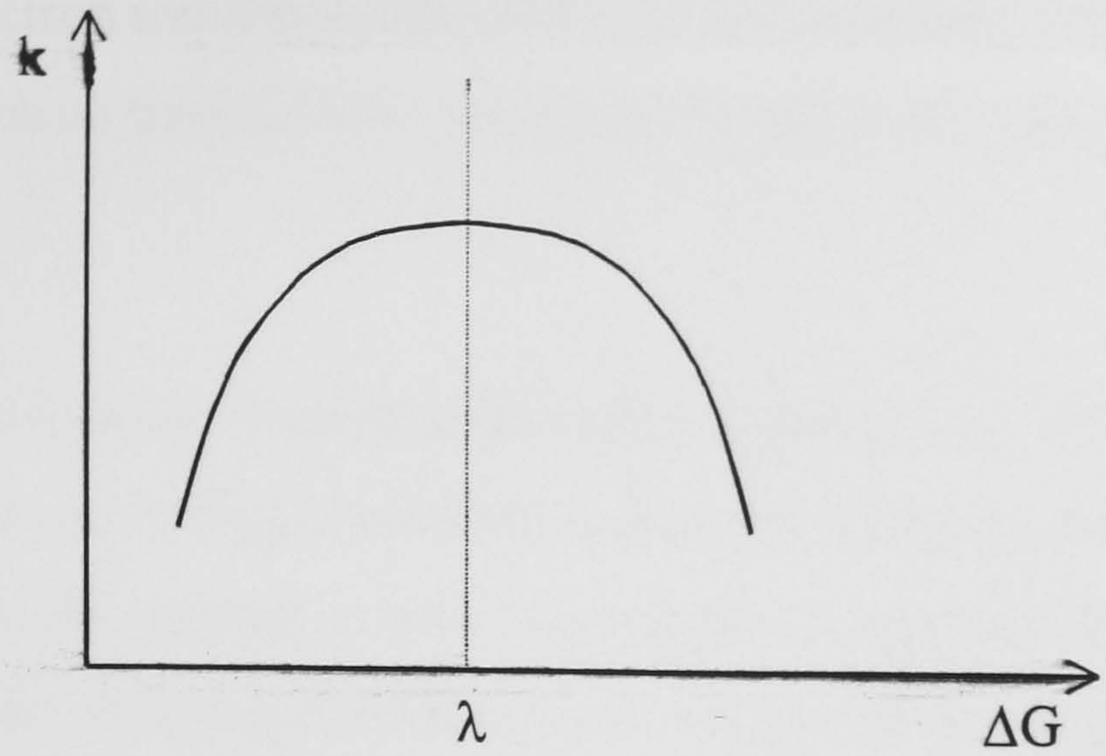
After the electron injection, the irreversibility of the reaction is attained either by fast diffusion of the electron at the semiconductor surface out of the reaction zone (an initially prepared product state), by inelastic scattering (electronic dephasing) for the electron in the conduction band of the semiconductor or by other redistribution of the vibrational energy in the product state (carrier thermalisation). The inelastic scattering

can occur with other electrons in the conduction band depending upon the density of electrons, or via release of heat.

*Comparison with homogeneous system for dependence of k upon $\Delta G^o$*

As shown in figure 3.15, slower electron transfer rate is observed when the system for the homogeneous reaction is in the inverted region ($-\Delta G^o > \lambda$). For the dye sensitisation, the reaction is always activationless if the free energy gap of the donor and acceptor states exceeds the reorganisation energy. Figure 3.18 compares the relations between the electron transfer rate and the free energy difference for the homogeneous reactions and the dye sensitisation. It can be expected that the electron injection rate becomes constant when $-\Delta G^o \geq \lambda$. It should be noted that the properties of oriented solvent relaxation for adsorbed dye molecules may be different from those in the bulk solvent, resulting in the different magnitude of the reorganisation energy.

(a) Homogeneous electron transfer




(b) Electron injection in dye sensitised semiconductor

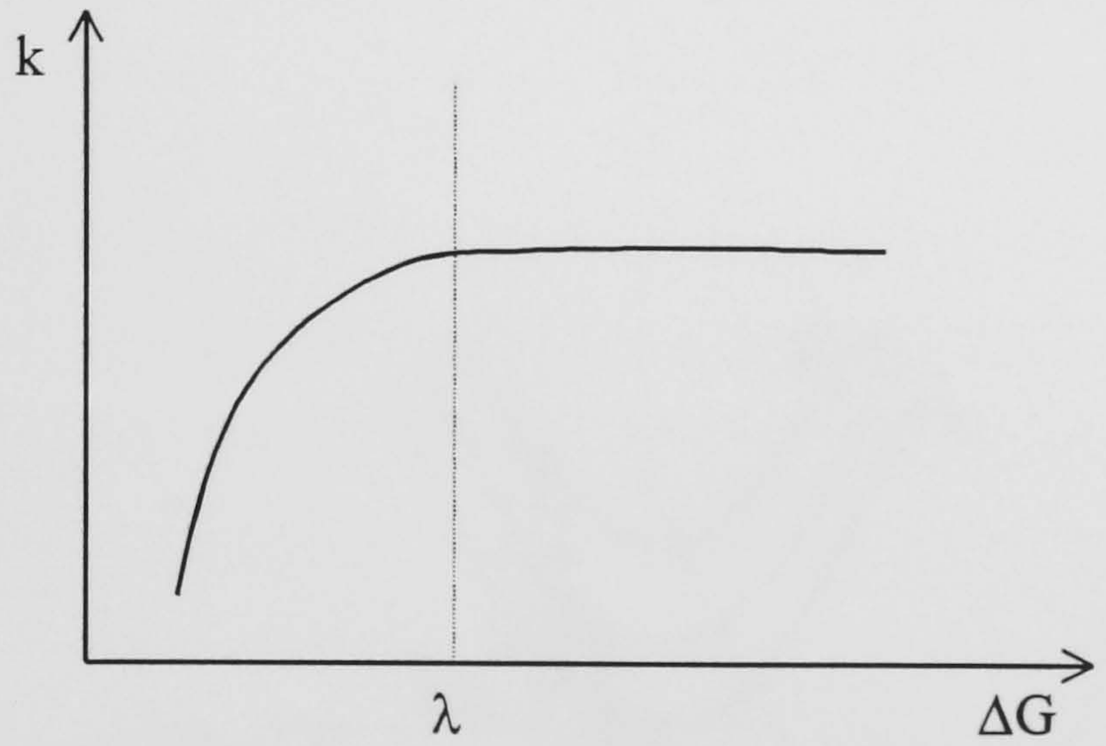



Figure 3.18. Comparison of the relationship between an electron transfer rate and free energy difference for the homogeneous reaction (a) and the dye sensitisation (b). Note that the inverted region does not exist for the electron injection process in the dye sensitised semiconductor, indicating that the reaction is always activationless when the largest free energy difference exceeds the reorganisation energy.

3.3.3.2 Adiabatic electron transfer

Consider that the adsorbed donor state is in the middle of a wide conduction band; the excited state of dye molecules is lifted at least by the reorganisation energy above the conduction band edge. When the nuclear configuration is relaxing to the equilibrium configuration in the excited electronic state of the donor molecule after its optical

excitation, the reaction system possibly passes many consecutive crossing points. In the adiabatic limit, the electron transmission time may compete with this nuclear relaxation time, i.e. the electron transfer reaction may be complete before the reactant system relaxes. The electron transfer rate may therefore be on the same timescale as the nuclear relaxation.

Such an electron transfer reaction is illustrated in figure 3.19. It is clear from the figure that crossing with one of many product curves occurs almost continuously when the system relaxes in the reactant surface (vibrational relaxation), and the electron transfer competes with the vibrational relaxation process at each crossing position. It should be noted that the magnitude of the electronic coupling may vary at each different crossing point. However for the adiabatic reaction, the electron transfer should occur at the first crossing point.

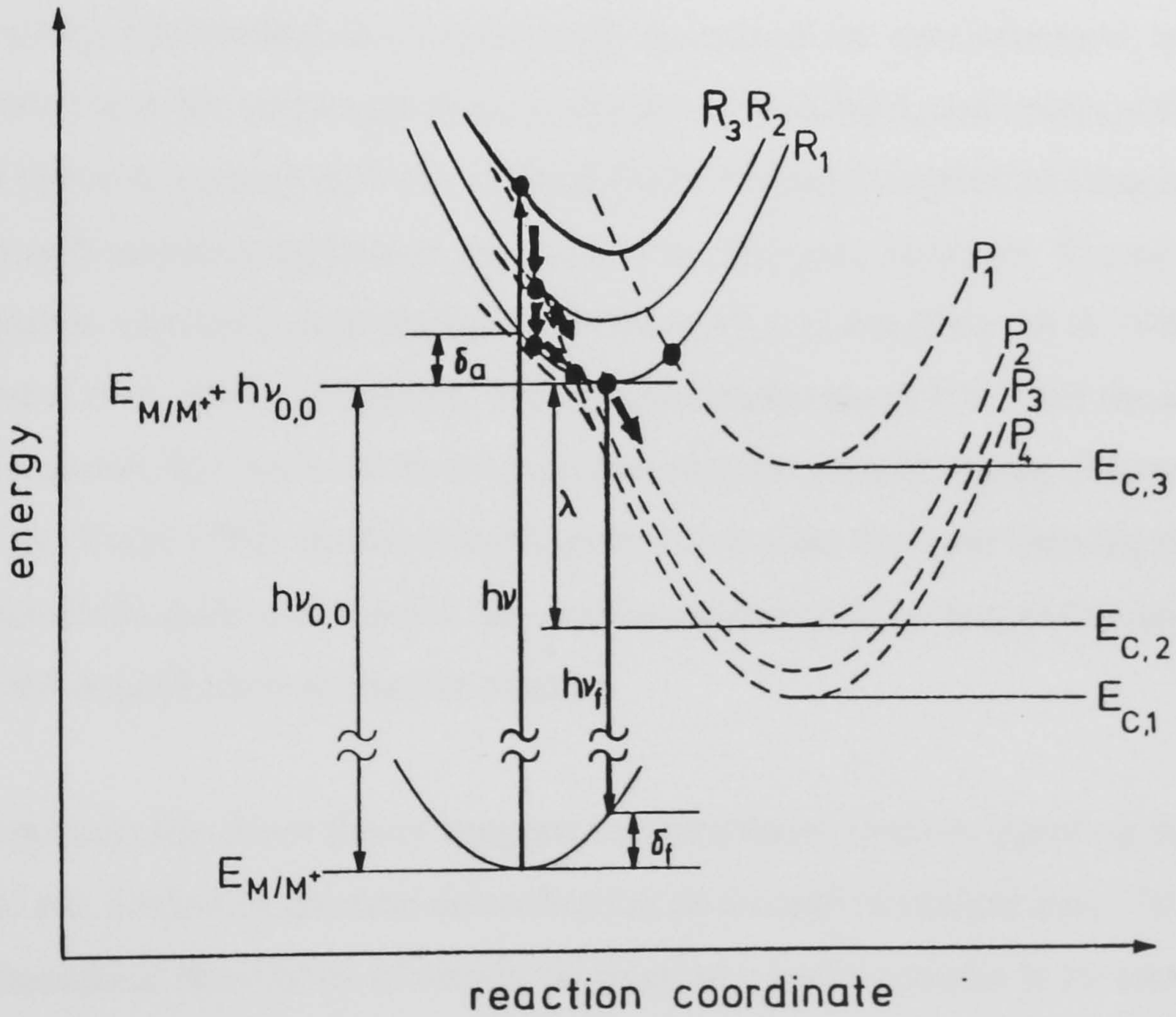



Figure 3.19. Free energy diagram of adiabatic electron injection reaction in the dye sensitised semiconductor. The vibrational relaxation process in the reactant state following optical excitation competes with the electron transmission process from the reactant to the product surface.

### *Incorporation of electron delocalisation model*

At semiconductor interfaces, the donor and the acceptor states are still considered as molecular levels, however, the semiconductor has a continuum of electronic states with considerable delocalisation of the wavefunction over many electronic states. The injected electron may therefore be delocalised in a mixed state of the coupled electronic states on a remarkably short timescale. Such delocalisation process should dephase an initially prepared product state or should occur when an electron is transmitted in order to stabilise the product states (charge separated state), and may be competitive with or even be faster than the nuclear relaxation process.

The model to incorporate this electron delocalisation process into the electron transfer theory has been presented by Lanzafame, Miller and co-workers (Lanzafame, et al. 1992, Lanzafame, et al. 1994). In the model, it is assumed that the electron resonantly tunnels across the interface to a single electronic state of the semiconductor, which is mixed with the entire continuum states in the conduction band, and subsequently the electron exists in a mixed state of a coupled band. The large number of these states prevents re-localisation process of the electron on the donor molecule. The rate for this delocalisation process is estimated to be as fast as 10 fs (Lanzafame, et al. 1992, Lanzafame, et al. 1994), contrasting with the maximum rate of 100 fs for the electron transfer reaction derived from the homogenous electron transfer theory (Marcus 1956, Marcus and Sutin 1985). As the delocalisation process can be faster than the nuclear relaxation of the molecular species, this nuclear relaxation is no longer the rate-limiting step for the overall electron transfer reaction.

In consequence, the above theory suggests that interfacial electron injection may be adiabatic and limited by electron delocalisation or thermal relaxation time. The validity of this theoretical description of interfacial electron transfer remains to be established, and it is therefore desirable to observe the dynamics directly in order to elucidate the parameters controlling the electron injection kinetics.

# Chapter 4: Assignment of interfacial electron transfer kinetics in $Ru(dcbpy)_2(NCS)_2$ sensitised $TiO_2$ films

## 4.1 Introduction

As explained in chapter 1, the photovoltaic function of the dye sensitised semiconductor solar cells is initiated by light induced separation of charge at the dye / semiconductor interface, followed by several electron transfer steps to avoid recombination of separated charges. However, at the start of my PhD studies, there was no detailed information available on the kinetics at the dye / semiconductor interface and their correlation with the device efficiency. Detailed kinetic studies were required to establish the mechanism of the electron transfer process and for further technological development of the cell.

Transient optical spectroscopies are increasingly being used to address the kinetics of both the photoinduced electron injection and recombination reactions. In the first half of this chapter, the studies of electron injection kinetics in the dye sensitised $TiO_2$ films carried out by other groups prior to my PhD study are summarised. To a large extent, the parameters controlling the rates of electron injection and recombination were not established.

In the previous steady state studies of the dye sensitisation, ruthenium (II) trisbipyridyl ($Ru(bpy)_3^{2+}$) complexes and their analogues have received the most attention (Hagfeldt and Grätzel 1995, Kalyanasundaram 1982) due to their superior performance as photosensitisers for their strong visible light absorption and resistance to ligand substitution (high stability). For my first studies of the interfacial electron transfer, *cis*-Ruthenium$^{II}$(2,2'-bipyridyl-4,4'-dicarboxylate)$_2$(NCS)$_2$ ($Ru(dcbpy)_2(NCS)_2$) was chosen as the sensitiser dye since this dye is the most efficient sensitiser dye reported to date for a photoelectrochemical solar cell (see chapter 1)(Nazeeruddin, et al. 1993) and is currently employed in commercial development of this technology. Choice of this dye was essential in order to relate interfacial kinetic measurements directly to the function of the devices. It is expected that the electron injection occurs on ultrafast timescales while

charge recombination is relatively slow. The characterisation of dye excited state dynamics and the method to assign the interfacial charge separation are also described.

## 4.2 Previous studies of interfacial electron injection kinetics

There had been no study reported for the kinetics of electron injection for nanocrystalline $TiO_2$ films employing $Ru(dcbpy)_2(NCS)_2$ as a sensitising dye. However, there had been several studies for $TiO_2$ semiconductor sensitised by related ruthenium dyes and other dyes by means of transient spectroscopies. Such studies including experimental conditions and kinetic results are summarised in table 4.1.

Table 4.1. Previous transient kinetic studies of electron injection in dye sensitised $TiO_2$.

| Sensitiser dye | Type of $TiO_2$ (particle diameter) | Type of apparatus (instrument response time) | Excitation wavelength | Electron injection rate | E-inj. yield | Authors |
|---|---|---|---|---|---|---|
| $Ru(dcbpy)(bpy)_2^{2+}$ | Nanocrystalline films | microwave absorption (7 ns) & luminescence (4 ns) | 532 nm | 5 & 50 ns (Biexponential) | | Kamat et al. (Fessenden, et al. 1995) |
| $Ru(dcbpy)_2(\mu\text{-}(CN)Ru(CN)(bpy)_2)_2$ | Nanocrystalline films | Transient luminescence | 600 nm | 172 ps | >0.9 | Willig et al. (Willig, et al. 1993) |
| $Ru(dcbpy)_2(H_2O)_2^{2-}$ | Nanocrystalline films | Transient luminescence (12 ps) | 580~605 nm | <7 ps | ≈1 | Willig et al. (Eichberger, et al. 1990) |
| $Ru(bpy)_3^{2+}$ | Anatase powders (500 nm) | Transient luminescence (2 ns) | 540 or 450 nm | Multi-exponentials 1 ns ~ 1 | | Hashimoto et al. (Hashimoto, |

| | | | | | | |
|---|---|---|---|---|---|---|
| | | | | μs | | et al. 1988) |
| Coumarin 343 | Colloidal particles (15 nm) | Fluorescence up-conversion (150 fs FWHM) | 400 nm | 180 fs | 0.9 | Rehm et al. (Rehm, et al. 1996) |
| Chlorine $e_6$ | Nanocry-stalline films (15 nm) | Transient luminescence & absorption (100 ps pulse) | 532 nm | 0.4 & 1.4 ns (Biexp-onentials) | 0.8 | Kay et al. (Kay, et al. 1994) |
| Copper chlorophyllin | Nanocry-stalline films (15 nm) | Transient luminescence & absorption (100 ps pulse) | 532 nm | 3 & 16 ns (Biexp-onentials) | 0.8 | Kay et al. (Kay, et al. 1994) |
| Copper phthalocyanine tetrasulphonate | Colloidal particles (5 nm) | Transient absorption (pulse duration = 30 ps) | 355 nm | 20~50 ps | | Kirk et al. (Kirk, et al. 1984) |
| Eosin Y | Colloidal particles (12 nm) | Transient absorption (40 ps) | 532 nm | 1 ns | 0.38 | Moser et al. (Moser, et al. 1985) |
| Eosin Y | Single crystal | Internal reflection transient absorption (100 ns) | 532 nm | from singlet (<100 ns) & triplet (5 μs) | 0.5 from tripl-et | Spitler et al. (Ryan, et al. 1989) |
| Eosin Y | Colloidal particles (9 nm) | Time-resolved Raman (pulse | 532 nm | <5 ns | low | Brus et al. (Rossetti, et al. 1984) |

| | | | | | | |
|---|---|---|---|---|---|---|
| | | duration = 2 ns) | | | | |

It is clear from table 4.1 that these studies reported wide variations in the rates of electron injection, ranging from picoseconds to nanoseconds. It was unclear to what extent the variations in experimental observations results from differences in the sensitiser dyes used, from differences in the $TiO_2$ particles, from limited time resolution of the apparatus, or from other variations in the experimental conditions. For example, the time resolution of the apparatus possibly limits the electron injection time, i.e. the slow instrument response may indicate slow electron injection rates. Kamat et al. suggested that difference in rate constants observed may originate from different methods in preparing semiconductors and samples, affecting the electronic interaction of the dye with the surface of the semiconductor (Fessenden and Kamat 1995).

When the redox potential of the dye excited state is well above the bottom of the conduction band, electron injection can proceed both from singlet and triplet states of dyes. This injection mechanism implies that there would be kinetic competition between the charge separation and the intersystem crossing of the dye. Willig et al. and Kay et al. reported (Kay, et al. 1994, Willig, et al. 1993) that the electron injection occurs from the triplet excited state of the dye to the conduction band of $TiO_2$. In contrast, Moser et al. observed the electron injection from the dye excited singlet state (Moser, et al. 1985). Electron injection processes from both singlet (<100 ns) and triplet (about 5 μs) states were suggested by Spitler et al (Ryan, et al. 1989).

There may be different kinetic components for electron injection into the dye sensitised $TiO_2$ films. If a component is attributed to a different adsorption site on the surface of the semiconductor, the kinetics may exhibit multi-exponentials. Most of authors as shown in table 4.1 reported single exponential rate constant (Moser, et al. 1985, Willig, et al. 1993) or instrument response limited rate (Eichberger and Willig 1990, Kirk, et al. 1984, Rossetti and Brus 1984). However, Hashimoto et al. observed multi-exponentials (sum of four exponentials) injection kinetics (Hashimoto, et al. 1988). Kamat et al. and

Kay et al. reported biexponential injection rates (Fessenden and Kamat 1995, Kay, et al. 1994).

In the case of close contact of the adsorbed dye molecules to the semiconductor surface, ultrafast electron injection can be expected to occur on femtosecond to picosecond timescales following the electron transfer theory described in chapter 3. It can therefore be expected that such fast injection kinetics result in high electron injection yield. Indeed, Rehm et al. and Willig et al. observed ultrafast electron injection rates with a quantum yield of nearly unity (Eichberger and Willig 1990, Rehm, et al. 1996, Willig, et al. 1993). However, despite these expectations, a number of studies reported relatively slow injection rates (Fessenden and Kamat 1995, Hashimoto, et al. 1988, Ryan, et al. 1989) and low sensitisation yield (Rossetti and Brus 1984). The low injection yield may originate from slower electron injection rate due to increased dye coverage (Eichberger and Willig 1990) or fast charge recombination rate lowering the net injection yield (Rossetti and Brus 1984).

In consequence at the start of my PhD studies, there was no consensus over the timescale of electron injection from ruthenium dye, nor indeed whether all dyes with similar excited state redox potential should exhibit similar electron injection kinetics. There had also been no systematic studies of the electron injection kinetics under reproducible experimental conditions, and the parameters which control the kinetics of the injection reaction remained poorly established.

## 4.3 Assignment of interfacial electron transfer rates in $Ru(dcbpy)_2(NCS)_2$ sensitised $TiO_2$ films

This section presents the detailed study with sub-picosecond time resolution of the kinetics of electron injection in nanocrystalline $TiO_2$ films sensitised by $Ru(dcbpy)_2(NCS)_2$ and the assignment of electron transfer kinetics in the dye / semiconductor interface. These electron transfer studies are complemented by ultrafast spectroscopic study of $Ru(dcbpy)_2(NCS)_2$ in ethanol solution, and adsorbed on nonquenching $ZrO_2$ films. $ZrO_2$ has a similar surface and optical properties to $TiO_2$, but a

conduction band potential ~1 V more negative than $TiO_2$, thus inhibiting the electron injection (Kay, et al. 1994).

### 4.3.1 Experimental conditions

#### 4.3.1.1 Samples

For measurements of dye solution phase, $Ru(dcbpy)_2(NCS)_2$ in acidic ethanol solution was placed in a sample cell with an optical path length of 2 mm for the femtosecond or of 4 mm for the nanosecond transient absorption spectroscopy (see chapter 2 for the preparation of the dye solution). $Ru(dcbpy)_2(NCS)_2$ sensitised $TiO_2$ or $ZrO_2$ films covered in ethylene carbonate / propylene carbonate (EC / PC = 1:1) solution were also used as samples. The optical density of all sensitised films was adjusted to be 0.2~0.4 at 538 nm (absorption peak), achieved by immersion of the film in the ethanol solution of $Ru(dcbpy)_2(NCS)_2$ ($2 \times 10^{-5}$ M) for four hours at room temperature.

The $Ru(dcbpy)_2(NCS)_2$ cation state in solution was produced photochemically using an electron acceptor, methyl viologen dichloride hydrate ($MVCl_2$, 98%), purchased from Aldrich Chemical Company, and it was used without any further purification. $MVCl_2$ was dissolved in ethanol (0.02 M). Prior to the optical experiment, a sample was prepared with mixture (50/50 %) of the dye ethanol solution ($10^{-4}$ M) and the above $MVCl_2$ solution, resulting in the solution containing $5 \times 10^{-5}$ M of $Ru(dcbpy)_2(NCS)_2$ and 0.01 M of $MVCl_2$. There was no precipitation in the sample, and steady state absorption spectra of the sample indicated no change before and after the optical experiment.

#### 4.3.1.2 Transient measurements

*Nanosecond-millisecond transient spectroscopy*

The details of the nanosecond-millisecond transient absorption and luminescence apparatuses are described in sections 2.3.3 and 2.3.4. The excitation wavelength was tuned to 510 nm with a pulse energy density of 0.3 $mJ/cm^2$ at 2 Hz. These excitation conditions resulted in the excitation of approximately 3 % of the dye molecules per

pulse. All luminescence data were collected at wavelengths of >660 nm, selected by a Schott glass high pass filter.

***Femtosecond dye laser transient absorption spectroscopy***

The excitation wavelength was tuned at a centre wavelength of 605 nm in the second amplifier in the dye laser system as described in section 2.2.1.4. The excitation energy density was ~0.4 mJ/cm$^2$ (the spot diameter at the sample was about 200 μm), corresponding to approximately 0.8~1 absorbed photons per particle per excitation pulse (see below for the calculation of the density of absorbed photons). Some data were collected with the sample spun at 60 Hz, such that the sample volume was replaced between excitation pulses. The data collected with and without spinning were indistinguishable, indicating the negligible accumulation of long-lived species between excitation pulses (excitation repetition rate: 3.25 kHz). The longest lived species was a charge separated state ($dye^+$ $e_{CB}^-$) whose lifetime is on μs ~ ms timescales (see below). The transient absorption data were collected over two timescales of 0-3 and 0-12 ps with a time delay of 16.7 and 66 fs between points, respectively using a multichannel detector (see chapter 2) between 500 and 900 nm. The instrument response of this apparatus is 150-250 fs depending upon the probe wavelength.

***Ti:sapphire laser transient absorption spectroscopy***

The femtosecond Ti:sapphire transient absorption spectrometer was readily tested after the construction of the OPA and the pump-probe apparatus in the Ti:sapphire laser system. The excited state dynamics of the dye standard samples (Nile Blue) obtained in the dye laser system was reproduced in the Ti:sapphire laser transient absorption spectrometer. The studies of electron injection kinetics for $Ru(dcbpy)_2(NCS)_2$ sensitised $TiO_2$ films were further extended with this apparatus. The experimental conditions were extensively summarised in papers submitted for publication (Tachibana, et al. 1999, Tachibana, et al. 1999).

Excitation pulses (30~40 fs) were tuned using the optical parametric amplifier (OPA, c.f. chapter 2) at 560 nm. Excitation intensities were reduced typically to 10~12 nJ (0.2~0.24 $mJcm^{-2}$) with a spot diameter of 60~80 μm. Transient absorption data were collected with timescales of 0-6 and 0-60 ps with a time delay of 33 and 330 fs between points at probe wavelengths between 680 and 770 nm using the multichannel detector (see chapter 2). All experiments were carried out with the magic angle configuration (ca. 54.7°) between pump and probe pulses with a repetition rate of 1 kHz at 20 °C. The stability of all samples was monitored by the change of the signal size during all of transient absorption experiments and by the change of the ground state absorption maximum before and after the transient absorption experiments. A fresh spot in the films was always used to collect data whenever the amplitudes of transient spectra are altered by 5~20 % (see section 4.4 for the detail).

The density of injected electrons was estimated both by determination of the number of excited dye molecules per unit area assuming unity electron injection yield (1), and by assessment of the number of dye cation molecules per unit area following the magnitude of the dye ground state absorption bleach resulting from cation formation (2).

1) The number of nanoparticles in 1 $cm^2$ of the film was calculated for an average $TiO_2$ particle diameter of 15 nm (see chapter 2) and a film thickness of 8 μm, and is approximately $2.4 \times 10^{14}$ particles in the film with an assumption of close packing. Using an excitation energy and an excitation area of the pump pulse to the sample, the number of absorbed photons, i.e. the number of the excited states per pulse, is estimated to be $2\sim4.5 \times 10^{14}$ / $cm^2$ (the error results from uncertainty of the diameter of the pump pulse). These values therefore result in 0.8~1.8 excited dyes / particle in the film.

2) The number of the dye cation molecules is calculated from determination of the concentration, c, in the $TiO_2$ film in equation 4.1.

$$\Delta OD(Ru^{III}) = \Delta\varepsilon(Ru^{III})c\ell \qquad \text{Equation 4.1}$$

$\Delta\varepsilon$ is the absorption coefficient difference and l is the optical path length of a sample. $\Delta\varepsilon(Ru^{III})$ is estimated with the excited state quenching of $Ru(dcbpy)_2(NCS)_2$ by $MVCl_2$. Since $\varepsilon$ of $MV^+$ radical cation ($\varepsilon$: 7000~9000 $lmol^{-1}cm^{-1}$ at 560 nm (Kosower, et al. 1964, Watanabe, et al. 1982)) state is known, $\Delta\varepsilon(Ru^{III})$ calculated is $-1\sim1.2 \times 10^4$ at 540 nm, resulting in 0.8~1 cation molecule / particle in the film.

These two methods yielded similar results within experimental uncertainties. In the experiments, the excitation intensity was therefore attenuated to yield $2\sim2.4 \times 10^{14}$ injected electrons / $cm^2$ film (0.8~1 injected electrons / nanoparticle).

All transient data collected with the dye coated $TiO_2$ and $ZrO_2$ films have been scaled to take account of different dye optical densities of these films at the excitation wavelength and difference in excitation intensities used in each experiment, allowing the quantitative comparison of amplitudes of the transient data collected with these two samples. Moreover, for all experiments, control data were collected with undyed nanocrystalline films in order to determine the magnitude of signals arising from the excitation of intra-band states of the semiconductor. In all cases the undyed films exhibited negligible transient signals.

### 4.3.2 Experimental results

#### 4.3.2.1. Steady state absorption and emission spectra

Figure 4.1a shows steady state absorption and emission spectra of $Ru(dcbpy)_2(NCS)_2$ dissolved in ethanol. Based upon analogies with these and other studies (for $(Ru^{III}(bpy)_2bpy^-)^{2+}$ complex and their analogue molecules) (Kalyanasundaram 1982), the 538 nm absorption band observed for $Ru(dcbpy)_2(NCS)_2$ can be assigned to a $t_{2g} \rightarrow \pi^*$ metal-to-ligand charge transfer (MLCT) transition (Nazeeruddin, et al. 1993). The dye moreover exhibits a weak absorption tail extending to 750 nm associated with lower energy electronic states. The emission also has a broad band, implying multiple excited states, and is moreover strongly red shifted (emission maximum at 755 nm) with a very low emission yield ($\Phi_{em} = 4 \times 10^{-3}$ at 125 K) (Nazeeruddin, et al. 1993). The low yield

and large red shift of the emission is consistent with rapid relaxation of the initially formed singlet excited state to lower energy, weakly emissive states (see below).

Low temperature luminescence studies for $(Ru^{III}(bpy)_2bpy^-)^{2+}$ have indicated that the lowest excited state comprises a manifold of MLCT (d, $\pi^*$) states of primarily triplet character, which decay on the nanosecond timescale (De Armond and Myrick 1989, Kalyanasundaram 1982). The weak long wavelength absorption tail has been attributed to direct excitation of this luminescent state (Kalyanasundaram 1982). Recent theoretical works with ruthenium bipyridyl complexes suggest that the lowest excited states are degenerate and have predominantly triplet character with mixture of weak singlet (Daul, et al. 1994). Kober et al. reported that $Ru(bpy)_3^{2+}$ contains only 0~10 % of singlet character (Kober, et al. 1982). Rensmo et al. recently suggested from the study with MO calculations that four different singlet excited states contribute to the ground state absorption between 500 and 700 nm (Rensmo, et al. 1998).

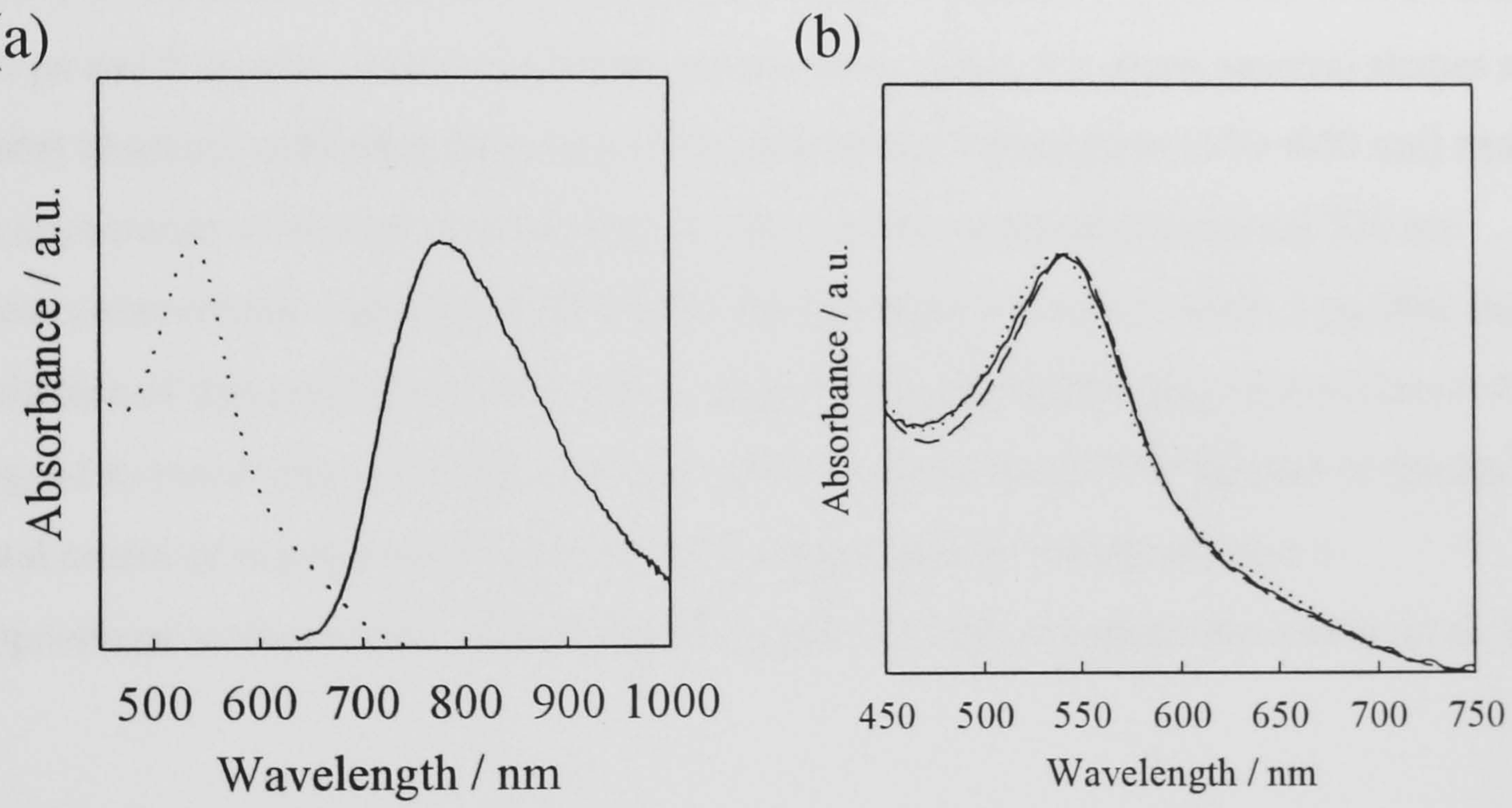



Figure 4.1. (a) Steady state absorption (·····) and emission (——) spectra of $Ru(dcbpy)_2(NCS)_2$. The emission was measured with an excitation wavelength of 531 nm. (b) Steady state absorption spectra of $Ru(dcbpy)_2(NCS)_2$ in ethanol (·····) and the same dye adsorbed onto the surface of a nanocrystalline $TiO_2$(——) and $ZrO_2$(– –) films. The spectra were normalised to the absorption maximum at 538 nm, after subtraction of the spectra obtained for undyed films, and were uncorrected for light scatter.

Figure 4.1b compares steady state absorption spectra of $Ru(dcbpy)_2(NCS)_2$ in ethanol with that of the dye adsorbed onto the nanocrystalline $TiO_2$ and $ZrO_2$ films. Adsorption onto the films results in only a slight change in the dye absorption spectrum, in contrast to results which were reported for other sensitiser dyes (e.g. $Ru(dcbpy)(bpy)_2^{2+}$ (Vinodgopal, et al. 1995)). This observation suggests that sensitisation of dye molecules on either $TiO_2$ or $ZrO_2$ surface indicates the same interaction as that of dyes with ethanol solvent molecules, and does not form a different type of absorption band such as a direct excitation band for the dye to $TiO_2$ charge transfer.

4.3.2.2 Transient results: solution phase

***Transient absorption of $Ru(dcbpy)_2(NCS)_2$ excited state***

Absorption difference spectra of $Ru(dcbpy)_2(NCS)_2$ in ethanol, obtained at a time delay of 5 ps and 5 ns after optical excitation, are shown in figure 4.2. Both spectral shapes are almost identical, exhibiting bleaching of the ground state absorption (500~600 nm) and the appearance of excited state absorption with a positive maximum around 720 nm. These observations suggest that the MLCT excited state is formed within 5 ps after the excitation of dye molecules. The positive excited state absorption may be associated with a ligand to metal charge transfer transition (LMCT) from the $(NCS)^-$ ligands to the $Ru^{3+}$ metal centre of the dye excited state since the magnitude of this absorption is proportional to the number of NCS ligands included in this complex (Noukakis, et al. ).

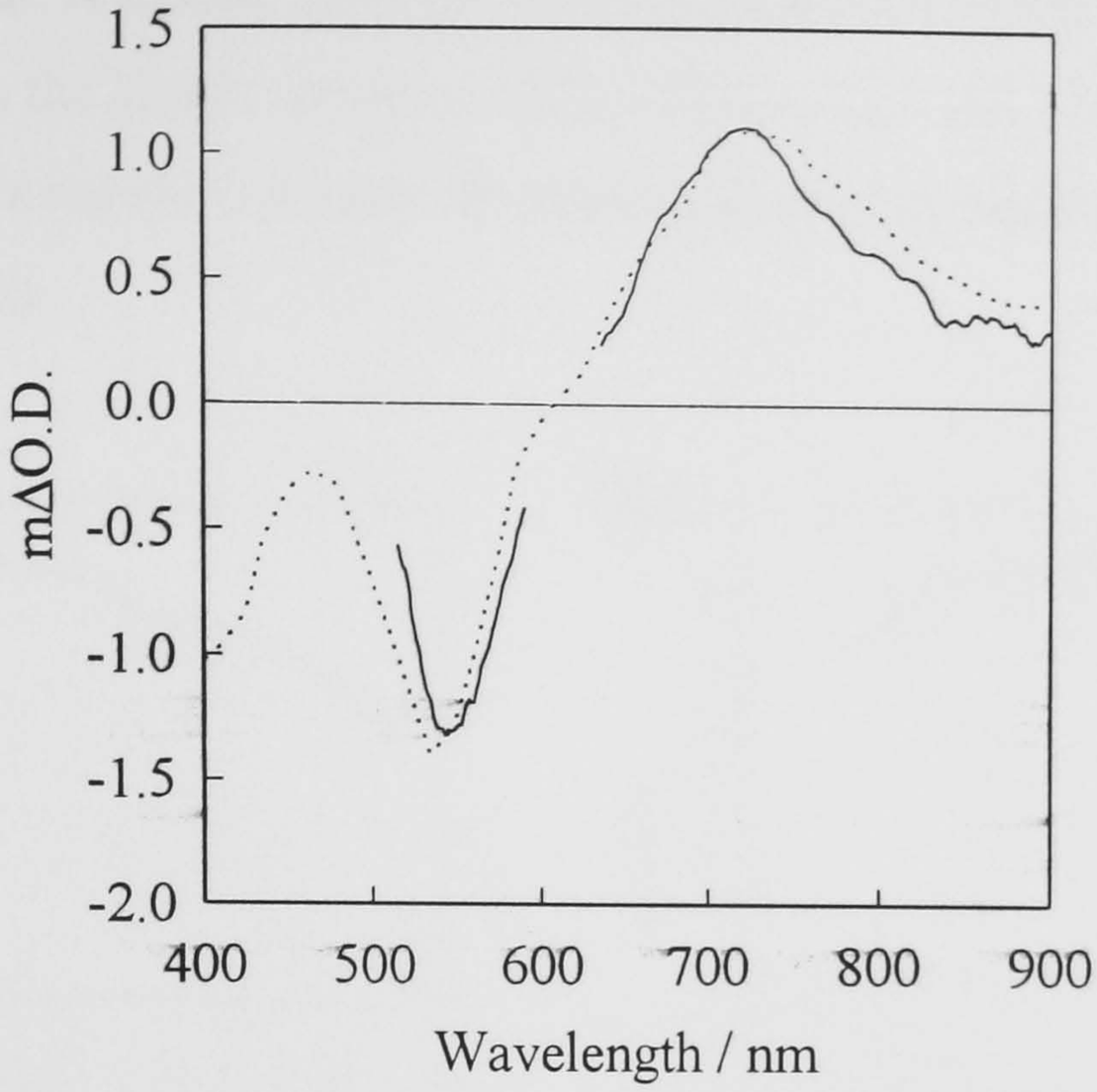



Figure 4.2. Absorption difference spectra of $Ru(dcbpy)_2(NCS)_2$ in ethanol solution. The spectra are obtained at time delays of 5 ps after 605 nm excitation (——) and 5 ns after 510 nm excitation (·····). The spectra are normalised at the maximum of transient absorption at 720 nm.

The presence of the fluorescent singlet excited state of $Ru(dcbpy)_2(NCS)_2$ would be readily detected in the data by the presence of stimulated emission from this state. Stimulated emission would appear in the transient spectra as a negative signal with a similar amplitude to the ground state bleach, but red shifted from it. The decay of this signal is associated with relaxation to the states with only weak radiative coupling to the ground state. However, no such decay is observed with excitation wavelengths of 525, 560 and 600 nm (see chapter 5 for the details), indicating that any singlet state populated during the experiments has decayed within the time resolution (100 fs) to the relaxed state.

After the rapid completion of the singlet excited state relaxation, the transient data indicate growth of transient absorption with a maximum around ~720 nm as shown in figure 4.3. Global analysis (see appendix B) results in, at least, two exponential components with lifetimes of 2.5 and 15 ps. The kinetic (or 'amplitude') spectra of these components are also shown in figure 4.3. The excitations at 525, 560 and 600 nm

exhibited identical kinetic spectra (data are not shown). The origin(s) of these relaxation processes is not clear. It should, however, be noted that these components are readily distinguishable from the kinetic spectrum of the electron injection process as they were not associated with a red shift towards the induced absorption maximum at 800 nm (see below for the details).

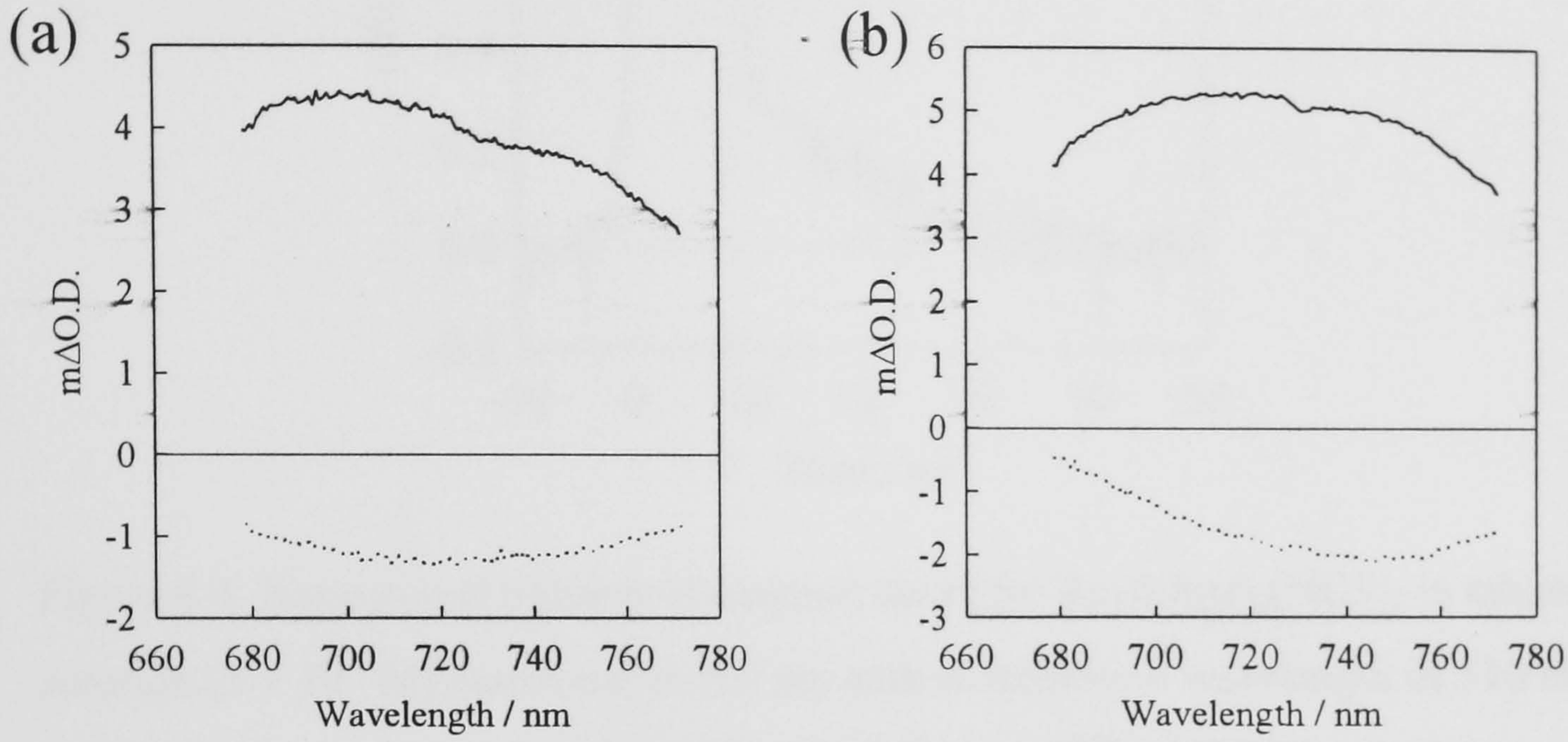



Figure 4.3. Absorption difference spectra (——) and kinetic spectra (·····) of the kinetic components obtained for $Ru(dcbpy)_2(NCS)_2$ in ethanol solution. The absorption difference spectra were observed at 6 (a) and 60 (b) ps following 560 nm excitation. The components with time constants of 2.5 and 15 ps result from global analysis over 680 ~ 770 nm.

Figure 4.4 shows a nanosecond transient absorption decay for $Ru(dcbpy)_2(NCS)_2$ in ethanol solution, indicating the decay of the lowest excited state to ground. The analysis of this decay results in biexponential kinetics with time constants of 5 and 18 ns. In degassed solutions of the same dye, the time constant of 50 ns has been reported (Nazeeruddin, et al. 1993).

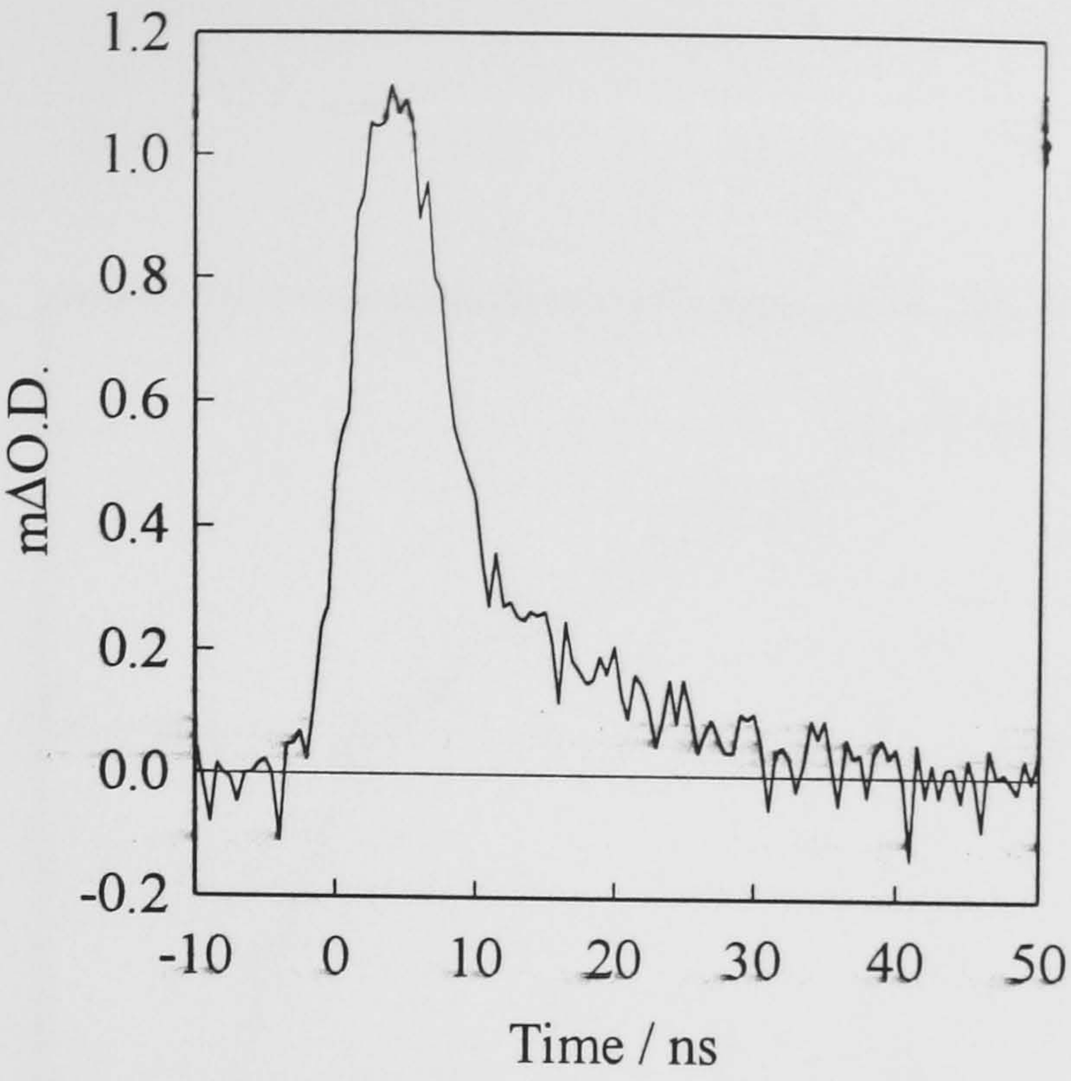



Figure 4.4. Nanosecond transient absorption decay for $Ru(dcbpy)_2(NCS)_2$ in ethanol solution ($5 \times 10^{-5}$ M) monitored at 700 nm with an excitation wavelength of 510 nm. The kinetics are attributed to decay from $Ru(dcbpy)_2(NCS)_2$ MLCT excited to ground states.

***Formation of cation spectrum***

$Ru(dcbpy)_2(NCS)_2$ cation difference spectrum was obtained by excitation (532 nm) of dye molecules in the presence of the electron acceptor methyl viologen ($MV^{2+}$), and taken at a time delay of 10 μs, to avoid any residual contributions from the dye excited state (decaying within 50 ns as shown in figure 4.4). Optical excitation of $Ru(bpy)_3^{2+}$ in the presence of $MV^{2+}$ has previously been shown (Darwent, et al. 1982) to generate the $Ru(bpy)_3^{3+}$ and radical $MV^{+}$ ions with a quantum yield of up to 0.4. Contributions to the experimental data resulting from formation of the $MV^{+}$ radical cation (absorption maximum at 610 nm) (Kosower and Cotter 1964, Watanabe and Honda 1982) have been subtracted from the transient data. The resultant absorption difference spectrum of the dye cation state is shown in figure 4.5. Also shown in figure 4.5 is a transient absorption different spectrum of $Ru(dcbpy)_2(NCS)_2$ excited state at 5 ps after 605 nm excitation for comparison with the dye cation spectrum, taken from figure 4.2. This dye cation difference spectrum also exhibits bleaching of ground state absorption, but can be readily

distinguished from the excited state by a red shift of the positive absorption maximum to 800~850 nm.

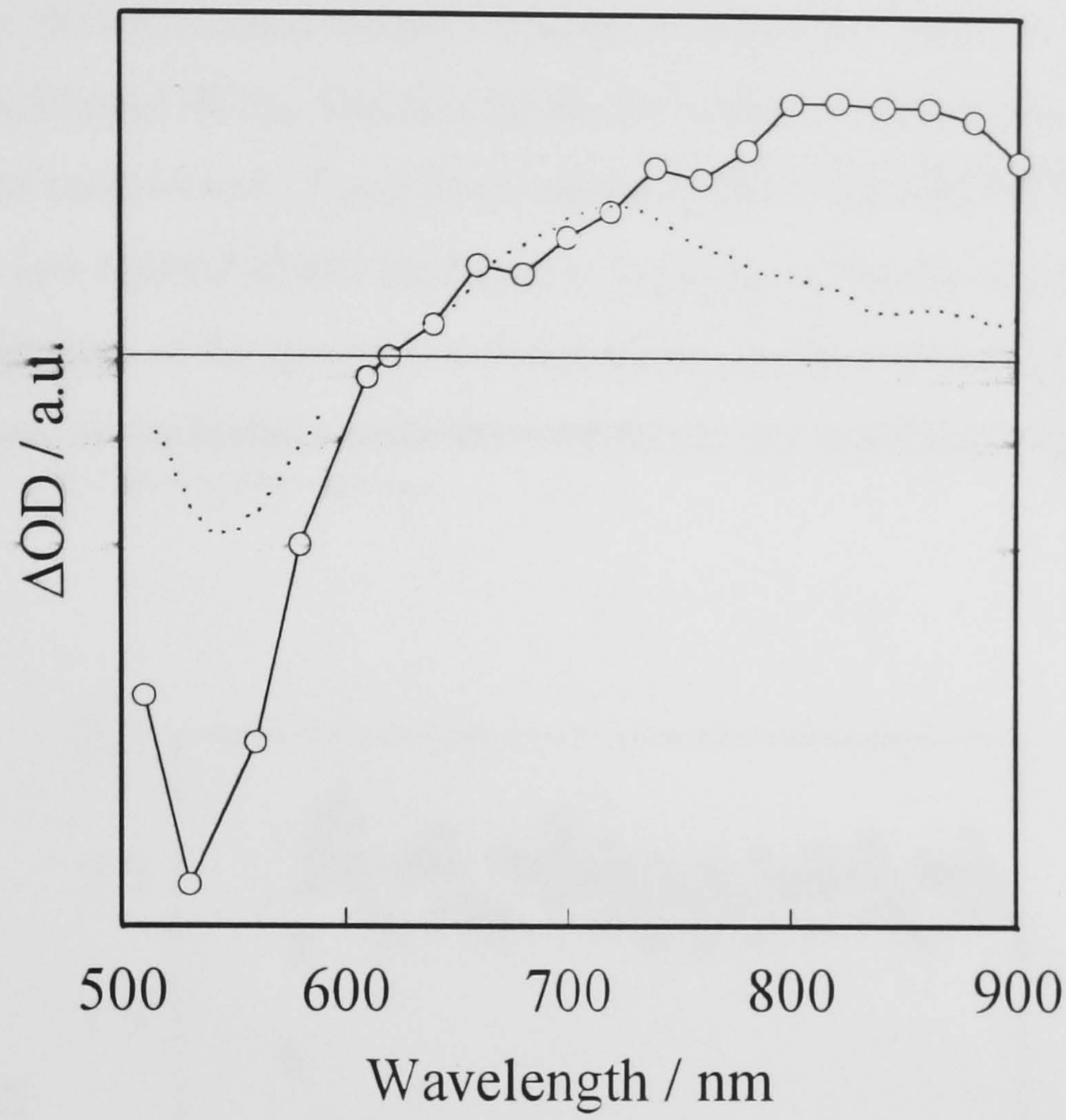



Figure 4.5. Absorption difference spectra of the formation of cation (—o—) and excited (·····) states of $Ru(dcbpy)_2(NCS)_2$ in ethanol solution. The difference spectrum for the excited state at a time delay of 5 ps after 605 nm excitation is taken from figure 4.2. The dye cation state spectrum was obtained at a time delay of 10 μs after excitation of $Ru(dcbpy)_2(NCS)_2$ in the presence of the electron acceptor methyl viologen ($MV^{2+}$). The spectrum does not contain any residual contributions from the dye excited state which decays within nanosecond timescales. Contributions to this difference spectrum of the $MV^{+}$ radical cation have been subtracted from the transient data.

4.3.2.3 Transient data: Nanocrystalline films

***Nanosecond transient absorption and luminescence decays***

Figure 4.6 shows the nanosecond transient absorption decays for $TiO_2$ and $ZrO_2$ films sensitised by $Ru(dcbpy)_2(NCS)_2$. The data for the $ZrO_2$ films exhibits biexponential decay kinetics with time constants of 3.5 and 24 ns, similar to those obtained for the dye in ethanol solution (see figure 4.4) and attributed to the decay of the dye excited state to ground (the assignment of the spectrum is discussed below). In contrast to the $ZrO_2$ films, no significant decay kinetics were observed for the dye sensitised $TiO_2$ films on this timescale.

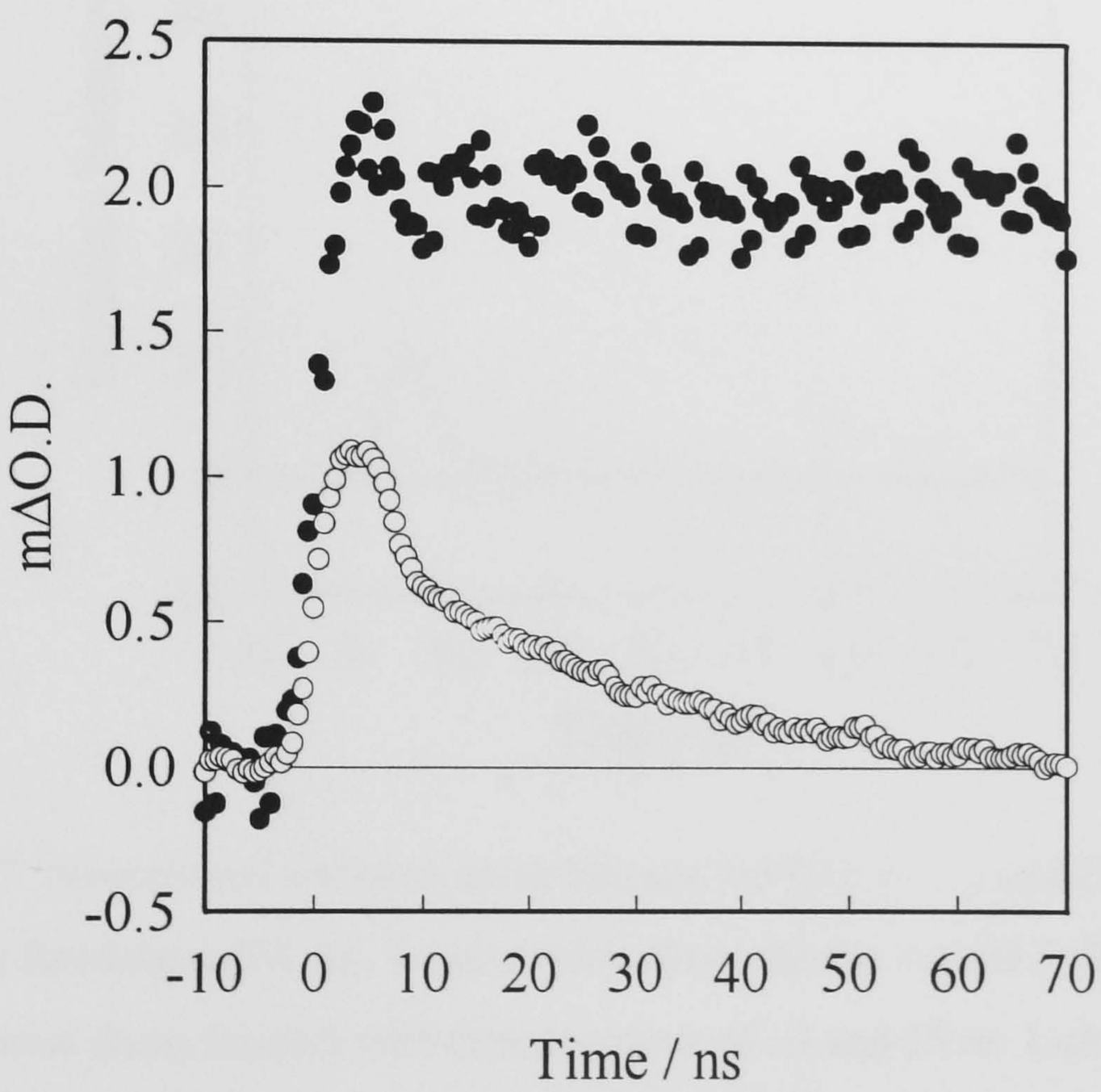



Figure 4.6. Nanosecond transient absorption decays for $Ru(dcbpy)_2(NCS)_2$ sensitised $TiO_2$ (•) and $ZrO_2$ (o) films. The kinetics are monitored at 800 nm for the $TiO_2$ film and at 700 nm for the $ZrO_2$ film following 510 nm excitation.

Figure 4.7 compares the nanosecond luminescence decay kinetics of $Ru(dcbpy)_2(NCS)_2$ adsorbed onto $TiO_2$ and $ZrO_2$ films. The $ZrO_2$ films exhibit biexponential decay kinetics

on nanosecond timescales (lifetimes of 3 and 25 ns), which are almost identical to the transient absorption decay kinetics described above. In contrast, luminescence from the dye coated $TiO_2$ film is strongly quenched, with its decay being primarily instrument response limited. From the extent of the quenching observed for the dye coated $TiO_2$ film, it is concluded that the lifetime of the dye luminescent excited state in the $TiO_2$ films is <500 ps. This is only an upper limit for this excited state lifetime, as luminescence from $TiO_2$ intra-band states (Willig, et al. 1993) and / or from a small sub-population (<10 %) of unquenched dye molecules may also contribute to the small residual signal.

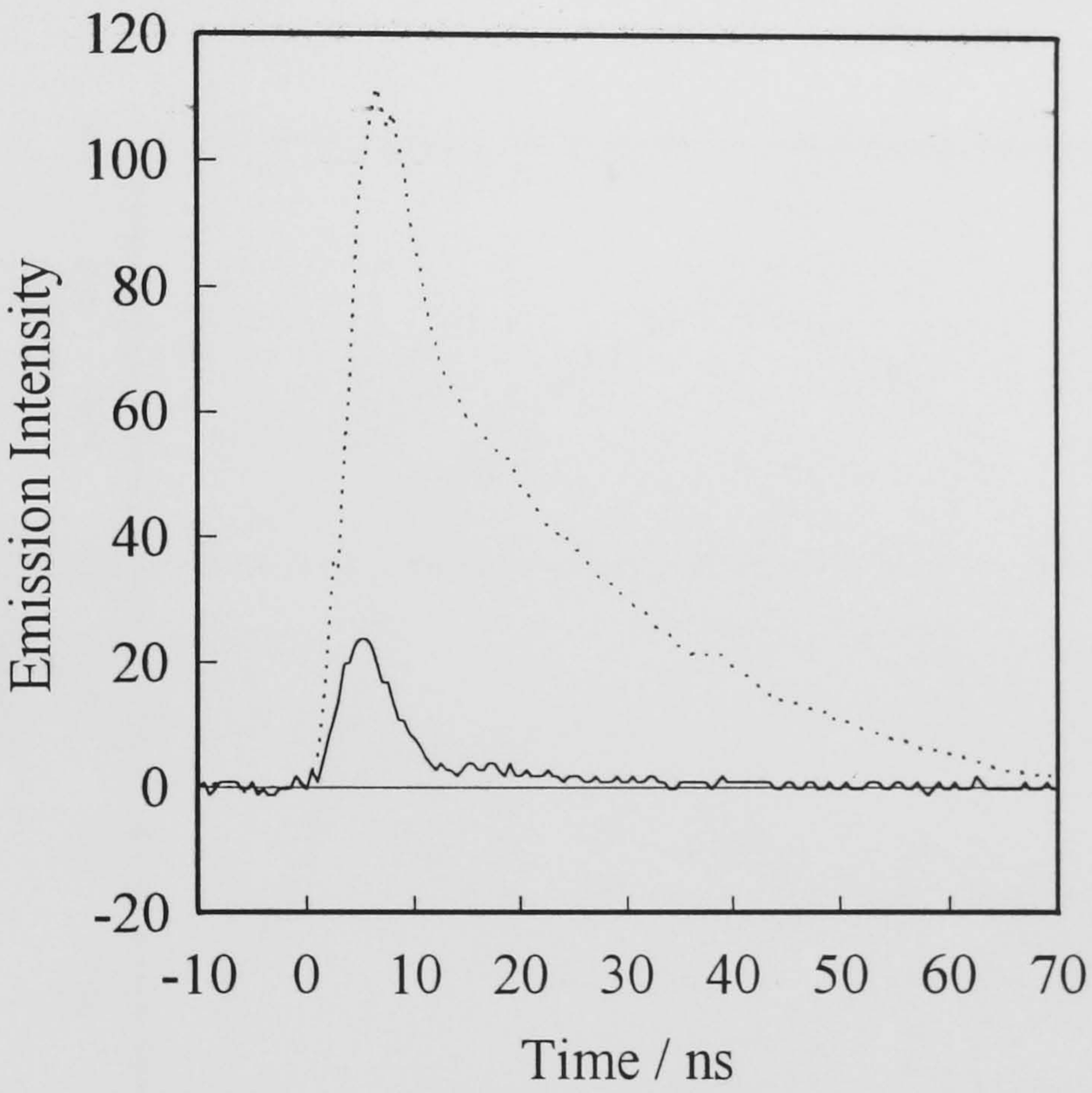



Figure 4.7. Nanosecond emission decay kinetics for $TiO_2$ (——) and $ZrO_2$ (·····) films coated by $Ru(dcbpy)_2(NCS)_2$. Luminescence from the dye coated $ZrO_2$ films exhibits biexponential decay kinetics with time constants of ~3 and 25 ns. Luminescence from the dye coated $TiO_2$ films is strongly quenched, and dominated by a fast, instrument response limited decay. A small amplitude of nanosecond decay can also be resolved. The quenching of dye luminescence observed for the $TiO_2$ film indicates that the dye excited state lifetime of these films is <500 ps.

### *Absorption difference spectra*

Figure 4.8 compares transient absorption difference spectra obtained at a time delay of 5 ns for $Ru(dcbpy)_2(NCS)_2$ sensitised $TiO_2$ and $ZrO_2$ films. The spectrum obtained for the $ZrO_2$ films sensitised by $Ru(dcbpy)_2(NCS)_2$ is very similar in shape to that obtained from the dye in ethanol solution as shown in figure 4.2, and therefore can be assigned to the dye excited state. In comparison with this dye excited state, the spectrum obtained for the $TiO_2$ films exhibits a positive absorption maximum at 800 nm, which is comparable to that of the cation state obtain from the dye in solution phase (see figure 4.5).

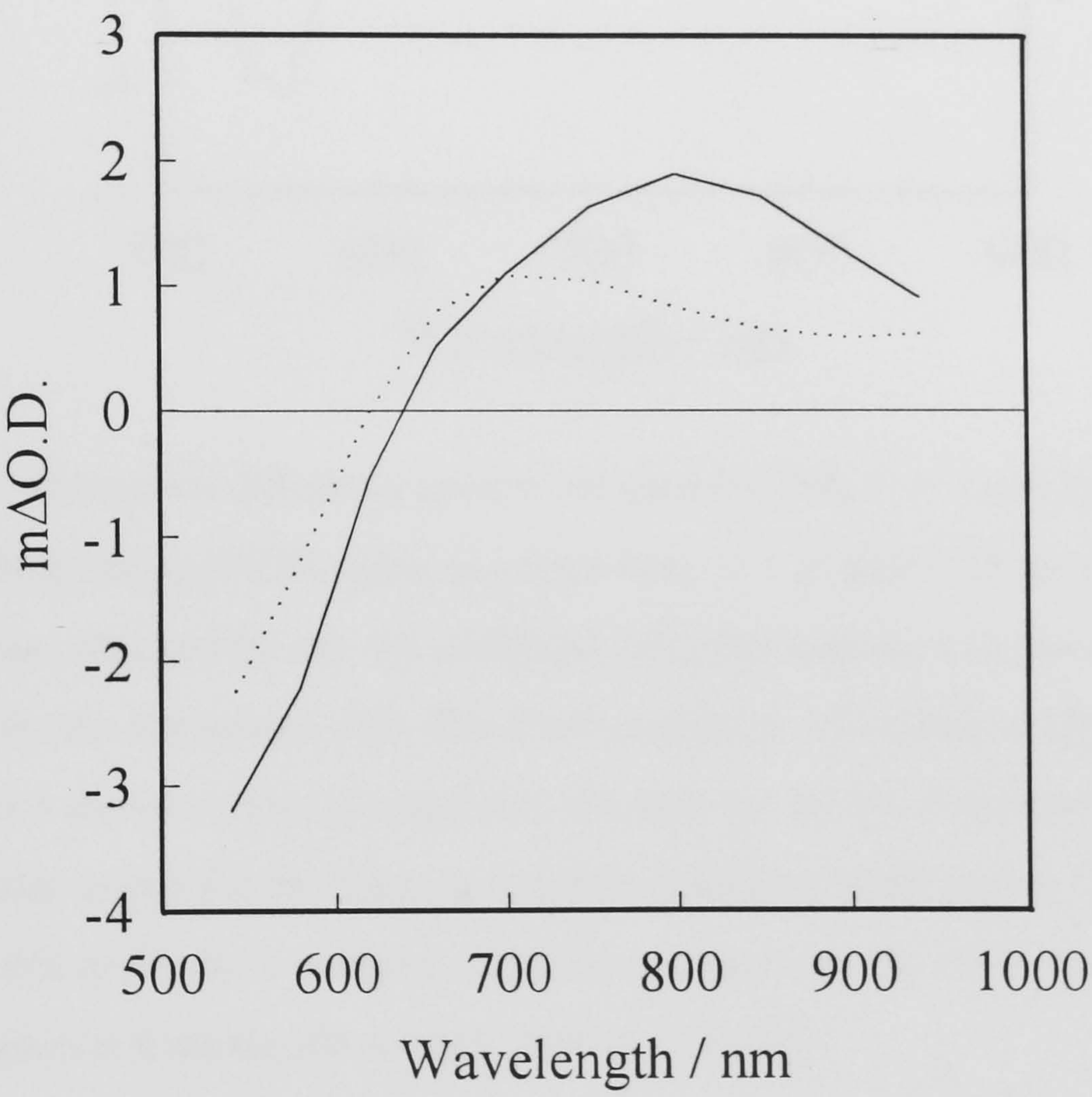



Figure 4.8. Transient absorption difference spectra obtained for $TiO_2$ (——) and $ZrO_2$ (·····) films sensitised by $Ru(dcbpy)_2(NCS)_2$ taken at a time delay of 5 ns following 510 nm excitation. Both spectra exhibit bleaching of the ground state. However, the spectrum obtained for the $ZrO_2$ films exhibits a positive absorption maximum at 700 nm while that for the $TiO_2$ films shows a maximum at 800 nm.

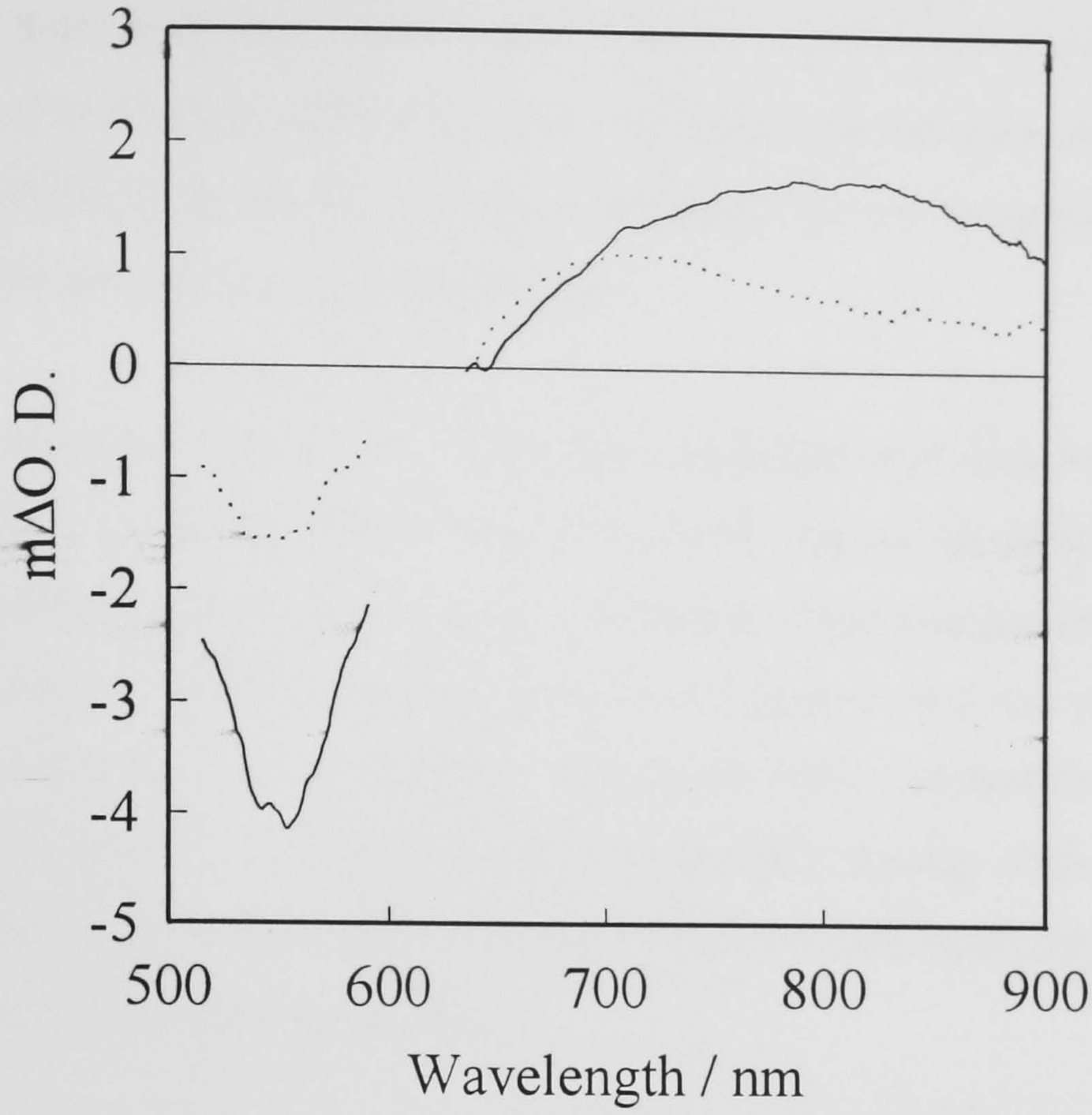



Figure 4.9. Absorption difference spectra obtained for $TiO_2$ (——) and $ZrO_2$ (·····) coated by $Ru(dcbpy)_2(NCS)_2$ taken at a time delay of 5 ps after 605 nm excitation. The spectrum obtained for the dye sensitised $ZrO_2$ film exhibits a maximum at 710 nm, while for the dye coated $TiO_2$ film this maximum is red shifted to 800 nm as observed at 5 ns. Moreover, the spectrum obtained for the dye sensitised $TiO_2$ films is very similar to that for the dye cation state in ethanol solution shown in figure 4.5. Therefore this spectrum is assigned to the charge separated state $dye^+ e_{cb}^-$ formed by electron injection from the dye excited state into the $TiO_2$.

Absorption difference spectra obtained for $TiO_2$ and $ZrO_2$ films coated with $Ru(dcbpy)_2(NCS)_2$, taken at a time delay of 5 ps, are shown in figure 4.9. Comparison of figures 4.5, 4.8 and 4.9 readily allows assignment of these spectra. The spectrum obtained for the dye coated $ZrO_2$ film exhibits a peak at 720 nm. As discussed above it is assigned to the dye MLCT excited state, which is consistent with the solution data. In contrast, the spectrum obtained with the dye coated $TiO_2$ film exhibits a red shift of this peak to 800 nm, as observed for cation state of $Ru(dcbpy)_2(NCS)_2$ in solution, and is

therefore assigned to the formation of this state. The formation of the dye cation state in this film is presumably coincident with the appearance of a conduction band electron in the $TiO_2$ ($e_{cb}^-$). Such an electron exhibits only relatively weak absorption throughout this spectral region (For example, $\Delta OD$ of about $4 \cdot 10^{-4}$ at 800 nm estimated from $\varepsilon_{800}$: 1200 $M^{-1}cm^{-1}$ (Willis, et al. 1999)), however its absorption can not be separated from the absorption by the dye cation in these experiments.

The transient absorption spectra taken for the dye coated films were observed under identical excitation conditions, and have been normalised to take account of small differences in optical density at the excitation wavelength. These spectra therefore correspond to those obtained for equal excited state populations, and may be quantitatively compared, as discussed below. The smaller signal observed between 500 and 600 nm for the dye coated $ZrO_2$ film may be attributed to overlap of the negative ground state bleach with positive signals associated with the LMCT and bipyridyl anion $\pi - \pi^*$ absorption of the dye excited state.

***Transient absorption kinetics***

The difference spectra obtained with $Ru(dcbpy)_2(NCS)_2$ coated $TiO_2$ films exhibit some temporal evolution. Figure 4.10 represents transient absorption spectra obtained for the dye sensitised $TiO_2$ films at probe wavelengths between 680~770 nm. As discussed above, electron injection from the photoexcited $Ru(dcbpy_2(NCS)_2$ to $TiO_2$ results in a red shift of a induced transient absorption maximum from ~700 nm for the dye excited state to ~800 nm for the $dye^+(TiO_2)^-$ state. It is therefore clear that the spectrum at 100 fs in figure 4.10 exhibits mixture of spectral shapes of the dye excited state and the charge separated state, suggesting some of electron injection processes complete within 100 fs (instrument response).

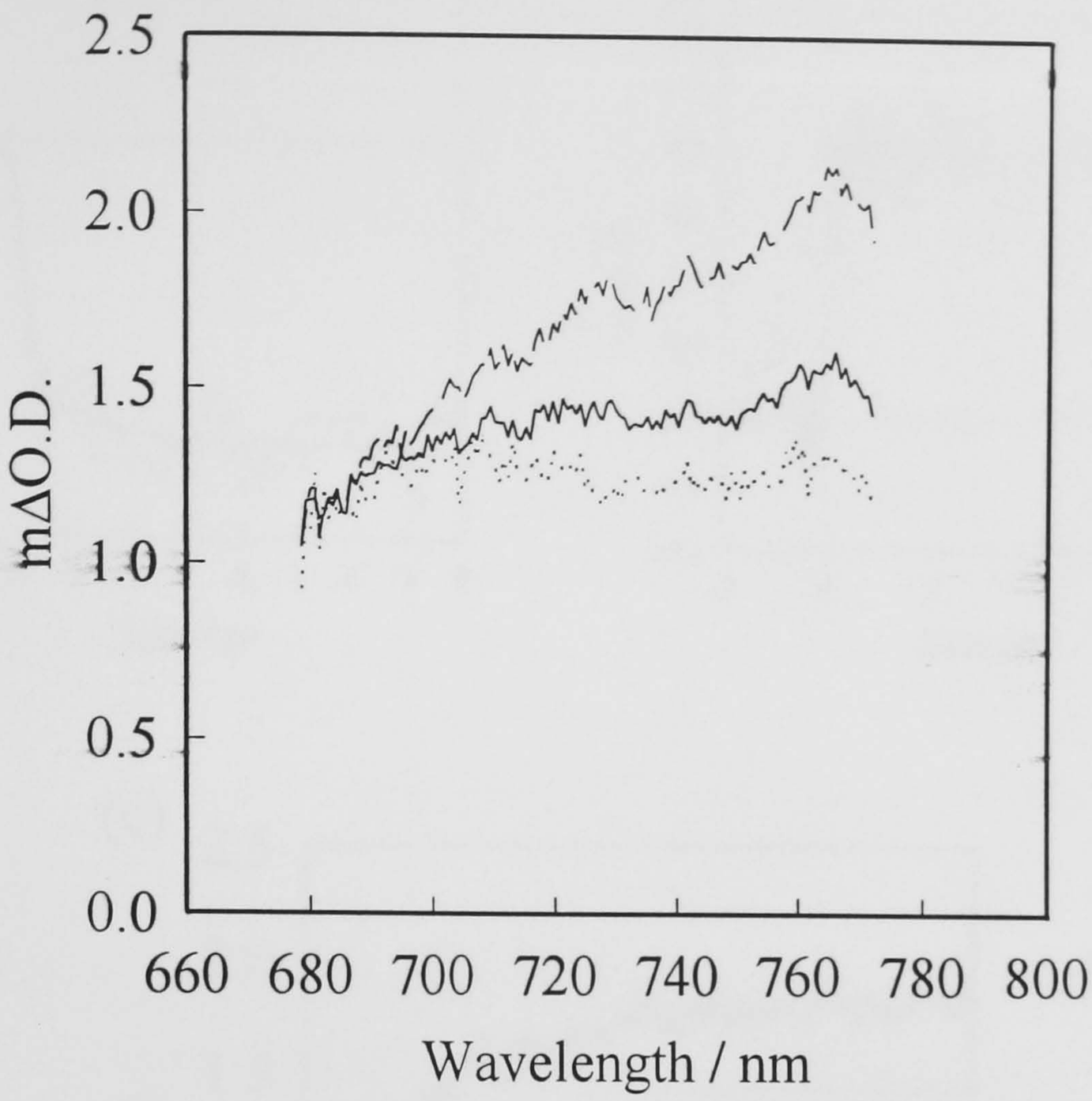



Figure 4.10. Transient absorption spectra obtained for $Ru(dcbpy)_2(NCS)_2$ sensitised $TiO_2$ films covered in EC / PC. The spectra were taken at 0.1 (·····), 6 (——) and 60 (– – –) ps after an excitation at 560 nm, exhibiting a positive absorption growth with a maximum towards 800 nm.

Typical transient absorption kinetics at probe wavelengths of 560, 680 and 760 nm are shown in figure 4.11. The insert in figure 4.11c shows an expansion of the data at early times. Also shown in the insert is data obtained for an undyed film in order to determine the magnitude of signals arising from the excitation of intra-band states of the semiconductor. The data exhibit negligible amplitude except for oscillatory signals for time delays less than our instrument response resulting from impulsive stimulated Raman scattering processes (Hong, et al. 1993) (see chapter 2 for the details). Moreover the transient data obtained for the undyed films in a wavelength range from 680 to 770 nm indicated no significant amplitude, resulting in negligible contribution to the transient absorption spectra obtained for the dye sensitised $TiO_2$ films.

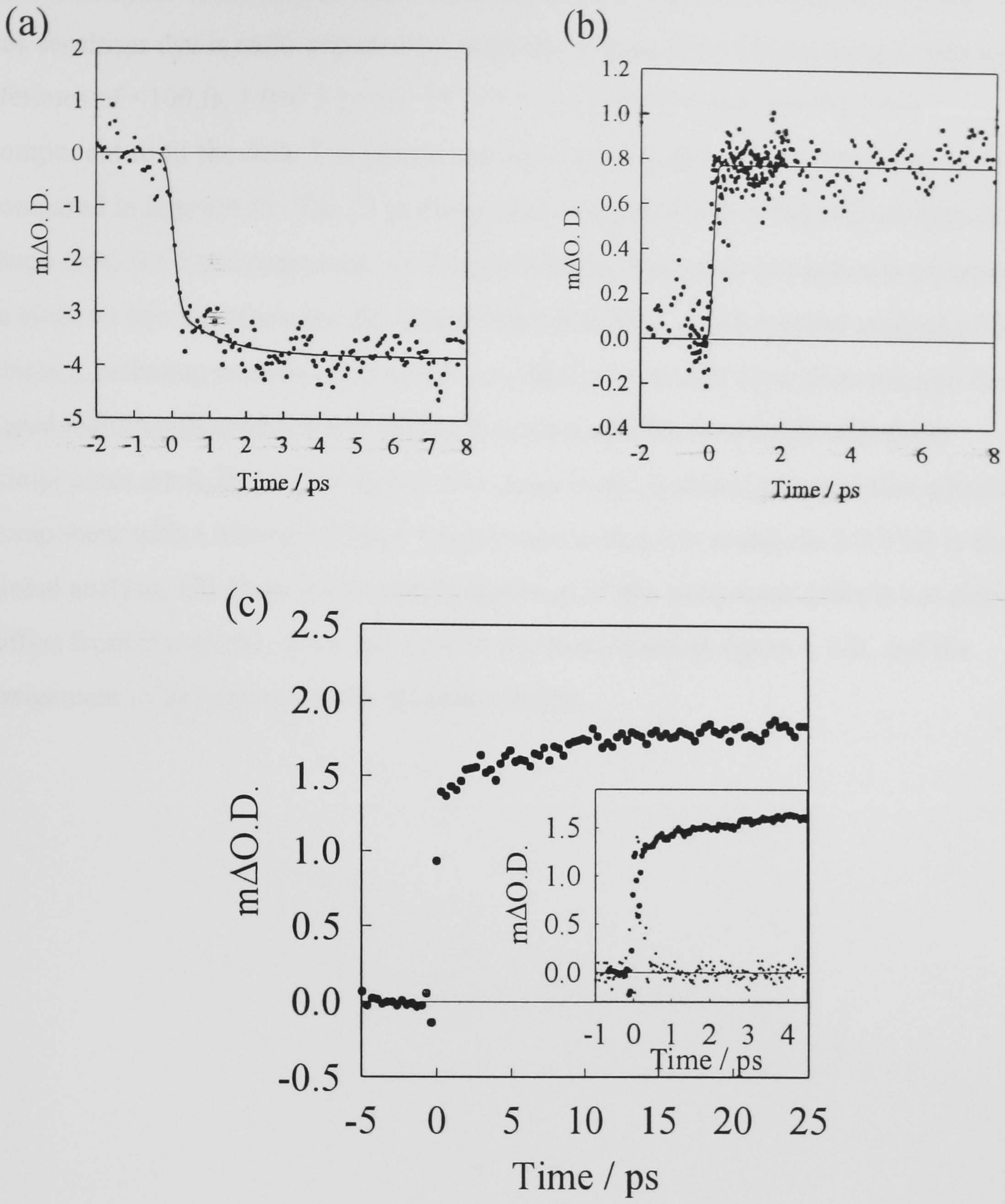
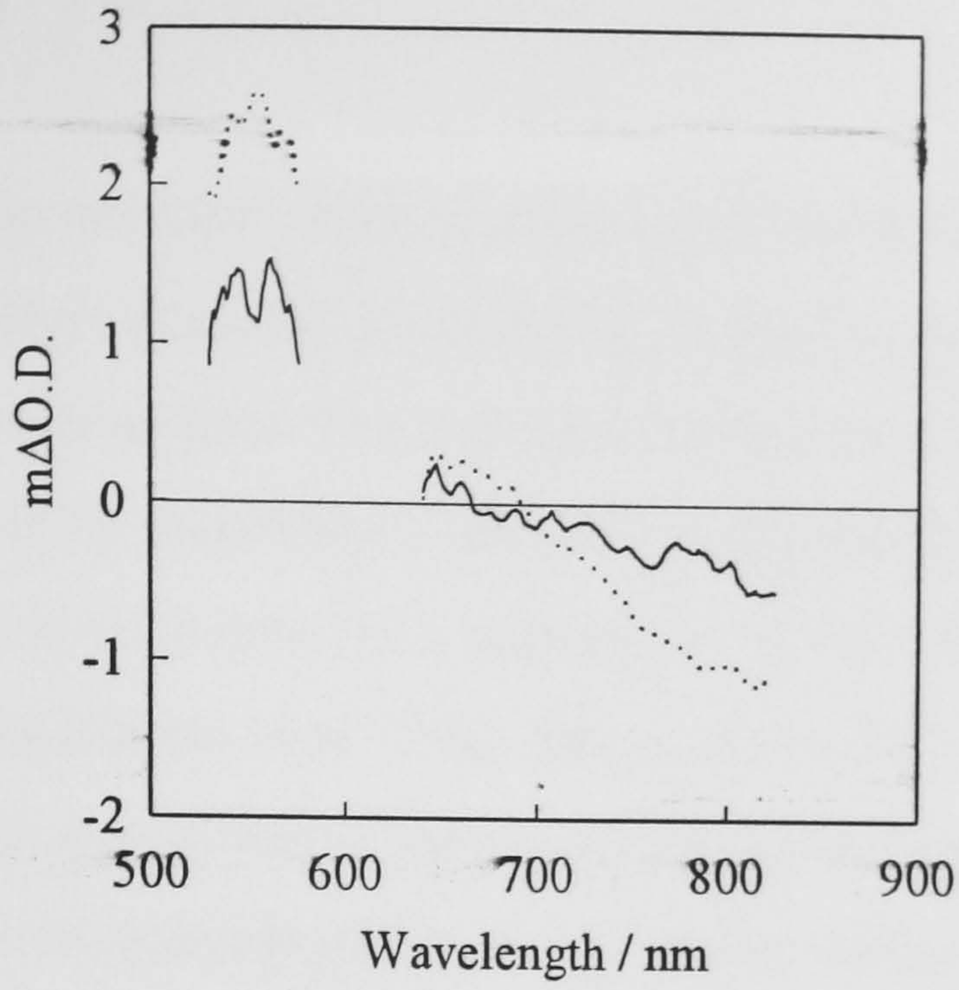



Figure 4.11. Transient absorption kinetics obtained for the $Ru(dcbpy)_2(NCS)_2$ coated $TiO_2$ films. The kinetics are monitored at 560 (a) and 680 (b) with the excitation at 605 nm by means of the femtosecond dye laser system. The solid lines indicate exponential analysis fits to the data. Also shown is the transient data observed at a probe wavelength of 760 nm (c) following 560 nm excitation by the femtosecond Ti:sapphire laser system. Control data is shown as unsensitised $TiO_2$ film (dagger) in the insert.

Global analyses of the kinetic data indicated that the dynamics of electron injection with this sensitiser dye is multi-exponential, requiring at least three kinetic components with lifetimes of <100 fs, 1.0±0.3 ps and 13.0±3.0 ps in addition to a non-decaying component to fit the data. The kinetic spectra of these 1 and 13 ps components were compared in figure 4.12. The 13 ps component in figure 4.12b is indistinguishable in shape from the 1 ps component. As discussed below, these two components are assigned to electron injection from the dye excited state into $TiO_2$. A full spectral analysis of these kinetics, including consideration of the contribution of excited state absorption to the signal indicates that the relative yields of electron injection associated with these components are 0.29, 0.25, 0.46 (± 0.05) respectively. It should be noted that a fourth component with a lifetime of 70 ps was resolved with a low amplitude (<10 %) in the global analysis. However the amplitude spectrum of this component (data is not shown) differs from that expected for the electron injection shown in figure 4.12b, and the assignment of this component is therefore unclear.

(a)




(b)

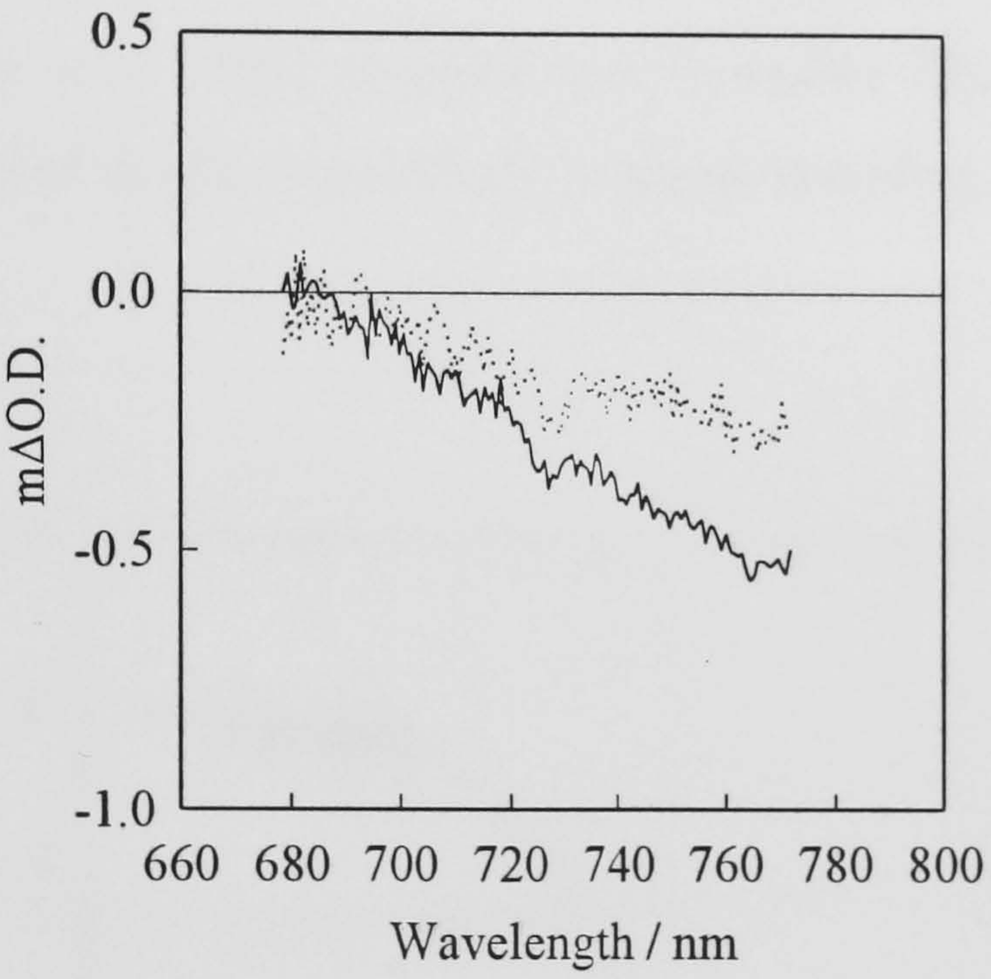



Figure 4.12. (a) Spectrum of the amplitude of the 1 ps component observed with the dye coated $TiO_2$ film (——) with 605 nm excitation. Also shown is the spectrum expected for the absorption changes associated with electron injection (·····), obtained by taking the difference between the two spectra shown in figure 4.9 assigned to the dye excited state and the charge separated state $dye^+e_{cb}^-$, respectively. It is apparent that the spectrum of the 1 ps component is very similar to that expected for electron injection. (b) Amplitude spectra of the 1 (·····) and 13 (——) ps components obtained as a result of global analysis for the data of the dye coated $TiO_2$ film with an excitation wavelength of 560 nm. It is apparent that the spectral shape of the 13 ps component is similar to that of 1 ps component.

### *Charge recombination*

A slower and multiphasic recovery of the cation absorption (figure 4.13) attributed to recombination of the charge separated state ($dye^+ e_{cb}^-$) was observed on the microsecond-millisecond timescales. These recombination kinetics are highly non-exponential and therefore for convenience plotted on a logarithmic time axis. The detailed studies of these kinetics have been reported by Mr. Saif Haque in Centre for Photomolecular Sciences (Haque, et al. 1998, Haque, et al. 1999). For all samples studied here, a significant proportion of this recombination occurred on timescales as slow as 1 ms, while the transient absorption change shown in figure 4.6 indicated only marginal decay on nanosecond timescales. Similar multi-phasic recombination kinetics have previously been reported for chlorophyll derivatives (Kay, et al. 1994) and for $Ru(dcbpy)_3^{2+}$ (O' Regan, et al. 1990) sensitised nanocrystalline $TiO_2$ films, and attributed to the disordered nature of the film (specifically electron tunnelling between trap states of the semiconductor).

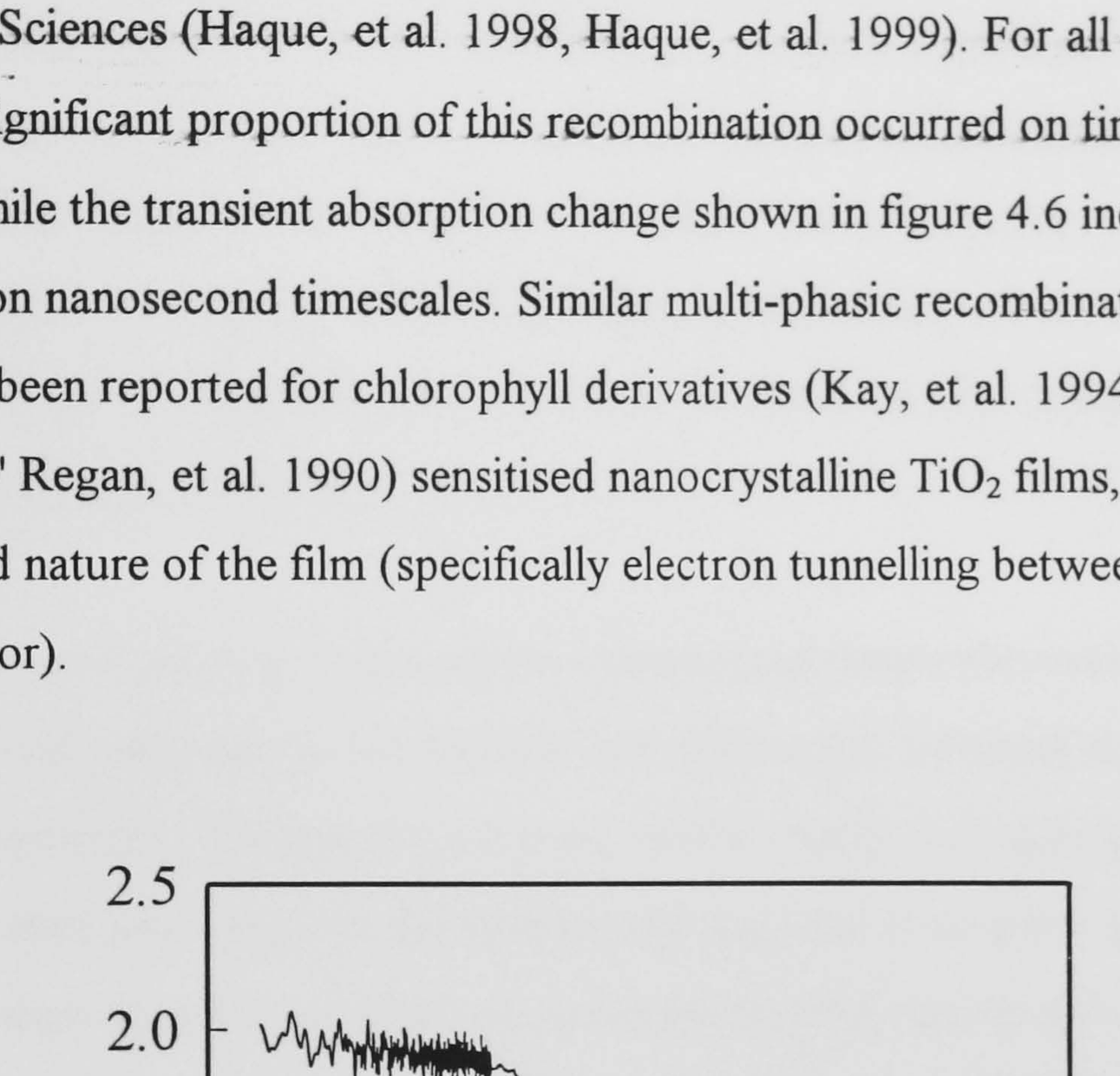



Figure 4.13. The kinetics of charge recombination for the $Ru(dcbpy)_2(NCS)_2$ coated $TiO_2$ film, monitored by the decay of the cation absorption band at 820 nm. The data

are shown on a ln / log plot and exhibit multi-phasic kinetics on micro-millisecond timescales.

### 4.3.3 Discussion

The dye coated nanocrystalline $TiO_2$ film was prepared with low dye coverage onto the surface of $TiO_2$ (only <20 % of monolayer) in order to minimise dye excited state interaction between neighbouring dyes (see chapter 5 for the calculation of dye coverage). The sample moreover did not include a redox active electrolyte which is employed in the commercial solar cells. The study performed in this chapter was aimed at characterising the interfacial electron transfer at the dye / semiconductor interface. The choice of this experimental system has necessitated a careful study of not only the sensitised film, but of the isolated dye in solution, as no transient absorption data have been reported previously for this dye.

The transient reaction kinetics in femtosecond / picosecond timescales were compared with the transient data obtained by the nanosecond-millisecond transient absorption and luminescence experiments. The dye excited state can be readily distinguished from the charge separated state ($dye^+ e_{CB}^-$) by the nanosecond transient absorption spectroscopy since the excited state decays in nanosecond timescale (see the results above), and this therefore makes possible and estimate of the electron injection efficiency of each sample. Moreover, the use of nonquenching control films (dye coated nanocrystalline $ZrO_2$) allows us to discriminate between changes in the transient data resulting solely from incorporation of the dye into a different nanocrystalline film and changes specifically associated with electron injection.

***$Ru(dcbpy)_2(NCS)_2$ excited state photophysics***

As discussed above in connection with figure 4.1, the excitation of $Ru(dcbpy)_2(NCS)_2$ indicates multiple MLCT absorption bands and their excited states are highly complex with the mixture of singlet and triplet character (De Armond and Myrick 1989, Kalyanasundaram 1982). The ultrafast measurement of the dye in ethanol solution indicated that the relaxation from the fluorescent singlet excited state completes within

the instrument response time of the apparatus (100 fs) as no stimulated emission is observed following the optical excitation at 525, 560 and 600 nm (see chapter 5 for the details of excitation wavelength dependence). Such a fast relaxation time is consistent with recent studies of analogous ruthenium bipyridyl dyes with a relaxation rate of <300 fs (Damrauer, et al. 1997) and with the results of picosecond Raman studies (Carroll and Brus 1987) of $Ru(bpy)_3^{2+}$ (see chapter 5 for the details). The ultrafast relaxation of the singlet state is also consistent with very weak fluorescence from this state in the steady state emission spectrum of this dye as shown in figure 4.1b (Nazeeruddin, et al. 1993).

Following the relaxation of the singlet excited state, the dye excited state exhibited multi-exponential relaxation processes as shown in figure 4.3. The interpretation of these processes is not obvious, and is beyond the aim of my PhD study. The comparison of the kinetic spectra associated with the electron injection (figure 4.12) and the excited state relaxation (figure 4.3), however, clearly indicated that the assignment of the electron injection is readily distinguishable to that for the excited state relaxation.

The excited state relaxation process is clearly one of energy loss processes to lower the efficiency of the solar cell, and its kinetics are competitive with the electron injection process as discussed above. However, this ultrafast relaxation process may facilitate stability of the dye molecules in the cells since the short lived singlet excited state produces a lower yield of singlet oxygen which possibly leads to degradation of the dye (Kay, et al. 1994). The relatively fast decay of the lowest excited state (nanosecond timescales as shown in figure 4.4) may moreover prevent the dye degradation.

### *Comparison of $Ru(dcbpy)_2(NCS)_2$ sensitised $TiO_2$ and $ZrO_2$ films*

The transient absorption and luminescence data indicate that the photophysics of $Ru(dcbpy)_2(NCS)_2$ adsorbed onto the $ZrO_2$ film is very similar to that observed in ethanol solution. This is consistent with previous studies (Kay, et al. 1994) of dye coated $ZrO_2$ films, which have also concluded that the 1 eV negative shift of the conduction band edge of $ZrO_2$ relative to $TiO_2$ inhibits electron injection in these films since available electron acceptor states in the mid-band gap of $ZrO_2$ is negligible. It can therefore be

concluded that the observation for this dye adsorbed onto $ZrO_2$ indicates only the dye excited state kinetics.

In contrast, the transient spectra obtained for the dye sensitised $TiO_2$ films are very similar to the cation spectra produced in the dye ethanol solution with MV. This data indicate that in this $TiO_2$ film electron injection occurs from the dye into the $TiO_2$ conduction band. Since only the small amplitude (<10 %) of the early nanosecond decay was observed (figure 4.6), being attributed to the decay of the dye excited states which cannot inject electrons, at least 90 % of the dye excited states are quenched by electron injection. This high yield for electron injection is consistent with the high energy conversion efficiencies achieved with photovoltaic solar cells employing such films (Nazeeruddin, et al. 1993).

***Kinetics of electron injection***

Electron injection kinetics should be determined with the transient absorption data as a loss of transient absorption signals resulting from the dye excited state, and the concomitant appearance of signals resulting from the charge separated state ($dye^+e_{cb}^-$). The two difference spectra shown in figure 4.9 have been assigned to these two states, and any kinetic component associated with electron injection should exhibit a wavelength dependence corresponding to the difference between these two spectra. Figure 4.12 compares this expected spectrum for the electron injection with the spectra of the 1 and 13 ps components observed with the dye sensitised $TiO_2$ film. It is apparent that the shapes of these spectra are similar, and therefore the 1 and 13 ps components are assigned to electron injection from the adsorbed dye into the $TiO_2$.

While it is concluded that the electron injection from the dye excited state into $TiO_2$ proceeds with time constants of 1 and 13 ps, the injection can be expected to occur on even shorter timescale. It is apparent from figure 4.10 that the transient spectrum at 100 fs exhibits a broad, flat positive absorption between 700 and 800 nm, consistent with a mixture of the spectra associated with the dye excited and $dye^+e_{cb}^-$ states. It can thus be concluded that the electron injection also occurs in less than the instrument response time of the apparatus (100 fs). In consequence, the electron injection kinetics observed for

$Ru(dcbpy)_2(NCS)_2$ sensitised $TiO_2$ films are multi-exponential where the global analysis requires a minimum of three exponentials with time constants of <100 fs, 1 ps and 13 ps to fit the data.

***Comparison with other studies***

The ultrafast electron injection (>$10^{13}$~$10^{11}$ $s^{-1}$) obtained for $Ru(dcbpy)_2(NCS)_2$ sensitised $TiO_2$ films in this study may originate from the use of the ruthenium dye since the ruthenium dyes have to date been the most efficient sensitiser dyes reported (Nazeeruddin, et al. 1993). According to the results of the previous studies by other research groups listed in table 4.1, $Ru(dcbpy)_2(H_2O)_2^{2+}$ also exhibits an electron injection rate of <7 ps (Eichberger and Willig 1990). However, Kamat and co-workers reported relatively slow injection rates of 2~10 ns employing $Ru(dcbpy)(bpy)_2^{2+}$ (Fessenden and Kamat 1995, Vinodgopal, et al. 1995). Some other dyes, e.g. coumarin and oxazine, were also reported to be efficient in terms of the electron injection process (Lanzafame, et al. 1992, Rehm, et al. 1996). These comparisons suggest that any dye may exhibit the ultrafast electron injection kinetics, however the detailed comparison with previous studies cannot be made since the origin of the wide variety of electron injection rates reported is unclear (see table 4.1). In chapter 5, the electron injection kinetics employing $Ru(dcbpy)_2(NCS)_2$ dye are compared with porphyrin sensitiser dyes using the same $TiO_2$ nanocrystalline film. The alternative candidate for the sensitiser dye for the solar cell is discussed in detail.

The electron injection kinetics employing the same sensitiser dye ($Ru(dcbpy)_2(NCS)_2$) as used in this project have been subsequently studied by other groups (Asbury, et al. 1999, Ellingson, et al. 1998, Hannappel, et al. 1997). In contrast to the multi-phasic injection kinetics observed here, Ellingson et al. and Willig et al. have reported that the electron injection kinetics are generally mono-exponential (Ellingson, et al. 1998, Hannappel, et al. 1997) with time constants of <50 fs. The disagreements with the results reported by Willig et al. are described in detail in section 4.4. Lian, Nozik and co-workers have recently reported biphasic injection kinetics, however in this case 84 % of the electron injection was found to occur in 50 fs, with only 16 % of slower (1.7 ps) injection (Asbury, et al. 1999). It should be noted that the observations of the electron injection by

these groups were carried out by monitoring absorption of the injected electron in the infrared region. In contrast, the injection kinetics obtained in this study were determined by the formation of the dye cation state. The difference in the probe source may result in the disagreement of the injection kinetics using this sensitiser dye. The origin of the discrepancies is discussed with the results obtained under different experimental conditions in chapter 5.

***Distribution analysis of the electron injection kinetics***

Following the global analysis assuming that each kinetic decay consists a sum of exponentials and a constant as shown in equation 2.13, it has been found that the electron injection kinetics are multi-exponential with time constants of <100 fs, 1 ps and 13 ps. The multi-exponential analyses were simply used as a useful quantification of the injection kinetics, however it is possible that these exponential components result from a continuous distribution of lifetimes. The analysis for the distribution of lifetimes was carried out for the data obtained for $Ru(dcbpy)_2(NCS)_2$ sensitised $TiO_2$ films. The detailed analytical method using a computer program is summarised in appendix.

As a result of the distribution analysis described in appendix, further improvement of the signal to noise for the kinetic data for the dye coated $TiO_2$ films will be necessary in order to clarify if the observed multi-exponential components are discrete or result from a distribution of injection time constants. It has been found that the number of the kinetic components can be relatively estimated from the distribution analysis when the Gaussian noise level is reduced within 1 % of the total signal size of the decay.

***Charge recombination kinetics***

In contrast to the ultrafast electron injection, the charge recombination exhibits relatively slow reaction times and its kinetics are highly non-exponential with time constants of $10^6 \sim 10^2\ s^{-1}$ as shown in figure 4.13. It has been found that the recombination kinetics between the $Ru(dcbpy)_2(NCS)_2$ dye cation and electrons injected into the $TiO_2$ film are very strongly dependent upon experimental conditions, with variations in the recombination rates from picoseconds to milliseconds depending upon the excitation

intensity, solvent / electrolyte composition and applied electrical bias (Haque, et al. 1999). The results of the ultrafast charge recombination observed under the application of external voltage into the $TiO_2$ electrode are described in chapter 5. It has been suggested by Dr. Jenny Nelson of the Physics Department that the recombination kinetics in this system are largely controlled by the occupancy of the trap sites within the $TiO_2$ nanoparticles (Nelson 1999), resulting in the observed dependency upon applied bias, electrolyte composition and excitation intensity.

***Relevance to photoelectrochemical solar cells***

The observed kinetics involved in the sensitiser dye / semiconductor interface are summarised in figure 4.14. The data presented here are limited to the observation of single sensitiser dye / semiconductor interface, and the sample does not include redox active species such as $I_3^-/I^-$, precluding a detailed comparison of the kinetic results with the function of the whole solar cell. Nevertheless, it is reasonable to relate the experimental results to the dye stability and the electron injection yield, which are of particular relevance to the development of dye sensitised photovoltaic cells.

# Kinetic summary

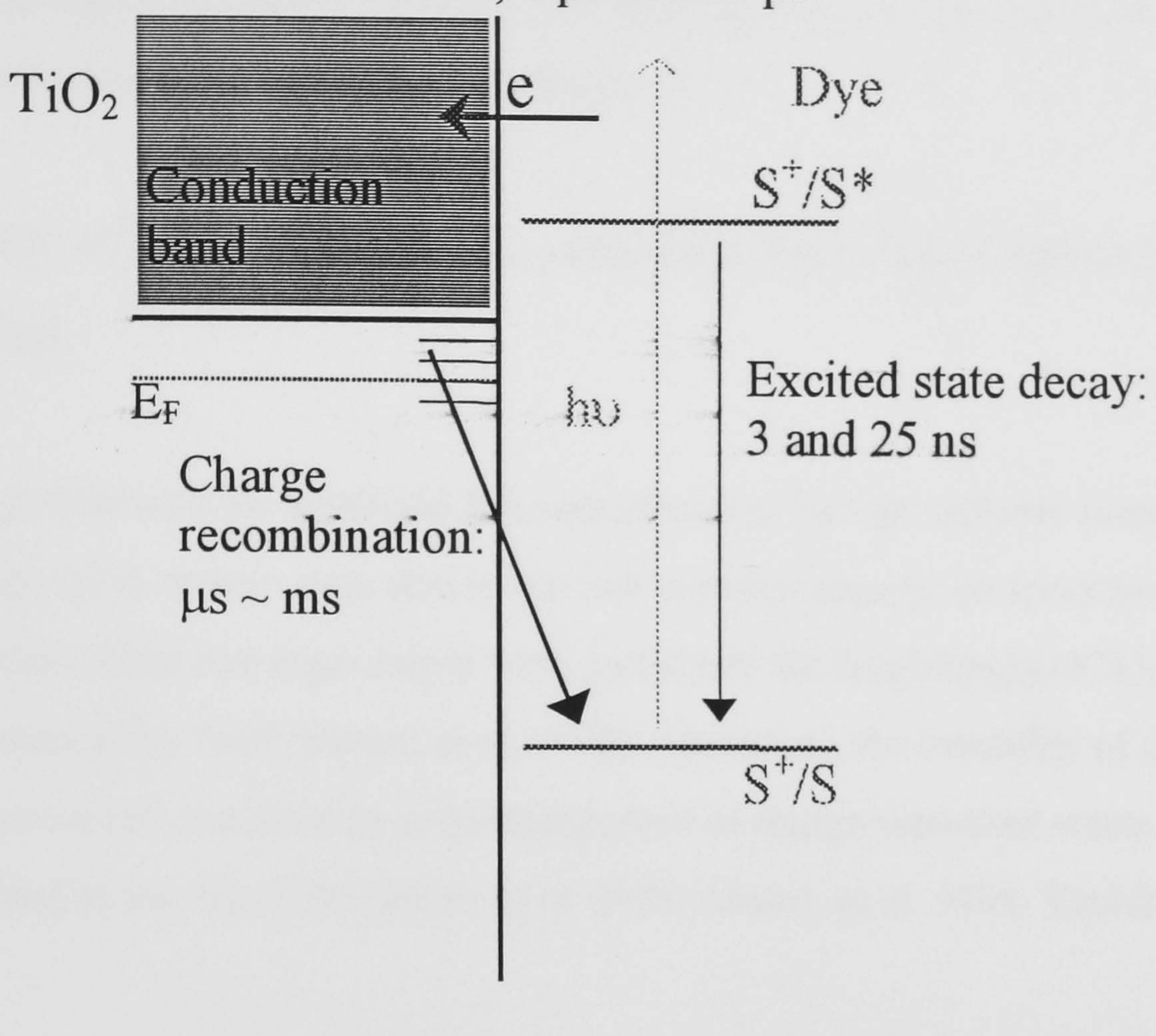



Figure 4.14. Summary presenting the interfacial electron transfer and the dye excited state kinetics for $Ru(dcbpy)_2(NCS)_2$ sensitised $TiO_2$ films.

1) The ultrafast rate of electron injection is likely to be a critical factor for the high stability of the solar cells employing this sensitiser dye (see section 4.4 for the detailed description of $Ru(dcbpy)_2(NCS)_2$ dye stability). Ligand substitution reactions from the excited state of $Ru(dcbpy)_2(NCS)_2$ have been estimated (Nazeeruddin, et al. 1993) to have a rate constant of the order of $10^4$ $s^{-1}$. The electron injection rates of $>10^{13}$~$10^{11}$ $s^{-1}$ indicates that the rates of the electron injection exceed degradation pathways by $10^9$~$10^7$. This is consistent with recent stability studies of photoelectrochemical solar cells which indicate that this dye can undergo $10^7$~$10^8$ turnovers per molecule without loss of photovoltaic performance (Kohle, et al. 1997). Such long-term stability is essential for the commercial application of this technology.

2) The observed injection rates ensure that the electron injection is achieved with a high quantum yield, as its rate is at least three orders of magnitude faster than the decay rate of the dye excited state observed in solution ($10^8$ $s^{-1}$). Given the rapid injection rates observed here, it is remarkable that very few other sensitiser dyes have been identified with a comparable efficiency to apply for the cell. Further study concerning this point is described in chapter 5.

## 4.4 Stability of $Ru(dcbpy)_2(NCS)_2$ sensitised $TiO_2$ films under optical experiments

The dye degradation of the sensitised films was found to be light induced reaction and can be monitored by steady state absorption and transient absorption spectroscopies. The detailed studies of the dye degradation were performed for $Ru(dcbpy)_2(NCS)_2$ (Das, et al. 1998, Kohle, et al. 1997, Moser, et al. 1998). Moreover, the instability of this sensitiser dye caused controversy in the assignment of charge separated states in the $TiO_2$ films sensitised by this dye (Hannappel, et al. 1998, Moser, et al. 1998, Tachibana, et al. 1996).

The prolonged storage of the $Ru(dcbpy)_2(NCS)_2$ sensitised films, particularly in the absence of the solvent to cover the surface of the film, results in a shift in the steady state absorption maximum from ~540 nm to ~500 nm. Moreover this shift was significantly accelerated by visible light irradiation, generating a stable yellow coloured product. The IR spectra of this yellow coloured product clearly indicated the absence of the SCN band at 2139 $cm^{-1}$. Further studies suggested that this change is most probably associated with an oxygen dependent desulphurisation reaction of the NCS ligands, yielding CN groups (Kohle, et al. 1997). In the electrochemical studies of $Ru(dcbpy)_2(NCS)_2$, the dye cation degradation lifetime was found to be 0.1~1 s (Kohle, et al. 1997, Moser, et al. 1998), whereas the charge recombination in the sensitised $TiO_2$ films covered in EC / PC completes on μs ~ ms timescales (see the section above), resulting in efficient dye regeneration under light irradiation.

Sub-picosecond transient absorption spectra for the degraded films indicated significant difference from those obtained with fresh films covered in EC / PC (Figure 4.15). The degradation of the sensitiser results in a loss of the characteristic 800 nm absorption increase assigned to a LMCT transition from the dye's NCS ligands to the Ru(III) centre (see the section above), and thus to a shift of the isosbestic point toward the red to ~750 nm. This loss of the LMCT transition is consistent with the modifications of the NCS ligands for the dye sensitiser, although the ground state absorption may be essentially unchanged (Moser, et al. 1998). This observation was supported by the flash photolysis data reported by Das et al (Das and Kamat 1998). Recently Willig et al. have reported that they were unable to observe this absorption band for the $Ru(dcbpy)_2(NCS)_2$ cation state (Hannappel, et al. 1997) (see figure 4.15). However the above discussion strongly suggests that this disagreement is most probably due to the degradation of the $Ru(dcbpy)_2(NCS)_2$ during the experiments of Willig et al.

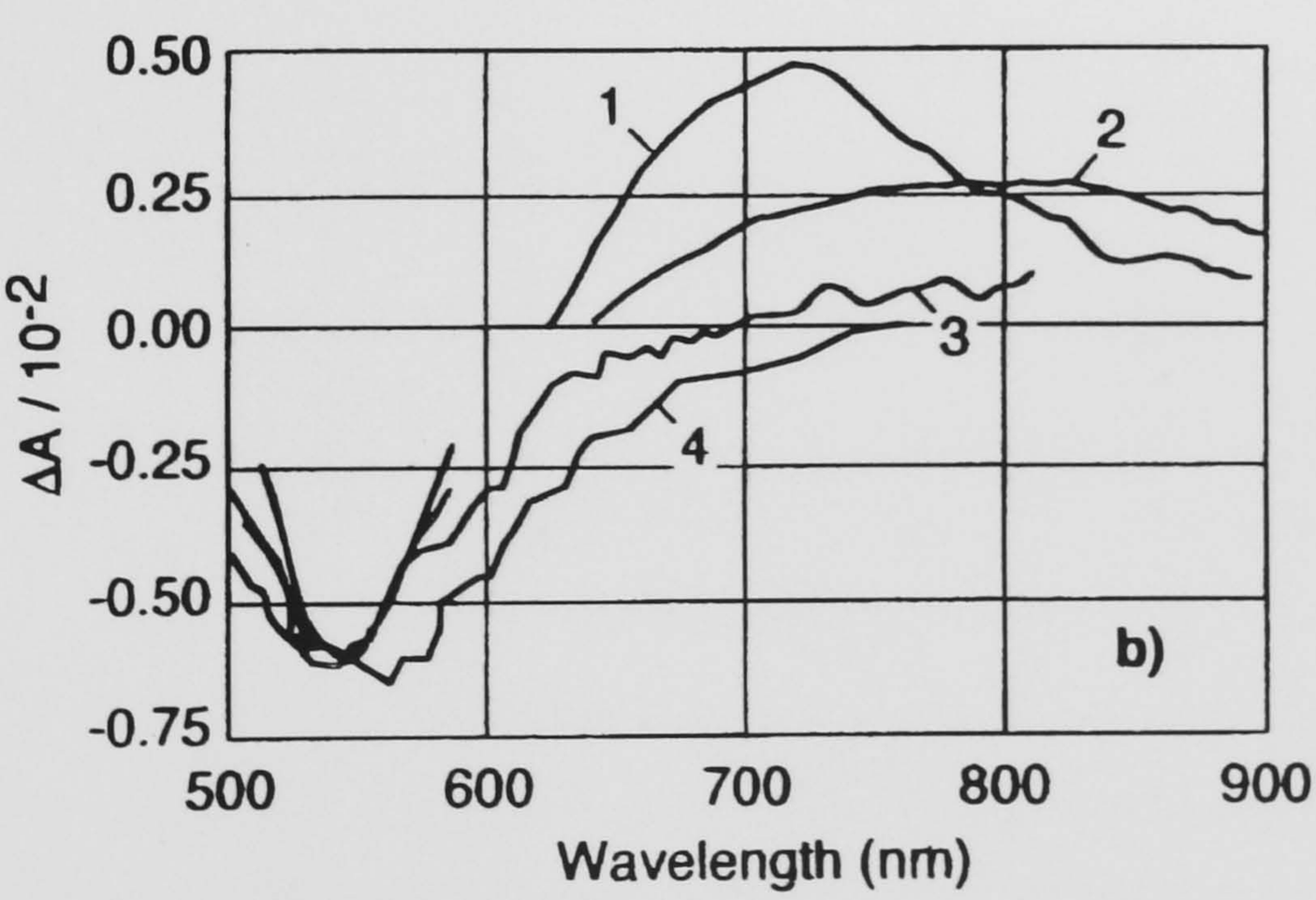



Figure 4.15. Comparison of the transient absorption spectra obtained for the dye in ethanol (1), the fresh dye sensitised $TiO_2$ films (2) and the sensitised films left for one day in air (3) at a time delay of 5 ps after 605 nm excitation. This figure is taken from the publication of Moser et al. (Moser, et al. 1998). The transient spectrum (4) for

the dye sensitised $TiO_2$ films reported by Willig et al. is also shown in the figure (Hannappel, et al. 1997).

In consequence of the instability of sensitiser dyes, the optical experiments were carefully performed. The stability of all samples was monitored by the change of the signal size during all transient absorption experiments and by the change of the ground state absorption maximum before and after the optical experiments. A new spot in the films was used to collect data whenever absorption difference amplitude was changed by 5~20 %.

# Chapter 5: Parameters influencing electron injection kinetics

## 5.1 Introduction

The transient absorption studies of the $Ru(dcbpy)_2(NCS)_2$ / $TiO_2$ interface presented in chapter 4 have revealed ultrafast electron injection (>$10^{11}$ $s^{-1}$), excited state decay to ground ($10^8$ $s^{-1}$) and slow charge recombination ($10^6$~$10^2$ $s^{-1}$). These observations are consistent with the efficient sensitisation in $Ru(dcbpy)_2(NCS)_2$ sensitised nanocrystalline $TiO_2$ films employed in the solar cells.

Since the first interfacial kinetic study in $Ru(dcbpy)_2(NCS)_2$ sensitised $TiO_2$ films in this project, several studies have been carried out to address the kinetics of the photoinduced electron injection by many other groups. These studies have focused upon nanocrystalline $TiO_2$ and have reported wide variations in the rates of the electron injection with time constants ranging from $10^8$ $s^{-1}$ to $10^{14}$ $s^{-1}$ (Asbury, et al. 1999, Burfeindt, et al. 1996, Cherepy, et al. 1997, Ellingson, et al. 1998, Heimer, et al. 1997, Hilgendorff, et al. 1998, Martini, et al. 1998, Spitler, et al. 1997). It is unclear if these variations in experimental observations result from differences in the sensitiser dyes used, from differences in the metal oxide particles prepared, or other variations in the experimental conditions.

Some progress has been made in elucidating the parameters influencing the electron injection kinetics. For example, the kinetics have been shown to be dependent upon the relative energies of the semiconductor conduction band and the dye excited state oxidation potential (Moser, et al. 1998, Thompson, et al. 1999). Following the electron transfer theory described in chapter 3, electron injection is expected to proceed largely on ultrafast timescales ($10^{12}$ – $10^{13}$ $s^{-1}$) with favourable energetics and strong dye binding to the film surface (Asbury, et al. 1999, Cherepy, et al. 1997, Hilgendorff and Sundström 1998, Martini, et al. 1998, Miller, et al. 1995, Rehm, et al. 1996, Tachibana, et al. 1996). At present there have however been very few systematic studies of the electron injection kinetics under different experimental conditions, and to a large extent, the parameters controlling the kinetics of electron injection remain poorly established. Addressing such parameters is clearly important both for a fundamental understanding

of the mechanism of dye sensitisation process and for further development of dye sensitised semiconductor photovoltaic devices.

This chapter presents studies of the parameters influencing the electron injection kinetics in $Ru(dcbpy)_2(NCS)_2$ sensitised nanocrystalline $TiO_2$ films. The newly built transient absorption spectrometer in the femtosecond Ti:sapphire laser system has been employed for the ultrafast measurements. The parameters compared for the electron injection kinetics are as follows:

1) **Excitation wavelengths**

   The electron injection kinetics for $Ru(dcbpy)_2(NCS)_2$ coated $TiO_2$ films covered in EC / PC are compared as a function of excitation wavelength resulting in formation of the excited state with a different redox potential.

2) **Solvents surrounding sensitiser dyes**

   Solvation of the dye excited state and the charge separated state for electron injection kinetics was investigated using different solvent.

3) **Fermi levels of $TiO_2$ films**

   The influence of the applied voltage to the dye sensitised $TiO_2$ electrode upon the electron injection kinetics was investigated using two different electrolytes (acetonitrile (B) and ethanol (A) electrolyte).

4) **Potential energy levels of electron acceptor states in $TiO_2$**

   The influence of the conduction band energetics upon the electron injection kinetics was investigated. The potential energy level of the conduction band was controlled by the addition of potential determining lithium ions.

5) **Sensitiser dyes ($Ru(dcbpy)_2(NCS)_2$) and two other porphyrins**

   The electron injection kinetics were compared for nanocrystalline $TiO_2$ films with different sensitiser dyes.

These issues were selected as they are of direct relevance to the design of photovoltaic devices employing these films, and have not been addressed in detail previously.

## 5.2 Experimental condition

### 5.2.1 Ti:sapphire laser transient absorption spectrometer

Excitation pulses (30~40 fs) were tuned using the optical parametric amplifier (OPA, c.f. chapter 2) for each different dye sample, at 525 ~ 625 nm for $Ru(dcbpy)_2(NCS)_2$, at 560 nm for Zinc tetracarboxyphenyl porphyrin (ZnTCPP) and at 645 nm for free base tetracarboxyphenyl porphyrin ($H_2TCPP$). Excitation intensities were reduced typically to 10~50 nJ (0.2~1 $mJcm^{-2}$) with a spot diameter of 60~80 μm. The density of injected electrons was estimated as described in chapter 4. In all experiments, the excitation intensity was attenuated to yield 0.8~1 excited dyes / nanoparticle except for power dependence data in section 5.7. All experiments were carried out with the magic angle configuration (ca. 54.7°) between pump and probe pulses with a repetition rate of 1 kHz at 20 °C. The stability of all samples was checked as described in chapter 4.

Transient absorption data were collected with some of six different timescales of 0-3, 0-6, 0-30, 0-60, 0-180 and 0-600 ps with a time delay of 16.5, 33, 165, 330, 990 and 3300 fs between points, respectively, and with probe wavelengths between 460 and 900 nm using a multichannel detector (see chapter 2). All transient data obtained with the dye standards and the samples indicated the negligible change of spectral shape, suggesting the negligible accumulation of transient species, e.g. electrons in the $TiO_2$, during the experiment under the 1 kHz repetition rate.

### 5.2.2 Photoelectrochemical experiments

The modulation of electronic state energy levels in the $TiO_2$ electrode can be controlled by application of an external voltage into $TiO_2$ electrode and by choosing the supporting electrolyte and the electrolytic solvent with the addition of "potential determining cations" (see section 5.6 for the effect of potential determining cations). The application of the external voltage into $Ru(dcbpy)_2(NCS)_2$ sensitised $TiO_2$ electrode controls the Fermi level of $TiO_2$ and was carried out in the three electrode optical cell with the potentiostat (see chapter 3 for the details). The appropriate supporting electrolyte and

electrolytic solvent were incorporated in the cell, which was placed into the sample area in the femtosecond Ti:sapphire laser system to perform the pump-probe experiments.

The bias was applied into the $TiO_2$ film electrode against the Ag/AgCl reference electrode at 20 °C. Following the application of a potential, it was necessary to stabilise the system, as monitored by the dark current which ceased changing after 5 min typically. It should be noted that shape and amplitude of transient absorption spectra were found to be identical when the data were collected at 5 and 30 minutes after the applied voltage was altered. The response time of the potentiostat upon the application of the voltages is estimated to be ~50 μs. During the photoelectrochemical experiments, a marginal increase in the current drawn by the potentiostat (10~20 % of dark current) was observed under laser light exposure. The estimate of this current increase resulted in the negative shift of the Fermi level of the film by ~20 mV.

The electrolyte combinations used for the experiments are as follows;

Electrolyte A: 0.1 M of tetrabutyl ammonium triflate, TBAT (99% grade Aldrich) and ethanol (Analar 99.7%)

Electrolyte B: 0.1 M of tetrabutyl ammonium perchlorate: TBAP (Sigma grade), 0.1 M of lithium perchlorate: $LiClO_4$ (Sigma grade) and dry acetnitrile (Fluka GLC grade)

Electrolyte C: 0.1 M of tetrabutyl ammonium perchlorate: TBAP (Sigma grade) and dry acetnitrile (Fluka GLC grade)

The acetonitrile was distilled over $CaH_2$ prior to use in order to minimise water content in the electrolyte. All electrolytes were degassed with dry argon gas prior to and during the optical experiments.

All of the transient data with the electrolyte A were collected with low intensity excitation pulses of 0.2 $mJ/cm^2$ at 525 nm. These conditions resulted in the excitation of 1.5 % of the dye molecules per pulse, which corresponds to 0.4~0.5 injected electron

per colloidal particle. For the experiments in the electrolyte B or C, excitation pulses were tuned at a wavelength of 623±3 nm, corresponding to the low energy absorption tail of the $Ru(dcbpy)_2(NCS)_2$ sensitiser dye. Pump pulse energy was typically reduced to 40~50 nJ (0.8~1 $mJ/cm^2$). Considering the relatively low absorbance of the dye at 623 nm, this excitation energy results in ≤ 0.8~1 injected electron per $TiO_2$ particle per pump pulse.

## 5.3 Dependence on excitation wavelengths

### 5.3.1 Introduction

As discussed in chapter 4, the MLCT absorption band of $Ru(dcbpy)_2(NCS)_2$ with a maximum at 538 nm is characterised as excitation to multiple electronic excited states based upon analogies with ruthenium (II) trisbipyridyl ($Ru(bpy)_3^{2+}$) complexes. For example, recent MO calculations suggest that four different states contribute to the ground state absorption between 500 and 700 nm (Rensmo, et al. 1998). Following excitation of these absorption bands, the initial excited states may exhibit different kinetics of excited state relaxation and electron injection. The electron injection process may compete with the singlet excited state relaxation when a higher excited state is initially formed.

In this section, the electron injection kinetics for $Ru(dcbpy)_2(NCS)_2$ coated $TiO_2$ films covered in EC / PC are compared as a function of excitation wavelength resulting in formation of the excited state with a different redox potential. Figure 5.1 illustrates the relation of $TiO_2$ conduction band energy level and excited state oxidation potentials of the dye estimated from excitation wavelengths and its ground state redox potential. The experimental conditions are identical except for the excitation wavelength (525, 560 and 600 nm) used. All of kinetic results obtained at a different wavelength are normalised for ease of comparison.

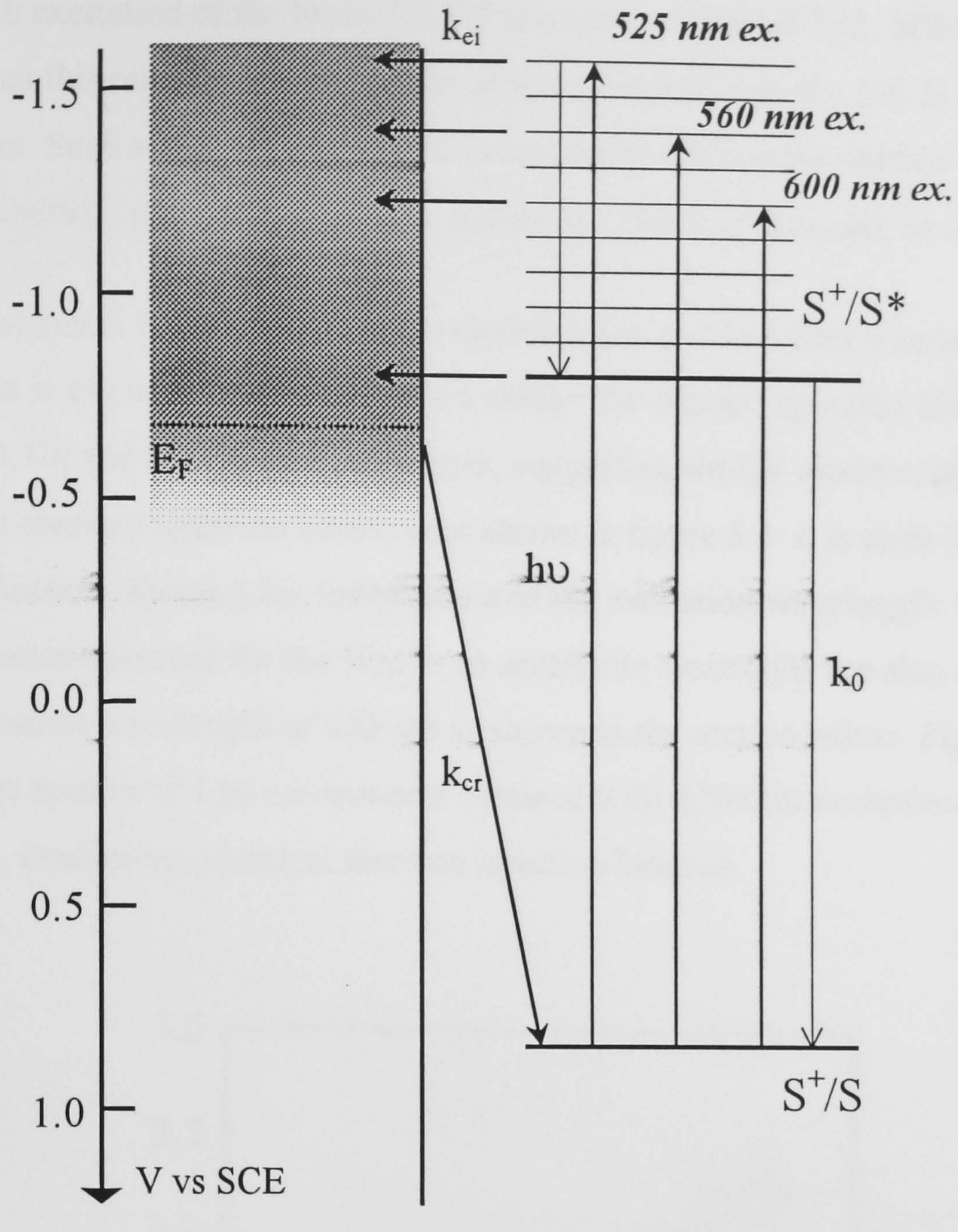



Figure 5.1. Schematic representation of potential diagram of dye sensitised $TiO_2$ nanocrystalline films. $k_{ei}$, $k_{cr}$ and $k_0$ refer to electron injection, charge recombination and excited state decay to ground, respectively. Dye ground state (vs SCE) was taken from previous solution phase studies (Hagfeldt and Grätzel 1995). Excitations to initially populated excited state of the dye by a series of excitation wavelengths were illustrated with thick solid arrows. The graduated shading of the conduction band in this figure illustrates the high density of sub-band gap (trap) states reported for such nanocrystalline $TiO_2$ film, resulting in a poorly defined conduction band edge (Rothenberger, et al. 1992).

### 5.3.2 Results

The rapid relaxation of the singlet excited state can be monitored by the presence of stimulated emission as described in chapter 4. However no stimulated emission could be

resolved with excitation of the broad MLCT absorption bands at 525, 560 and 600 nm, indicating that this relaxation process was complete in less than the 100 fs instrument response time. Such a fast relaxation time is consistent with recent studies of analogous ruthenium bipyridyl dyes with a relaxation time of <300 fs (Damrauer, et al. 1997).

Figure 5.2 compares transient absorption spectra taken at 60 ps after a series of excitations. It is apparent that all of spectra exhibit the charge separated state (compare with figure 4.10) and similar spectral shapes, suggesting similar electron injection yield at 60 ps. The electron injection kinetics are shown in figure 5.3. It is clear that the kinetics of electron injection are independent of the excitation wavelength. Note that identical kinetics observed for the film in an acetnitrile electrolyte are also obtained with an excitation wavelength of 623 nm as shown in the section below. Figure 5.4 shows kinetic spectra of 1 ps components obtained with different excitation wavelengths, confirming identical electron injection kinetics.

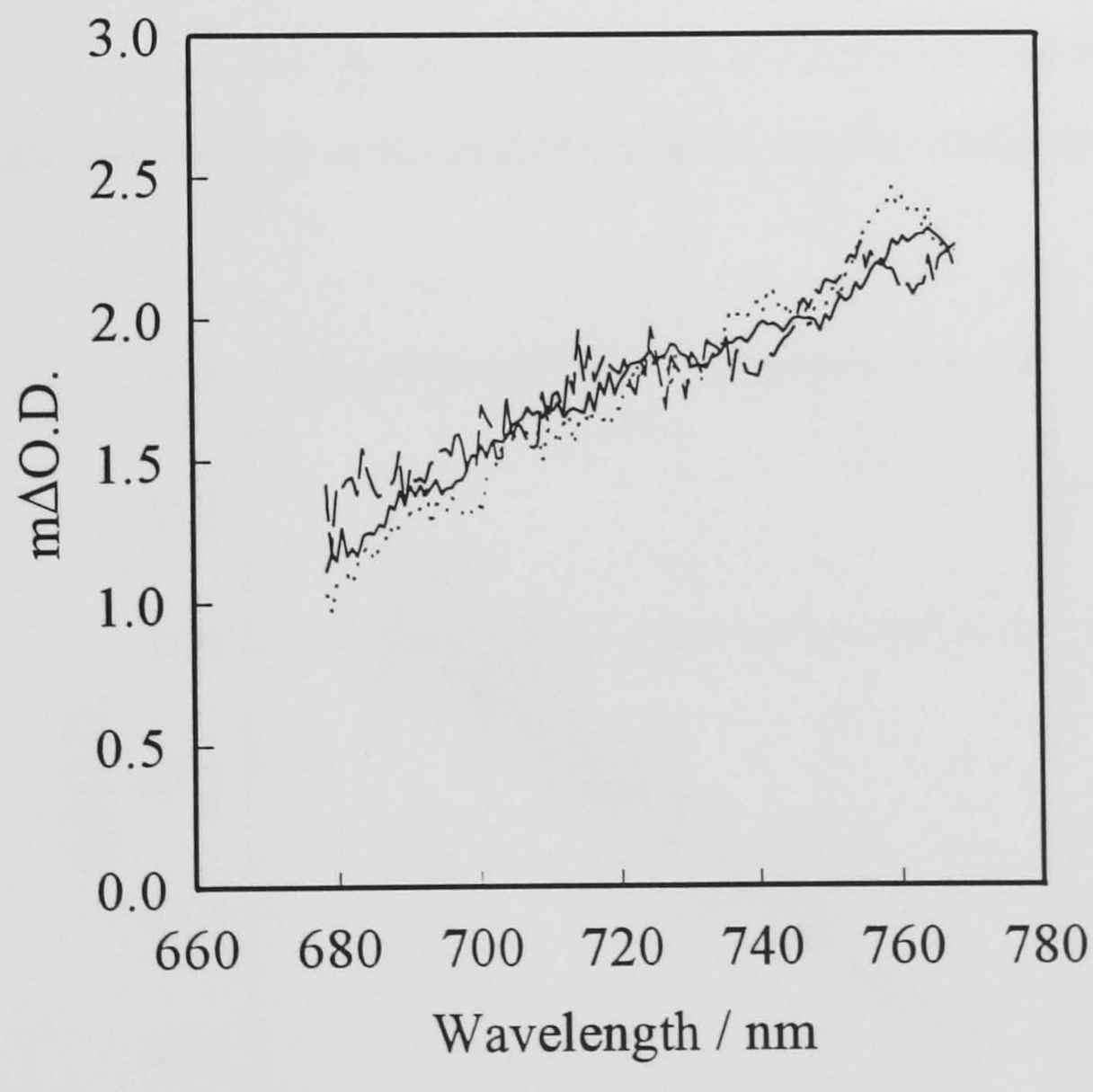



Figure 5.2. Absorption difference spectra obtained for $Ru(dcbpy)_2(NCS)_2$ sensitised $TiO_2$ films covered in EC / PC at a time delay of 60 ps after 525 (·····), 560 (——) and 600 (------) nm excitations. The amplitudes of the spectra are normalised for ease of comparison.

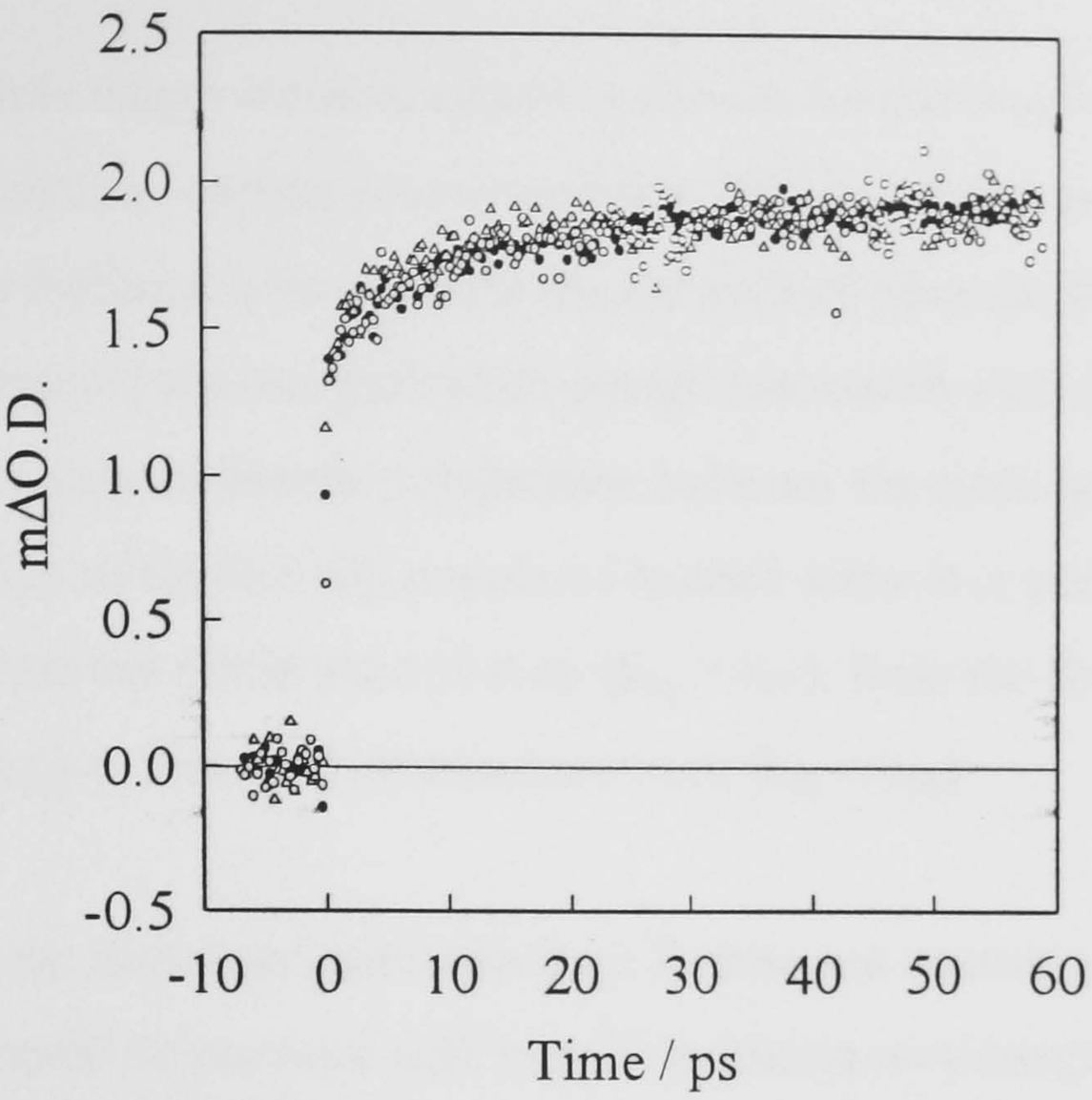



Figure 5.3. Transient kinetics obtained for the dye coated $TiO_2$ films with excitation wavelengths of 525 (Δ), 560 (•) and 600 (o) nm at a probe wavelength of 760 nm. The kinetics are normalised to the amplitude at 60 ps after excitation.

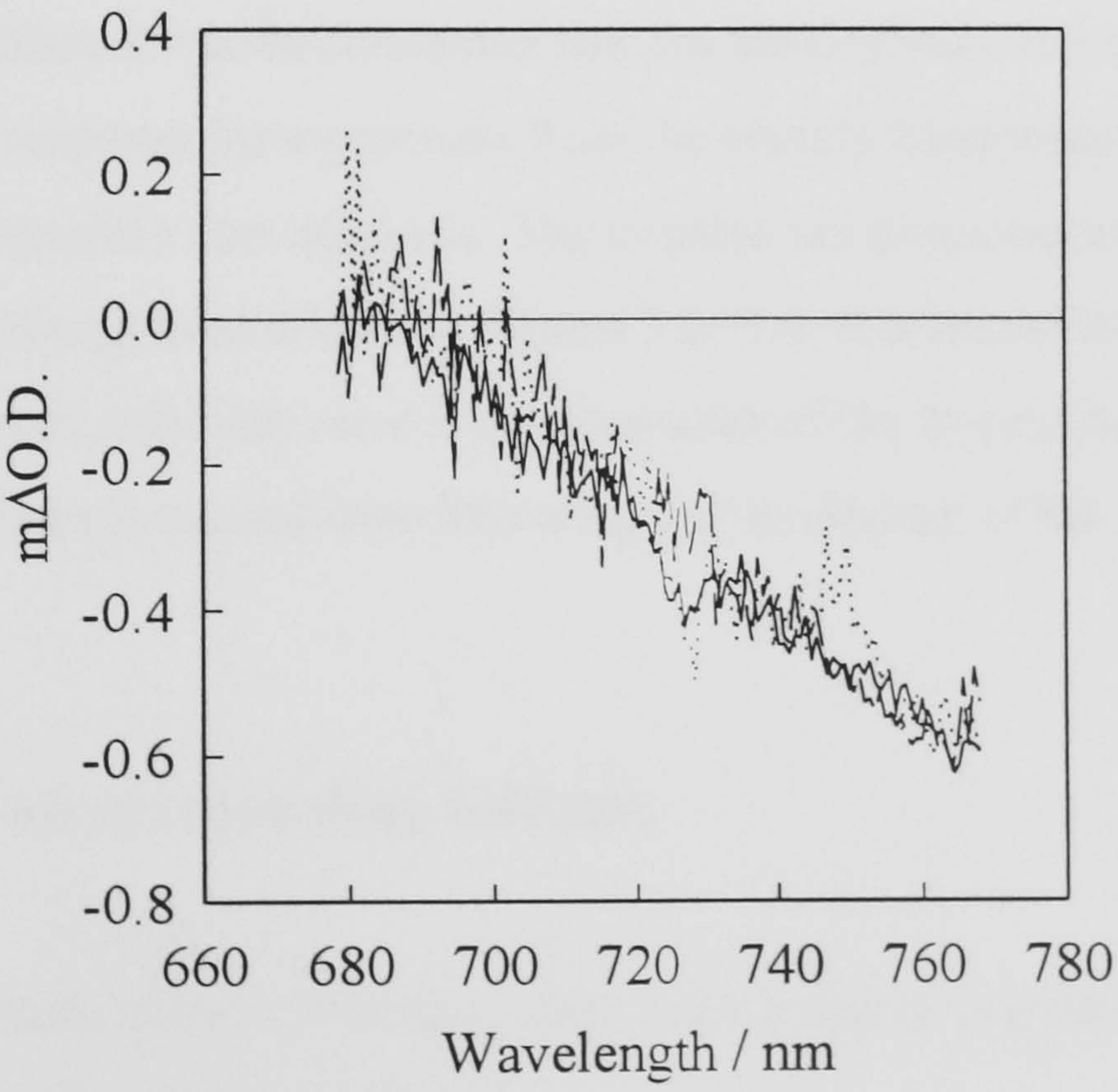



Figure 5.4. Kinetic spectra obtained for the dye coated $TiO_2$ films with excitation wavelengths of 525 (·····), 560 (——) and 600 (------) nm.

### 5.3.3 Discussion

Since there are multiple empty states available in the conduction band as an acceptor state, the electron injection reaction is activationless with any populated excited state when the free energy difference between the lowest excited state and the bottom of conduction band is beyond the reorganisation energy associated with electron transfer (see chapter 3). There may be kinetic competition between the electron injection ($k_{inj}$) and the relaxation ($k_{rel}$) of the initially populated excited state. It is possible that electron injection proceeds from the initial excited state ($k_{inj} > k_{rel}$), from the thermally relaxed excited state ($k_{inj} < k_{rel}$) or from the intermediate state ($k_{inj} \approx k_{rel}$).

As discussed above, no stimulated emission from fluorescent excited states of $Ru(dcbpy)_2(NCS)_2$ could be resolved with any of excitation wavelengths of 525, 560 and 600 nm, i.e. the dye excited state relaxation completes within 100 fs. As the fast phase of electron injection occurs within 100 fs (see figure 5.3), it is not possible to determine whether this phase of electron injection proceeds before or after the relaxation of the dye excited state. The data could not thus be analysed for such fast kinetics by the electron transfer theory. It is possible that the fastest phase (<100 fs) of the injection process may proceed adiabatically prior to thermalisation of the dye excited state. In contrast, it can be concluded that the multi-phasic electron injection after the instrument response time proceeds from the weakly luminescent excited state, and the reaction is therefore non-adiabatic. The kinetics are moreover independent of those excitation wavelengths as shown in figures 5.2~5.4. It is however reasonable to observe similar electron injection rates if the relaxation of the dye excited state populates the same lowest excited state following any excitation of the multiple absorption bands.

## 5.4 Dependence on surrounding solvents

In this section, solvation of the dye excited state and the charge separated state upon electron injection kinetics was investigated.

### 5.4.1 Results

For the femtosecond measurements, the sensitised $TiO_2$ films were either exposed to air, or covered in EC / PC, ethanol (electrolyte A) or dry acetnitrile (electrolyte B). Figure 5.5 compares the kinetics obtained for $Ru(dcbpy)_2(NCS)_2$ coated films under the different solvent environment. Although each data was collected with a different excitation wavelength, the data described in the above section support the fact that electron injection kinetics are independent of excitation wavelength. It is therefore clear from the figure that the injection kinetics are independent of the solvent employed, suggesting that solvation of the reactant and the product state does not have a significant effect upon the injection kinetics. It should be noted that the ethanol solution was not dried, and therefore must have some water content. This water content evidently has a negligible effect upon the kinetics of electron injection. Also note that accelerated dye degradation rates were readily observed even under the low intensity of the laser light when the measurement was carried out for the films exposed in air, and therefore the data collection times were kept short for each spot in the sample.

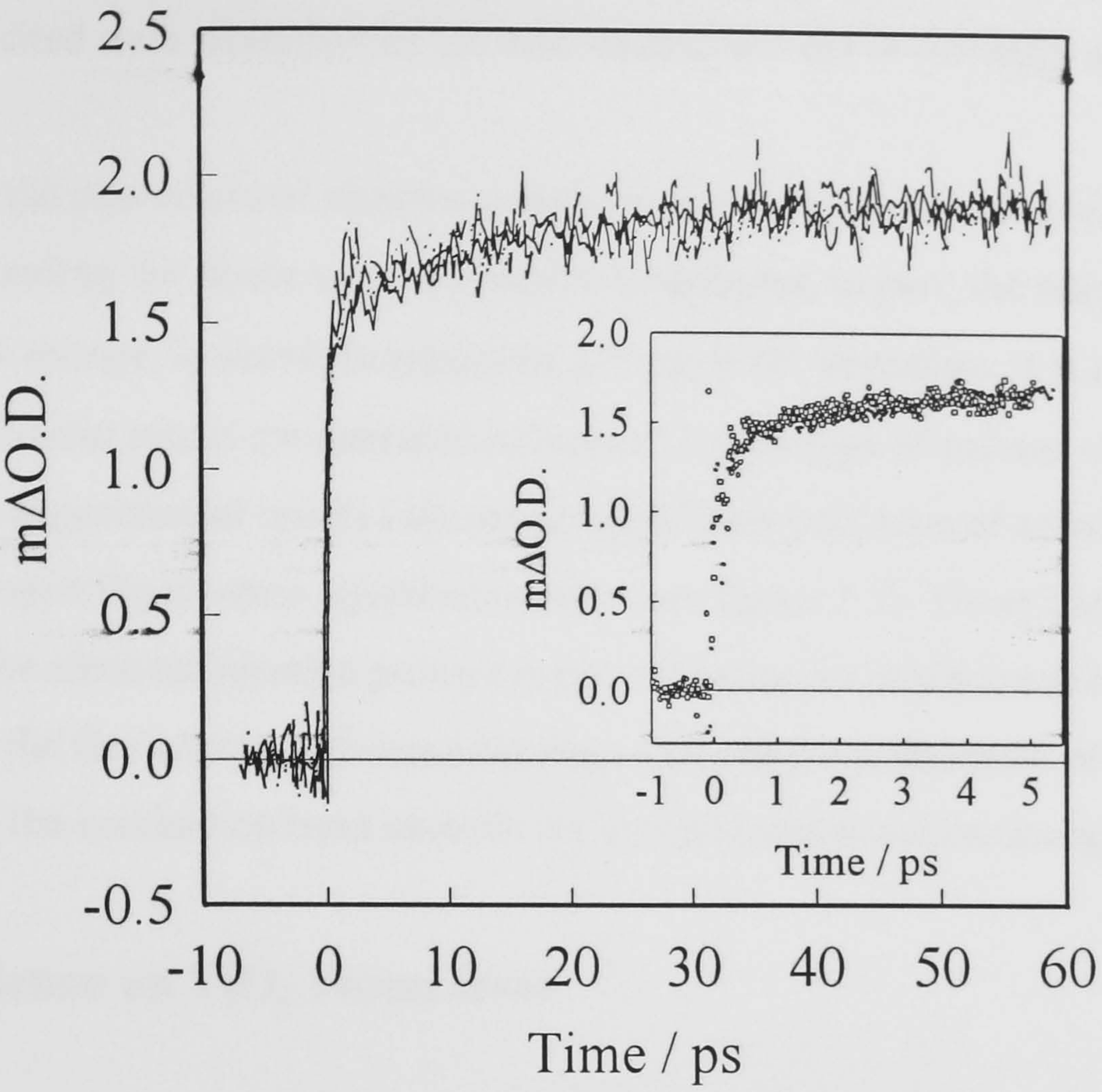



Figure 5.5. Electron injection kinetics for the dye coated $TiO_2$ films under different solvent environments at a probe wavelength of 760 nm. The films were either exposed to air (------), or covered in EC / PC (——), dry acetnitrile (·····) or ethanol (— - —). The kinetic data for the films covered in EC / PC was taken from figure 4.11c. The transient data for the air exposed films and for the film covered in ethanol (electrolyte A) were measured with an excitation wavelength of 525 nm. The data for the film covered in acetnitrile (electrolyte B) was collected with 623 nm excitation. Insert shows an expansion of the data at early times for the air exposed films (open square) and the films covered in EC / PC (dagger) and acetnitrile (open circle). All of the kinetic data were normalised to the amplitude at 60 ps after excitation.

### 5.4.2 Discussion

An electrolyte is one of the elements to control the over-all efficiency of the dye sensitised semiconductor solar cells as the dye regeneration process by the electroactive redox species ($I_3^-/I^-$) competes with the charge recombination process. The mobility of

such an electroactive electrolyte is supported by the electrolytic solvent. The choice of the electrolyte therefore influences the dye regeneration rate. Moreover, the influence on the dye excited state relaxation by the surrounding solvent is currently not clear.

According to the non-adiabatic electron transfer theory described in chapter 3, the solvent surrounding the donor and the acceptor contributes, in part, the magnitude of the reorganisation energy, $\lambda$, shown in equations 3.9 and 3.10. Therefore, it is expected that the electron transfer rate is considerably influenced by the type of solvent chosen. However, the experimental results indicate no significant influence of solvent environment upon the electron injection kinetics (see figure 5.5). These observations suggest that the electron injection process is activationless for any solvent employed, and therefore the free energy difference between the lowest excited state of the dye and the bottom of the conduction band exceeds the overall reorganisation energy.

## 5.5 Dependence on $TiO_2$ Fermi level

### 5.5.1 Introduction

Nanocrystalline $TiO_2$ films are characterised by a high density of sub-band gap (surface / defect) states below the conduction band edge (see chapter 3). The occupancy of these sub-band gap states, and of the conduction band states, is defined by the position of the Fermi level within the film. These sub-band gap states are thought to play a key role in device function. For example, current transport in these films is thought to be dominated by trapping / detrapping kinetics associated with these states (Nelson 1999), while the occupancy of these trap states (and therefore the Fermi level) is dependent upon light flux incident upon the device and the electron collection yield at the back electrode in the solar cells.

Several studies have indicated that yield and kinetics of electron injection are dependent upon the relative energetics of the electron donating and accepting states, corresponding typically to the dye excited state and the conduction band states of the semiconductor. For example, Spitler et al. has reported the dependence of electron injection rate upon the free energy gap $\Delta G$ between the dye excited state and the conduction band edge for

silver halide films sensitised by a series of cyanine dyes, and found a clear energetic threshold for the electron injection process (Spitler, et al. 1997). A similar conclusion has also been reached from the wavelength dependence of steady state photocurrent quantum efficiencies by Moser and co-workers (Moser and Grätzel 1998). As described in chapter 3, when -ΔG exceeds the reorganisation energy associated with the electron transfer, the reaction is expected to be activationless (Miller, et al. 1995), consistent with the above studies.

In this section, the influence of the voltage applied to the dye sensitised $TiO_2$ electrode upon the electron injection kinetics is described. The ultrafast studies were carried out using acetonitrile (B) or ethanol (A) electrolyte solution. The conduction band energetics in both electrolytes are expected to be similar potential levels as they both contain potential determining cations (see section 5.6 for the details).

### 5.5.2 Results

***Injection kinetics in acetonitrile electrolyte (B)***

Figure 5.6 shows the influence of the applied voltage upon the absorption transients at 760 nm. Data are taken with the films covered in EC / PC in the absence of applied bias as a comparison, and shown for the sample with application of external potentials of –0.2 and –0.4 V vs Ag/AgCl. The bias range was limited to –0.4 V as it has been shown that the prolonged application of more negative biases resulted in some irreversible desorption / degradation of the sensitiser dye (see below). It is clear that in this bias range, the electron injection kinetics and yield are independent of the applied bias.

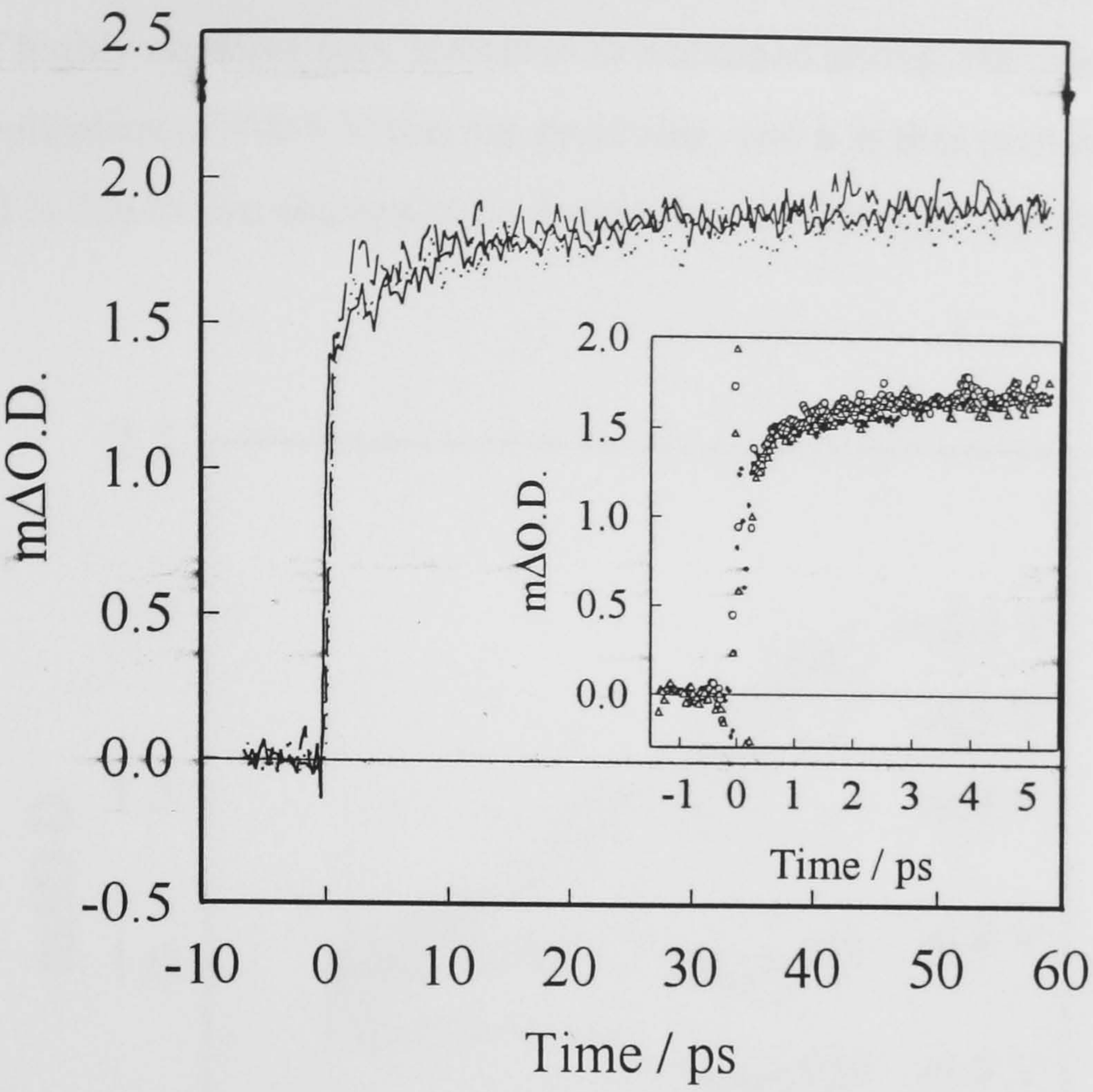



Figure 5.6. Dependence of electron injection kinetics upon the magnitude of the external voltages applied to $Ru(dcbpy)_2(NCS)_2$ sensitised $TiO_2$ electrode. The transient data were obtained for the films covered in EC / PC with no applied voltage (————) and in the three electrode cell with electrolyte B with external applied voltages of –0.2 V (- - - - - - -) and –0.4 V (·····) vs Ag/AgCl at a probe wavelength of 760 nm. Insert represents earlier timescale for the films covered in EC / PC (dagger), and covered in the electrolyte with voltages of -0.2 V (circles) and –0.4 V (triangles).

Despite the irreversibility of the dye sensitised film upon a bias application of <-0.5 V, the electron injection kinetics were monitored up to -0.9 V vs Ag/AgCl. Absorption difference spectra at a time delay of 60 ps with applied voltages from >-0.4 V to -0.9 V are compared in figure 5.7. It is clear from the figure that the spectral shape changes with applied biases of <-0.6 V. At -0.9 V the spectrum is very similar to that of the dye excited state (compare with figure 4.3). Figure 5.8 represents transient kinetics monitored at 760 nm with applied biases of -0.4 ~ -0.9 V. It is apparent that the electron injection yield is significantly decreased at <-0.6 V. One possible explanation for this

decreased yield is that the electron injection is inhibited due to highly raised Fermi level of the $TiO_2$, i.e. some of electron acceptor states to be injected are occupied by the application of highly negative bias. However as explained above, the injection kinetics with a bias application of <-0.5 V was not reversible, and it is thus possible that this low injection yield is due to dye desorption or degradation by the high applied bias.

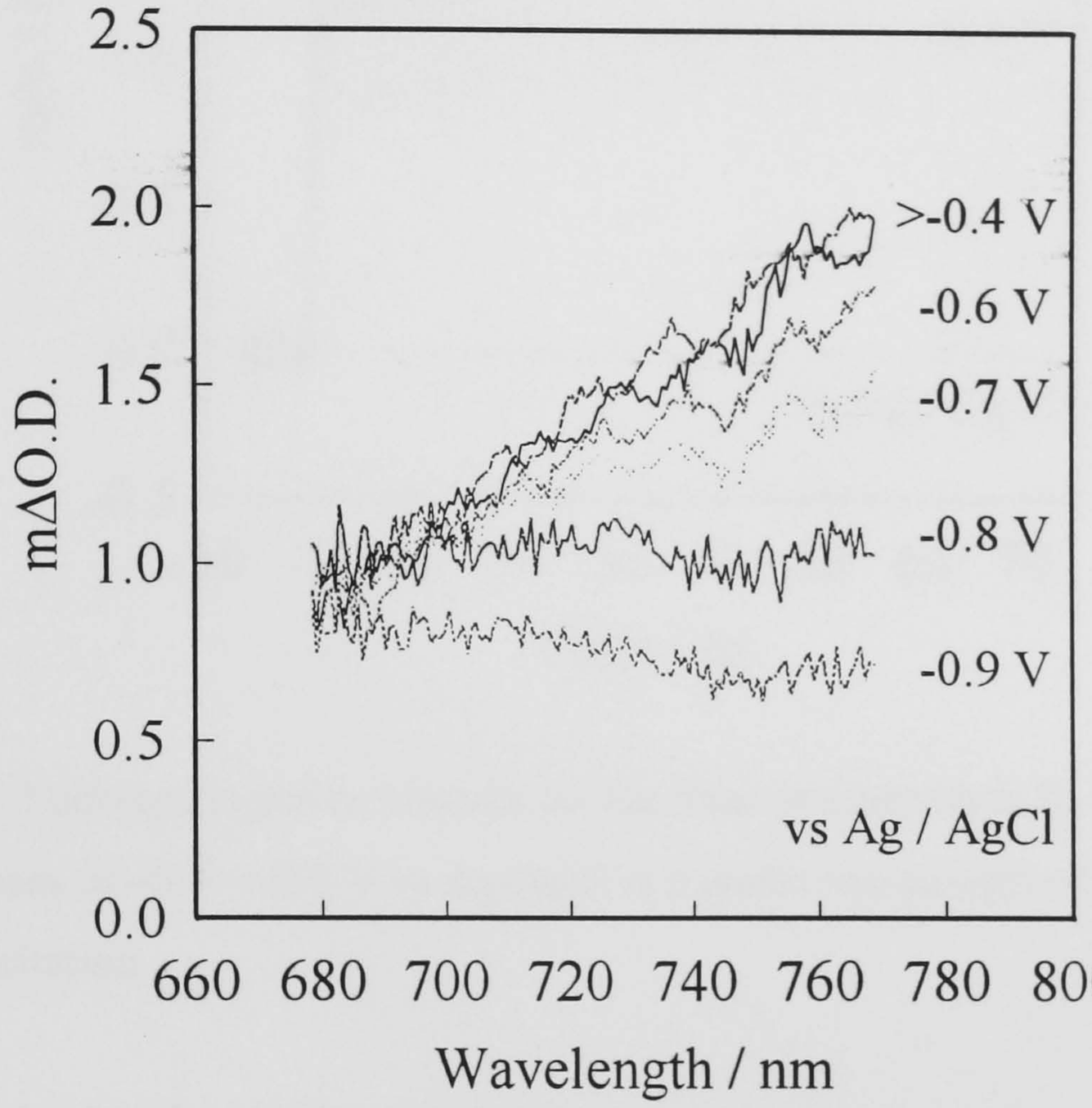



Figure 5.7. Transient absorption spectra taken at 60 ps after 623 nm excitation with bias application of >-0.4 ~ -0.9 V vs Ag/AgCl to the dye sensitised $TiO_2$ electrode in electrolyte B.

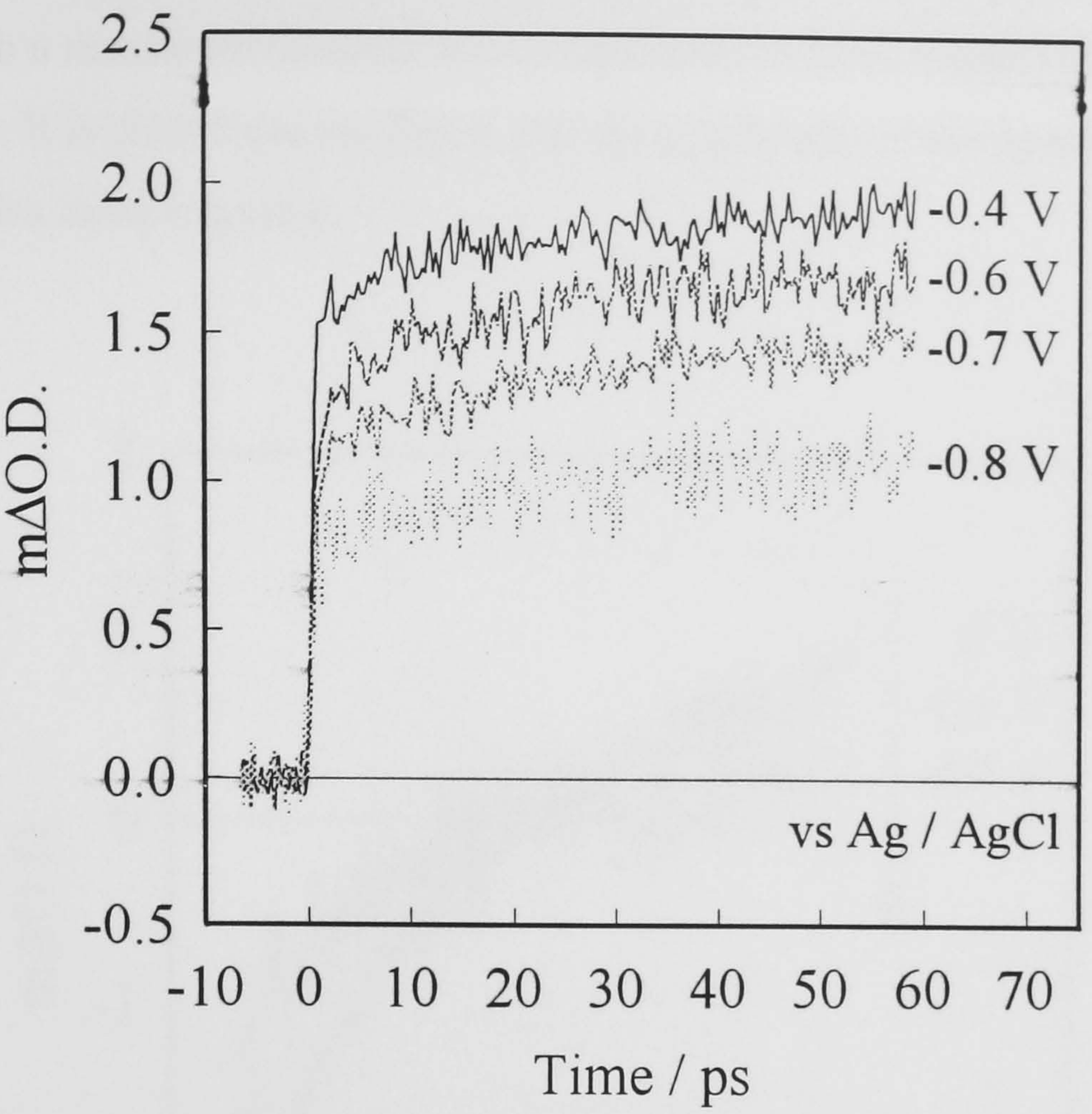



Figure 5.8. Transient injection kinetics for the films in electrolyte B, obtained with applied biases of –0.4 ~ -0.8 V vs Ag/AgCl at a probe wavelength of 760 nm with 623 nm excitation.

***Injection kinetics in ethanol electrolyte (A)***

It has been found that charge recombination rates in electrolyte A are strongly dependent upon the applied bias using $Ru(dcbpy)_2(NCS)_2$ sensitised $TiO_2$ electrodes (Haque, et al. 1998). The recombination kinetics are accelerated by an order of 4 by voltage application from 0 V to -0.5 V vs Ag/AgCl. At –0.4 V, a recombination half lifetime (time for 50 % recombination, $t_{50\%}$) is about 40 μs. This observation implies that charge recombination process involves non-geminated electrons, i.e. electronic states occupied in the $TiO_2$ film by the applied bias. These studies were extended to more negative biases by the femtosecond pump-probe spectrometer in order to investigate further acceleration of the recombination kinetics.

Figure 5.9 compares transient absorption spectra obtained at a time delay of 8 ps with applied voltages of 0, -0.6 and -0.8 V vs Ag/AgCl. All spectra exhibit positive absorption with a maximum towards 800 nm and are therefore assigned to the charge separated state. It is clear from the figure that the amplitudes of the spectra decrease as the bias becomes more negative.

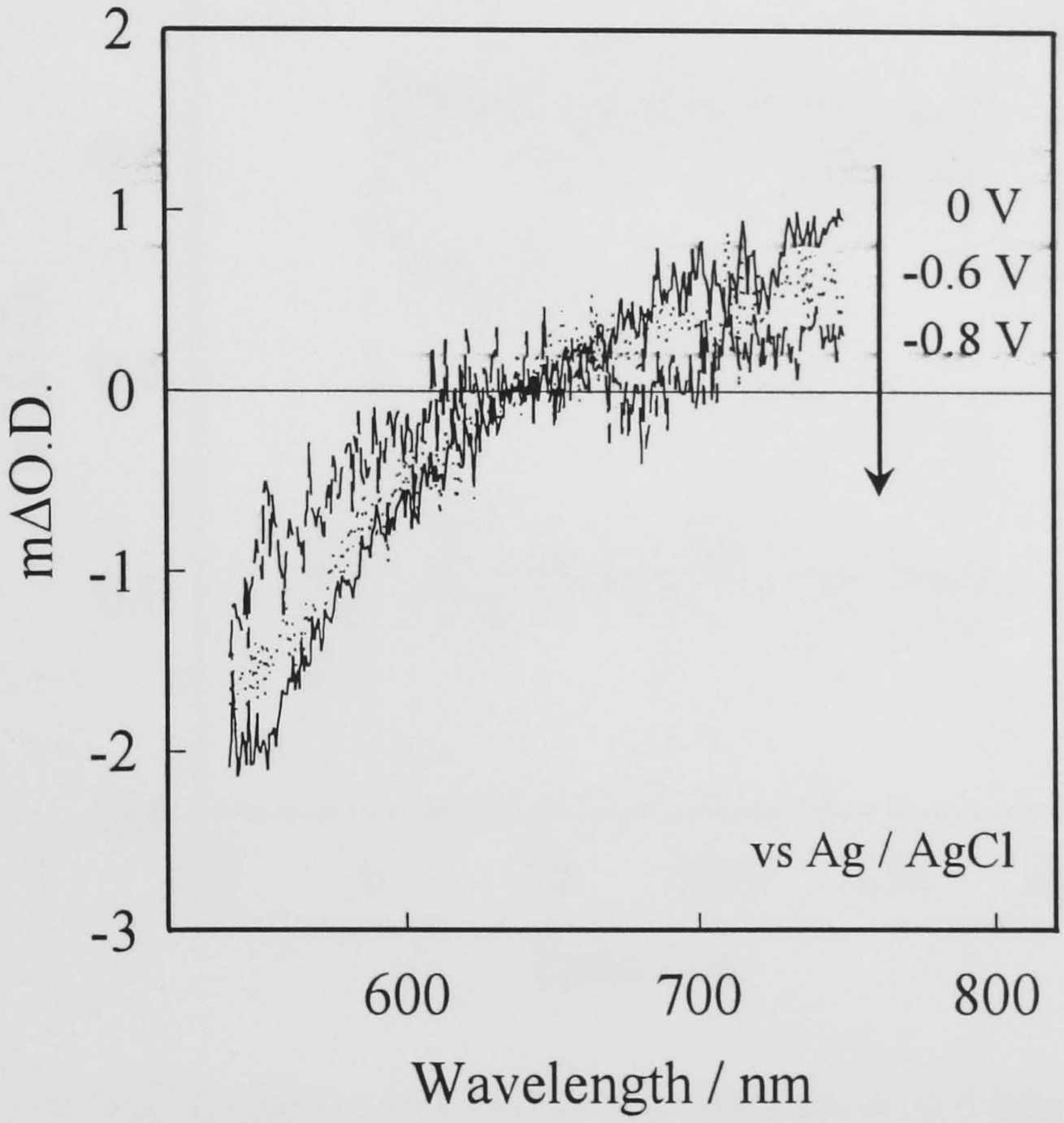



Figure 5.9. Absorption difference spectra taken at a time delay of 8 ps following 525 nm excitation with bias application of 0, -0.6 and –0.8 V vs Ag/AgCl into the dye sensitised $TiO_2$ electrode in electrolyte A.

The transient kinetics were monitored at 760 nm as shown in figure 5.10. The data were independent of the voltage application up to –0.4 V on this timescale. At –0.6 V, the transient signal is observed to decay with a lifetime of 100 ± 30 ps, attributed to picosecond charge recombination induced by this applied bias. The amplitude of the transient signal at early times was however unchanged by the application of this potential within the signal to noise level, indicating that the electron injection kinetics were invariant up to –0.6 V within 1 ps. Further acceleration of the decay rate to 3±1 ps was observed by an application of –0.8 V. However at this negative potential, the initial

amplitude of the signal is reduced. This reduction in amplitude may result from reduction in the injection yield at this potential. It should be noted that the changes observed at an application of –0.8 V were not fully reversible, indicating possible dye degradation or desorption induced at this potential.

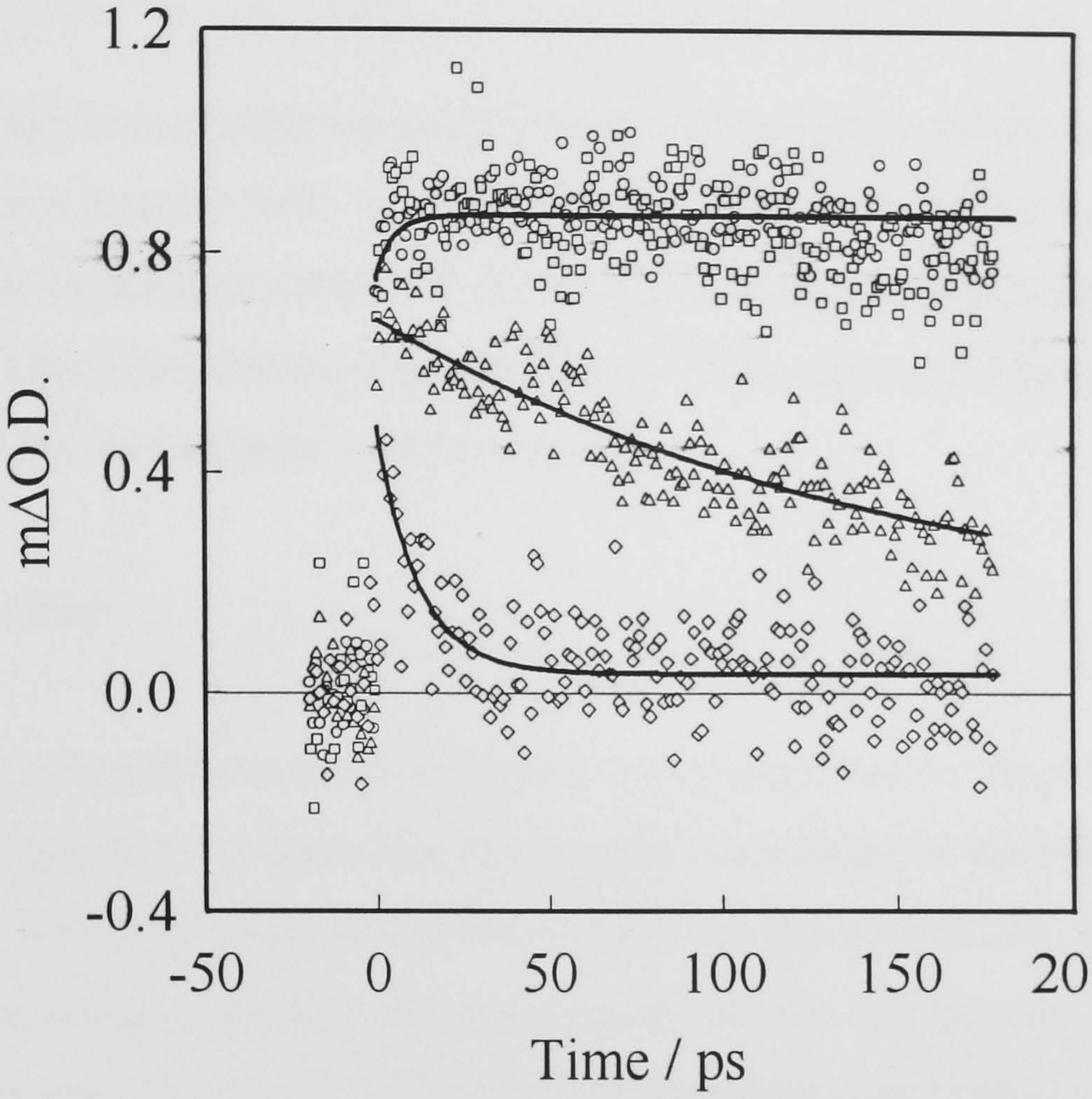



Figure 5.10. Transient kinetics collected at bias application of 0 (circle), -0.4 (square), -0.6 (triangle) and -0.8 (diamond) V vs Ag/AgCl to $Ru(dcbpy)_2(NCS)_2$ sensitised $TiO_2$ electrode in electrolyte A at a probe wavelength of 760 nm following 525 nm excitation. The results of the kinetic fitting are shown as solid lines.

### 5.5.3 Discussion

As described in chapter 3, the potential tail of the bottom of the conduction band in nanocrystalline $TiO_2$ films have been characterised as a density of sub-band gap or 'trap' states attributed, at least in part, to surface states. The application of an electric potential modulates the occupancy of conduction / trap states of the $TiO_2$ film. It has been found that this variation in occupancy has a dramatic effect upon the rate of charge

recombination following electron injection in dye sensitised nanocrystalline $TiO_2$ films (Haque, et al. 1998, Haque, et al. 1999). It has been suggested (Haque, et al. 1998, Haque, et al. 1999, Nelson 1999) that such strong dependence of the recombination kinetics upon the applied bias may be associated with these trap states. The acceleration in the charge recombination kinetics at negative applied potentials was attributed to increase in the electron occupancy of these trap states as the Fermi level was raised.

The electron injection process proceeds from the dye excited state into unoccupied electron acceptor states in $TiO_2$. It is expected that the electron injection yield should decrease when the electron acceptor states in $TiO_2$ are increasingly occupied by the applied bias. Therefore, decreased population of charge separated states and increased population of dye excited states will be observed.

***Electron injection***

Following the non-adiabatic electron transfer theory described in chapter 3, the injection kinetics are expected to be dependent upon applied voltage when the free energy gap between the Fermi level of the semiconductor and the dye excited state is less than the reorganisation energy associated with the electron transfer. Using a dye excited state oxidation potential of –0.75~-0.7 V vs Ag/AgCl (Hagfeldt and Grätzel 1995, Nazeeruddin, et al. 1993), the data shown in electrolyte B in figure 5.6 would yield reorganisation energy associated with this reaction of at most 0.35~0.3 eV since the electron injection kinetics are independent of the applied voltages up to –0.4 V vs Ag/AgCl. This observation also implies that the potential energy levels of available electron acceptor states are located above –0.4 V vs Ag/AgCl when using electrolyte B.

The electrostatic interaction with the electrons occupying trap / conduction band states of the $TiO_2$ might also be expected to retard the rate of electron injection at negative applied potentials. However consideration of the Coulombic interaction energy, using a dielectric constant of 100 for $TiO_2$ (Cao, et al. 1995, Krol, et al. 1997), indicates the repulsion energy for two electrons separated by 10 nm within a nanoparticle is of the order of only 1 mV. It should be noted that most reported values of dielectric constant for anatase nanocrystalline $TiO_2$ films significantly vary from 100 to 180, however a much lower value of <60 was also reported (Krol, et al. 1997). It should also be noted

that this calculation neglects screening of the electronic charge by the electrolyte, and is therefore an upper limit for the interaction energy. On this basis, significant retardation of the injection rate would only be expected for electron occupancies of 10's-100 per nanoparticle. Such electron occupancies are much greater than those achieved under the bias range considered here.

In an applied potential range of –0.5 ~ –0.8 V vs Ag/AgCl in electrolyte B, the gradual decrease of the electron injection yield was observed, which was inferred from the transient spectral change (see figures 5.7 and 5.8). In contrast, the electron injection kinetics remained similar to those obtained at the lower applied voltages. Since the transient data were not reproducible with the application of external voltages over –0.5 V vs Ag/AgCl and steady state absorption measurements exhibited gradual spectral change at the same bias range, it is not clear that the kinetics are similar even at high negative applied voltages. It can however be deduced from these observations that decreased injection yields probably originate from the irreversible change of sensitiser dye molecules, e.g. degradation or desorption from the $TiO_2$ surface. In order to clarify if this low injection yield originates from the desorption of $Ru(dcbpy)_2(NCS)_2$, strong adsorption of the dye on the surface is necessary under a wide range of applied bias. For example, it is known that the phosphonate form of the ruthenium dye strongly adsorb onto the $TiO_2$ film compared to $Ru(dcbpy)_2(NCS)_2$ (over a wide pH range) (Péchy, et al. 1995). Therefore, this type of dye can be considered to employ as a sensitiser dye.

In electrolyte A, it has been observed that the electron injection kinetics are independent of the application of the bias up to –0.6 V vs Ag/AgCl. Contrast to the data obtained in electrolyte B suggests that the irreversibility of the sample upon the bias application may be dependent upon the choice of the electrolyte. Further work should be carried out for the influence of the bias application on the $TiO_2$ surface under the combination of different electrolytes.

### *Charge recombination*

It has been found that the modulation of the recombination rate is correlated with the potential energy level of the conduction band (Haque, et al. 1999) which is largely controlled by the potential determining ions as discussed in section 5.6. For example, if

the band energy level is shifted positively, the recombination rate is accelerated at lower negative applied bias. In the present case, it has been found that the band energy level in electrolyte A is more positively shifted by 0.2 V than in electrolyte B, and thus the acceleration occurs at lower negative applied bias (by 0.2 V) in electrolyte A than electrolyte B.

It has been shown that modulation of the applied potential from 0 to -0.4 V in electrolyte B results in a $10^2$ fold acceleration in the half lifetime for charge recombination (Haque, et al. 1999). At -0.4 V, the recombination reactions occurs from sub-microsecond to millisecond timescales (Haque, et al. 1999). Even at higher bias application up to -0.7 V vs Ag/AgCl, the recombination rate is only accelerated to microsecond timescales (Haque, et al. 1999). These recombination kinetics are consistent with the data shown in figure 5.6, which demonstrates that the injection kinetics are unchanged over this potential range.

In contrast, the half lifetime of the recombination for the sensitised $TiO_2$ films in electrolyte A is accelerated by 4 orders of magnitude from microsecond to nanosecond timescales by voltage application from 0 V to -0.5 V vs Ag/AgCl. Figures 5.9 and 5.10 indicate that this remarkable acceleration of the recombination kinetics occurs on picosecond timescales at high negative applied biases. These ultrafast recombination processes become competitive with the multi-phasic electron injection process with rates of femtosecond to several tens of picosecond, resulting in reduction of initial amplitudes. It is not likely that these amplitude decays can be assigned to back electron transfer process to form the dye excited state. The spectral shapes for these decays are not associated with the spectrum of the excited state and the kinetic spectra exhibit similar to that for charge separated state decay. It should, however, be noted that for these experiments a more limited signal to noise precluded detailed assignment of the kinetic components.

In consequence, variation in the applied potential from 0 V to –0.6 V (vs Ag/AgCl) in electrolyte A resulted in an acceleration of the recombination reaction from ~1 ms to 100 ps, while the electron injection kinetics are not significantly influenced. Previous studies have exhibited widely differing results for the influence of applied bias voltage on charge recombination kinetics. O'Regan et al. demonstrated acceleration of the

recombination rate by a $10^3$ fold with application of negative voltages (O' Regan, et al. 1990). On the other hand, Kamat and co-workers observed that the recombination kinetics were independent of applied voltages (Kamat, et al. 1996).

## 5.6 Dependence on conduction band energetics

### 5.6.1 Introduction

The conduction band energetics of nanocrystalline $TiO_2$ films are strongly dependent upon the electrolyte composition with which the film is in contact. Spectroelectrochemical studies have demonstrated that the flat band potential of such films can shift by over one volt depending upon the presence in the electrolyte of small 'potential determining' cations such as protons or $Li^+$ ions (Redmond and Fitzmaurice 1993), suggesting that the density of electron acceptor states in $TiO_2$ can be controlled by such cations.

In the Centre for Photomolecular Sciences, both spectroelectrochemical measurement analogous to those reported previously (Rothenberger, et al. 1992) and chronoamperometric capacitance measurement (Willis, et al. 1999) were carried out in order to investigate the influence of the electrolytes (electrolyte B or C) upon the energetics of conduction band / trap states of the $TiO_2$ films. Typical spectroelectrochemical data are shown in figure 5.11, plotted as absorption of electrons in the $TiO_2$ film at 800 nm as a function of applied potential (the data were taken by Mr. Richard Willis and Mr. Saif Haque). Both measurements showed that, when $TiO_2$ films were incorporated as the working electrode of a photoelectrochemical cell, the conduction band energetics were shifted by 1 V to more positive potentials in the presence of 0.1 M $Li^+$ ions, in agreement with previous studies. It is also apparent from figure 5.11 that the data exhibits an approximately exponential tail towards more positive biases. This is attributed to the presence of sub-band gap defect or surface states, as has been discussed previously (Rothenberger, et al. 1992). Note that it has been found that small amount of impurity (possibly water) content significantly shifts the potential energy level of the density of states negatively (Heinzel, et al. 1981), and thus the electrolyte must be well dried to obtain reproducible conduction band

energetics. It should also be noted that the spectroelectrochemical data shown here were collected on unsensitised $TiO_2$ films, however data collected on sensitised films were indistinguishable, i.e. this shift was not affected by adsorbed dyes.

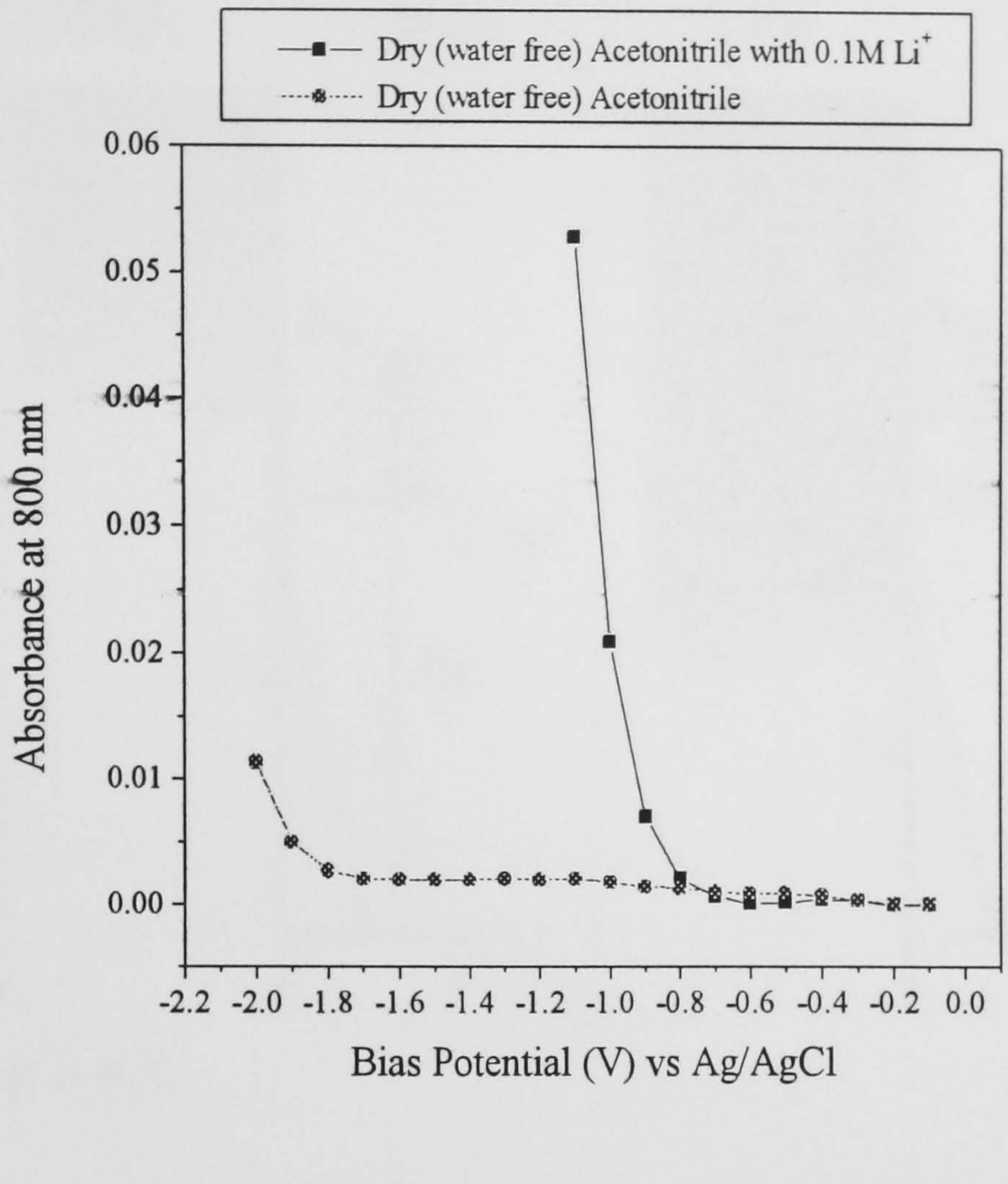



Figure 5.11. Absorbance of electrons collected in the $TiO_2$ electrode in the anhydrous acetonitrile electrolyte (0.1 M TBAP contained) in the presence (square) and the absence (circle) of 0.1 M $LiClO_4$. Data were obtained at a probe wavelength of 800 nm under the application of external voltages to the $TiO_2$ film incorporated as the working electrode of a three electrode cell.

In this section, the two electrolytes (B and C) were employed for transient absorption measurements in order to address whether this shift of the density of electron acceptor states in $TiO_2$ influences electron injection kinetics. $Ru(dcbpy)_2(NCS)_2$ sensitised $TiO_2$ films were excited at 623 nm, corresponding to the low energy absorption tail of the dye. The experimental conditions differed only in the addition or absence of 0.1 M lithium perchlorate ($LiClO_4^-$), however both contain 0.1 M of TBAP. The addition of $Li^+$ ions to the electrolyte has strong influence upon the acceptor density of states available for electron injection from the $Ru(dcbpy)_2(NCS)_2$ excited state (figure 5.11).

Figure 5.12 compares the redox potentials of the conduction band and the excited state (-0.75 ~ -0.7 V vs Ag/AgCl) of $Ru(dcbpy)_2(NCS)_2$ in solution (see chapter 1 for the details).

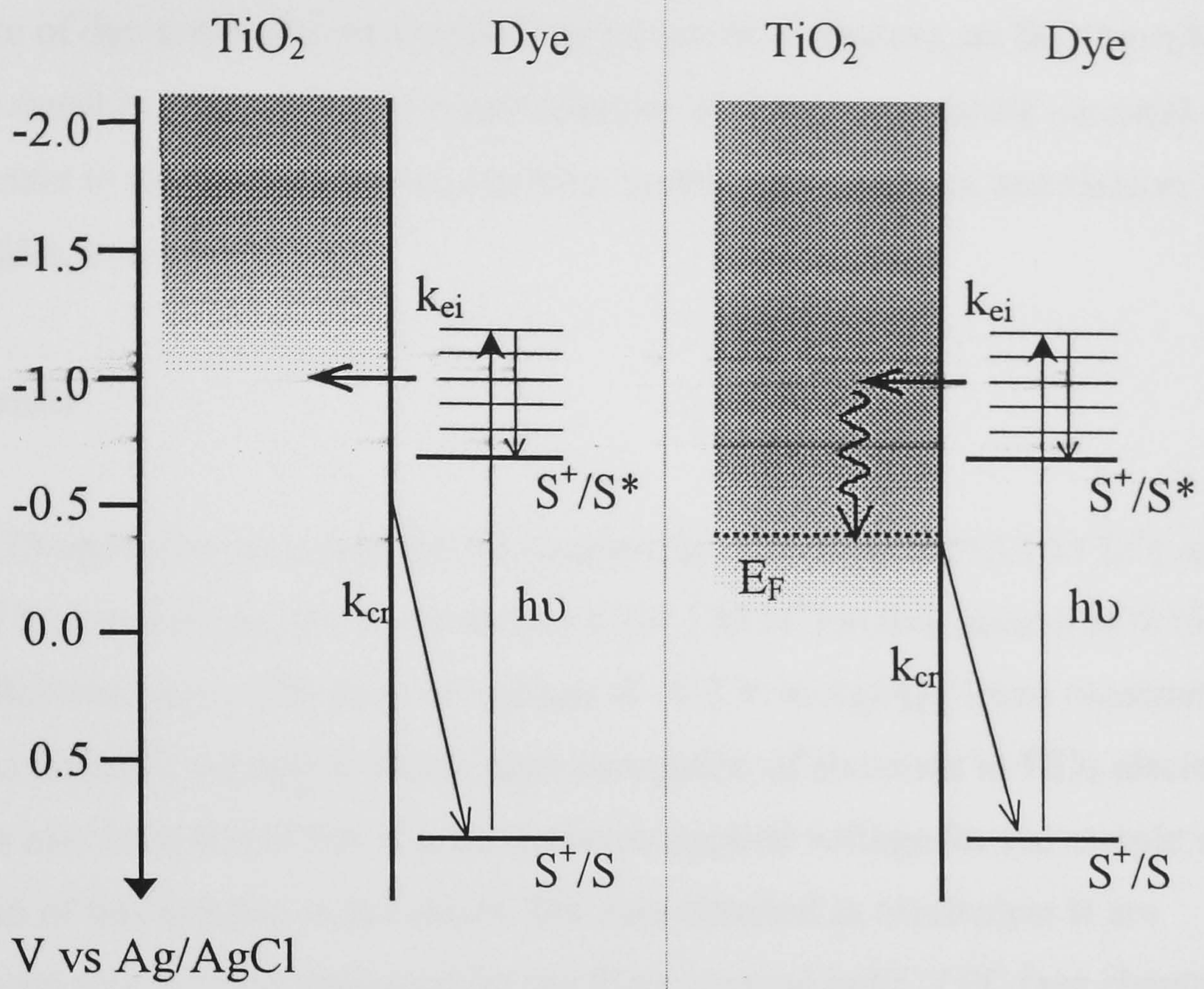



Figure 5.12. Schematic representation of potential energy diagram of dye sensitised $TiO_2$ nanocrystalline films covered in electrolyte B and C. $k_{ei}$ and $k_{cr}$ refer to electron injection and charge recombination, respectively. It has been assumed in this figure that the redox potentials of the dye ground state (vs SCE) were not altered by the addition of lithium ions. The graduated shading of the conduction band illustrates the high density of sub-band gap (trap) states, resulting in a poorly defined conduction band edge (Rothenberger, et al. 1992) as discussed in figure 5.1.

The oxidation potential of the lowest dye excited state may be to some extent modulated by the presence / absence of potential determining ions. Zaban et al. have reported that whereas in the presence of $Li^+$ ions adsorbed sensitiser dyes exhibit similar redox potentials to those observed in solution, these potentials may be shifted more negative by 0.3~0.4 V in the absence of $Li^+$ (Zaban, et al. 1998). In contrast with this study, Yan and Hupp have reported that the redox potentials of the dye adsorbed onto the surface of nanocrystalline $TiO_2$ films are essentially independent of solution pH (Yan and Hupp

1997). Despite both of these cases, it is clear from figures 5.11 and 5.12 that whereas in the presence of $Li^+$ electron injection can proceed to a high density of conduction band states, in the absence of $Li^+$, electron injection will only be possible into relatively low density of sub-band gap states. It should be noted that $Li^+$ ions are routinely added to the electrolyte of dye sensitised nanocrystalline photovoltaic devices, as they have been shown to result in improved device performance, although the specific cause(s) of this improvement in device function has not been established (Hagfeldt and Grätzel 1995, Nazeeruddin, et al. 1993).

### 5.6.2 Results

Figure 5.13 represents transient spectra obtained in electrolyte B (+0.1 M $Li^+$) at time delays of 0.15 and 60 ps, and in electrolyte C (-0.1 M $Li^+$) at time delays of 0.15 and 600 ps after excitation. The external voltage of –0.2 V vs Ag/AgCl was constantly applied to maintain negligible steady state occupation of electrons in $TiO_2$ electrode, and it has also been found that it is the optimum applied voltage for the sample stability (the origin of this stability is not clear). The data obtained in electrolyte B are indistinguishable to those described for the films covered in EC / PC (see chapter 4). Comparison of figures 5.13a and b indicates that on longer timescales the data are essentially independent of electrolyte composition and the spectra exhibit increasing amplitude towards 800 nm, indicative of the dye cation absorption. This comparison also indicates that the yield of electron injection was not sensitive to electrolyte composition. This conclusion was further supported by µs-ms data obtained by Mr. Saif Haque, which also indicated that the dye cation yields in electrolytes B and C were indistinguishable within ±20 %. In contrast, it is apparent from figure 5.13 that the transient spectra at 150 fs are strongly dependent upon the presence of $Li^+$ ions to the electrolyte. In the presence of $Li^+$, the spectrum is approximately flat between 700 and 800 nm, due to contributions from both the dye excited state (maximum 720 nm) and the $dye^+(TiO_2)^-$ state (maximum 800 nm) at this time delay. In the absence of $Li^+$, the spectrum at 150 fs is dominated by a maximum at 720 nm, indicating that the spectrum results primarily from the dye excited state.

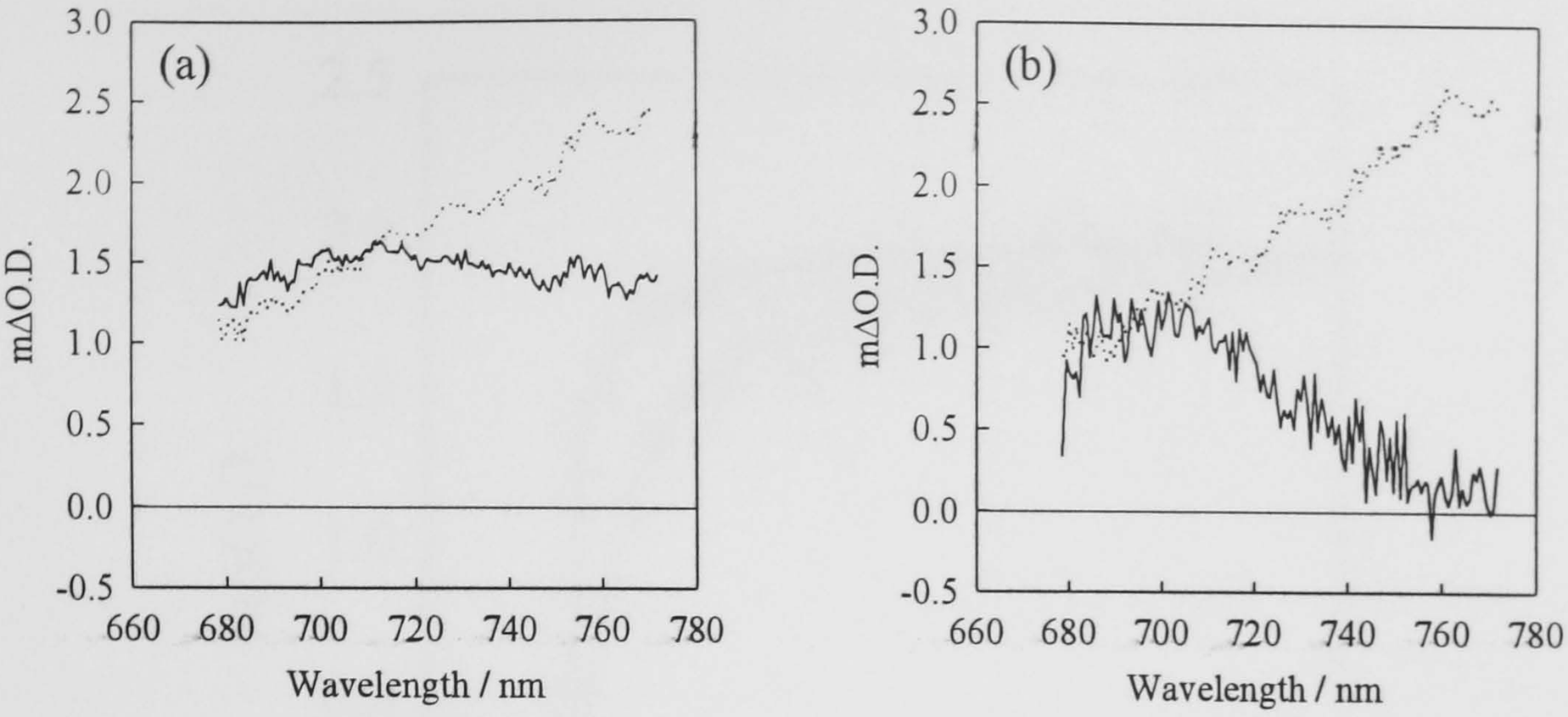



Figure 5.13. Transient absorption spectra obtained (a) at 150 fs (————) and 60 ps (·····) in the presence of 0.1 M $Li^+$ (electrolyte B) and (b) at 150 fs (————) and 600 ps (·····) in the absence of $Li^+$ (electrolyte C). An external voltage of –0.2 V vs Ag/AgCl was applied during data collection, as this was found to be optimum for sample stability.

The dependence of the electron injection kinetics upon $Li^+$ is further demonstrated in figure 5.14, which compares the transient kinetics at 760 nm obtained for electrolytes B (circle) and C (triangle). The global analysis of the kinetic data obtained in electrolyte B results in a minimum of three components being required to fit the injection kinetics, with lifetimes (relative amplitudes) of <150 fs (0.4±0.03), 850±250 fs (0.28±0.03) and 15±3 ps (0.32±0.03). As concluded from figure 5.13, it is apparent that the absence of $Li^+$ ions results in retardation of the injection kinetics. Note that prolonged (>5 minutes) excitation of one spot of the $TiO_2$ film in electrolyte C resulted in a gradual acceleration of the injection kinetics; the origin of this kinetic change is currently unclear. Global analyses of the data obtained with electrolyte C yielded lifetimes (amplitudes) for electron injection of <150 fs (0.075±0.03), 680±80 fs (0.365±0.03), 20±7 ps (0.35±0.03) and >60 ps (0.21±0.03). Consideration of a half lifetime associated with electron injection exhibits at least a 7±1 fold retardation for electrolyte C compared to electrolyte B. In consequence, whereas in the presence of $Li^+$ a significant proportion (~40 %) of the electron injection proceeds in <150 fs, in the absence of $Li^+$ (and any other potential determining ions) electron injection proceeds almost entirely on timescales longer than 150 fs.

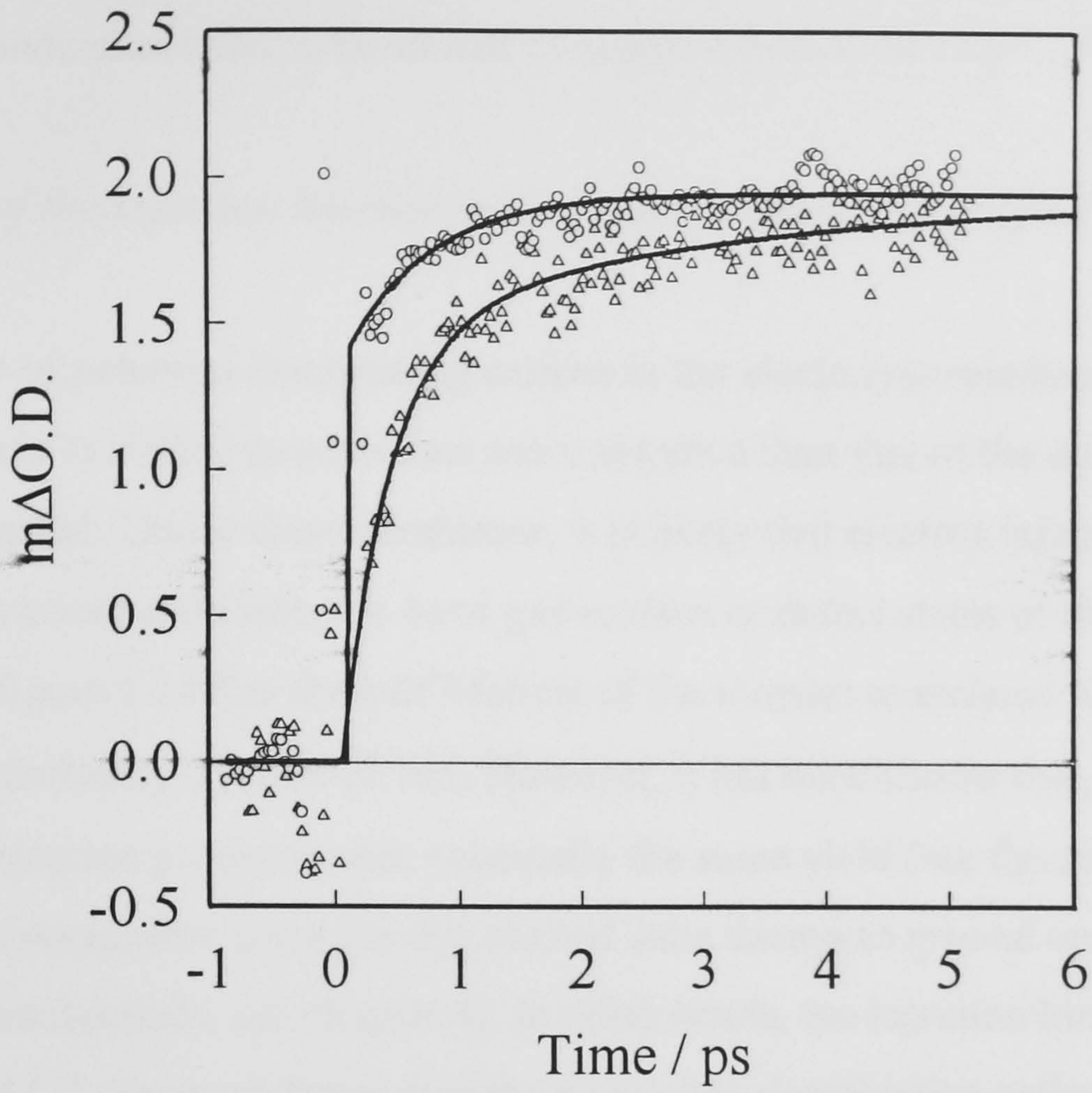



Figure 5.14. Electron injection kinetics for $Ru(dcbpy)_2(NCS)_2$ sensitised $TiO_2$ films collected in the presence (circle) and the absence (triangle) of $Li^+$ in electrolyte (electrolytes B and C respectively) at a probe wavelength of 760 nm following 623 nm excitation. Results of the kinetic fitting are shown as solid lines.

### 5.6.3 Discussion

The energetics of the conduction band / trap states of the nanocrystalline $TiO_2$ film are influenced by the presence of small 'potential determining' cations, including both $Li^+$ and protons. The presence of $Li^+$ ions in the cell correlates the injection kinetics and the potential energy of the $TiO_2$ conduction band / trap density of states, as presented in figures 5.11, 5.12 and 5.14.

The shift of the spectroelectrochemical data to negative potentials (at approx. -2 V vs Ag/AgCl) was only observed when such ions had been removed from the electrolyte solution. For example, if the electrolyte solution was not sufficiently anhydrous, spectroelectrochemical data are rather similar to that for electrolyte B, being

independent of the presence of $Li^+$ ions. The slower injection kinetics were only observed under conditions in which the capacitance and spectroelectrochemical data showed the conduction band to be shifted to negative potentials (e.g. –2 V vs Ag/AgCl).

***Comparison of the injection kinetics in the presence and absence of $Li^+$***

In the absence of potential determining cations in the electrolyte solution, the conduction band is shifted to potentials more negative than that of the dye excited state oxidation potential. Under these conditions, it is likely that electron injection proceeds from the dye excited state into sub-band gap surface or defect states of the $TiO_2$ film. It is clear from figure 5.14 that the half lifetime of the kinetics associated with electron injection is retarded by a factor of 7±1. However, it has been shown that, remarkably, the electron injection proceeds with essentially the same yield (see figure 5.14). This observation is reasonable since the dye excited state decays to ground on relatively slow timescales (nanoseconds, see chapter 4). In other words, the injection kinetics even with the absence of $Li^+$ are much faster than the competing deactivation pathway of excited state decay to ground, suggesting that the electron injection occurs with a high yield.

It is possible that the observation of the retarded injection kinetics (figure 5.14) results from the reduction in acceptor density of states. In such a condition, electron injection reaction may not always be activationless as the number of reactant and product states is considerably decreased (see chapter 3 in the electron transfer theory for the details). At present, more quantitative consideration of the relationship between injection rate and $TiO_2$ density of states is precluded by uncertainty over the redox potentials of the adsorbed dyes and potentials of the electron acceptor states in the $TiO_2$ as discussed above. Since the electron injection kinetics are independent of surrounding solvent and electrolyte employed to cover the films, the correlation of a positive shift of the spectroelectrochemical data with an acceleration of injection kinetics in the presence of any potential determining ions strongly suggests the retardation results from a reduction in the acceptor density of states.

It is also possible that the strong adsorption / intercalation of $Li^+$ ions to the $TiO_2$ nanoparticles would be expected to favour electron injection from simple electrostatic

considerations. For example, for the case of surface adsorbed $Li^+$ ions, the surface layer of positive $Li^+$ ions between the $TiO_2$ and the adsorbed dye would generate strong electric fields favouring electron injection. However, a quantitative analysis of the relationship between injection rate and $TiO_2$ density of states is required to confirm this conclusion.

Meyer et al. recently reported by means of the nanosecond flash photolysis system that the addition of potential determining ions such as $Li^+$ into the electrolyte of dye sensitised $TiO_2$ solar cells has strong influence upon the mechanism of the electron injection process (Thompson, et al. 1999). Electron injection proceeds rapidly from the dye excited state into the conduction band of $TiO_2$ in the presence of $Li^+$. On the other hand, in the absence of $Li^+$ and the presence of electroactive redox couple ($I_3^-/I^-$), the dye excited state is initially quenched by this redox couple, and subsequently the dye anion injects an electron into the $TiO_2$. This observation originates from slow electron injection rate from the dye excited state into the $TiO_2$, being competitive with electron transfer process from the iodine redox couple to the dye excited state (Thompson, et al. 1999). Such a slow electron injection into the $TiO_2$ is qualitatively consistent with the data obtained here. However, they also concluded (Kelly, et al. 1999) that the addition of $Li^+$ ions strongly influenced the electron injection yield, in contrast to the observations here. The cause of this difference is unclear, but may be associated with differences in the injection and / or excited state deactivation rates resulting from the use of different sensitiser dyes and / or other experimental conditions.

## 5.7 Dependence on sensitiser dyes

### 5.7.1 Introduction

Ruthenium bipyridyl analogues are the most efficient sensitiser dyes reported to date for dye sensitised solar energy conversion (Nazeeruddin, et al. 1993) despite their generally rather poor red / near infrared light absorption (>700 nm). Extensive studies of alternative organometallic sensitiser dyes, including porphyrins (Boschloo and Goossens 1996, Kalyanasundaram, et al. 1987, Kay and Grätzel 1993), phthalocyanines (Nazeeruddin, et al. 1998, Shen, et al. 1995), squarine dyes (Kamat, et al. 1993) and

xanthene dyes (Sayama, et al. 1998), have failed to identify any dye with improved sensitising efficiency. The cause(s) of these lower efficiencies is not clear, and also the correlation between dye photophysics and kinetics of interfacial electron transfer reactions has not been established.

In this section, a detailed comparison of the electron injection kinetics between $Ru(dcbpy)_2(NCS)_2$ and two porphyrin dyes adsorbed to nanocrystalline $TiO_2$ films is discussed. The porphyrins selected were Zinc and Free Base tetracarboxyphenyl porphyrins (ZnTCPP and $H_2$TCPP respectively) since their electronically excited state structures and electrochemical data have been well established (Darwent, et al. 1982, Gouterman 1978). ZnTCPP has previously been shown to sensitise nanocrystalline $TiO_2$ films, although with a lower efficiency (Boschloo and Goossens 1996, Kalyanasundaram, et al. 1987) than reported for $Ru(dcbpy)_2(NCS)_2$. For all three dyes, linkage to the semiconductor surface is achieved by carboxylate groups (see figure 2.13 for dye structures). For all optical experiments in this section, the dye sensitised $TiO_2$ films were covered in ethylene carbonate / propylene carbonate (EC / PC = 1:1) solution.

The solution phase ground and excited state redox potentials have been well characterised for all three dyes as shown in figure 5.15 (Darwent, et al. 1982, Gouterman 1978, Hagfeldt and Grätzel 1995, Nazeeruddin, et al. 1993). The previous studies suggest that the excited state $dye^+$ / dye* redox potentials of $H_2$TCPP and $Ru(dcbpy)_2(NCS)_2$ are rather similar (-0.85 and –0.75~-0.8 V vs SCE in solution respectively), while ZnTCPP's redox potential is significantly more negative (-1.5 V). It should be noted that the potential for $H_2$TCPP is estimated comparing with analogous free base porphyrins (Kalyanasundaram and Neumann-Spallart 1982). Also, note that although it has been reported (Heimer, et al. 1996) that the values of the dye redox potentials obtained in the solution phase may be altered by <100 mV after their sensitisation onto the surface of $TiO_2$ films, they are still useful for relative comparison of different dye redox potentials. Therefore, the correlation between dye photophysics / redox potential and interfacial electron transfer kinetics can directly be investigated.

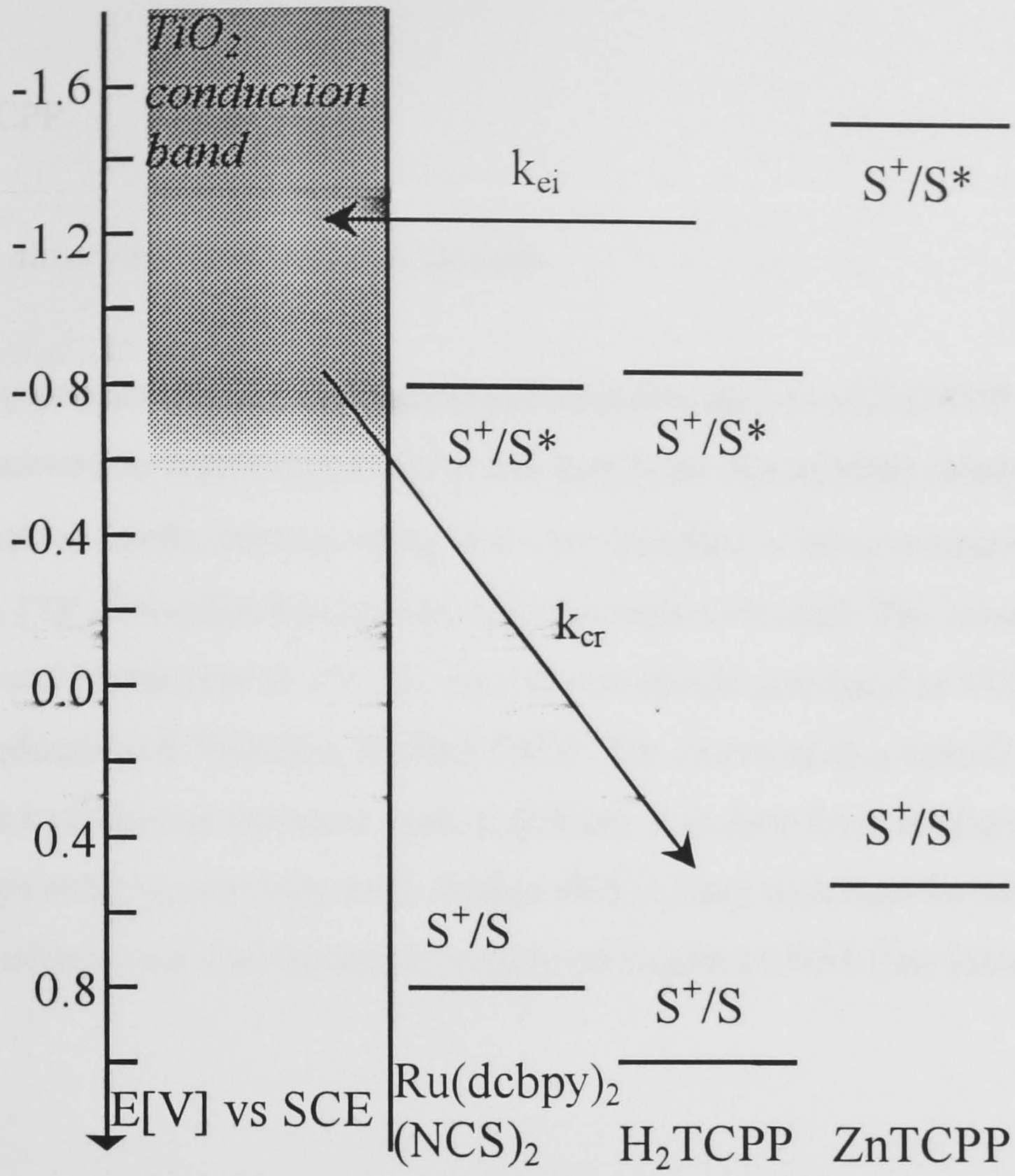



Figure 5.15. Schematic representation of potential energy diagram of dye sensitised $TiO_2$ nanocrystalline films. $k_{ei}$ and $k_{cr}$ refer to electron injection and charge recombination, respectively. Dye ground state and lowest excited state oxidation potentials (vs SCE) were taken from previous solution phase studies (Hagfeldt and Grätzel 1995, Kalyanasundaram 1982). The oxidation potentials for $H_2TCPP$ were estimated by comparison with analogous free base porphyrins (Kalyanasundaram and Neumann-Spallart 1982). It should be noted that the dye oxidation potentials may change when adsorbed to the $TiO_2$, as has recently been discussed (Zaban, et al. 1998, Zaban, et al. 1997).

## 5.7.2 Results

### 5.7.2.1 $Ru(dcbpy)_2(NCS)_2$

The steady state absorption and emission spectra for the dye in ethanol solution, and the electron injection kinetics in the dye sensitised $TiO_2$ films are shown in chapter 4.

5.7.2.2 ZnTCPP

***Steady state absorption and emission spectra***

Figure 5.16 shows steady state absorption and emission spectra of ZnTCPP dissolved in ethanol. In contrast to $Ru(dcbpy)_2(NCS)_2$, this porphyrin dye exhibits relatively narrow visible absorption bands, corresponding to $\pi$ - $\pi^*$ transition of the conjugated macrocycles ('Q' absorption bands), and its vibrational side band. The lowest energy Q absorption band is observed at 598 nm, with its vibrational side band at 558 nm (Kalyanasundaram and Neumann-Spallart 1982). The observed $Q_{0,0}$ emission band is at 609 nm with a vibrational emission band at 658 nm. It is clear from the figure that this porphyrin dye exhibits relatively small Stokes shift (11nm) with high fluorescence intensity consistent with their relatively long lived singlet excited state lifetimes (see below).

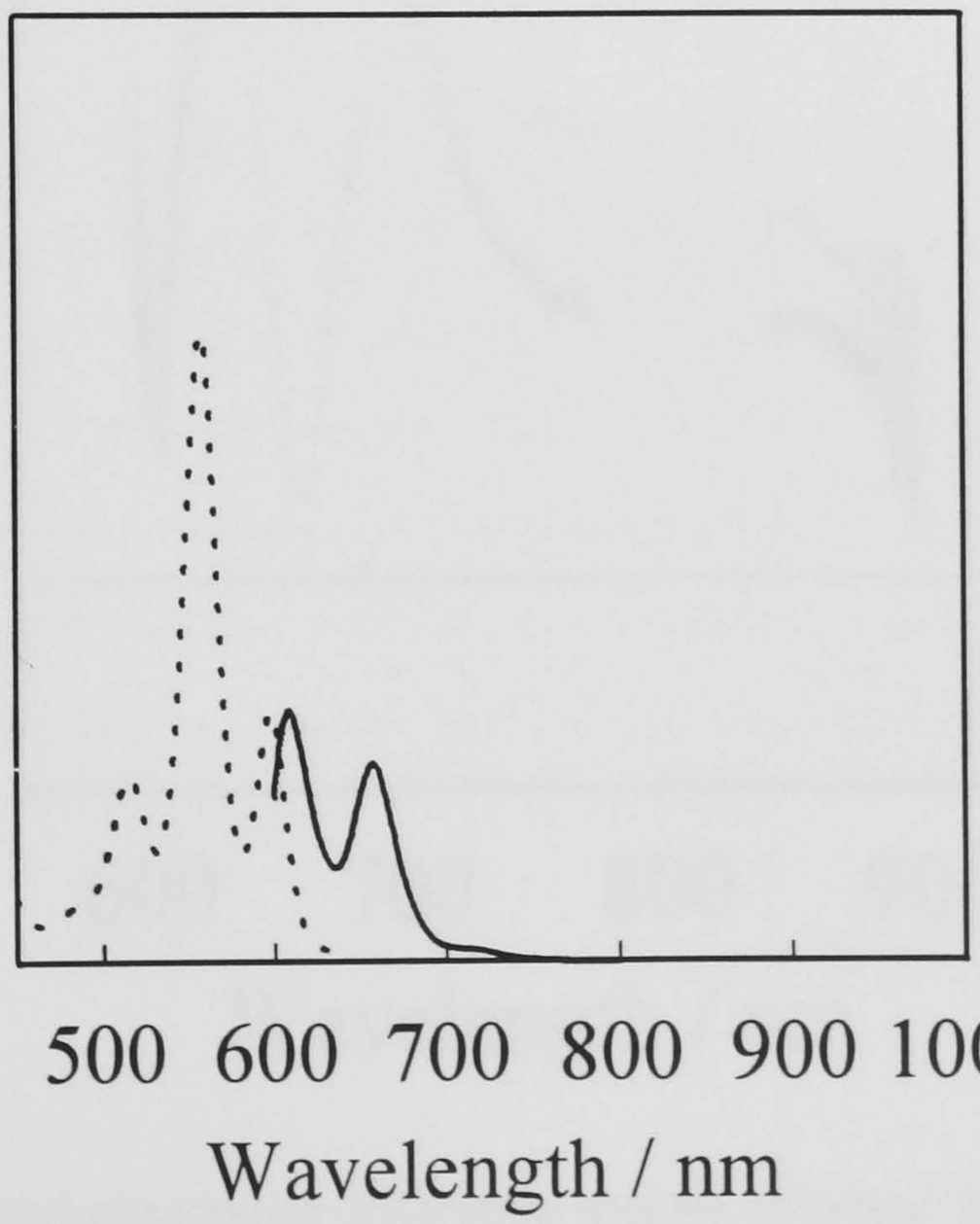



Figure 5.16. Steady state absorption (·····) and emission(——) spectra of ZnTCPP in ethanol. An excitation wavelength for the emission was 560 nm.

### *Transient absorption spectra*

Figure 5.17 compares transient absorption spectra obtained for ZnTCPP in ethanol and for the sensitised $TiO_2$ films. The spectrum for ZnTCPP in ethanol exhibits a prominent stimulated emission band at 660 nm (c.f. figure 5.16), confirming the assignment of this spectrum to the singlet excited state. Adsorption of the dye to $TiO_2$ results in quenching of the stimulated emission, consistent with electron injection into the $TiO_2$ resulting in formation of $dye^+(TiO_2)^-$. This spectral shape was almost identical to the preliminary data (400 nm excitation) obtained by Dr. Richard Tompkins (Tompkins 1998). The assignment of the electron injection was also confirmed by the observation that the resultant spectrum was essentially invariant on timescales up to microseconds by Mr. Saif Haque in Centre for Photomolecular Sciences.

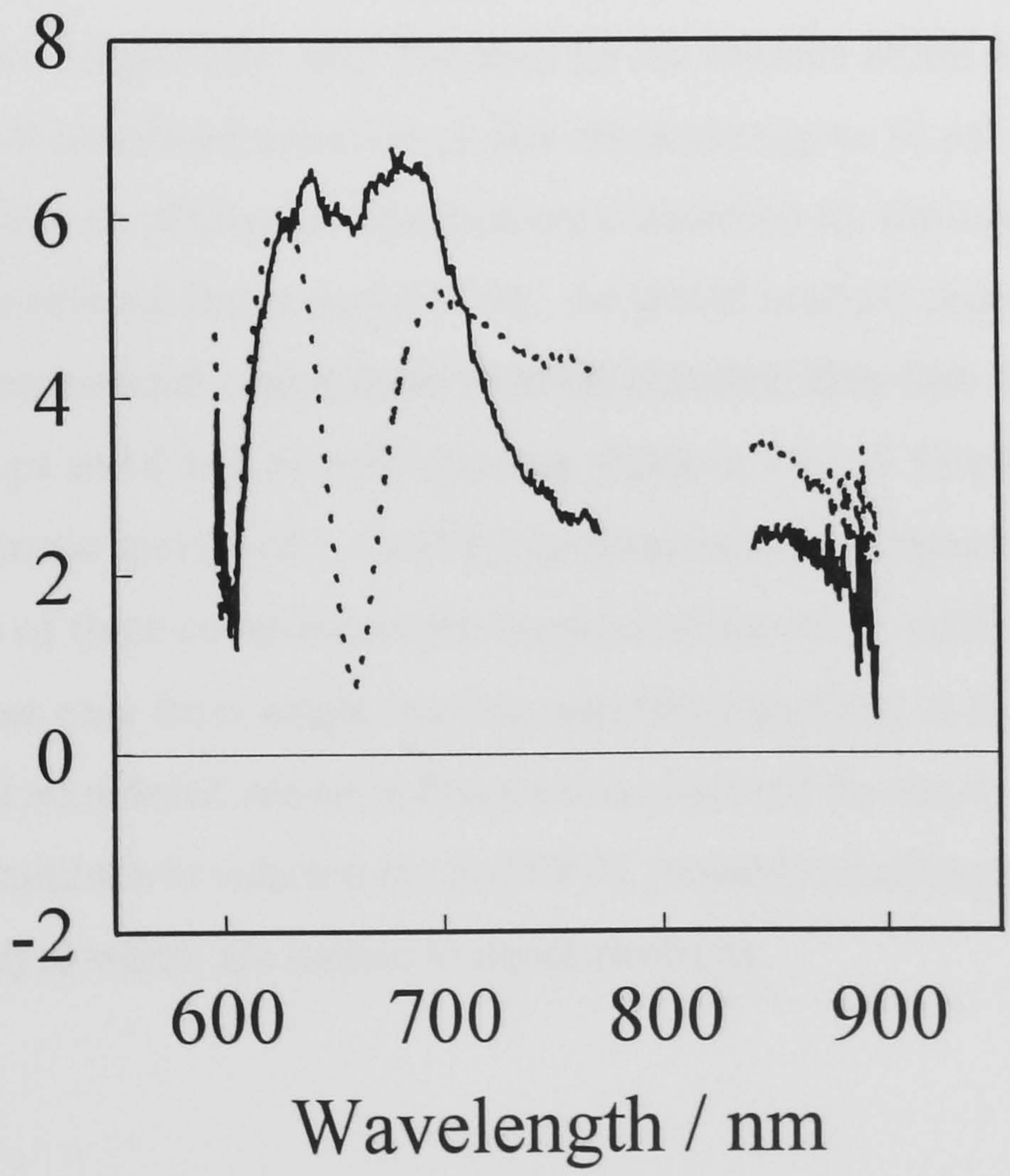



Figure 5.17. Picosecond absorption difference spectra obtained for ZnTCPP in ethanol (·····) and sensitised $TiO_2$ films (——) at time delays of 6 and 60 ps, respectively, with an excitation wavelength of 560 nm.

Picosecond transient data for ZnTCPP in ethanol demonstrated a single exponential kinetic component with a lifetime of approximately 3 ns consistent with stimulated emission decay (data are not shown), again suggesting relaxation of the singlet excited state. The observation of the long-lived singlet excited state is consistent with the strong fluorescence measured by the steady state emission spectroscopy (see figure 5.16).

***Kinetics of electron injection***

The spectral range including the stimulated emission bands is generally used for the assignment of electron injection kinetics for the sensitised $TiO_2$ films. Transient spectra obtained for the dye sensitised $TiO_2$ films show a time dependent disappearance of their vibronic stimulated emission bands, as illustrated in figures 5.18. As described above, the decay of this stimulated emission is assigned to electron injection from the singlet excited state into the $TiO_2$. Figure 5.19 represents the transient kinetics at the peak of the stimulated emission band (665 nm). The data for the solution phase exhibits negligible kinetics of stimulated emission on this timescale (up to 30 ps). In contrast, multi-exponential kinetics of electron injection were observed for the sensitised $TiO_2$ films. Similar to the case for $Ru(dcbpy)_2(NCS)_2$, the global analysis required a minimum of three exponential components to fit the transient data with time constants of <100 fs, 1.1±0.4 ps and 8.5±2 ps with injection yields of 0.37, 0.12 and 0.51 (±0.05), respectively. The kinetic spectra of 1.1 and 8.5 ps components are shown in figure 5.20. The spectral shapes of these components are identical within error, confirming that each component originates only from single reaction (electron injection). It should be noted that a small residual stimulated emission feature was observed for the dye adsorbed to $TiO_2$ (7 % of the amplitude in solution for ZnTCPP), probably resulting from sub-populations of the dyes which are unable to inject electrons.

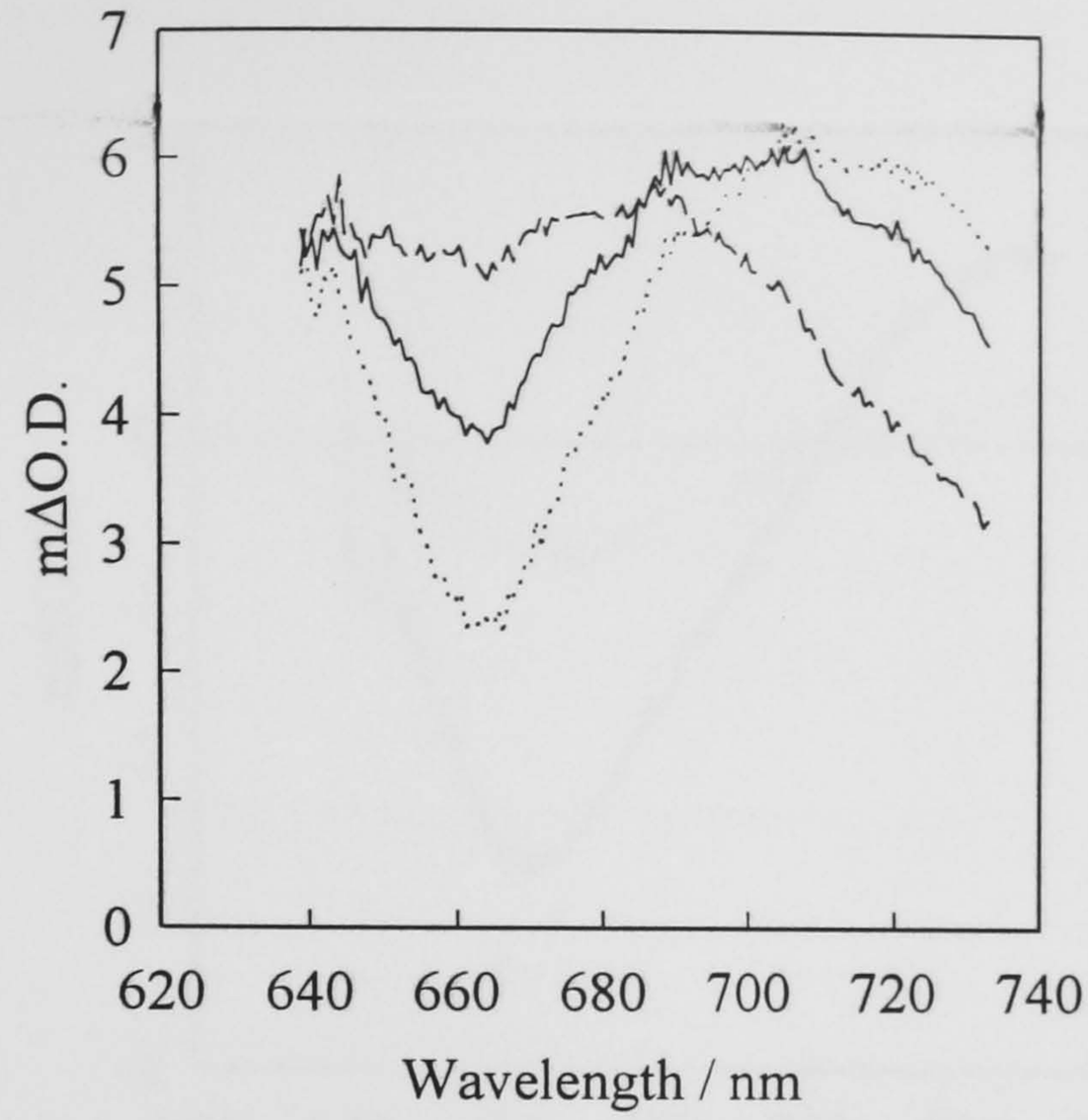



Figure 5.18. Transient absorption spectra obtained for ZnTCPP coated $TiO_2$ films taken at time delays of 0.1 (·····), 3 (————) and 30 (--------) ps following 560 nm excitation.

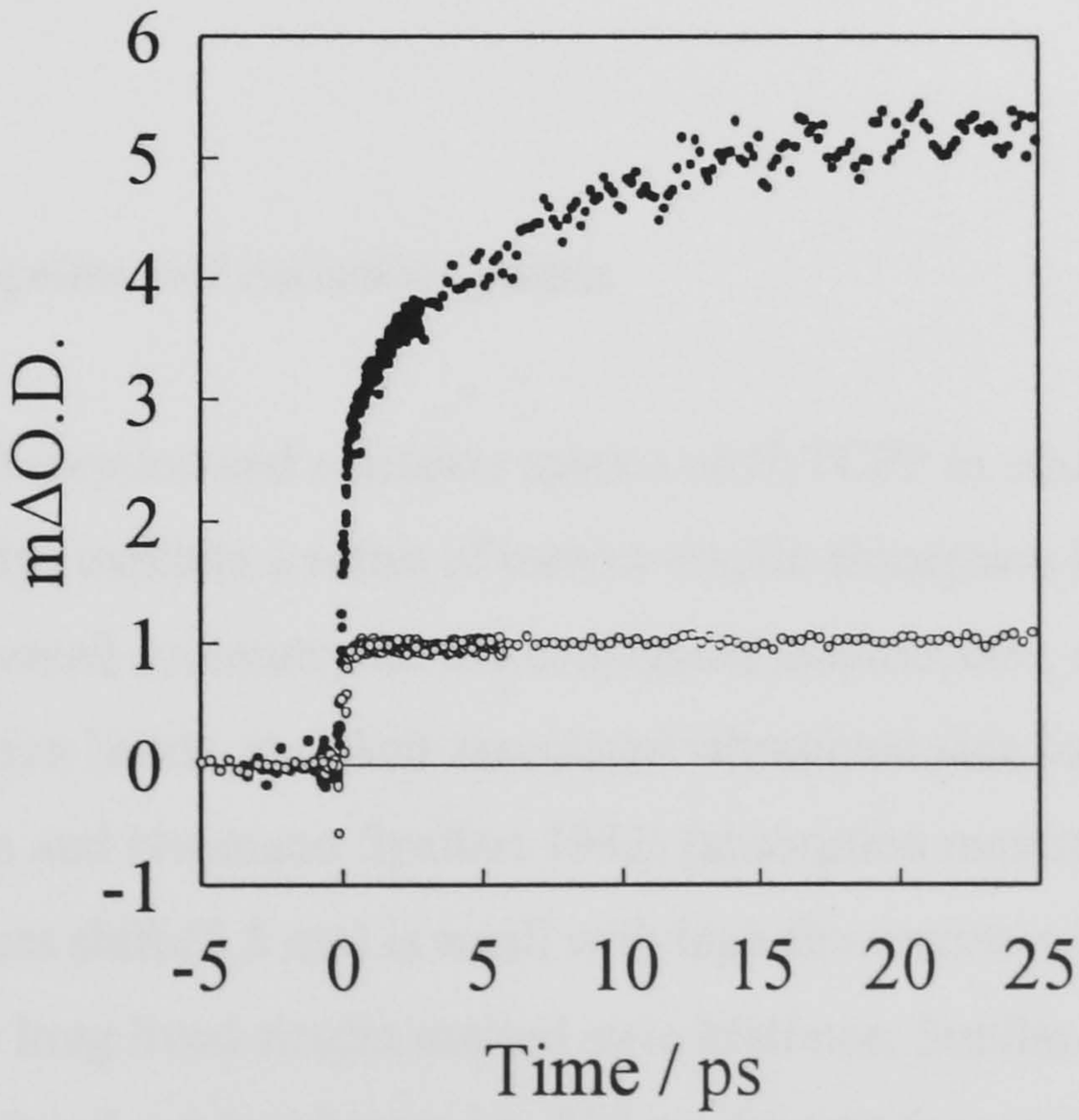



Figure 5.19. Transient absorption kinetics obtained for ZnTCPP in ethanol (o) and sensitised $TiO_2$ film (•) at a probe wavelength of 665 nm after 560 nm excitation.

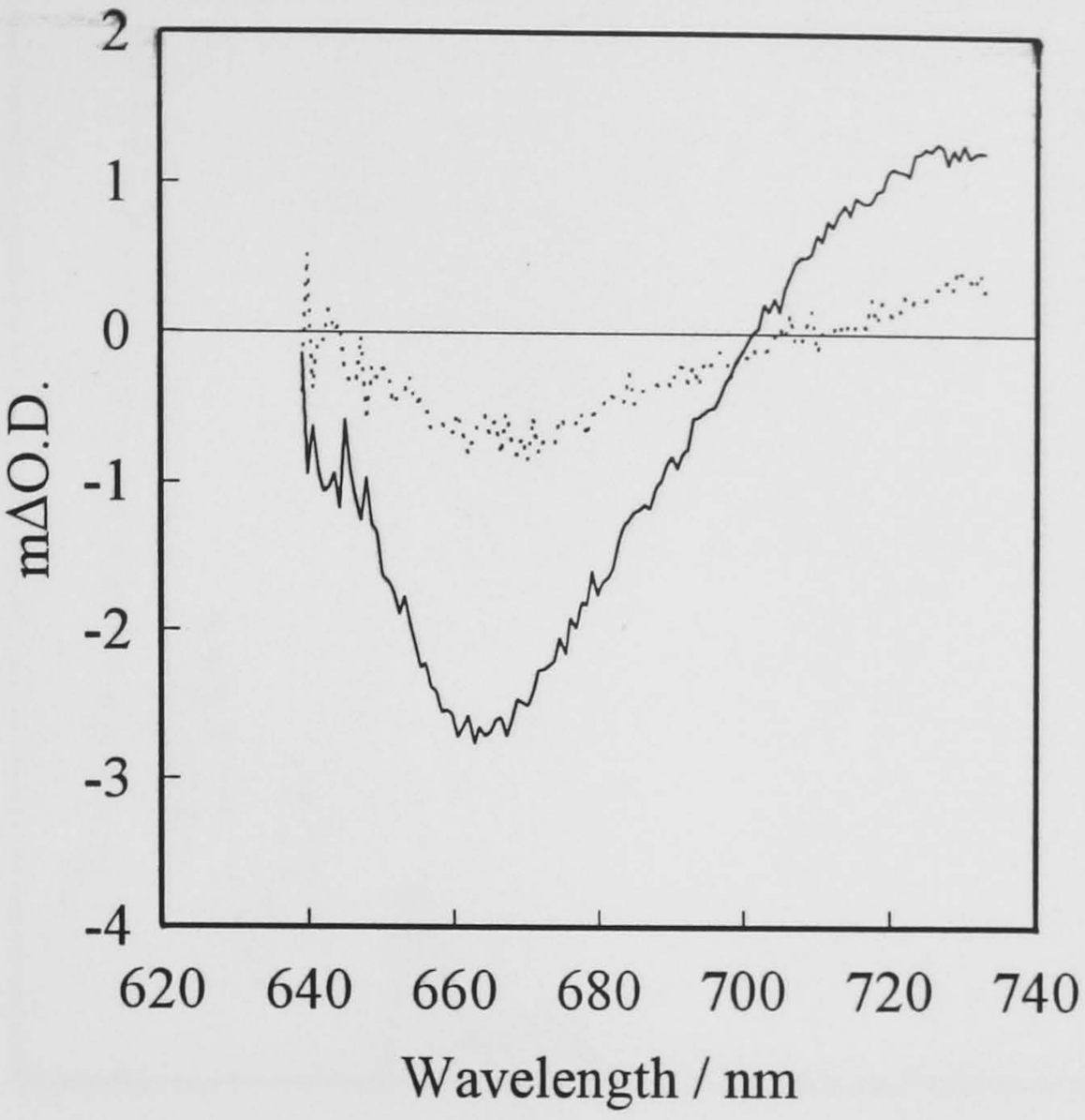



Figure 5.20. Amplitude spectra of the 1.1 (·····) and 8.5 (——) ps components obtained for ZnTCPP coated $TiO_2$ film by global analysis. It is apparent that the spectral shapes of both components are almost identical.

### 5.7.2.3 $H_2$TCPP

***Steady state absorption and emission spectra***

The steady state absorption and emission spectra of $H_2$TCPP in ethanol are shown in Figure 5.21. The dye exhibits a series of narrow visible absorption bands as a result of the reduction of overall symmetry for the conjugated macrocycles, resulting in distinct $Q_x$ and $Q_y$ absorption bands, and their associated vibrational side bands (Kalyanasundaram and Neumann-Spallart 1982) (absorption maxima of 512, 547, 589 and 645 nm). Stokes shift (5.5 nm) is small with high fluorescence intensity consistent with the relatively long lived singlet excited state lifetimes. Similar to ZnTCPP, the vibronic emission band can be observed at 720 nm for transient measurements.

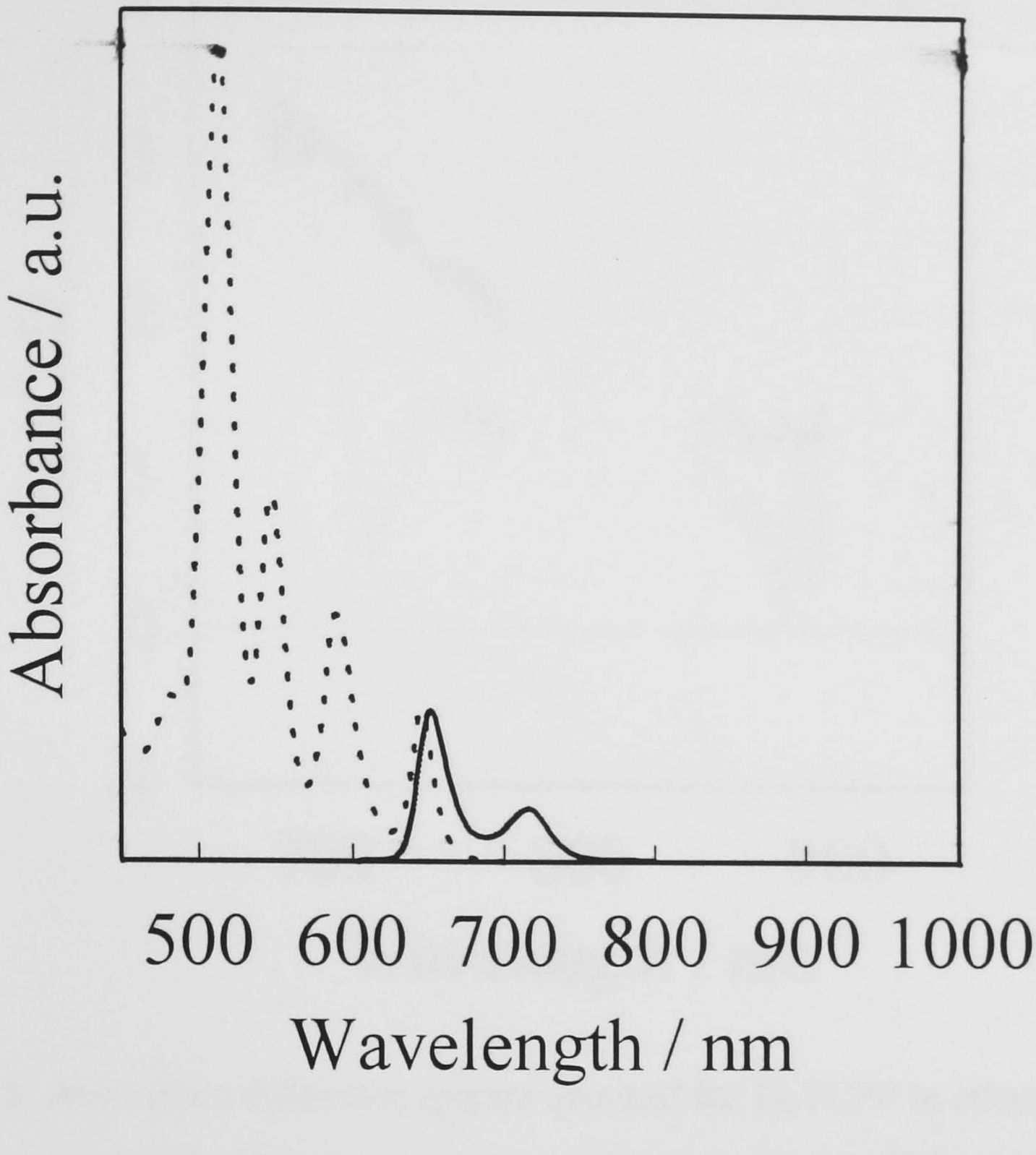



Figure 5.21. Steady state absorption (·····) and emission (——) spectra of $H_2TCPP$ in ethanol. The emission was observed at an excitation wavelength of 589 nm.

***Transient absorption spectra***

The transient absorption spectra obtained for $H_2TCPP$ in ethanol and the sensitised $TiO_2$ films are shown in figure 5.22. The spectrum for solution phase clearly exhibits a stimulated emission band at 720 nm (c.f. figure 5.21), and therefore the spectrum is assigned to the singlet excited state. In contrast, such stimulated emission was quenched for the sensitised $TiO_2$ films due to electron injection from the dye excited states to $TiO_2$. This spectral shape obtained for the dye sensitised $TiO_2$ films is almost identical to those taken at microsecond time, and therefore the resultant spectrum is assigned to a charge separated state.

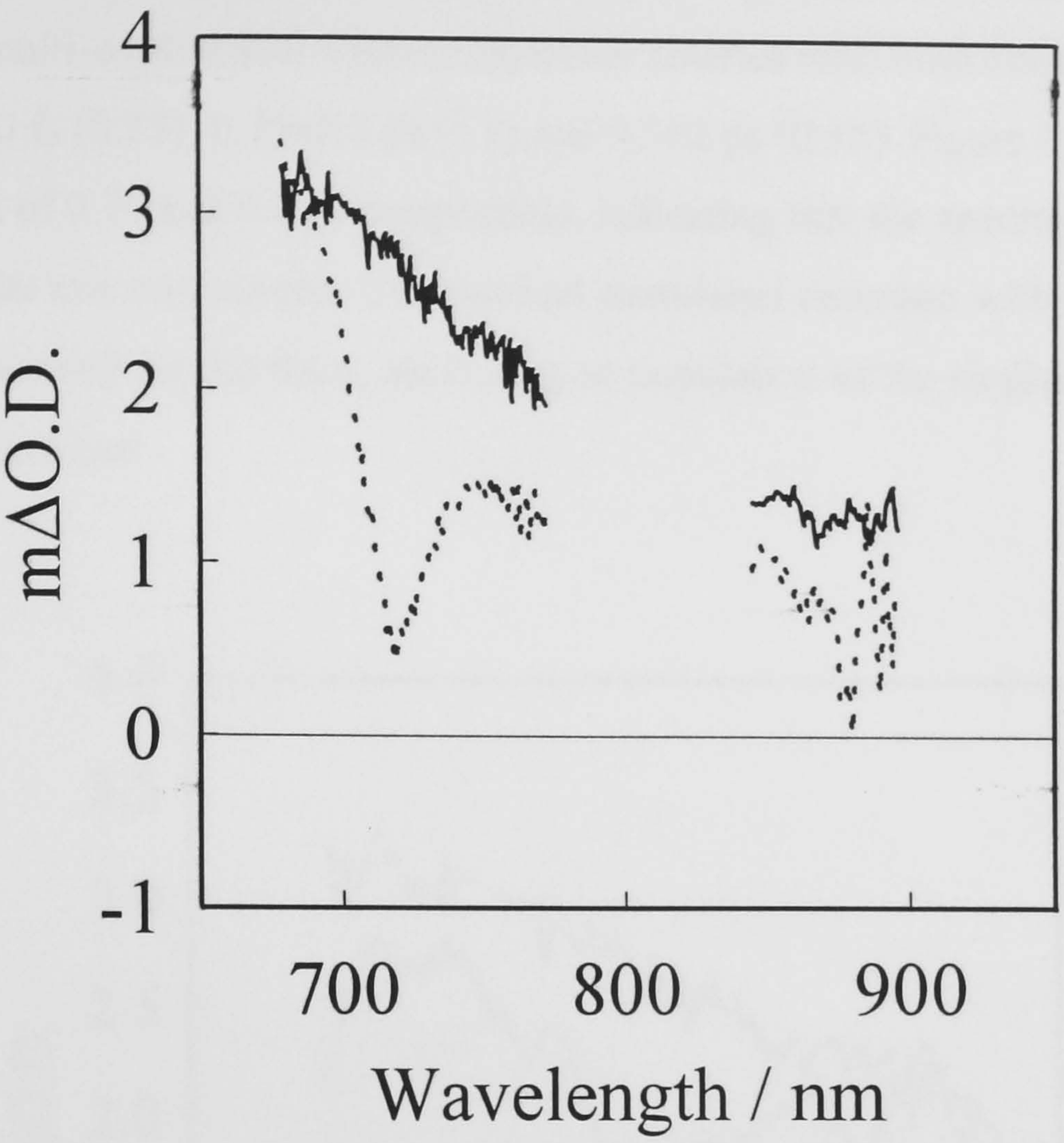



Figure 5.22. Absorption difference spectra obtained for $H_2TCPP$ in ethanol (·····) and the sensitised $TiO_2$ films (——), observed at time delays of 60 and 600 ps, respectively with an excitation wavelength of 645 nm.

The stimulated emission decay was monitored by means of nanosecond transient absorption spectroscopy. The data analysis results in the long-lived singlet excited state with a lifetime of approximately 9 ns (data is not shown) consistent with the intense steady state fluorescence (see figure 5.21)

***Electron injection kinetics***

Figure 5.23 represents transient absorption spectra obtained for the dye sensitised $TiO_2$ films, exhibiting a time dependent quenching of the vibronic stimulated emission band. This quenching process is assigned to the electron injection reaction from the singlet excited state of the dye as discussed above. The kinetics were monitored at 720 nm (peak of the stimulated emission band) as shown in figure 5.24. The dye in ethanol

exhibits negligible kinetics of the stimulated emission up to 60 ps in consistent with the singlet excited state decay on nanosecond timescales. In contrast, the sensitised $TiO_2$ films exhibit multi-exponential electron injection kinetics with time constants (injection yields) of <100 fs (0.35), 0.75±0.3 ps (0.3) and 9.5±2 ps (0.35). Figure 5.25 shows kinetic spectra of 0.75 and 9.5 ps components, indicating that the spectral shapes of the two components are very similar. The residual stimulated emission with amplitude of 16 % was also observed for the films, attributing to population of the singlet excited states not to inject electrons.

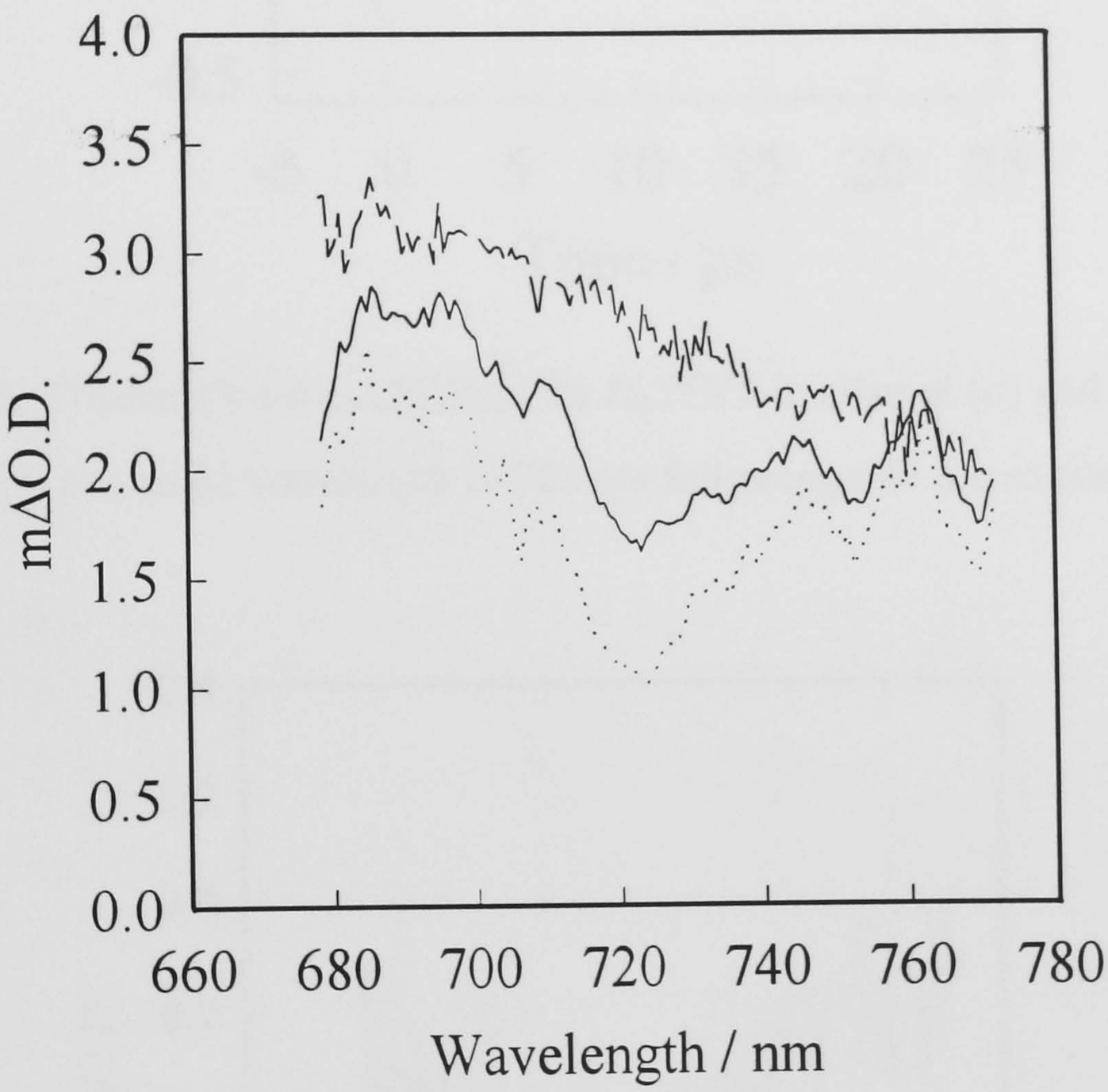



Figure 5.23. Transient absorption spectra observed for $H_2TCPP$ sensitised $TiO_2$ films at time delays of 0.1 (·····), 6 (————), 600 (--------) ps after 645 nm excitation.

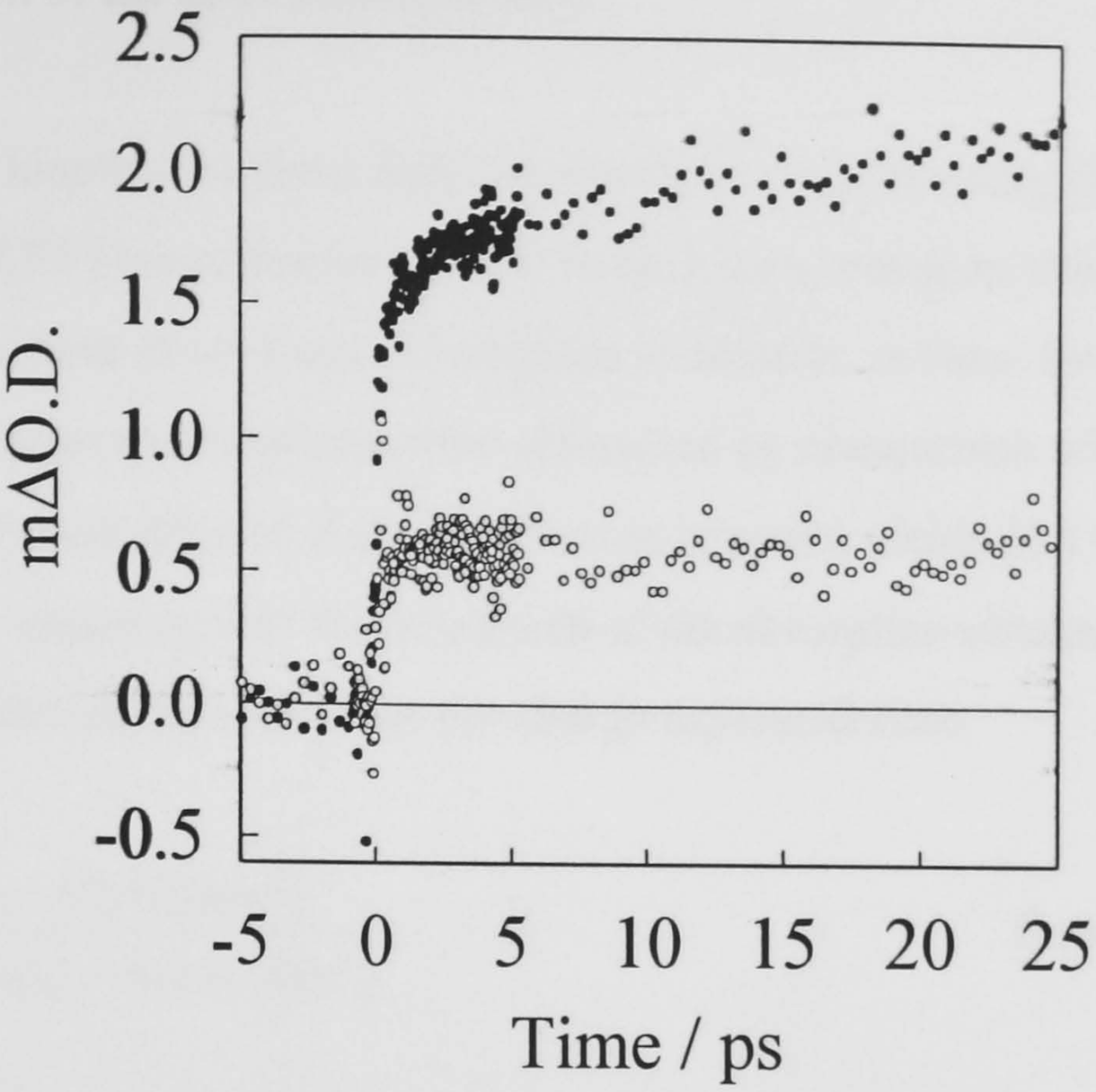



Figure 5.24. Transient kinetics obtained for $H_2TCPP$ in ethanol (o) and its coated $TiO_2$ film (•) at a probe wavelength of 720 nm following 645 nm excitation.

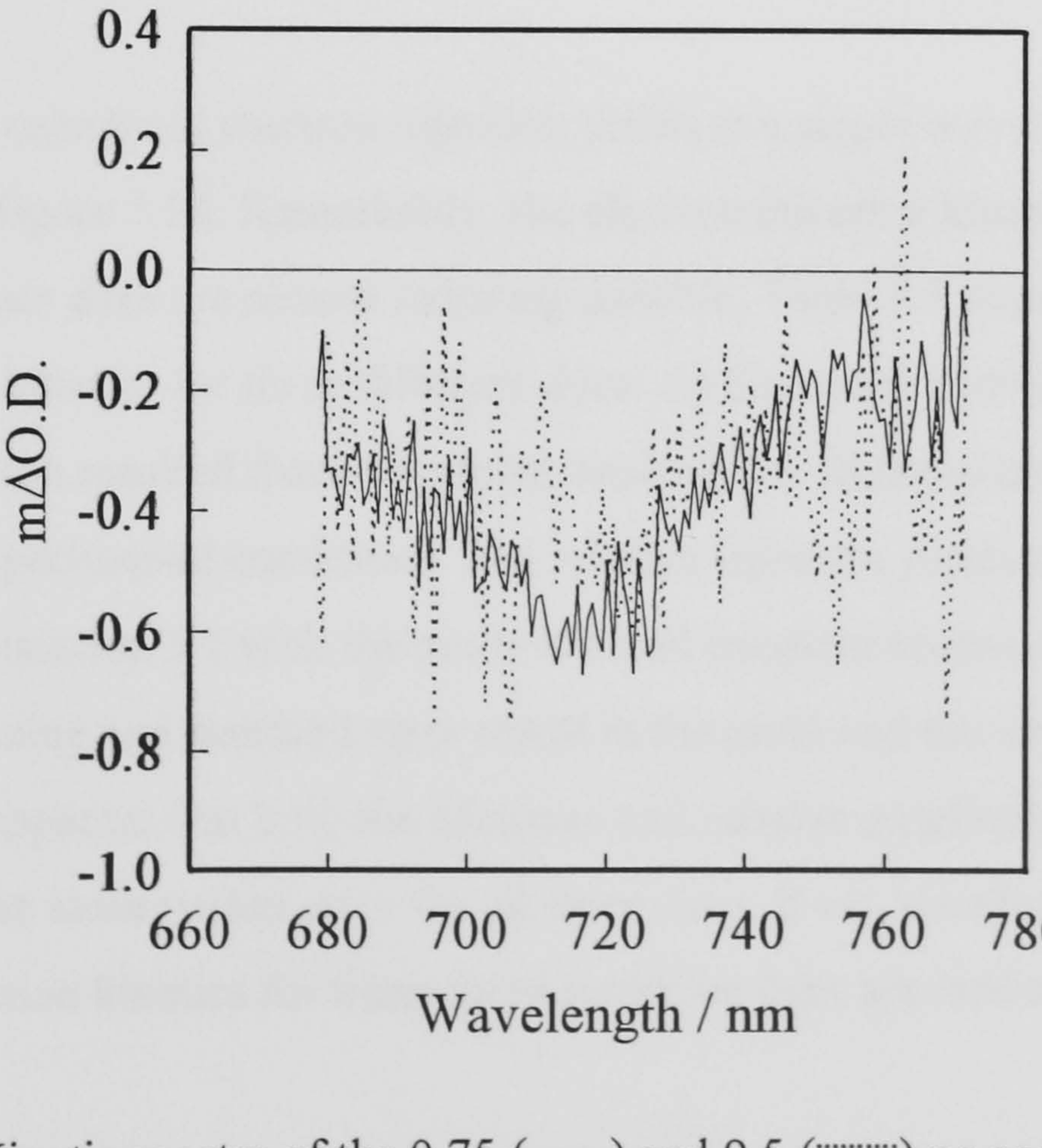



Figure 5.25. Kinetic spectra of the 0.75 (——) and 9.5 (·····) ps components obtained as a result of global analysis for $H_2TCPP$ sensitised $TiO_2$ films.

### 5.7.2.4 Comparison of the three sensitiser dyes

Electron injection kinetics for three different sensitiser dyes ($Ru(dcbpy)_2(NCS)_2$, ZnTCPP and $H_2TCPP$) are compared below. In each case, transient absorption data have contributions from excited state absorption in addition to those for the charge-separated states. Those contributions were subtracted by comparison with the data collected for the dyes in ethanol. Relative electron injection yields $\phi(t)$ were calculated with equation 5.1, assuming that the amplitude of the absorption obtained for the dye sensitised $TiO_2$ films results only from the charge separated state.

$$\phi(t) = \frac{\Delta O.D.(t) - \Delta O.D.(dye^*)}{\Delta O.D.(dye^+ e^-_{CB}) - \Delta O.D.(dye^*)} \qquad \text{Equation 5.1}$$

where $\Delta O.D.(t)$ is transient absorption difference observed for dye sensitised $TiO_2$ films, $\Delta O.D.(dye^*)$ is absorption difference of the dye excited state and $\Delta O.D.(dye^+e_{CB}^-)$ is absorption difference of the charge separated state. For ease of comparison, the electron injection yields were normalised to unity at 25 ps after excitation.

The results of the calculated electron injection yields at a single wavelength for each dye are shown in figure 5.26. Remarkably, the electron injection kinetics obtained for these three sensitiser dyes are almost indistinguishable. Table 5.1 summarises the electron injection kinetics for three different dyes. As discussed above, the lifetimes of the electron injection resulted from the global analysis for all transient data obtained under identical experimental conditions. The relative injection yields were further calculated using equation 5.1 with the multi-channel transient kinetic data; the calculated mean value and standard error result in the yield and the error, respectively, in table 5.1. It is apparent that both the lifetimes and relative amplitudes of these components are the same within error for all three dyes. It can therefore be concluded that electron injection kinetics for these three sensitiser dyes are indistinguishable.

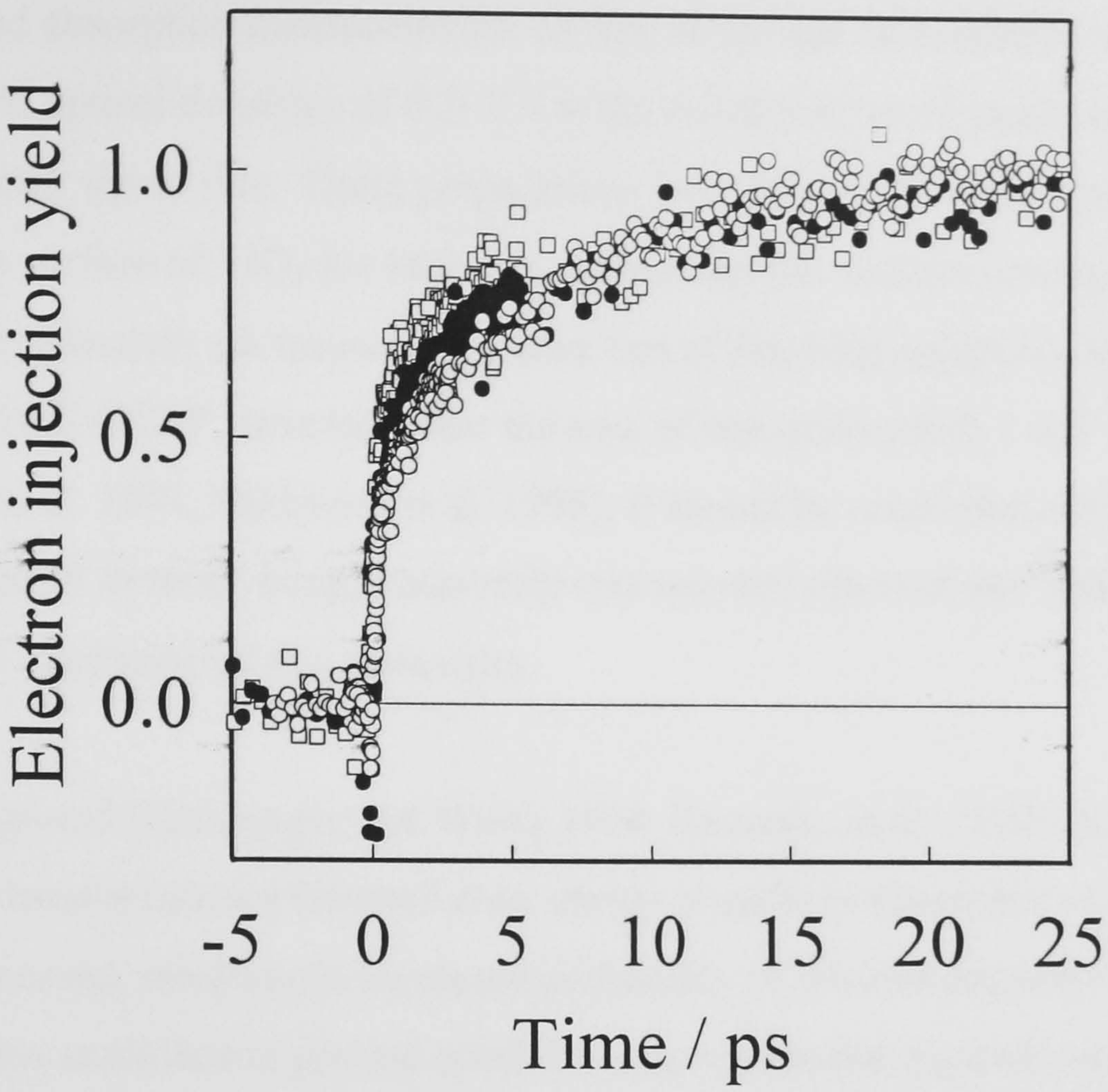



Figure 5.26. Comparison of electron injection yield for $TiO_2$ films sensitised by $Ru(dcbpy)_2(NCS)_2$ (filled circle), ZnTCPP (open circle) and $H_2TCPP$ (open square). The data were obtained by taking contribution of dye excited state absorption out from the transient absorption data collected for the dye sensitised $TiO_2$ films, and then by normalising to unity at 25 ps after optical excitation.

Table 5.1. Lifetimes and amplitudes[b] of normalised electron injection yield[a]

| $Ru(dcbpy)_2(NCS)_2$ | ZnTCPP | $H_2TCPP$ |
|---|---|---|
| <100 fs (0.29) | <100 fs (0.37) | <100 fs (0.35) |
| 1.0±0.3 ps (0.25) | 1.1±0.4 ps (0.12) | 0.75±0.3 ps (0.30) |
| 13±3.0 ps (0.46) | 8.5±2 ps (0.51) | 9.5±2 ps (0.35) |

[a] Results are presented as lifetime (relative amplitude). [b] Deviation of amplitude is ± 0.05 for all sensitiser dyes.

### 5.7.2.5 Excitation power dependence

For femtosecond absorption measurements, all dye sensitised $TiO_2$ sample were prepared to yield optical densities of 0.2~0.4 at the excitation wavelengths used in order to obtain sufficient signal size. These preparations therefore result in different dye coverage on the surface of $TiO_2$ for each dye, indicating that surface coverage of $H_2TCPP$ is approximately six times higher than that of $Ru(dcbpy)_2(NCS)_2$ and three times higher than ZnTCPP, assuming that the area of one molecule is 1 $nm^2$ for all dyes (Nazeeruddin, et al. 1993, Shklover, et al. 1998). It should be noted that excitation laser power was adjusted to result in approximately one injected electron per $TiO_2$ particles after the optical excitation of dye molecules.

It has been suggested (Eichberger and Willig 1990, Kemnitz, et al. 1987) that the excited dye molecules interact (excited state energy transfer is observed) as dye coverage is increased, resulting in increased probability of excited-excited states annihilation. This annihilation process could be observed as fast excited state decay to ground when the population of the excited states is increased, e.g. by increased excitation laser power. For three dyes studied here, the excitation laser power was altered by a factor of two with the same excitation wavelength. Figure 5.27 compares kinetic spectra obtained for each dye sensitised $TiO_2$ film. The spectra obtained for $Ru(dcbpy)_2(NCS)_2$ and ZnTCPP exhibit indistinguishable spectral shapes for high and low excitation powers used, and are similar to the spectra of the kinetic component assigned to the electron injection reaction as shown in figures 4.12b and 5.20, respectively. In contrast, the spectrum obtained for $H_2TCPP$ with the higher excitation power exhibits a different spectral shape from that with the lower power associated with the electron injection (see figure 5.25). Considering the excited state spectrum of $H_2TCPP$ in ethanol shown in figure 5.22 and the kinetic spectrum associated with the electron injection for its sensitised films shown in figure 5.25, the spectrum obtained with the higher excitation power in figure 5.27c may be regarded as the mixture of excited state and electron injection. The higher dye coverage on the semiconductor and the higher excitation power may therefore increase a rate and a yield of the excited state annihilation, which competes with the electron injection kinetics. Indeed, a faster stimulated emission decay with a lifetime of 340 ps was observed for $H_2TCPP$ coated $TiO_2$ films (high monolayer coverage) with higher excitation power as shown in figure

5.28 (compare with the spectrum of the dye excited state in figure 5.22). Such a fast decay is in contrast with the singlet excited state lifetime of approximately 9 ns obtained for the dye in ethanol.

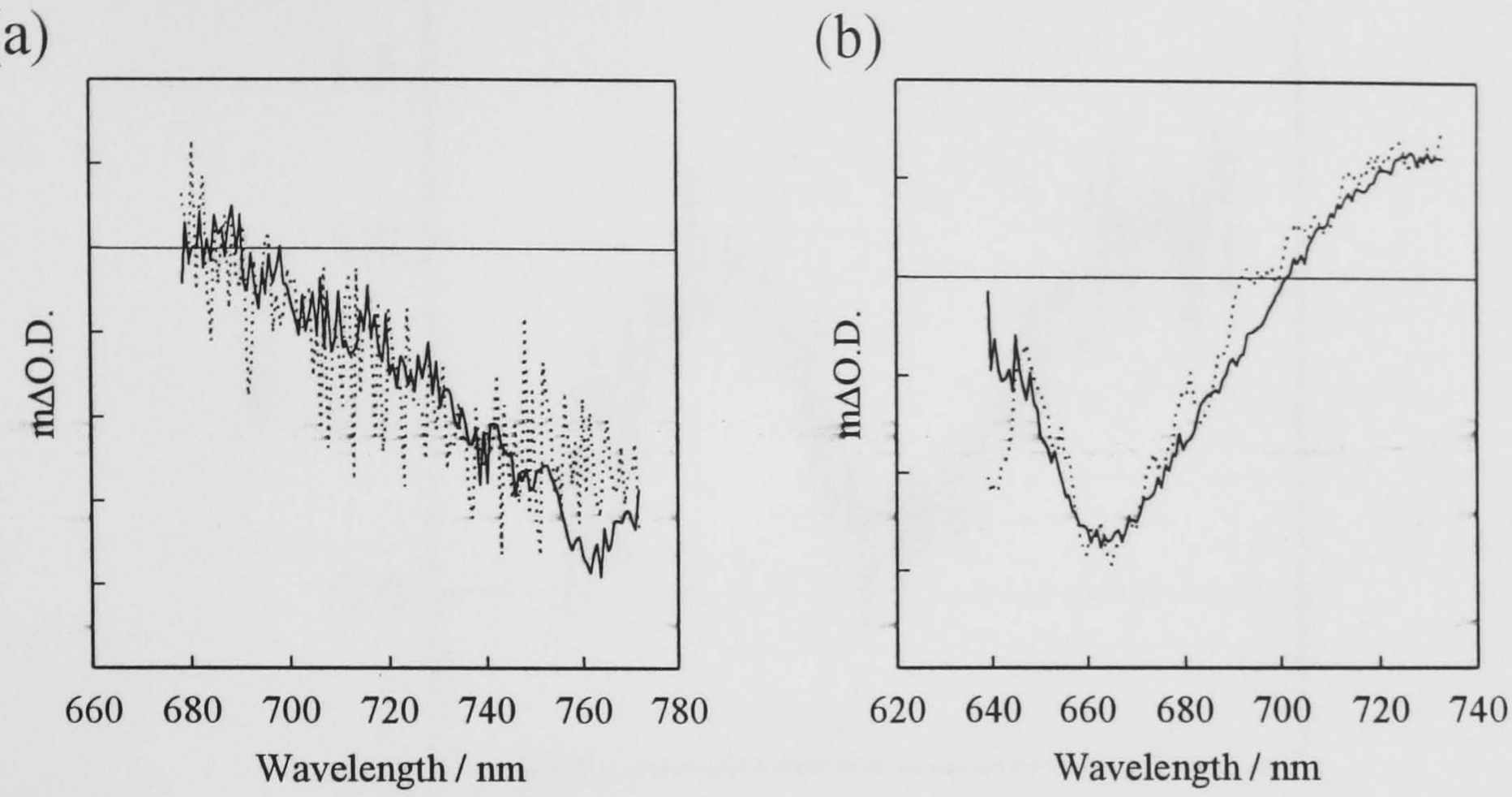



Figure 5.27. Kinetic spectra obtained for $TiO_2$ films sensitised by $Ru(dcbpy)_2(NCS)_2$ (a), ZnTCPP (b) and $H_2TCPP$ (c) with high (——) or low (·····) excitation power. The excitation power increased was double the lower power. The spectra were normalised for ease of comparison.

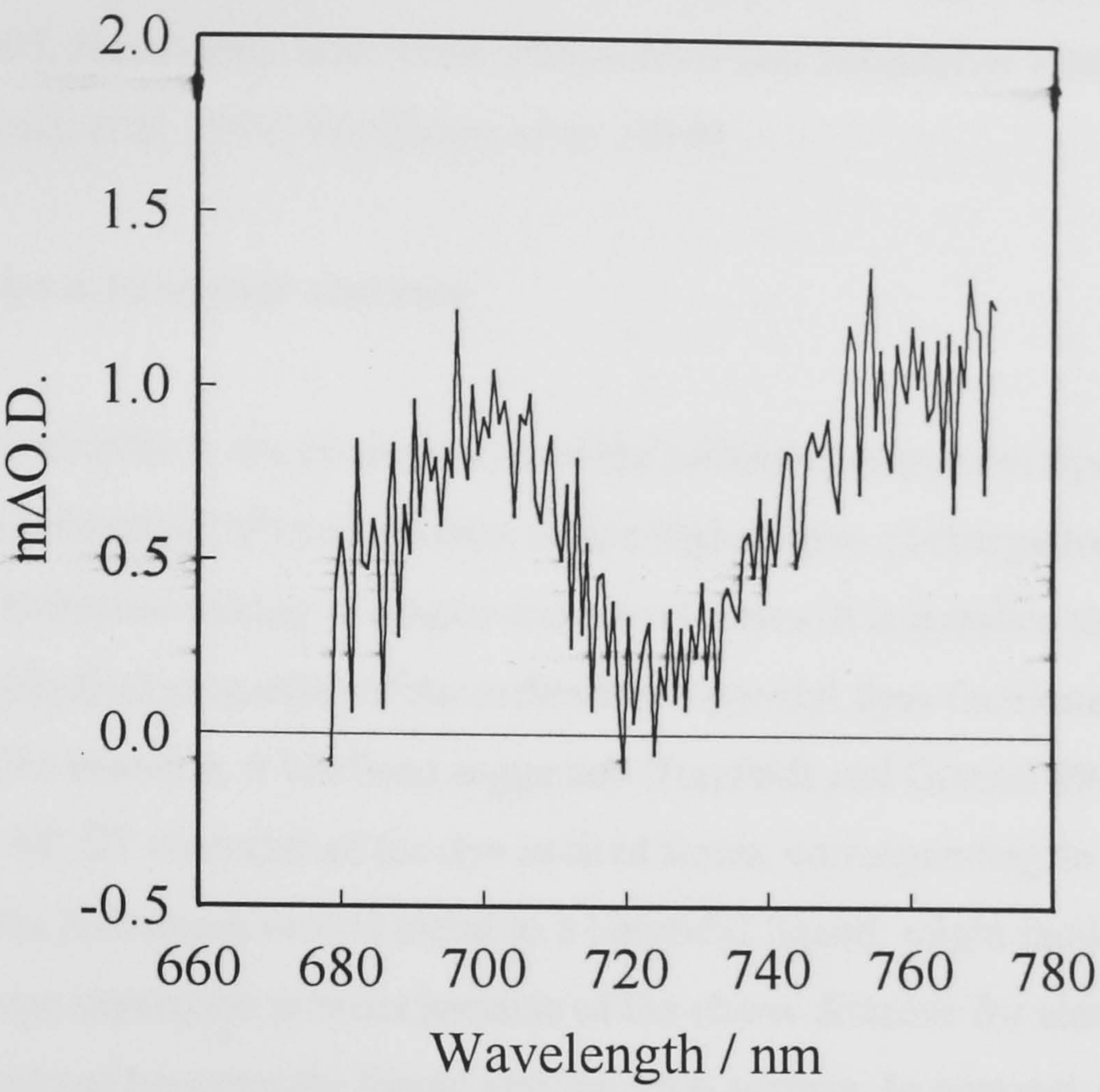



Figure 5.28. Kinetic spectrum of the 340 ps component obtained for $H_2$TCPP sensitised $TiO_2$ films with the higher excitation power at an excitation wavelength of 645 nm.

### 5.7.3 Discussion

Electron injection kinetics for the $TiO_2$ films sensitised by $Ru(dcbpy)_2(NCS)_2$ were compared with different sensitiser dyes in order to investigate why this ruthenium dye is the most efficient sensitiser dye to date compared to other dyes (Nazeeruddin, et al. 1993). Three different sensitiser dyes; $Ru(dcbpy)_2(NCS)_2$, ZnTCPP and $H_2$TCPP differ significantly in both their excited state photophysics and their excited state redox potentials, but they share similar carboxylate binding motifs to the $TiO_2$ surface. It has been found that in all cases the electron injection kinetics are multi-exponential and indistinguishable. These observations contrast with the different IPCE of ~90 and ~25 % at the excitation wavelengths for $Ru(dcbpy)_2(NCS)_2$ and ZnTCPP, respectively (Boschloo and Goossens 1996, Kalyanasundaram, et al. 1987, Nazeeruddin, et al. 1993). Moreover, these observations contrast with the wide variations in injection and

recombination time constants observed in the literature for different sensitiser dyes (Burfeindt, et al. 1996, Cherepy, et al. 1997, Eichberger and Willig 1990, Fessenden and Kamat 1995, Hashimoto, et al. 1988, Hilgendorff and Sundström 1998, Martini, et al. 1998, Stipkala, et al. 1997, Tachibana, et al. 1996).

***Influence of dye excited state structure***

As discussed in chapter 4, the photophysics of the ruthenium bipyridyl dyes is complex, resulting from a manifold of excited states with a high degree of charge transfer character and extensive mixing of singlet and triplet states. It is possible that such specific photophysical properties of the ruthenium bipyridyl dyes facilitate efficient sensitisation. For example, it has been suggested (Hagfeldt and Grätzel 1995, Meyer 1997) that the MLCT character of the dye excited states, corresponding to an electron transfer from the ruthenium central metal to a bipyridyl ligand, might facilitate the interfacial charge separation process because of the closer distance for electron transfer with a direct linkage between the ligand and the $TiO_2$ surface. In contrast, the localisation of the dye cation on the ruthenium metal, $Ru^{III}$, minimises the electronic coupling between this cation and the $TiO_2$, and could thereby slow the rate of the charge recombination.

The excited state structure of the ruthenium complex has been intensively studied by several groups. It has been reported that the excited electron of $Ru(bpy)_3^{2+}$ localises in one of bipyridine ligands (Bradley, et al. 1981, Braterman, et al. 1983, Carroll and Brus 1987, De Armond and Myrick 1989, Forster, et al. 1981, Mabrouk, et al. 1986), and the time constant of the localisation and relaxation were estimated to be $>10^{11}$ $s^{-1}$ from luminescence data (Demas, et al. 1971, Lytle, et al. 1969). Picosecond Raman spectroscopy for $Ru(bpy)_3^{2+}$ has demonstrated that formation of the $Ru^{III}$ / bipyridine anion charge transfer states occurs within a few picosecond (Carroll and Brus 1987).

It is reasonable to expect from the above studies that an excited electron of $Ru(dcbpy)_2(NCS)_2$ also localises one of two dcbpy ligands. Since adsorption of the dye onto semiconductor surface does not influence the absorption spectra (see figure 4.1), it is uncertain for the sensitised $TiO_2$ films which dcbpy ligand the electron is localised on. Shklover et al. have recently reported a molecular structural model of

$Ru(dcbpy)_2(NCS)_2$ on the surface of $TiO_2$ using crystal structure of anatase $TiO_2$ and X-ray crystal structure of the dye (Shklover, et al. 1998). The model favours linkages of both dcbpy ligands onto the surface of $TiO_2$ by carboxylate groups as shown in figure 5.29, and therefore suggests that identical contribution to the electron injection kinetics will be expected from the localisation of the excited electron on either of two dcbpy ligands.

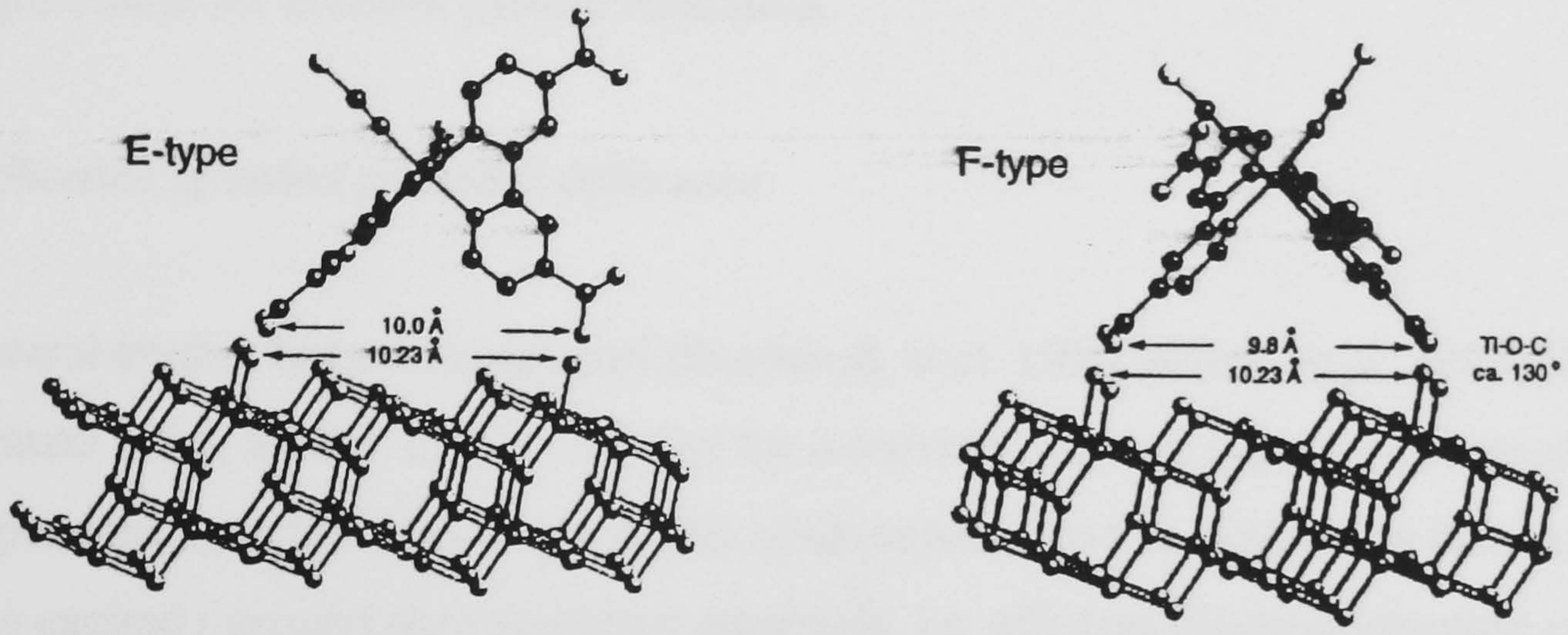



Figure 5.29. Examples of the geometrical structures presenting the linkage of $Ru(dcbpy)_2(NCS)_2$ onto $TiO_2$ surface taken from Shklover et al. (Shklover, et al. 1998). E-type and F-type indicate three-bond and four-bond types, respectively. These two binding types are most favourable, assessed from the crystal structure of anatase $TiO_2$ and the X-ray crystal structure of the dye.

In contrast, the excited state for ZnTCPP and $H_2$TCPP porphyrins is long-lived (ns timescale) and the excited electron almost localises in the inner $\pi$ ring with possibly partial conjugation with the aryl ring (Hoard 1971, Jakobsen, et al. 1982, Krieger, et al. 1985, Sessler, et al. 1990), indicating no charge transfer character for the excited state. The electron injection thus proceeds from a singlet excited state corresponding to a $\pi^*$ orbital of the conjugated macrocycle.

Despite the above differences in the photophysics of the ruthenium dye and porphyrins, it has been demonstrated that the electron injection kinetics of these three sensitiser dyes are very similar. These observations suggest that the MLCT and singlet / triplet character of the dye excited state is not critical to the injection process. The observation that the injection kinetics are independent of the character of excited molecules is

consistent with similar observations reported by a number of groups. Hashimoto et al. observed similar electron injection rates of ruthenium complexes with two different linkage groups being responsible for the change of distance between chromophores and $TiO_2$ surface (Hashimoto, et al. 1987). Meyer et al recently reported fast electron injection rates and high light-to-electrical energy conversion efficiency even though the sensitiser is remote to the semiconductor surface (Argazzi, et al. 1997), supporting that a direct chemical bond between $Ru^{II}$ sensitiser and the $TiO_2$ surface is not a critical requirement for efficient charge separation.

***Influence of redox potential difference***

Several studies have demonstrated (Burfeindt, et al. 1996, Miller, et al. 1995, Moser and Grätzel 1998, Spitler, et al. 1997) that the interfacial electron injection processes are dependent upon the relative energetics of the semiconductor conduction band and the dye excited / ground state oxidation potentials, i.e. efficient electron injection requires the dye excited state oxidation potential to be more negative than the semiconductor conduction band edge.

The excited state redox potentials of ZnTCPP and $H_2$TCPP determined from solution phase electrochemical data differ by 0.6 V (see figure 5.15). This potential difference is equivalent to the free energy difference between the dye excited state potential and the bottom of the conduction band, assuming that the redox potential of the dye is not altered by the adsorption onto the $TiO_2$ surface, or if it is, the shift of the potential is identical for both dyes. Despite this free energy difference, similar injection kinetics with these two dyes were observed, suggesting that the kinetics are not sensitive to the excited state redox potential.

It can therefore be concluded that the electron injection kinetics in dye-sensitised $TiO_2$ films is independent of the sensitiser dye linked to the $TiO_2$ surface with carboxyl groups. Such a conclusion is rather surprising in terms of the resultant performance of the solar cells employing different dyes. The detailed discussion for this issue is described in section 5.9.

### *Comparison with the electron transfer theory*

As described above, $Ru(dcbpy)_2(NCS)_2$, ZnTCPP and $H_2TCPP$ indicate different excited state photophysics and different excited state redox potentials. Despite these differences, the electron injection kinetics are indistinguishable within error. These kinetic results are compared with the electron transfer theory described in chapter 3. The free energy term is included in the exponent as shown in equations 3.8~3.10. Since the continuous empty electron acceptor states are available in the conduction band, the electron transfer reaction is expected to be activationless, provided that the redox potential of the dye excited state is raised at least by the reorganisation energy above the bottom of the conduction band. The transient data indicated that the electron transfer kinetics are independent of their excited state redox potentials, facilitating such an activationless condition.

The difference in distance between the donor and the acceptor correlates to the magnitude of $\kappa$ in equation 3.9 or the electronic coupling term $V_{RP}$ in equation 3.10. As discussed above, the localisation of the excited electron for ZnTCPP and $H_2TCPP$ is not clear due to the possibility of partial delocalisation of the electron in the aryl ring. There is also no information available on the geometrical structure of adsorption of these porphyrins. Moreover, the value of the damping parameter ($\beta$) in equation 3.11 is uncertain for the dye sensitised $TiO_2$ nanocrystalline films. These uncertain factors preclude a quantitative estimate of the electronic coupling, and it is therefore not possible to compare $\kappa$ or $V_{RP}$ term for three different dyes. It is however suggested that the relative electronic coupling can be compared with the same sensitiser chromophore, but with a series of different spacers to the semiconductor surface, resulting in different electron transfer distances. Such an experiment should allow investigation of influence of the electronic coupling term on the electron injection kinetics.

## 5.8 General discussion

The kinetic components associated with electron injection are clearly distinguishable from the kinetic components obtained for the dye excited state as discussed above by

comparing kinetic spectra resulted from the global analysis for each sample. Analyses assuming multi-exponential kinetics require a minimum of three exponentials to fit the data. Remarkably this multi-exponential behaviour is indistinguishable for the three sensitiser dyes as shown in figure 5.26, excitation wavelength (figures 5.2~5.4) and solvent environment (figure 5.5) of the films. Thus, the injection kinetics observed in these studies are independent of relaxation / solvation dynamics of the sensitiser dye. However, the electron injection yield gradually decreased as the externally voltage is negatively applied from -0.4 V vs Ag/AgCl in the electrolyte B. Moreover, the rate is modulated by shifts in the energetics of the electronic states of the $TiO_2$. It can therefore be concluded that the nature of $TiO_2$ films dominantly influences the electron injection kinetics and yield in this system.

Ellingson et al. have recently reported (Ellingson, et al. 1998) that the injection kinetics is mono-exponential with a lifetime of <50 fs employing $TiO_2$ films sensitised by $Ru(dcbpy)_2(NCS)_2$ (the same sensitiser dye used in this study), but on air exposed films (see also chapter 4). Such a kinetic difference may suggest that the multi-exponential injection kinetics could be associated with a dynamic relaxation of the dye excited state by the solvent environment. It has however been found that the injection kinetics are independent of solvent environment, and therefore the solvation is not the cause of the multi-exponential behaviour. As discussed in chapter 4, Ellingson et al. observed the injection kinetics by monitoring absorption of the injected electron in the infrared region (Ellingson, et al. 1998), while the kinetics studied here were determined by probing absorption of the dye cation state and the injected electron. This difference in experimental conditions may suggest that the multi-exponential kinetics originate from the relaxation of the dye cation. It has however been shown that the kinetics are indistinguishable for the three sensitiser dyes. The multi-exponential behaviours for porphyrin dyes were monitored by the disappearance of the stimulated emission, implying that the electron transmission is responsible for such kinetics. Moreover, Skinner et al. reported (Skinner, et al. 1995) that electron trapping following the excitation of $TiO_2$ was observed as a first order decay with a time constant of 180 fs, implying that the kinetics of the trapping should be observed for the injected electron. However, there is no relaxation process of the injected electron observed by Ellingson et al. It is thus more likely that this discrepancy is associated with differences in the

nanocrystalline $TiO_2$ films used by different groups or other different experimental conditions.

In consequence, the above observations of the kinetic independence suggest that the multi-exponential behaviour of the electron injection kinetics originates from heterogeneity of the nanocrystalline $TiO_2$ film. This heterogeneity could result from heterogeneous interactions of dye molecules with the surface of the film. For example, the distance of the electron transfer reaction may be dependent upon the dye adsorption site (how the dye molecule adsorbs on the surface), indicating that the multi-exponential kinetics originate from such sites responsible for the injection process. It is also possible that the injection processes involve a number of electron acceptor states with different potential levels, e.g. the delocalised state in the conduction band, the surface / defect state or impurity (adsorbed molecular) state (if there are). If the number of different acceptor states is limited in the vicinity of the excited dye molecule, this variance of states may contribute to the multi-exponential kinetics. Since the characteristics of the intra-band (trap or surface) states are not unambiguously identified, the influence of the different states upon the injection kinetics could not be clarified. In order to investigate these issues, the system requires well defined $TiO_2$, for example, plain single crystal $TiO_2$ could be used for the transient experiments.

The conclusion that the observed multi-exponential behaviour results from heterogeneity of the $TiO_2$ is consistent with previous photoluminescence measurements of electron injection. Hashimoto et al. reported multi-exponential electron injection rates of $10^9$~$10^6$ $s^{-1}$ (Hashimoto, et al. 1988) for $Ru(bpy)_3^{2+}$ sensitised $TiO_2$ powder, and concluded that the kinetics is dependent upon $TiO_2$ adsorbed sites for dye molecules (heterogeneous binding to the $TiO_2$ surface), i.e. each site indicates a different electron transfer rate. More recently Lu et al. reached a similar conclusion from single molecule emission studies (Lu, et al. 1997) of indium tin oxide films sensitised by cresyl violet. They found that whereas the bulk sample exhibited multi-exponential decay kinetics, mono-exponential kinetics was observed for each single adsorbed molecule. Meyer et al studied distribution of electron injection rates with a maximum amplitude at ~$10^9$ $s^{-1}$ for $Ru(dcbpy)(bpy)_2^{2+}$ sensitised $TiO_2$ films (Heimer, et al. 1996, Stipkala, et al. 1997). They pointed out that it has largely been assumed that the complex kinetics are a result of underlying heterogeneity and the decay kinetics are modelled as a sum of discrete

rates. It should however be noted that the interpretation of these photoluminescence studies is limited by their relatively poor time resolution of the apparatus, and therefore the data may be observing the tails of the emission decays.

Comparison of all of the kinetic results with the heterogeneous electron transfer theory as described in chapter 3 suggests the kinetic mechanism for the electron injection. As discussed in section 5.3, the injection from the weakly luminescent excited state is non-adiabatic. However, it is not clear that the fastest phase (<100 fs) of the injection is adiabatic or non-adiabatic since it is not possible to observe the kinetic competition between the electron injection and the dye excited state relaxation due to the instrument response limit of the apparatus. The observation that the injection kinetics are independent of the sensitiser dyes, excitation wavelength and solvent environment suggests that the adiabacity of the injection process is insensitive to the limited experimental conditions.

## 5.9 Relevance to solar cells

### *Sensitising efficiency*

As discussed above, the electron injection kinetics in dye-sensitised $TiO_2$ films are independent of three different sensitiser dyes; $Ru(dcbpy)_2(NCS)_2$, ZnTCPP and $H_2TCPP$. It has also been found out by Mr. Saif Haque in Centre for Photomolecular Sciences that the recombination rates observed with these three sensitiser dyes are very similar (Tachibana, et al. 1999). As a result of the analysis for the transient data, the $TiO_2$ films sensitised by $Ru(dcbpy)_2(NCS)_2$ and ZnTCPP remarkably indicate high electron injection yields of >0.9. In contrast, the cells employed with $Ru(dcbpy)_2(NCS)_2$ and ZnTCPP exhibit the IPCE of ~90 and ~25 % at the same excitation wavelengths, respectively (Boschloo and Goossens 1996, Kalyanasundaram, et al. 1987, Nazeeruddin, et al. 1993).

This high injection yield and the observation of indistinguishable electron injection and recombination kinetics suggest that many sensitiser dyes can potentially be alternative candidates for highly efficient photovoltaic cells. At least in terms of its electron

injection and recombination kinetics, there appears to be nothing unique about $Ru(dcbpy)_2(NCS)_2$. However other dyes have generally been reported to date to be less efficient sensitisers than $Ru(dcbpy)_2(NCS)_2$. Thus, our kinetic observations studied here raise the question as to why $Ru(dcbpy)_2(NCS)_2$ is a more efficient sensitiser dye in photoelectrochemical cells (Boschloo and Goossens 1996, Kalyanasundaram, et al. 1987, Nazeeruddin, et al. 1993).

It is possible that the high efficiency reported for $Ru(dcbpy)_2(NCS)_2$ originates from differences in the rate of electron transfer to the dye cation from the iodide redox active electrolyte used in these devices. The lower efficiencies observed for osmium bipyridyl dyes compared to their ruthenium analogues have been attributed to slower electron transfer from the iodide electrolyte to the osmium dye cation (Alebbi, et al. 1998). Rensmo et al. studied the electronic structure of $Ru(bpy)_2(NCS)_2$ by semiempirical quantum chemical (INDO/S) calculations (Rensmo, et al. 1998) and by photoelectron spectroscopy (Rensmo, et al. 1997). They demonstrated that a large part of the HOMO orbitals is shifted from the centre Ru metal towards the NCS ligands, indicating that the positive charge in the oxidised form of $Ru(bpy)_2(NCS)_2$ is shifted towards the NCS ligands. These ligands rather face towards the electrolyte containing iodine redox couples, which may facilitate relatively fast dye regeneration reaction. Further studies are necessary to address the point whether the ligand co-ordination in ruthenium complex influences its dye regeneration kinetics.

Since the nanocrystalline $TiO_2$ films employed in the solar cells are usually prepared with high dye monolayer coverage (absorbance of ~2), it is also possible that the lower efficiency of porphyrin sensitisers results from an increased probability of exciton annihilation. The strong transition dipole of the porphyrin singlet excited state suggests that at high dye coverage, dipole / dipole interactions will allow rapid migration of the excited state between neighbouring dyes, increasing the probability of exciton annihilation. The low emission dipole of the $Ru(dcbpy)_2(NCS)_2$ MLCT state, however, would comparably prevent such migration. As discussed in section 5.7, the comparison of the kinetic spectra shown in figure 5.27 indeed indicates kinetic dependence upon laser intensity of the transient data for $H_2TCPP$ sensitised $TiO_2$ films at high dye coverage indicative of exciton annihilation at higher intensities. At lower coverage for $Ru(dcbpy)_2(NCS)_2$ and ZnTCPP, but with comparable densities of photons absorbed,

this dependency upon laser power was not observed. Further work should be carried out to confirm this point with a series of dye coverages and with a range of excitation powers.

*Choice of electrolytic solvent*

As shown in figure 5.5, the electron injection kinetics observed for $Ru(dcbpy)_2(NCS)_2$ sensitised $TiO_2$ films are independent of solvent environments employed. These observations suggest that any solvent can be potentially used as electrolytic solvent provided that the solvent are suitable for mobility of the redox active electrolyte and for the long term stability (wide potential range). However the data shown in figures 5.9 and 5.10 indicate that charge recombination rates at >-0.6 V vs Ag/AgCl are faster than the dye regeneration process (nanosecond timescales) by the electroactive redox couples ($I_3^-/I^-$) in ethanol electrolyte A (Hagfeldt and Grätzel 1995, Haque, et al. 1998, Haque, et al. 1999), limiting an open circuit voltage of the cell. Such ultrafast recombination processes were not observed in acetnitrile electrolytes B and C. The dependence of the charge recombination kinetics upon the applied voltage therefore provides an important justification for choosing an electrolytic solvent in order to control the open circuit voltage.

*Influence of potential energy levels of $TiO_2$*

The conduction band / trap state energetics are dependent upon the details of the electrolyte composition. Detailed comparison between the data obtained for electrolytes B and C, and dye sensitised photovoltaic device function with the redox active electrolyte is therefore not possible. However, it is apparent that the injection kinetics are much less sensitive to the electrical bias across the film than the recombination kinetics. It thus appears at present unlikely that, at least in the presence of potential determining ions in the electrolyte, the bias dependence of the injection kinetics plays a key role in limiting the energy conversion efficiency of such devices.

In acetnitrile electrolyte B, it has been observed that the electron injection yield decreases with occupancy of electron acceptor states in $TiO_2$ at >–0.5 V vs Ag/AgCl (see figures 5.7 and 5.8) due, in part, to the instability of the sensitiser dye. These

observations suggest that the decreased electron injection yield may limit the open circuit voltage to 0.75 V using the acetnitrile electrolyte in the cell, assuming that the redox potential of the commonly used iodide electrolyte is +0.25 V vs Ag/AgCl (Hagfeldt and Grätzel 1995).

As discussed in section 5.6, $Li^+$ ions are routinely added to the electrolyte in the solar cells since they have been shown to result in improved device performance (Hagfeldt and Grätzel 1995, Nazeeruddin, et al. 1993). However, the transient data observed in both electrolyte B and C exhibit high electron injection yields of >0.9 (figure 5.14) although the potential of the conduction band was shifted positively more than 1 eV with addition of $Li^+$. It has also been shown that the recombination kinetics are almost identical either in the presence or absence of $Li^+$. The absence of $Li^+$ (or other potential determining ions) thus appears to have no influence for the solar cell performance in terms of the dye / semiconductor interface. In addition, it is expected that in the absence of the potential determining ions, the open circuit voltage may increase because of the negative shift of the conduction band energy, improving the efficiency of the cell. It is however possible as discussed above that the redox potentials of the dye may be negatively shifted in the absence of $Li^+$ (electrolyte C), resulting in relatively slow electron transfer process to the dye cation state from the iodine redox electrolyte and therefore lowering the efficiency of the cell. Further studies with the iodine electrolyte are required to establish the role of $Li^+$ in device performance.

# Chapter 6: Electron injection kinetics in dye sensitised solar cells

## 6.1 Introduction

In chapter 5, the parameters controlling the electron injection kinetics in the dye sensitised $TiO_2$ nanocrystalline films were investigated. It was demonstrated that the electron injection kinetics are remarkably insensitive to variation of sensitiser dyes (for a limited range of dyes), excitation wavelength, solvent environment and externally applied voltage up to -0.4 V vs Ag/AgCl. However the injection rate is modulated by shifts in the energetics of the electronic states of the $TiO_2$. It was concluded that the nature of $TiO_2$ films dominantly influences the electron injection kinetics. The conduction band / trap state energetics controlling the electron injection kinetics are dependent upon electrolyte composition, and therefore the injection kinetics studied in chapter 4 and 5 may not directly correlate to those in the dye sensitised photovoltaic device with the redox active electrolyte.

In this chapter, the studies of the electron injection kinetics are extended to a solar cell employing the dye sensitised $TiO_2$ films. The apparent differences in experimental conditions between the solar cell and the dye sensitised films studied in chapter 5 are higher dye coverage on the $TiO_2$ surface and use of a redoxactive electrolyte. The preliminary results were obtained for the cell with an incident photon-to-current conversion efficiency (IPCE) of 45 %.

## 6.2 Experiment

### 6.2.1 Fabrication of the solar cell

N719 sensitised $TiO_2$ film prepared on fluorine doped $SnO_2$ conducting (F-$SnO_2$) glass was employed as a working electrode for a thin-layer sandwich-type solar cell. A platinum counter electrode was prepared by forming a thin layer of $H_2PtCl_6$ in isopropanol (0.05 M) on F-$SnO_2$ glass and heating it at 400 °C for 10 minutes. The electrolyte used in this study was prepared with tetrabutyl ammonium iodide (0.6 M),

lithium iodide (0.1 M), tert-butylpyridine (0.5 M) and iodine (0.1 M) in methoxypropionitrile. The electrolyte was applied into the sandwich type cell by capillary forces immediately after the counter electrode was placed directly on top of the dye sensitised $TiO_2$ electrode and tightly clamped together.

### 6.2.2 Experimental condition of the fs transient measurement

Excitation pulses (30~40 fs) were tuned using the optical parametric amplifier (OPA, c.f. chapter 2) to an absorption tail of the dye with a centre wavelength of 630 nm in order to obtain homogeneous population of excited dye molecules throughout the $TiO_2$ film. An intensity of the pulse is approximately 55 nJ (1.1 $mJcm^{-2}$) with a spot diameter of 60~80 μm. This excitation intensity for the solar cell (high dye coverage sample) corresponds to approximately 2.5 injected electrons per pulse per $TiO_2$ particle (c.f. chapter 4 for the detailed calculation of the number of injected electrons). The samples were excited from the $TiO_2$ film side through the back conducting glass as the illumination from this side generally shows higher incident photon-to-current conversion efficiency (IPCE) values (Hagfeldt and Grätzel 1995, Nazeeruddin, et al. 1993).

The experiments were carried out with the magic angle configuration (ca. 54.7°) between pump and probe pulses with a repetition rate of 1 kHz at 20 °C. Transient absorption data were collected with timescales of 0-6 and 0-60 ps with a time delay of 33 and 330 fs between points respectively, and at 600 ps. The data were probed between 680 and 770 nm using a multi-channel detector (see chapter 2) in order to avoid severe loss of probe laser light resulting from absorption by dye molecules at shorter wavelengths. The stability of all samples was confirmed with the transient and the steady state absorption spectrometers as described in chapter 4.

## 6.3 Results

### *Steady state absorption spectra*

Figure 6.1 represents steady state absorption spectra of the solar cell employing N719 sensitised $TiO_2$ films and the dye free cell. Subtraction of these two spectra indicates spectral contribution of dye molecules. As discussed in chapter 4, the spectrum exhibits the broad MLCT absorption band (peak: 535 nm), and the sample absorbs >95 % of incident light at 535 nm. Note that transmission losses by light scatter in the samples were not corrected in figure 6.1.

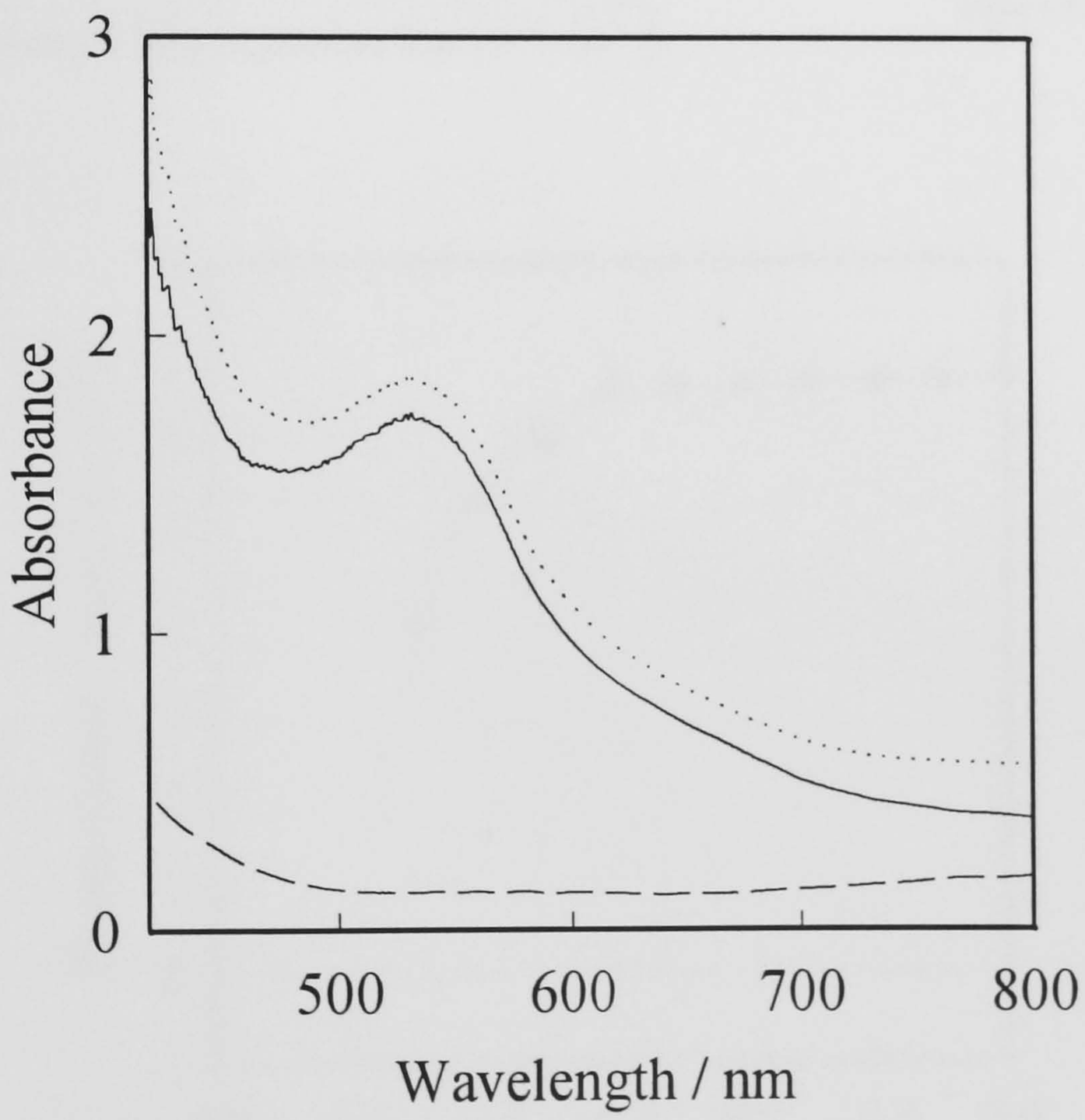



Figure 6.1. Steady state absorption spectra of the dye sensitised $TiO_2$ solar cell (.....) and the dye free cell (_ _ _ _ _ _). Also shown is the spectrum after subtraction of the dye free cell spectrum from the dye sensitised cell spectrum (_____). Light scattering loss in the cell is not corrected.

### *Photoelectrical characterisation*

The characteristics of the sandwich type solar cell were tested immediately after the fabrication. Figure 6.2 shows the current measured as a function of voltage applied to the cell under illumination of monochromatic light at 535 nm (344 μW). The cell was illuminated from the dye sensitised $TiO_2$ film side through the conducting glass, resulting in a short circuit current of 67 $\mu A/cm^2$ and an open circuit voltage of 495 mV. The monochromatic IPCE is defined as the number of electrons generated by light in the external circuit divided by the number of incident photons (Nazeeruddin, et al. 1993), and is calculated with equation 6.1.

$$\text{IPCE} = \frac{\left[1240 \times \text{photocurrent density}\left(\text{A} / \text{cm}^2\right)\right]}{\left[\text{wavelength}\left(\text{nm}\right) \times \text{photon flux}\left(\text{W} / \text{cm}^2\right)\right]} \qquad \text{Equation 6.1}$$

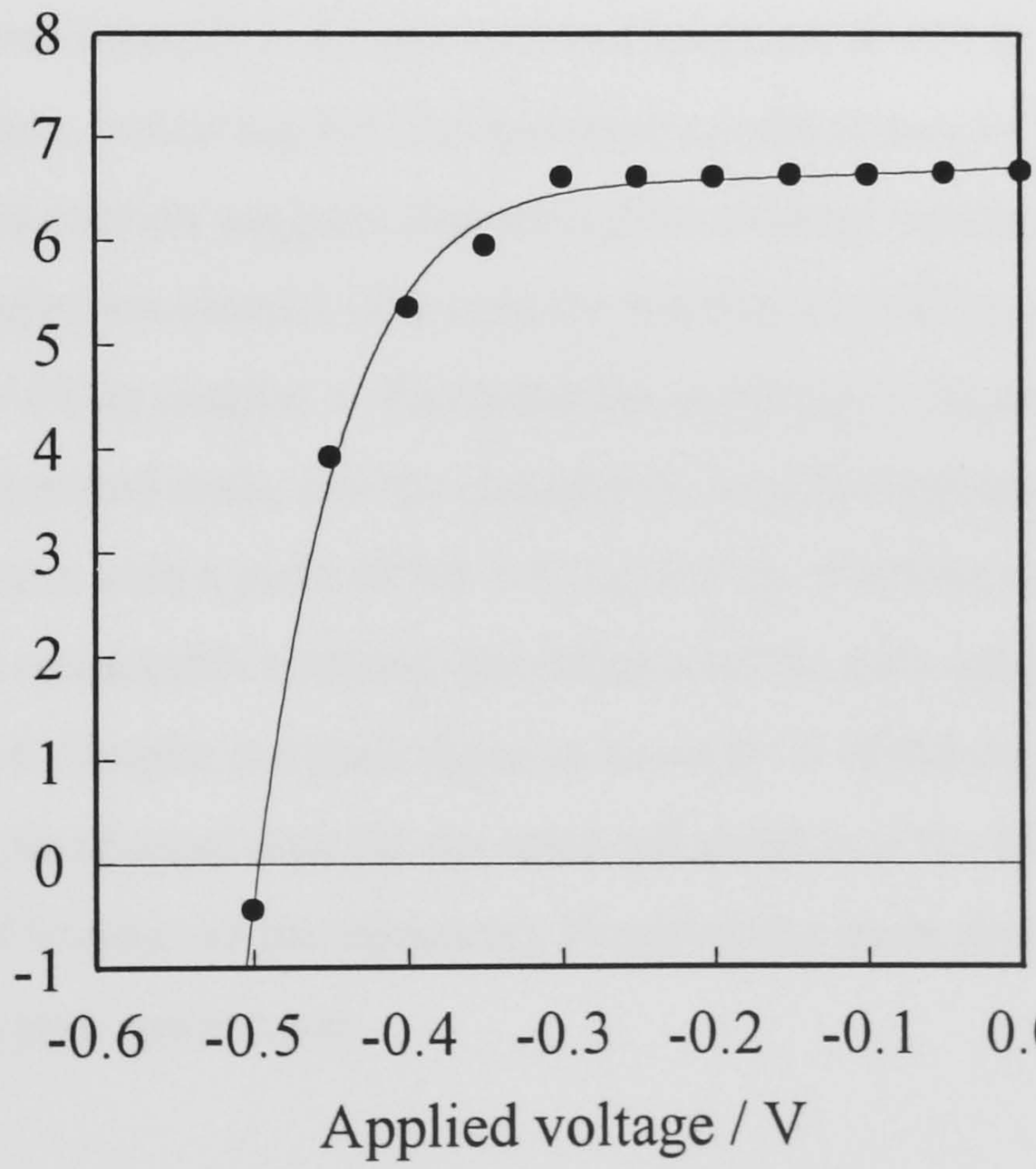



Figure 6.2 Current-voltage characteristics of a sandwich type solar cell employing N719 sensitised $TiO_2$ film. The cell was illuminated by monochromatic light at a centre wavelength of 535 nm with intensity of $3.44 \times 10^{-4}$ W from the dye sensitised $TiO_2$ film side through the conducting glass. The illumination area was approximately 1 $cm^2$.

The photocurrent to calculate the IPCE was obtained under a short circuit condition, i.e. the potential of the working electrode is the same as that of the counter electrode and the electrolyte. Taking the value of 67 $\mu A/cm^2$ from figure 6.2, the calculated IPCE at 535 nm excitation is 45 %. It should be noted that this yield was uncorrected for the transmission loss of the incident light (for example, scatter by $TiO_2$ particles) in the sample.

***Electron injection kinetics***

Figure 6.3 represents transient spectra obtained for the solar cell at time delays of 0.15 and 600 ps after 630 nm excitation under open circuit conditions. As discussed in chapters 4 and 5, the spectra were assigned by comparison of typical absorption difference spectra for the dye excited state (maximum: 720 nm, see for example figure 4.2) and the charge separated state (maximum: 800 nm, see for example figures 4.8 and 4.9). It is apparent from figure 6.3 that the transient spectrum at 150 fs is very similar to that for the excited state, indicating that the spectrum results primarily from the dye excited state. This observation suggests that negligible electron injection occurs in <150 fs in contrast to the injection kinetics observed for $Ru(dcbpy)_2(NCS)_2$ sensitised $TiO_2$ films covered in EC / PC in chapter 4. The spectrum at 600 ps in figure 6.3 is similar to that for the charge separated state, and the quantitative analysis indicates that the electron injection occurs with a yield of $0.8 \pm 0.1$ in 600 ps. Furthermore, the electron injection kinetics are remarkably retarded compared with the data obtained for the films employed in chapter 4. Despite the poor signal to noise level of the data, it was estimated that the multi-channel data for the solar cell exhibits a $10\sim10^2$ fold retardation (comparison of a half lifetime of the injection). However the more detailed analysis was precluded due to this poor noise level.

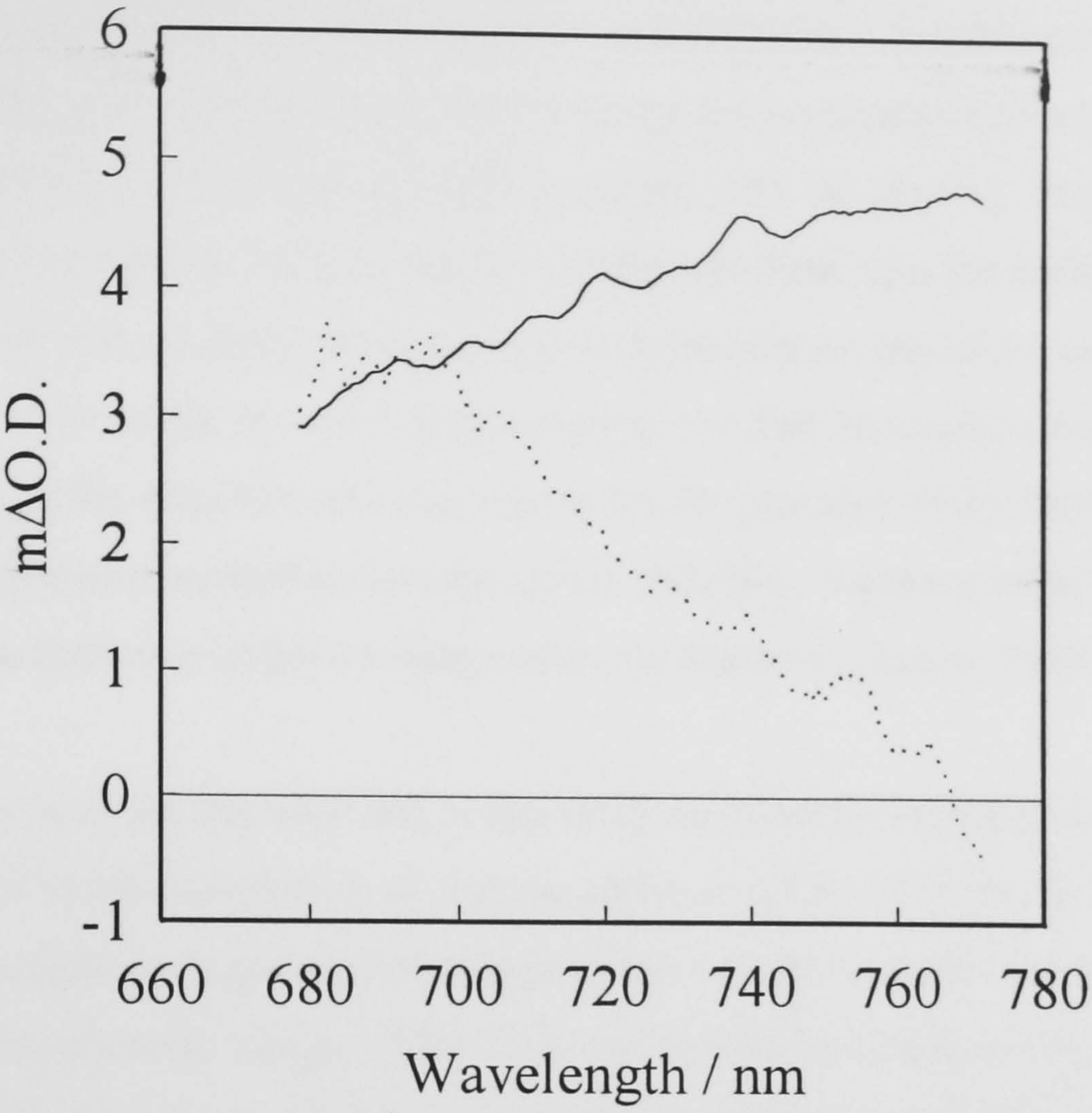



Figure 6.3. Transient absorption spectra obtained for the solar cell employing the $TiO_2$ film sensitised by N719 at time delays of 150 fs (·····) and 600 ps (———) following an excitation at 630 nm under the open circuit condition. The dye was excited from the $TiO_2$ side through the conducting glass.

## 6.4 Discussion

### *Electron injection kinetics*

The transient absorption study for the solar cell employing N719 sensitised $TiO_2$ films indicated that the injection kinetics are remarkably retarded by a factor of $10\sim10^2$, resulting from the global analysis. The differences in experimental conditions between the solar cell and the dye sensitised films studied previously (for example in chapter 5) are higher dye coverage on the $TiO_2$ surface and composition of the electrolyte, for example, the presence of redox active electrolyte ($I_3^-/I^-$) and tert-butylpyridine in this study.

The dye sensitised $TiO_2$ film employed in this study indicates relatively high absorbance (absorbance of ~1.5 at absorption maximum). It is possible that the coverage of dye molecules on the semiconductor surface may not be a monolayer; for example, some dye molecules may be aggregated (see chapter 2 for the details). Thus, the excitation may not entirely be achieved for the dye adsorbed onto the surface, and therefore the electron injection from the excited molecules on top of the sensitiser dye may be retarded. It should be noted as discussed above that the excitation of the absorption tail of the dye (630 nm) was chosen for the injection study here in order to achieve homogeneous excitation throughout the $TiO_2$ film. Further studies are necessary to establish the influence of dye coverage upon the electron injection kinetics.

The electrolyte used for the solar cell in this study contains tert-butylpyridine. It has been suggested by Nazeeruddin et al. that the addition of tert-butylpyridine in the electrolyte increases the open circuit voltage of the cell (Nazeeruddin, et al. 1993). They reported that the potential energy of the $TiO_2$ conduction band is negatively shifted by 0.2~0.3 V in the electrolyte with tert-butylpyridine compared to that in the acetnitrile electrolyte B (the presence of $Li^+$) (Haque, et al. 1999, Nazeeruddin, et al. 1993). In chapter 5, it has been demonstrated that the retarded injection kinetics for the sensitised $TiO_2$ films in the absence of the potential determining cations (figure 5.14) results from the reduction in acceptor density of states. In such conditions, the electron injection reaction may not always be activationless as the number of reactant and product states is considerably decreased. The conduction band potential shift under the presence of tert-butylpyridine may also produce the situation that activationless electron injection cannot be achieved. However, it is not likely that this potential shift results in a $10^2$ fold retardation of the injection rate compared to a 7±1 fold retardation in the absence of the potential determining cations. At present, a more quantitative consideration of the relationship between injection rate and $TiO_2$ density of states is precluded by uncertainty over the redox potentials of the adsorbed dyes as discussed in chapter 5.

The electron injection kinetics of the solar cell were measured in the presence of the redox active electrolyte ($I_3^-/I^-$) in contrast to the studies presented in chapter 5. Such negatively charged species may be present beside $Li^+$ ions near the $TiO_2$ surface in order to compensate excess positive charges (see chapter 3 for the details), and may therefore

influence electron injection kinetics by electrostatic repulsion. The presence of the redox active electrolyte may also influence the redox potentials of the adsorbed dyes, precluding the kinetic analysis by comparison of relative energy levels between the dye excited state and the conduction band. Further works should be carried out to clarify these possibilities.

***Influence of electron injection kinetics on the solar cell performance***

Although the injection kinetics in the solar cell were significantly retarded, the kinetics are still sufficiently fast to obtain the high injection yield of 0.8 ± 0.1 at 600 ps. The observation suggests that the injection process is not a limiting step to achieve high IPCE under the condition of the excitation of absorption tail (630 nm) with light intensity of 1.1 $mJcm^{-2}$. Since the IPCE data were not collected with an excitation wavelength of 630 nm for this solar cell, the detailed analysis could not be performed to identify a rate limiting step for the efficiency.

# Chapter 7: Conclusion

The mechanism of the interfacial electron injection in dye sensitised $TiO_2$ nanocrystalline films has been investigated using femtosecond-to-millisecond transient spectroscopies. The development of the OPA, the femtosecond and the nanosecond transient spectrometers has facilitated assignment of interfacial electron transfer reactions and detailed analysis of electron injection kinetics. This chapter presents summary of these interfacial kinetic studies.

1) ***A method to assign the kinetics of interfacial electron transfer reactions in $Ru(dcbpy)_2(NCS)_2$ sensitised $TiO_2$ films has been established.***

   The charge separated state as a result of the electron injection is readily distinguishable from the dye excited state using the spectral region of 680~770 nm. It has been found that the electron injection is multi-exponential, requiring at least three kinetic components with lifetimes (relative amplitudes) of <100 fs (0.29), 1.0±0.3 ps (0.25) and 13.0±3.0 ps (0.46). In contrast, the charge recombination completes on microsecond-millisecond timescales.

2) ***The multi-exponential electron injection kinetics originate from the heterogeneity of the nanocrystalline $TiO_2$ film.***

   The multi-exponential behaviour is indistinguishable for different sensitiser dyes (limited number of dyes), excitation wavelengths, solvent environments and the application of external voltages (<-0.4 V vs Ag/AgCl). These observations suggest that the heterogeneity of the $TiO_2$ film result in the multi-phasic electron injection kinetics (also see No. 4 below). This heterogeneity results probably from heterogeneous interactions of dye molecules with the surface of the film or from other microscopic variations in the $TiO_2$ nanoparticles.

3) ***The slow phase of the electron injection (>100 fs) observed for $Ru(dcbpy)_2(NCS)_2$ sensitised $TiO_2$ films occurs from relaxed, weakly luminescent, excited states.***

   The initially formed singlet excited state of $Ru(dcbpy)_2(NCS)_2$ decays to weakly luminescent excited state within 100 fs. Therefore, the multi-phasic electron injection at >100 fs proceeds from the weakly luminescent excited state. However, it

is not possible to determine whether the fast phase of the injection (<100 fs) proceeds before or after the relaxation of the dye excited state.

4) ***The electron injection rate can be controlled by modulation of the conduction band energy levels.***

In the absence of potential determining cations in the electrolyte solution, the potential of the conduction band is shifted negatively (by up to 1 V). Under these conditions, the injection rate is retarded by a factor of 7±1. It is suggested that the retardation results from a reduction in acceptor density of states.

5) ***The resultant electron injection kinetics were discussed with homogeneous and heterogeneous electron transfer theories.***

The injection kinetics are indistinguishable for different sensitiser dyes (limited number of dyes), excitation wavelengths and solvent environments. These observations suggest that the injection process is activationless, since the continuous empty electron acceptor states are available in the conduction band. The injection kinetics are retarded as the acceptor density of states is reduced.

6) ***The electron injection kinetics are retarded in the solar cells.***

The preliminary study of the injection kinetics was carried out for the dye sensitised $TiO_2$ solar cell. The injection rate for the solar cell has exhibited 1~2 orders of retardation compared with those obtained for the dye sensitised films covered in redox inactive solvent.

***Remarks***

Since my PhD study started, the dye sensitised solar cells have attracted remarkable attention, and intensive studies have been carried out for their commercial application. Further studies are still necessary to understand the kinetic mechanism of the solar cell function, preventing development of more efficient cells. However, my PhD study was intended to identify the parameters controlling the kinetics from the fundamental process, and indeed has clarified that the electron injection kinetics are generally insensitive to the experimental conditions, and therefore has little influence upon the

electron injection yield, although further study is necessary to establish the complete mechanism of the injection kinetics. I hope my study will be considered for further interpretation of the solar cell performance and for further improvement of the solar cell efficiency in the future.

# Appendix A: Distribution analysis of electron injection kinetics

The multi-exponential electron injection kinetics observed for $Ru(dcbpy)_2(NCS)_2$ sensitised $TiO_2$ films result from the global analysis assuming that each kinetic decay consists a sum of exponentials and a constant as shown in equation 2.13. Global kinetic fitting with two exponential components result in the most adequate fit to the kinetics for time delays greater than the instrument response (see, for example, table 5.1 for the fitting results). Such multi-exponential analyses are used simply as useful quantification of the injection kinetics. It is therefore not clear that these exponential components are discrete or result from a distribution of injection time constants.

In this section, the electron injection kinetics observed are analysed as a distribution of kinetic components using a computer program "ESM Distribution analysis Version 2.60". For the analysis, the number of time constants are initially chosen for the kinetic components and equally distributed on logarithmic timescales (up to 60 components) as shown in figure A1. Amplitudes for all time constants are subsequently varied and fitted with the transient kinetics until amplitude deviations are satisfactorily minimised. For example, if there is single exponential component in the reaction, only one peak in figure A1 will be appeared as a result of the analysis. If there are two, the result of the fitting has two peaks.

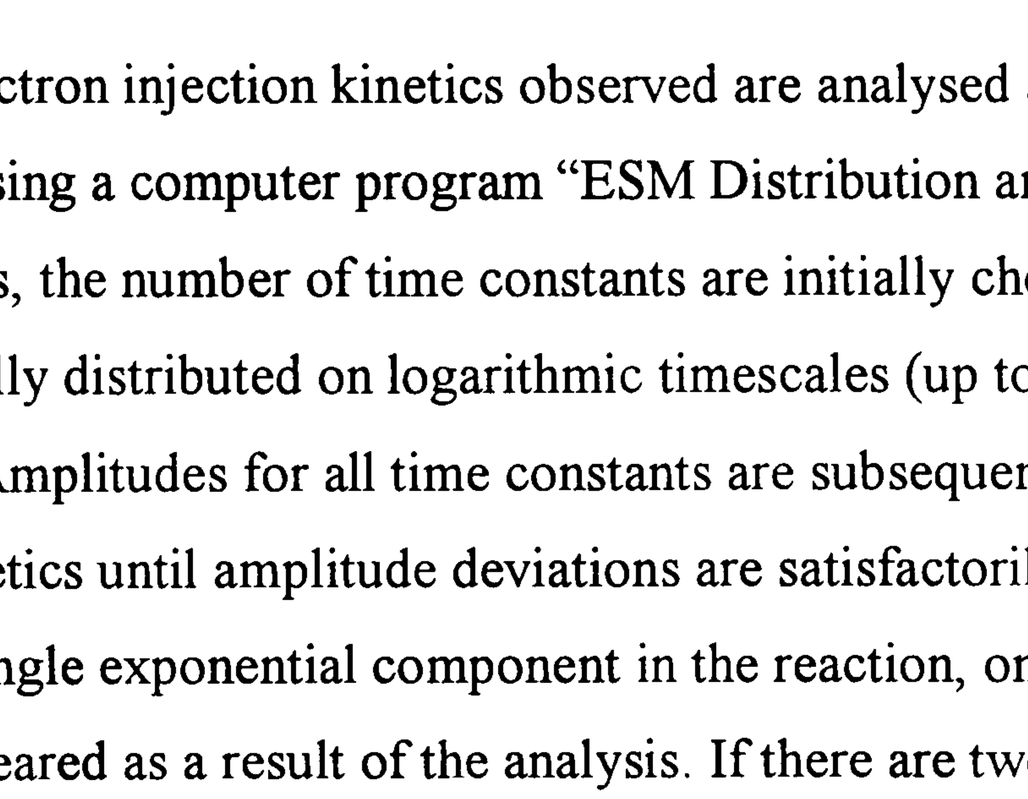



Figure A1. Time / amplitude (A) relations for distribution analysis. Initially determined time constants are equally distributed over logarithmic time shown as

lines on time axis. Amplitudes of all time constants are relatively varied to fit a transient kinetics.

It has been found that the analysis program fitting does not interpret the offset amplitude precisely, resulting in inadequate time constants and their amplitudes. For analysis the offset amplitude is therefore not included. Moreover, it does not recognise negative kinetic amplitude, i.e. an amplitude decay can only be analysed. This means that the absorption kinetic growth obtained for $Ru(dcbpy)_2(NCS)_2$ sensitised $TiO_2$ films as shown in figure 4.11c can not be analysed. Thus, these limits for the analysis required manipulation of the kinetic data to result in the decay without any offset amplitude as shown in figure A2 in order to perform distribution analysis for the electron injection kinetics.

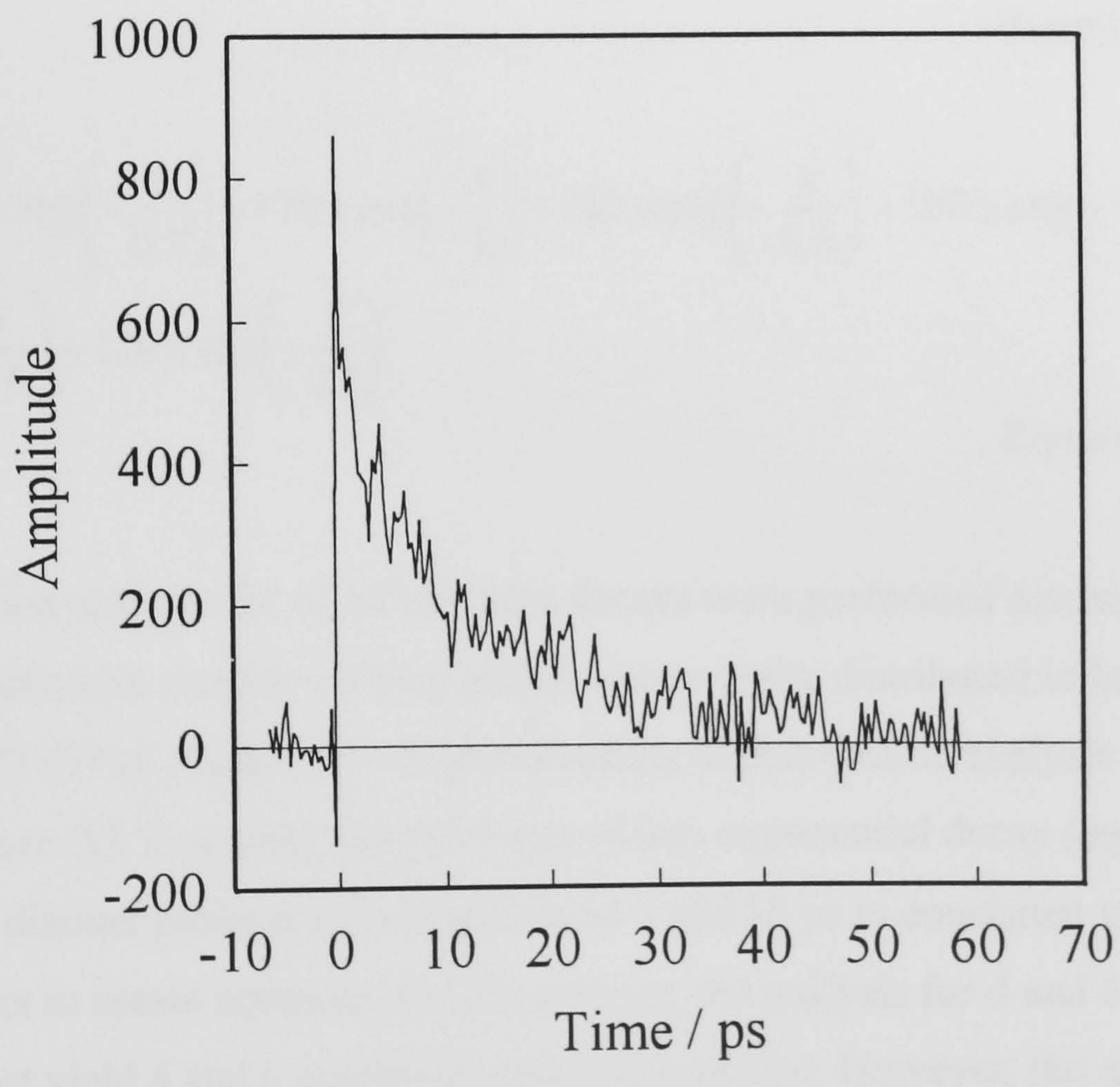



Figure A2. Kinetic decay obtained by arithmetic manipulation of the transient data observed for $Ru(dcbpy)_2(NCS)_2$ sensitised $TiO_2$ film covered in EC / PC at a probe wavelength of 760 nm with an excitation wavelength of 560 nm as shown in figure 4.11c.

The validity of the distribution analysis with this program is tested by fitting decay curves created using arbitrary amplitudes and time constants with a series of Gaussian noise. The created decays based upon equation 2.13 are shown in equation A1 and figure A3 (a), (b) and (c) with components of 2, 4 and 6 exponentials. The time constants chosen were 1 and 15 ps, 1, 4, 8 and 20 ps, and 0.7, 2, 4.5, 8, 15 and 25 ps for equation A1 (a), (b) and (c), respectively. Amplitude as a function of time, A(t), is used instead of ΔOD(t). The shape of the decay curves shown in figure A3 were produced to resemble closely to that of the decay shown in figure A2.

$$A_2(t) = 430 \times \exp\left(-\frac{t}{1}\right) + 430 \times \exp\left(-\frac{t}{15}\right)$$

Equation A1a

$$A_4(t) = 270 \times \exp\left(-\frac{t}{1}\right) + 170 \times \exp\left(-\frac{t}{4}\right) + 200 \times \exp\left(-\frac{t}{8}\right) + 220 \times \exp\left(-\frac{t}{20}\right)$$

Equation A1b

$$A_6(t) = 180 \times \exp\left(-\frac{t}{0.7}\right) + 170 \times \exp\left(-\frac{t}{2}\right) + 130 \times \exp\left(-\frac{t}{4.5}\right) + 130 \times \exp\left(-\frac{t}{8}\right) + 130 \times \exp\left(-\frac{t}{15}\right) + 120 \times \exp\left(-\frac{t}{25}\right)$$

Equation A1c

The distribution analysis for all of transient decays were performed assuming 60 time constants (maximum number chosen) which were equally distributed in logarithmic time over 0.33~57 ps. Figure A4 compares results of distribution analysis for the decays shown in figure A3. It is clear that the result of two-exponential decay (equation A1a) exhibits two distinct peaks at time constants of 1 and 15 ps in consistent with the chosen time constants to create equation A1a. In contrast, the analysis for 4 and 6 exponential decays did not yield 4 and 6 amplitude peaks as expected. However, the amplitudes as a result of the 6 exponential decay analysis are remarkably broadened over <1 ~ 40 ps compared to the result obtained for the 4 exponential decay. These observations suggest that the time constants from <0.1 to 25 ps contained in the transient data can be considerably determined up to two exponentials. The kinetics which have more than two exponential components can only be assessed by relative broadness of time constants.

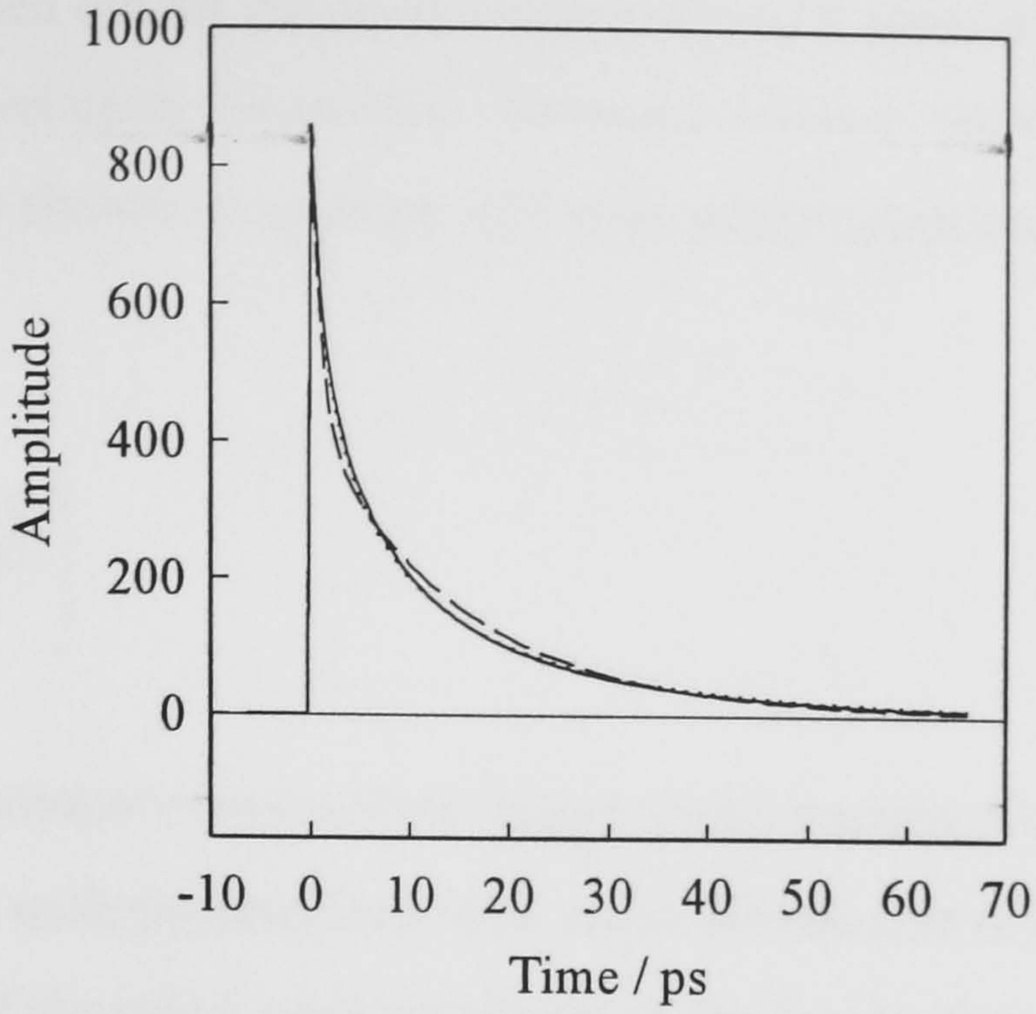



Figure A3. Transient decays of equations A1a (-------), A1b (———) and A1c (·····) created with arbitrary time constants and amplitudes. The shape of the decays are closely resembled to that of the manipulated transient kinetic data obtained for $Ru(dcbpy)_2(NCS)_2$ sensitised $TiO_2$ film (see figure A2).

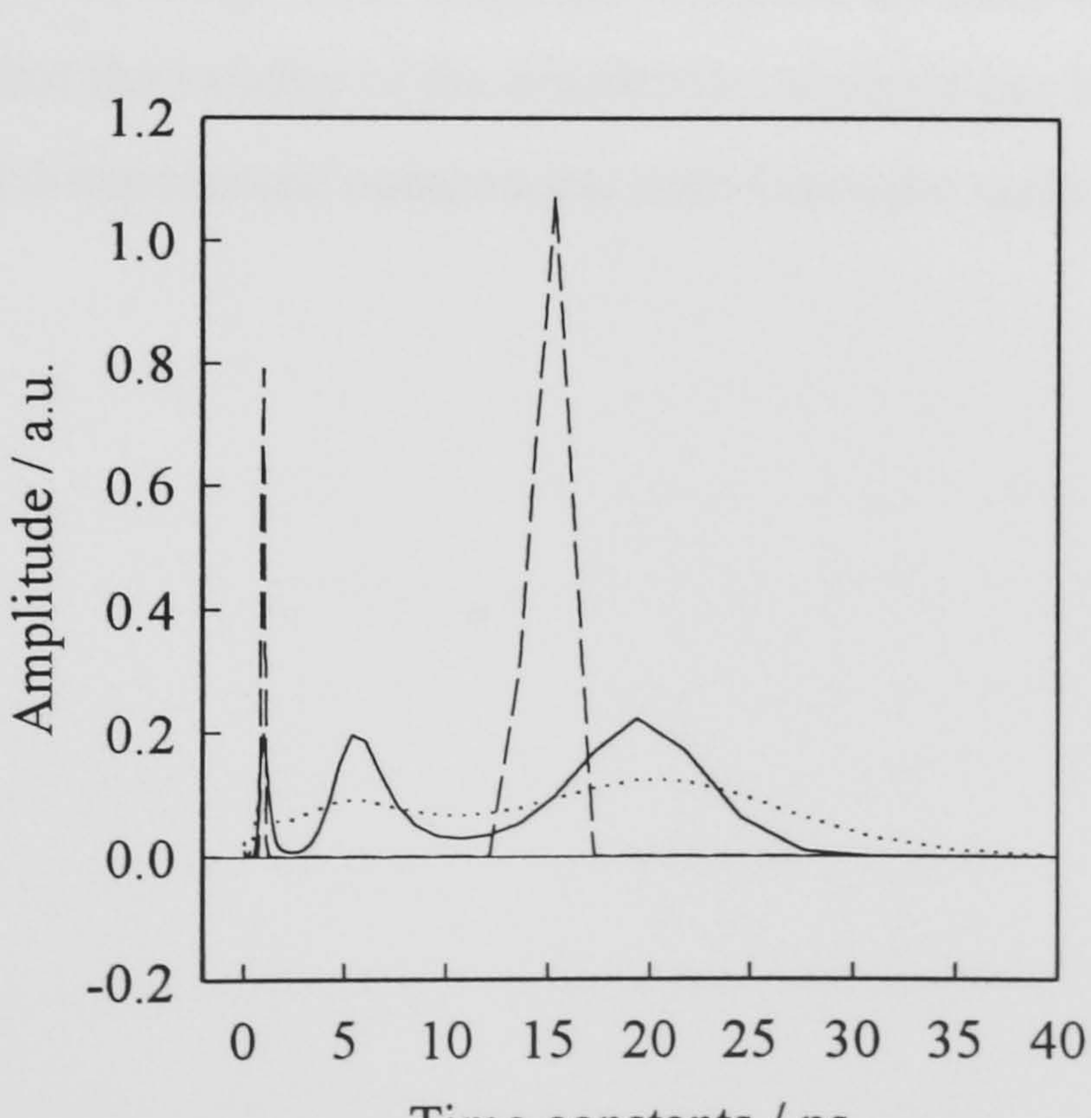



Figure A4. Results of distribution analysis for the transient kinetics of equations A1a (--------), A1b (———) and A1c (·····). The analysis were carried out assuming equally distributed 60 kinetic components on logarithmic time from 0.33 to 57 ps. The data are shown as arbitrary amplitudes as a function of time constants.

Further test was carried out for the decays with a series of noise in order to clarify influence of noise level upon the analysis. Adequate levels of the Gaussian noise (Gaussian function is shown in equation A2) were added to the transient decays shown in figure A3.

$$y = \frac{1}{\sigma\sqrt{2\pi}} \exp\left[\frac{(x-u)^2}{2\sigma^2}\right]$$ Equation A.2

Figure A5 (bottom) compares noise levels created with a series of σ-values in equation A2. Note that for the analysis described here, noise distribution of $\sigma = 4$ corresponds to approximately 1 % of the initial peak amplitude of the decays shown in figure A3. Each noise was subsequently added to the decays with 2, 4 and 6 exponential components as shown in equation A1. The transient decay obtained by addition of equation A1a and Gaussian noise generated with $\sigma = 35$ is shown in figure A5 (top) as an example. The decay for $Ru(dcbpy)_2(NCS)_2$ sensitised $TiO_2$ film taken from figure A2 is also shown as comparison. It is clear from figure A5 (top) that the noise levels of two decays are very similar, suggesting that the validity of the distribution analysis can be assessed using the decays with 2, 4 and 6 exponential components with Gaussian noise of $\sigma = 35$.

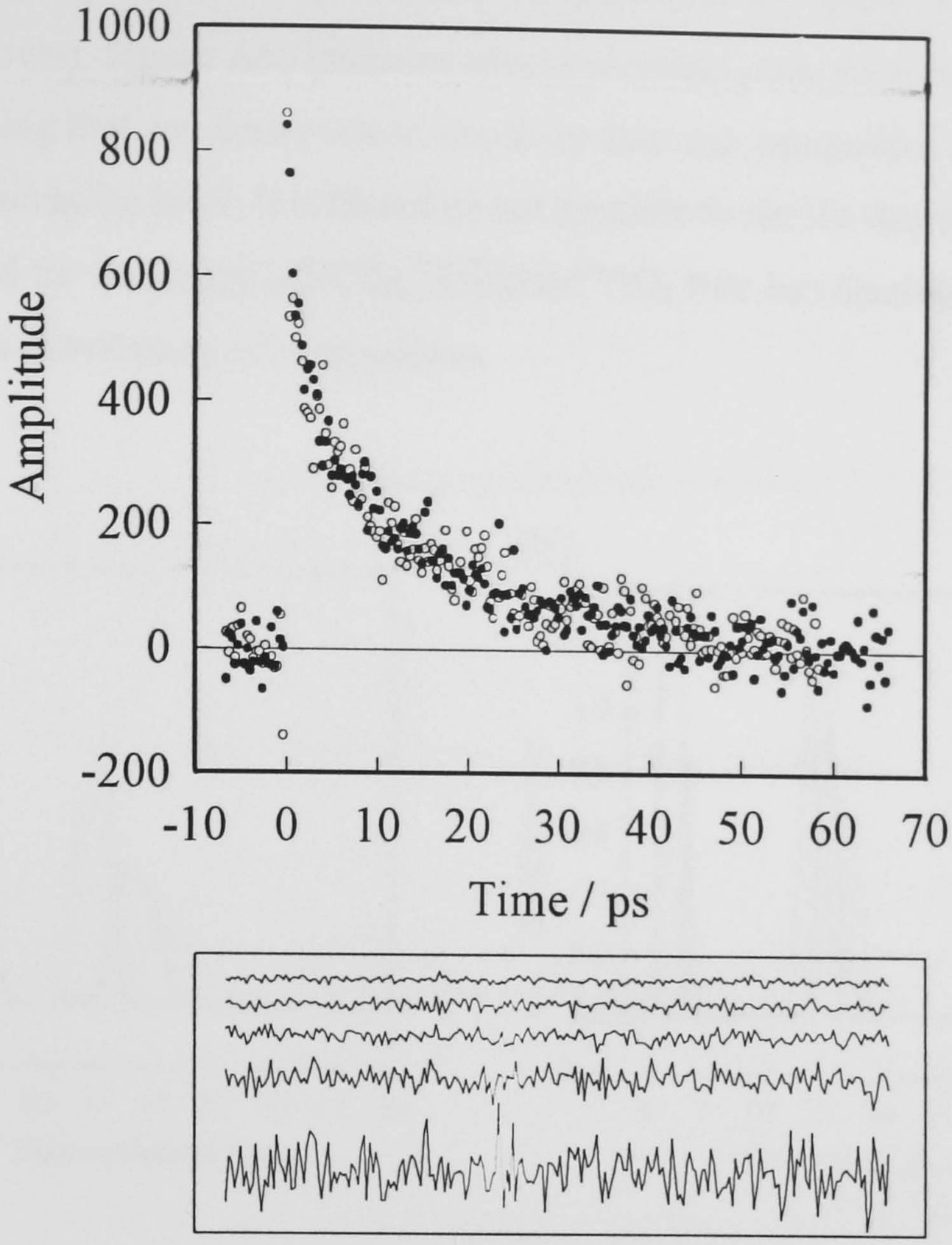



Figure A5. Transient decay (filled circle) obtained by addition of equation A1a and Gaussian noise generated by equation A2 with $\sigma = 35$. Also shown is the decay (open circle) for $Ru(dcbpy)_2(NCS)_2$ sensitised $TiO_2$ film taken from figure A2. The bottom figure shows generated Gaussian noise with equation A2. From the top, the noise is introduced with sigma, $\sigma$, of 4, 6, 8, 15 and 35.

Some results of the distribution analyses for all decays created with a series of Gaussian noise were shown in figure A6. The results obtained for the decay with $\sigma = 4$ (figure A6a) are very similar to those obtained in figure A4, indicating that this noise level does not severely affect the analysis. In contrast, the analyses for the decays with 4 and 6 exponential components with $\sigma = 6$ (figure A6b) exhibit similar three distinct peaks instead of broad time constants. These observations suggest that the distribution analysis cannot distinguish time constants of more than three components of the decay

at this noise level. The analysis for the decays with $\sigma = 8$ and 15 indicate similar results to that for $\sigma = 6$, however all decays exhibit even narrower and closer time constants (data are not shown). Figure A6c indicates almost identical peak positions for all decays analysed, implying that any decay which has more than one component exhibits the same result at this noise level. It is therefore not possible to clarify that the injection kinetics obtained for $Ru(dcbpy)_2(NCS)_2$ sensitised $TiO_2$ film has discrete exponential components or a distribution of components.

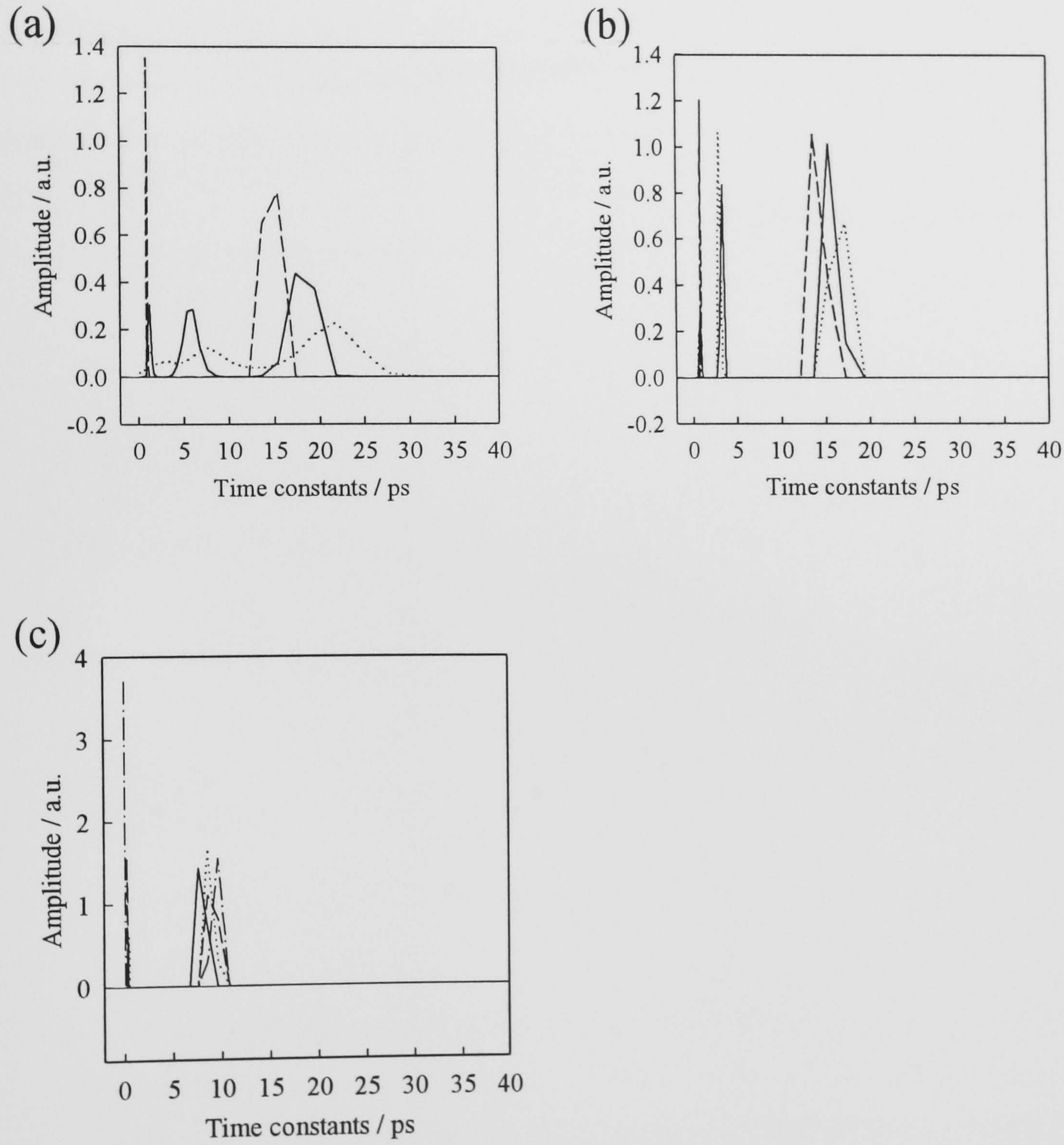



Figure A6. Results of distribution analysis for the decays generated by combinations of equations A1a (-------), A1b (———) and A1c (·····), and Gaussian noise with $\sigma = 4$ (a), 6 (b) and 35 (c). Figure A6c also represents the result of the analysis for the transient decay for $Ru(dcbpy)_2(NCS)_2$ sensitised $TiO_2$ film (—·—).

In consequence, further improvement of the signal to noise for the kinetic data for the dye coated $TiO_2$ films is necessary in order to identify if the observed multi-exponential components are discrete or result from a distribution of injection time constants. It has been found that the number of the kinetic components can be relatively estimated from the distribution analysis when the Gaussian noise level is reduced within 1 % of the initial signal size of the decay ($\sigma = 4$ in the present case).

# Appendix B: Global analysis

The multi-channel transient absorption data consist of 128 kinetic data over a spectral range of 95 nm as shown in figure B1, and can be analysed either individually or simultaneously (globally). Global analysis conducts simultaneous fitting for all kinetic data sets, e.g. from equation 2.13, pre-exponential factors ($A_{1,2,3....}$) are varied independently and a lifetime ($\tau_{1,2\ or\ 3...}$) is fitted to be the same value for all wavelengths. The main advantage of this method is the reduction in the number of free parameters to be optimised. Consider the multi-channel data set for which the kinetics are described with two exponential components. In this case, global analysis treats the two lifetimes as common parameters for all the kinetic data. The number of optimised parameters becomes 386 ($3 \times 128$ amplitudes including $A_{const}$ in equation 2.13 and 2 lifetimes) instead of $5 \times 128$ in the case of individual analysis.

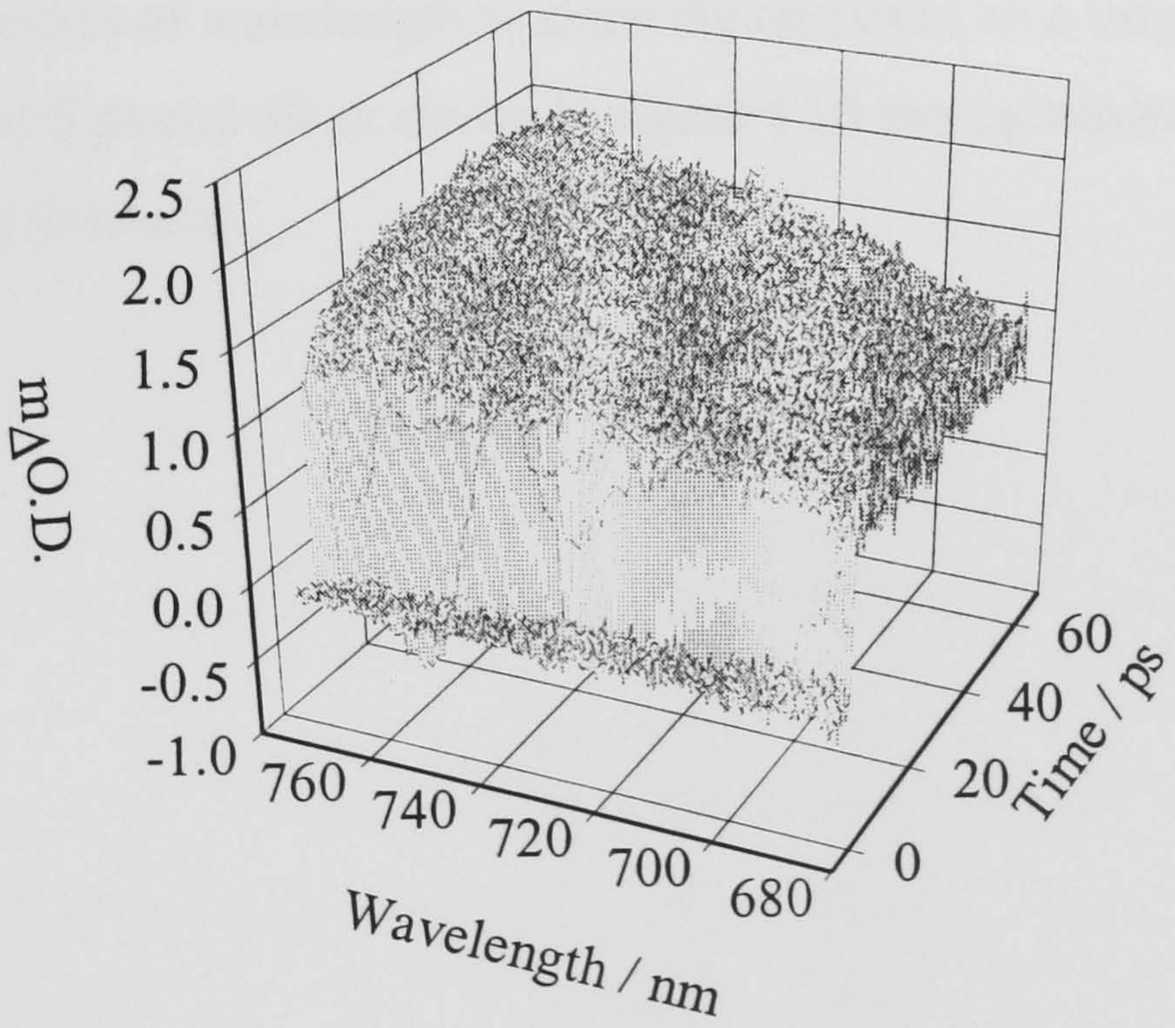



Figure B1. Multi-channel transient absorption data obtained for $Ru(dcbpy)_2(NCS)_2$ sensitised $TiO_2$ films covered in EC / PC. The data were taken in a range from 685 nm to 780 nm following an excitation at 560 nm, exhibiting a positive absorption growth with a maximum towards 800 nm.

After the lifetimes are determined by the global kinetic fitting, the pre-exponential factor for each lifetime component can be plotted as a function of wavelength. This

spectrum for one fixed lifetime is called "a kinetic (or amplitude) spectrum". Generation of a kinetic spectrum mathematically is clearly useful since one exponential lifetime indicates one type of chemical or physical reaction, and it is therefore possible that a kinetic spectrum can be used to determine what type of reaction proceeds in the sample. Note that a positive amplitude of the spectrum indicates the kinetic decay as a function of time and a negative amplitude indicates the kinetic growth of signal. Consider the multi-channel data obtained for $Ru(dcbpy)_2(NCS)_2$ sensitised $TiO_2$ films covered in EC / PC as shown in figure B1. Global analysis of the data collected on two timescales result in two exponential lifetimes of 1 ps and 13 ps. Kinetic spectra with 1 ps and 13 ps time constants are therefore generated and shown in figure 4.12. Since both spectra show similar shape and more negative amplitude towards 800 nm, the transient spectra are growing to a positive maximum at 800 nm. In addition, the kinetic spectral shape is almost identical to the spectrum expected for the absorption changes associated with electron injection. The reactions with 1 ps and 13 ps time constants can therefore be assigned to electron injection. Moreover, the amplitude of $A_{const}$ in equation 2.13 can be generated as a function of wavelength to show the spectrum on a long timescale. For example, spectra at 6 ps and 60 ps shown in figure 4.10 were generated after analysing 0-6 ps and 0-60 ps data sets.

References

Alebbi, M., Bignozzi, C. A., Heimer, T. A., Hasselmann, G. M. and Meyer, G. J. (1998). "The Limiting Role of Iodide Oxidation in cis-$Os(dcb)_2(CN)_2/TiO_2$ Photoelectrochemical Cells." J. Phys. Chem. B **102**(39): 7577-7581.

Anderson, S., Constable, E. C., Dare-Edwards, M. P., Goodenough, J. B., Hamnett, A., Seddon, K. R. and Wright, R. D. (1979). "Chemical Modification of a Titanium (IV) Oxide Electrode to Give Stable Dye Sensitisation without a Supersensitiser." Nature **280**: 571-573.

Argazzi, R., Bignozzi, C. A., Heimer, T. A. and Meyer, G. J. (1997). "Remote Interfacial Electron Transfer from Supramolecular Sensitizers." Inorg. Chem. **36**(1): 2-3.

Asbury, J., B., Ellingson, R., J., Ghosh, H., N., Ferrere, S., Nozik, A., J. and Lian, T. (1999). "Femtosecond IR Study of Excited-State Relaxation and Electron-Injection Dynamics of $Ru(dcbpy)_2(NCS)_2$ in Solution and on Nanocrystalline $TiO_2$ and $Al_2O_3$ Thin Films." J. Phys. Chem. B **103**(16): 3110-3119.

Bard, A. J. (1980). "Photoelectrochemistry." Science **207**(4427): 139-144.

Bard, A. J. and Fox, M. A. (1995). "Artificial Photosynthesis: Solar Splitting of Water to Hydrogen and Oxygen." Acc. Chem. Rev. **28**(3): 141-145.

Bockris, J. O. M. and Khan, S. U. M. (1993). Surface Electrochemistry: A Molecular Level Approach. New York, Plenum Press.

Bolts, J. M. and Wrighton, M. S. (1976). "Correlation of Photocurrent-Voltage Curves with Flat-Band Potential for Stable Photoelectrodes for the Photoelectrolysis of Water." J. Phys. Chem. **80**(24): 2641-2645.

Boschloo, G. and Goossens, A. (1996). "Electron Trapping in Porphyrin-sensitized Porous Nanocrystalline $TiO_2$ Electrodes." J. Phys. Chem. **100**(50): 19489-19494.

Bradley, P. G., Kress, N., Hornberger, B. A., Dallinger, R. F. and Woodruff, W. H. (1981). "Vibrational Spectroscopy of the Electronically Excited State. 5. Time-Resolved Resonance Raman Study of Tris(bipyridine)ruthenium(II) and Related Complexes. Definitive Evidence for the "Localized" MLCT State." J. Am. Chem. Soc. **103**(25): 7441-7446.

Braterman, P. S., Harriman, A., Heath, G. A. and Yellowlees, L. J. (1983). "The Electronic Absorption Spectrum and Structure of the Emitting State of the Tris(2,2'-bipyridyl)ruthenium(II) Complex Ion." J. Chem. Soc. Dalton Trans.: 1801-1803.

Burfeindt, B., Hannappel, T., Storck, W. and Willig, F. (1996). "Measurement of Temperature-Independent Femtosecond Interfacial Electron Transfer from an Anchored Molecular Electron Donor to a Semiconductor as Acceptor." J. Phys. Chem. **100**(41): 16463-16465.

Cao, F., Oskam, G., Searson, P. C., Stipkala, J. M., Heimer, T. A., Farzad, F. and Meyer, G. J. (1995). "Electrical and Optical Properties of Porous Nanocrystalline $TiO_2$ Films." J. Phys. Chem. **99**(31): 11974-11980.

Carroll, P. J. and Brus, L. E. (1987). "Picosecond Raman Scattering Study of Electron Localization in the Charge-Transfer Excited State of Tris(bipyridine)ruthenium(II)." J. Am. Chem. Soc. **109**(25): 7613-7616.

Cerullo, G., Nisoli, M. and Silvestri, S. D. (1997). "Generation of 11 fs Pulses Tunable across the Visible by Optical Parametric Amplificaiton." Appl. Phys. Lett. **71**(25): 3616-3618.

Cherepy, N. J., Smestad, G. P., Grätzel, M. and Zhang, J. Z. (1997). "Ultrafast Electron Injection: Implication for a Photoelectrochemical Cell Utilizing an Anthocyanin Dye-Sensitized $TiO_2$ Nanocrystalline Electrode." J. Phys. Chem. B **101**(45): 9342-9351.

Christensen, P. A. and Hamnett, A. (1994). Techniques and Mechanisms in Electrochemistry. Glasgow, Blackie Academic & Professional.

Closs, G. L. and Miller, J. R. (1988). "Intramolecular Long-Distance Electron Transfer in Organic Molecules." Science **240**: 440-447.

Damrauer, N. H., Cerullo, G., Yeh, A., Boussie, T. R., Shank, C. V. and McCusker, J. K. (1997). "Femtosecond Dynamics of Excited-State Evolution in $[Ru(bpy)_3]^{2+}$." Science **275**: 54-57.

Danielius, R., Piskarskas, A., Stabinis, A., Banfi, G. P., Trapani, P. D. and Righini, R. (1993). "Traveling-Wave Parametric Generation of Widely Tunable, Highly Coherent Femtosecond Light Pulses." J. Opt. Soc. Am. B **10**(11): 2222-2232.

Darwent, J. R., Douglas, P., Harriman, A., Porter, G. and Richoux, M.-C. (1982). "Metal Phthalocyanines and Porphyrins as Photosensitizers for Reduction of Water to Hydrogen." Coord. Chem. Rev. **44**(1): 83-126.

Das, S. and Kamat, P. V. (1998). "Spectral Characterization of the One-Electron Oxidation Product of cis-bis(isothiocyanato)bis(4,4'-dicarboxylato-2,2'-bipyridyl) Ruthenium(II) Complex Using Pulse Radiolysis." J. Phys. Chem. B. **102**(45): 8954-8957.

Daul, C., Baerends, E. J. and Vernooijs, P. (1994). "A Density Functional Study of the MLCT States of $[Ru(bpy)_3]^{2+}$ in D3 Symmetry." Inorg. Chem. **33**(16): 3538-3543.

Davis, C. C. (1996). Lasers and Electro-optics: Fundamentals and Engineering. Cambridge, Cambridge University Press.

De Armond, M. K. and Myrick, M. L. (1989). "The Life and Times of $[Ru(bpy)_3]^{2+}$: Localized Orbitals and Other Strange Occurrences." Acc. Chem. Res. **22**(10): 364-370.

Demas, J. N. and Crosby, G. A. (1971). "Quantum Efficiencies on Transition Metal Complexes. II. Charge-Transfer Luminescence." J. Am. Chem. Soc. **93**(12): 2841-2847.

Devault, D. (1980). "Quantum Mechanical Tunnelling in Biological Systems." Q. Rev. Biophys. **13**(4): 387-564.

Duffy, N. W., Dobson, K. D., Gordon, K. C., Robinson, B. H. and McQuillan, A. J. (1997). "In Situ Infrared Spectroscopic Analysis of the Adsorption of Ruthenium (II) Bipyridyl Dicarboxylic Acid Photosensitisers to $TiO_2$ in Aqueous Solutions." Chem. Phys. Lett. **266**: 451-455.

Durrant, J. R. (1992). "Transient Absorption Spectroscopy of Photosystem II."Ph.D., University of London.

Durrant, J. R., Hastings, G., Hong, Q., Barber, J., Porter, G. and Klug, D. R. (1992). "Determination of P680 Singlet State Lifetimes in Photosystem Two Reaction Centres." Chem. Phys. Lett. **188**(1, 2): 54-60.

Durrant, J. R., Hastings, G., Joseph, D. M., Barber, J., Porter, G. and Klug, D. R. (1992). "Subpicosecond Equilibration of Excitation Energy in Isolated Photosystem II Reaction Centers." Proc. Natl. Acad. Sci. U.S.A. **89**: 11632-11636.

Eichberger, R. and Willig, F. (1990). "Ultrafast Electron Injection from Excited Dye Molecules into Semiconductor Electrodes." Chem. Phys. **141**: 159-173.

Ellingson, R., J., Asbury, J., B., Ferrere, S., Ghosh, H., N., Sprague, J., Lian, T. and Nozik, A., J. (1998). "Dynamics of Electron Injection in Nanocrystalline Titanium Dioxide Films Sensitized with [Ru(4,4'-Dicarboxy-2,2'-Bipyridine)$_2$(NCS)$_2$] by Infrared Transient Absorption." J. Phys. Chem. B **102**(34): 6455-6458.

Fessenden, R. W. and Kamat, P. V. (1995). "Rate Constants for Charge Injection from Excited Sensitizer into $SnO_2$, ZnO and $TiO_2$ Semiconductor Nanocrystallites." J. Phys. Chem. **99**(34): 12902-12906.

Finklea, H. O. (1988). Semiconductor Electrodes. Amsterdam, Elsevier Science.

Fork, R. L., Shank, C. V., Hirlimann, C., Yen, R. and Tomlinson, W. J. (1983). "Femtosecond White-Light Continuum Pulses." Opt. Lett. **8**: 1.

Forster, M. and Hester, R. E. (1981). "Resonance Raman Investigation of Electronically Excited Ru(bipyridine)$_3^{2+}$ Using a CW Laser." Chem. Phys. Lett. **81**(1): 42-47.

Fujihira, M., Ohishi, N. and Osa, T. (1977). "Photocell Using Covalently-Bound Dyes on Semiconductor Surfaces." Nature **268**: 226-228.

Fujishima, A. and Honda, K. (1972). Nature **238**: 37.

Gerischer, H. (1970). Physical Chemistry. New York / London, Academic Press.

Gerischer, H. (1990). "The Impact of Semiconductors on the Concepts of Electrochemistry." Electrochimica Acta **35**(11/12): 1677-1699.

Goossens, A. (1996). "Potential Distribution in Semiconductor Particles." J. Electrochem. Soc. **143**(6): L131-133.

Gouterman, M. (1978). In The Porphyrins. New York, Academic Press.

Greenfield, S. R. and Wasielewski, M. R. (1995). "Optical Parametric Amplification of Femtosecond Pulses Tunable from the Blue to the Infrared with Microjoule Energies." Applied Optics **34**(15): 2688-2691.

Guenther, R. D. (1990). Modern Optics. New York, John Wiley & Sons.

Hagfeldt, A. and Grätzel, M. (1995). "Light-Induced Redox Reactions in Nanocrystalline Systems." Chem. Rev. **95**(1): 49-68.

Hannappel, T., Burfeindt, B., Storck, W. and Willig, F. (1997). "Measurement of Ultrafast Photoinduced Electron Transfer from Chemically Anchored Ru-Dye Molecules into Empty Electronic States in a Colloidal Anatase $TiO_2$ film." J. Phys. Chem. B **101**(35): 6799-6802.

Hannappel, T., Zimmermann, C., Meissner, B., Burfeindt, B., Storck, W. and Willig, F. (1998). "Reply to Comment on "Measurement of Ultrafast Photoinduced Electron Transfer from Chemically Anchored Ru-Dye Molecules into Empty Electronic States in a Colloidal Anatase $TiO_2$ Film"." J. Phys. Chem. B **102**(18): 3651-3652.

Haque, S. A., Tachibana, Y., Klug, D. R. and Durrant, J. R. (1998). "Charge Recombination Kinetics in Dye-Sensitized Nanocrystalline Titanium Dioxide Films." J. Phys. Chem. B **102**(10): 1745-1749.

Haque, S. A., Tachibana, Y., Willis, R., Moser, J. E., Grätzel, M., Klug, D. R. and Durrant, J. R. (1999). "Parameters Influencing Charge Recombination Kinetics in Dye Sensitised Nanocrystalline Titanium Dioxide Films." J. Phys. Chem. **Submitted**.

Hashimoto, K., Hiramoto, M., Lever, A. B. P. and Sakata, T. (1988). "Luminescence Decay of Ruthenium(II) Complexes Adsorbed on Metal Oxide Powders in Vacuo: Energy Gap Dependence of the Electron-Transfer Rate." J. Phys. Chem. **92**(5): 1016-1018.

Hashimoto, K., Hiramoto, M., Sakata, T., Muraki, H., Takemura, H. and Fujihira, M. (1987). "Time-Resolved Measurements of Luminescence of Ru(II) Complexes Chemically or Physically Immobilized on Semiconductor or Insulator Particles in Various Solvents." J. Phys. Chem. **91**(24): 6198-6203.

Hastings, G., Durrant, J. R., Barber, J., Porter, G. and Klug, D. R. (1992). "Observation of Pheophytin Reduction in Photosystem 2 Reaction Centers Using Femtosecond Transient Absorption-Spectroscopy." Biochemistry **31**(33): 7638-7647.

Heimer, T. A., D'Arcangelis, S. T., Farzad, F., Stipkala, J. M. and Meyer, G. J. (1996). "An Acetylacetonate-Based Semiconductor-Sensitizer Linkage." Inorg. Chem. **35**(18): 5319-5324.

Heimer, T. A. and Heiweil, E. J. (1997). "Direct Time-Resolved Infrared Measurement of Electron Injection in Dye-Sensitized Titanium Dioxide Films." J. Phys. Chem. B **101**(51): 10990-10993.

Heimer, T. A. and Meyer, G. J. (1996). "Luminescence of Charge Transfer Sensitizers Anchored to Metal Oxide Nanoparticles." J. Lumin. **70**: 468-478.

Heinzel, A. B., Teschner, D. M. and Schumacher, R. (1981). "Influence of Water on the Capacitance / Potential Distribution at the $TiO_2$ / $CH_3CN$ Junction." Ber. Bunsenges. Phys. Chem. **85**: 1117-1119.

Hilgendorff, M. and Sundström, V. (1998). "Dynamics of Electron Injection and Recombination of Dye Sensitized $TiO_2$ Particles." J. Phys. Chem. B **102**(51): 10505-10514.

Hoard, J. L. (1971). "Stereochemistry of Hemes and Other Metalloporphyrins." Science **174**: 1295-1302.

Hong, Q., Durrant, J., Hastings, G., Porter, G. and Klug, D. R. (1993). "Sub-picosecond Oscillatory Phenomena in Silica Glasses." Chem. Phys. Lett. **202**(3,4): 183-185.

Howe, R. F. and Grätzel, M. (1985). "EPR Observation of Trapped Electrons in Colloidal $TiO_2$." J. Phys. Chem. **89**(21): 4495-4499.

Huang, C., Kapteyn, H. C., McIntosh, J. W. and Murnane, M. M. (1992). "Generation of Transform-Limited 32-fs Pulses from a Self-Mode-Locked Ti:sapphire Laser." Opt. Lett. **17**(2): 139-141.

Jakobsen, H. J., Ellis, P. D., Inners, R. R. and Jensen, C. F. (1982). "Multinuclear, Multifield, and Multiphase Nuclear Magnetic Resonance Study of Cadmium meso-Tetraphenylporphyrin and Its Phyridine Adduct." J. Am. Chem. Soc. **104**(26): 7442-7452.

Joosen, W., Bakker, H. J., Noordam, L. D., Muller, H. G. and Heuvell, H. B. (1991). "Parametric Generation in B-barium Borate of Intense Femtosecond Pulses Near 800 nm." J. Opt. Soc. Am. B **8**: 2087-2093.

Jortner, J. (1980). "Dynamics of Electron Transfer in Bacterial Photosynthesis." Biochim. Biophys. Acta **594**: 193-230.

Joseph, D. M. T. (1996). "Energy and Electron Transfer in Photosystem Two.", University of London.

Kalyanasundaram, K. (1982). "Photophysics, Photochemistry and Solar Energy Conversion with Tris(bipyridyl)ruthenium(II) and Its Analogues." Coord. Chem. Rev. **46**: 159-244.

Kalyanasundaram, K. and Neumann-Spallart, M. (1982). "Photophysical and Redox Properties of Water-Soluble Porphyrins in Aqueous Media." J. Phys. Chem. **86**(26): 5163-5169.

Kalyanasundaram, K., Vlachopoulos, N., Krishnan, V., Monnier, A. and Grätzel, M. (1987). "Sensitization of $TiO_2$ in the Visible Light Region Using Zinc Porphyrins." J. Phys. Chem. **91**(9): 2342-2347.

Kamat, P. V., Bedja, I., Hotchandani, S. and Patterson, L. K. (1996). "Photosensitization of Nanocrystalline Semiconductor Films. Modulation of Electron Transfer between Excited Ruthenium Complex and $SnO_2$ Nanocrystallites with an Externally Applied Bias." J. Phys. Chem. **100**(12): 4900-4908.

Kamat, P. V., Hotchandani, S., Lind, M., Thomas, K. G., Das, S. and George, M. V. (1993). "Excited-State Properties and Photosensitization Behaviour of Bis(2,4-Dihydroxyphenyl)Squaraine." J. Chem. Soc. Faraday Trans. **89**(14): 2397-2402.

Kato, K. (1986). "Second-Harmonic Generation to 2048 Å in β–$BaB_2O_4$." IEEE J. Quantum Electron. **QE-22**(7): 1013-1014.

Kavan, L. and Grätzel, M. (1989). "Nafion Modified $TiO_2$ Electrodes: Photoresponse and Sensitization by Ru(II)-Bipyridyl Complexes." Electrochimica Acta **34**(9): 1327-1334.

Kay, A. and Grätzel, M. (1993). "Artificial Photosynthesis. 1. Photosensitisation of $TiO_2$ Solar Cells with Chlorophyll Derivatives and Related Natural Porphyrins." J. Phys. Chem **97**: 6272-6277.

Kay, A., Humphry-Baker, R. and Grätzel, M. (1994). "Artificial Photosynthesis. 2. Investigations of the Mechanism of Photosensitization of Nanocrystalline $TiO_2$ Solar Cells by Chlorophyll Derivatives." J. Phys. Chem. **98**(3): 952-959.

Kelly, C. A., Farzad, F., Thompson, D. W., Stipkala, J. M. and Meyer, G. J. (1999). "Cation Controlled Interfacial Charge Injection in Sensitized Nanocrystalline $TiO_2$." **Submitted**.

Kemnitz, K., Tamai, N., Yamazaki, I., Nakashima, N. and Yoshihara, K. (1987). "Site-Dependent Fluorescence Lifetimes of Isolated Dye Molecules Adsorbed on Organic Single Crystals and Other Substrates." J. Phys. Chem. **91**(6): 1423-1430.

Kirk, A. D., Langford, C. H., Joly, C. S., Lesage, R. and Sharma, D. K. (1984). "Sub-nanosecond Processes in the Quenching of a Copper Phthalocyanine Dye Adsorbed on $TiO_2$." J. Chem. Soc., Chem. Commun.: 961-962.

Klug, D. R., Rech, T., Joseph, D. M., Barber, J., Durrant, J. R. and Porter, G. (1995). "Primary Processes in Isolated Photosystem II Reaction Centres Probed by Mgic Angle Transient Absorption Spectroscopy." Chem. Phys. **194**: 433-442.

Kober, E. M. and Meyer, T. J. (1982). "Concerning the Absorption Spectra of the Ions $M(bpy)_3^{2+}$ (M = Fe, Ru, Os; bpy = 2,2'-Bipyridine)." Inorg. Chem. **21**(11): 3967-3977.

Kohle, O., Grätzel, M., Meyer, A. F. and Meyer, T. B. (1997). "The Photovoltaic Stability of Bis(isothiocyanato)ruthenium(II)- bis-2,2'-bipyridine-4,4'-dicarboxylic Acid and Related Sensitizers." Adv. Mater. **9**(11): 904-906.

Kosower, E. and Cotter, J. L. (1964). "Stable Free Radicals. II. The Reduction of 1-Methyl-4-cyanopyridinium Ion to Methylviologen Cation Radical." J. Am. Chem. Soc. **86**(5524-5527).

Krieger, C., Weiser, J. and Staab, H. A. (1985). "Molecular Structure and Fluorescence Behaviour of a Benzoquinone/Porphyrin/Benzoquinone Sandwich-Molecule." Tetrahedron Lett. **26**: 6055-6058.

Krol, R. V., Goossens, A. and Schoonman, J. (1997). "Mott-Schottky Analysis of Nanometer-Scale Thin-Film Anatase $TiO_2$." J. Electrochem. Soc. **144**(5): 1723-1727.

Lanzafame, J. M., D., M. R. J., Muenter, A. A. and Parkinson, B. A. (1992). "Ultrafast Charge-Transfer Dynamics at $SnS_2$ Surfaces." J. Phys. Chem. **96**(7): 2820-2826.

Lanzafame, J. M., Palese, S., Wang, D., Miller, R. J. D. and Muenter, A. A. (1994). "Ultrafast Nonlinear Optical Studies of Surface Reaction Dynamics: Mapping the Electron Trajectory." J. Phys. Chem. **98**(43): 11020-11033.

Lewis, N. S. (1996). "Photoelectrochemistry: Energy Conversion Using Semiconductor Electrodes." Interface (The Electrochemical Society): 28-31.

Lindström, H., Södergren, S., Solbrand, A., Rensmo, H., Hjelm, J., Hagfeldt, A. and Lindquist, S. E. (1997). "$Li^+$ Ion Insertion in $TiO_2$ (Anatase). 1. Chronoamperometry on CVD Films and Nanoporous Films." J. Phys. Chem. B **101**(39): 7710-7716.

Livage, J., Henry, M. and Sanchez, C. (1988). "Sol-Gel Chemistry of Transition Metal Oxides." Prog. Solid St. Chem. **18**: 259-341.

Lu, H., P. and Xie, X., S. (1997). "Single-Molecule Kinetics of Interfacial Electron Transfer." J. Phys. Chem. B **101**(15): 2753-2757.

Lytle, F. E. and Hercules, D. M. (1969). "The Luminescence of Tris(2,2'-bipyridine)ruthenium(II) Dichloride." J. Am. Chem. Soc. **91**(2): 253-257.

Mabrouk, P. A. and Wrighton, M. S. (1986). "Resonance Raman Spectroscopy of the Lowest Excited State of Derivatives of Tris(2,2'-bipyridine)ruthenium(II): Substituent Effects of Electron Localization in Mixed-Ligand Complexes." Inorg. Chem. **25**(4): 526-531.

Marcus, R. A. (1956). "On the Theory of Oxidation-Reduction Reactions Involving Electron Transfer. I." J. Chem. Phys. **24**(5): 966-978.

Marcus, R. A. (1964). "Chemical and Electrochemical Electron-Transfer Theory." Annu. Rev. Phys. Chem. **15**: 155-196.

Marcus, R. A. (1965). "On the Theory of Electron-Transfer Reactions. VI. Unified Treatment for Homogeneous and Electrode Reactions." J. Chem. Phys. **43**(2): 679-701.

Marcus, R. A. and Sutin, N. (1985). "Electron Transfers in Chemistry and Biology." Biochim. Biophys. Acta **811**: 265-322.

Martini, I., Hodak, J. H. and Hartland, G. V. (1998). "Effect of Structure on Electron Transfer Reactions between Anthracene Dyes and TiO2 Nanoparticles." J. Phys. Chem. B **102**(47): 9508-9517.

Matousek, P., Parker, A. W., Taday, P. F., Toner, W. T. and Towrie, M. (1996). "Two Independently Tunable and Synchronised Femtosecond Pulses Generated in the Visible at the Repetition Rate 40 kHz Using Optical Parametric Amplifiers." Optics Comm. **127**(4-6): 307-312.

Merry, S. A. P. (1998). "Exciton Transfer and Trapping in Photosystem II.", University of London.

Merry, S. A. P., Kumazaki, S., Tachibana, Y., Joseph, D. M., Porter, G., Yoshihara, K., Barber, J., Durrant, J. R. and Klug, D. R. (1996). "Sub-picosecond Equilibration of Excitation Energy in Isolated Photosystem II Reaction Centers Revisited: Time-Dependent Anisotropy." J. Phys. Chem. **100**(24): 10469-10478.

Meyer, G. J. (1997). "Efficient Light-to-Electrical Energy Conversion: Nanocrystalline $TiO_2$ Films Modified with Inorganic Sensitizers." J. Chem. Edu. **76**(6): 652-656.

Miller, J. R., Calcaterra, L. T. and Closs, G. L. (1984). "Intramolecular Long-Distance Electron Transfer in Radical Anions. The Effects of Free Energy and Solvent on the Reaction Rates." J. Am. Chem. Soc. **106**: 3047-3049.

Miller, R. J. D., McLendon, G. L., Nozik, A. J., Schmickler, W. and Willig, F. (1995). Surface Electron Transfer Processes. New York, VCH Publ., Inc.

Moser, C. C., Keske, J. M., Warncke, K., Farid, R. S. and Dutton, P. L. (1992). "Nature of Biological Electron Transfer." Nature **355**: 796-802.

Moser, J., Grätzel, M., Sharma, D. K. and Serpone, N. (1985). "Picosecond Time Resolved Studies of Photosensitized Electron Injection in Colloidal Semiconductors." Helv. Chim. Acta **68**: 1686-1690.

Moser, J. E. and Grätzel, M. (1998). "Excitation-Wavelength Dependence of Photoinduced Charge Injection at the Semiconductor-Dye Interface: Evidence for Electron Transfer from Vibrationally Hot Excited States." Chimia **52**(4): 160-162.

Moser, J. E., Noukakis, D., Bach, U., Tachibana, Y., Klug, D. R., Durrant, J. R., Humphry-Baker, R. and Grätzel, M. (1998). "Comment on "Measurement of Ultrafast Photoinduced Electron Transfer from Chemically Anchored Ru-Dye Molecules into Empty Electronic States in a Colloidal Anatase $TiO_2$ Film"." J. Phys. Chem. B **102**(18): 3649-3650.

Murakoshi, K., Kano, G., Wada, Y., Yanagida, S., Miyazaki, H., Matsumoto, M. and Murasawa, S. (1995). "Importance of Binding States between Photosensitizing Molucules and the $TiO_2$ Surface for Efficiency in a Dye-Sensitized Solar Cell." J. Electroanal. Chem. **396**(27-34).

Nakato, Y., Tsumura, A. and Tsubomura, H. (1983). "Photo- and Electroluminescence Spectra from an n-$TiO_2$ Semiconductor Electrode as Related to the Intermediates of the Photooxidation Reaction of Water." J. Phys. Chem. **87**(13): 2402-2405.

Nazeeruddin, M. K., Humphry-Baker, R., Grätzel, M. and Murrer, B. A. (1998). "Efficient Near IR Sensitization of Nanocrystalline $TiO_2$ Films by Ruthenium Phthalocyanines." Chem. Commun.: 719-720.

Nazeeruddin, M. K., Kay, A., Rodicio, I., Humphry-Baker, R., Muller, E., Liska, P., Vlachopoulos, N. and Grätzel, M. (1993). "Conversion of Light to electricity by cis-$X_2$Bis(2,2'-bipyridyl-4,4'-dicarboxylate)ruthenium(II) Charge - Transfer Sensitizers (X =$Cl^-$, $Br^-$, $I^-$, $CN^-$, and $SCN^-$) on Nanocrystalline $TiO_2$ Electrodes." J. Am. Chem. Soc. **115**(14): 6382-6390.

Nelson, J. (1999). "Continuous-Time Random-Walk Model of electron transport in nanocrystalline $TiO_2$ electrodes." Phys. Rev. B **59**(23): 15374-15380.

Nikogosian, D. N. (1997). Properties of Optical and Laser Related Materials: a Handbook. Chichester, John Wiley & Sons Ltd.

Noukakis, D. and Moser, J. E. Unpublished data.

Nozik, A. J. (1980). "Photoelectrochemical Cells." Phil. Trans. R. Soc. Lond. A **295**: 453-470.

O' Regan, B. and Grätzel, M. (1991). "A low-cost, high-efficiency solar cell based on dye sensitized colloidal $TiO_2$ films." Nature **353**: 737-739.

O' Regan, B., Moser, J. E., Anderson, M. and Grätzel, M. (1990). "Vectorial Electron Injection into Transparent Semiconductor Membranes and Electric Field Effects on the Dynamics fo Light-Induced Charge Separation." J. Phys. Chem. **94**(24): 8720-8726.

Pasternack, R. F., Huber, P. R., Boyd, P., Engasser, G., Francesconi, L., Gibbs, E., Fasella, P., Venturo, G. C. and Hinds, L. d. (1972). "On the Aggregation of Meso-Substituted Water-Soluble Porphyrins." J. Amer. Chem. Soc. **94**: 4511-4517.

Péchy, P., Rotzinger, F. P., Nazeeruddin, M. K., Kohle, O., Zakeeruddin, S. M., Humphry-Baker, R. and Grätzel, M. (1995). "Preparation of Phosphonated Polypyridyl Ligands to Anchor Transition-metal Complexes on Oxide Surfaces: Application for the Conversion of Light to Electricity with Nanocrystalline $TiO_2$ Films." J. Chem. Soc. Chem. Commun.: 65-66.

Porter, G. (1950). "Flash Photolysis and Spectroscopy. A New Method for the Study of Free Radical Reactions." Proc. Roy. Soc. A **200**: 284-300.

Rech, T., Durrant, J. R., Joseph, D. M., Barber, J., Porter, G. and Klug, D. R. (1994). "Does Slow Energy Transfer Limit the Observed Time Constant for Radical Pair Formation in Photosystem Two Reaction Centres?" Biochemistry **33**(49): 14768-14774.

Redmond, G. and Fitzmaurice, D. (1993). "Spectroscopic Determination of Flatband Potentials for Polycrystalline TiO2 Electrodes in Nonaqueous Solvents." J. Phys. Chem. **97**(7): 1426-1430.

Reed, M. K., Steiner-Shepard, M. K., Armas, M. S. and Negus, D. K. (1995). "Microjoule-Energy Ultrafast Optical Parametric Amplifiers." J. Opt. Soc. Am. B **12**(11): 2229-2236.

Rehm, J. M., Mclendon, G. L., Nagasawa, Y., Yoshihara, K., Moser, J. and Grätzel, M. (1996). "Femtosecond Electron Transfer Dynamics at a Sensitizing Dye-Semiconductor ($TIO_2$) Interface." J. Phys. Chem. **100**(23): 9577-9578.

Rensmo, H., Lunell, S. and Siegbahn, H. (1998). "Absorption and electrochemical properties of ruthenium (II) dyes, studied by semiempirical quantum chemical calculations." J. Photochem. Photobiol. A **114**: 117-124.

Rensmo, H., Södergren, S., Patthey, L., Westermark, K., Vayssieres, L., Kohle, O., Brühwiler, P. A., Hagfeldt, A. and Siegbahn, H. (1997). "The electronic structure of the cis-bis(4,4'-dicarboxy-2,2'-bipyridine) -bis(isothiocyanato) ruthenium(II) complex and its ligand 2,2'-bipyridyl-4,4'-dicarboxylic acid studied with electron spectroscopy." Chem. Phys. Lett. **274**: 51-57.

Rossetti, R. and Brus, L. E. (1984). "Time-Resolved Raman Scattering Study of Adsorbed, Semioxidized Eosin Y Formed by Excited-State Electron Transfer into Colloidal $TiO_2$ Particles." J. Am Chem. Soc. **106**(16): 4336-4340.

Rothenberger, G., Fitzmaurice, D. and Grätzel, M. (1992). "Spectroscopy of Conduction Band Electrons in Transparent Metal Oxide Semiconductor Films: Optical Determination of the Flatband Potential of Colloidal Titanium Dioxide Films." J. Phys. Chem. **96**(14): 5983-5986.

Ryan, M. A., Fitzgerald, E. C. and Spitler, M. T. (1989). "Internal Reflection Flash Photolysis Study of the Photochemistry of Eosin at $TiO_2$ Semiconductor Electrodes." J. Phys. Chem. **93**(16): 6150-6156.

Sakamaki, K., Itoh, K., Fujishima, A. and Gohshi, Y. (1990). "Surface Density of States of $TiO_2$(110) Single Crystal and Adsorbed Molecular Observation by Scanning Tunneling Microscopy and Tunneling Spectroscopy." J. Vac. Sci. Technol. A **8**(1): 614-617.

Saleh, B. E. A. and Teich, M. C. (1991). Fundamentals of Photonics. New York, John Wiley & Sons.

Sayama, K., Sugino, M., Sugihara, H., Abe, Y. and Arakawa, H. (1998). "Photosensitization of Porous $TiO_2$ Semiconductor Electrode with Xanthene Dyes." Chem. Lett.: 753-754.

Schmickler, W. (1996). Interfacial Electrochemistry. New York, Oxford University Press.

Sessler, J. L., Johnson, M. R., Creager, S. E., Fettinger, J. C. and Ibers, J. A. (1990). "Synthesis and Characterization of Quinone-Substituted Octaalkyl Porphyrin Monomers and Dimers." J. Am. Chem. Soc. **112**(25): 9310-9329.

Shen, Y., Wang, L., Lu, Z., Wei, Y., Zhou, Q., Mao, H. and Xu, H. (1995). "Fabrication, Characterization and Photovoltaic Study of a $TiO_2$ Microporous Electrode." Thin Solid Films **257**(144-146).

Shirakawa, A., Sakane, I. and T., K. (1998). "Sub-5-fs Pulse Generation by Pulse-front-matched Optical Parametric Amplification." Ultrafast Phenomena.

Shklover, V., Ovchinnikov, Y. E., Braginsky, L. S., Zakeeruddin, S. M. and Grätzel, M. (1998). "Structure of Organic/Inorganic Interface in Assembled Materials Comprising

Molecular Components. Crystal Structure of the Sensitizer Bis[(4,4'-carboxy-2,2'-bipyridine)(thiocyanato)]ruthenium(II)." Chem. Mater. **10**(9): 2533-2541.

Sibbett, W., Grant, R. G. and Spence, D. E. (1994). "Broadly Tunable Femtosecond Solid-State Laser Sources." Appl. Phys. B **58**: 171-181.

Skinner, D. E., Colombo, D. P., Cavaleri, J. J. and Bowman, R. M. (1995). "Femtosecond Investigation of Electron Trapping in Semiconductor Nanoclusters." J. Phys. Chem. **99**(20): 7853-7856.

Smith, W. L., Lui, P. and Bloembergen, N. (1977). "Superbroadening in $H_2O$ and $D_2O$ by Self-Focusing Picosecond Pulses from a Nd:YAG Laser." Phys. Rev. A **15**: 2396-2403.

Sosnowski, T. S., Stephens, P. B. and Norris, T. B. (1996). "Production of 30-fs Pulses Tunable throughout the Visible Spectral Region by a New Technique in Optical Parametric Amplification." Opt. Lett. **21**(2): 140-142.

Spence, D. E., Kean, P. N. and Sibbett, W. (1991). "60-fsec Pulse Generation from a Self-Mode-Locked Ti:sapphire Laser." Opt. Lett. **16**(1): 42-44.

Spitler, M. T. (1986). "Quenching of Dye-Sensitized Photocurrents at ZnO Semiconductor Electrodes." J. Phys. Chem. **90**(10): 2156-2159.

Spitler, M. T. and Calvin, M. (1977). "Electron Transfer at Sensitized $TiO_2$ Electrodes." J. Chem. Phys. **66**(10): 4294-4305.

Spitler, M. T., Ehret, A., Kietzmann, R. and Willig, F. (1997). "Electron Transfer Threshold for Spectral Sensitization of Silver Halides by Monomeric Cyanine Dyes." J. Phys. Chem. B **101**(14): 2552-2557.

Stipkala, J. M., Castellano, F. N., Heimer, T. A., Kelly, C. A., Livi, K. J. T. and Meyer, G. J. (1997). "Light-Induced Charge Separation at Sensitized Sol-Gel Processed Semiconductors." Chem. Mater. **9**(11): 2341-2353.

Tachibana, Y., Haque, S. A., Mercer, I. P., Durrant, J. R. and Klug, D. R. (1999). "Electron injection and recombination in dye sensitised nanocrystalline titanium dioxide films: a comparison of ruthenium bipyridyl and porphyrin sensitiser dyes." J. Phys. Chem. B **submitted**.

Tachibana, Y., Haque, S. A., Willis, R. L., Mercer, I. P., Moser, J. E., Klug, D. R. and Durrant, J. R. (1999). "Modulation of the Rate of Electron Injection in Dye Sensitised Nanocrystalline $TiO_2$ Films by Electrolyte Control of the Semiconductor Conduction Band Energetics." J. Phys. Chem. B **submitted**.

Tachibana, Y., Moser, J. E., Grätzel, M., Klug, D. R. and Durrant, J. R. (1996). "Subpicosecond Interfacial Charge Separation in Dye-Sensitized Nanocrystalline Titanium Dioxide Films." J. Phys. Chem **100**(51): 20056-20062.

Tani, T. (1990). "New Aspects of the Electron Transfer Mechanism for Spectral Sensitization and Supersensitization." J. Imaging Sci. **34**(4): 143-148.

Tani, T., Suzumoto, T. and Ohzeki, K. (1990). "Energy Gap Dependence of Efficiency of Photoinduced Electron Transfer from Cyanine Dyes to Silver Bromide Microcrystals in Spectral Sensitization." J. Phys. Chem. **94**(4): 1298-1301.

Thompson, D. W., Kelly, C. A., Farzad, F. and Meyer, G. J. (1999). "Sensitization of Nanocrystalline $TiO_2$ Initiated by Reductive Quenching of Molecular Excited States." Langmuir **15**(3): 650-653.

Tompkins, R. J. (1998). "The Design and Construction of a Solid-State Femtosecond Laser System and Its Application to Chemistry.", University of London.

Vinodgopal, K., Hua, X., Dahlgren, R., L., Lappin, A., G., Patterson, L., K. and Kamat, P., V. (1995). "Photochemistry of $Ru(bpy)_2(dcbpy)^{2+}$ on $Al_2O_3$ and $TiO_2$ Surfaces. An Insight into the Mechanism of Photosensitization." J. Phys. Chem. **99**(27): 10883-10889.

Watanabe, T. and Honda, K. (1982). "Measurement of the Extinction Coefficient of the Methyl Viologen Cation Radical and the Efficiency of Its Formation by Semiconductor Photocatalysis." J. Phys. Chem. **86**(14): 2617-2619.

Willig, F., Kietzmann, R. and Schwarzburg, K. (1993). Time-Resolved Luminescence, Photocurrent and Simple Reaction Scheme for a Folded Ultra-Thin-Layer Solar Cell. Photochemical and Photoelectrochemical Conversion and Storage of Solar Energy, Beijing, China, International Academic Publishers.

Willis, R. L., Olson, C. L., Nelson, J. and Durrant, J. R. (1999). Manuscript in preparation.

Yan, S. G. and Hupp, J. T. (1997). "Energetics of Electron Transfer at the Nanocrystalline Titanium Dioxide Semiconductor/Aqueous Solution Interface: pH Invariance of the Metal-Based Formal Potential of a Representative Surface-Attached Dye Couple." J. Phys. Chem. B **101**(9): 1493-1495.

Zaban, A., Ferrere, S. and Gregg, B., A. (1998). "Relative Energetics at the Semiconductor/Sensitizing Dye/Electrolyte Interface." J. Phys. Chem. B **102**(2): 452-460.

Zaban, A., Ferrere, S., Sprague, J. and Gregg, B., A. (1997). "pH-Dependent Redox Potential Induced in a Sensitizing Dye by Adsorption onto $TiO_2$." J. Phys. Chem. B **101**(1): 55-57.